Klaus Hornberger

Spectral Properties of Magnetic Edge States

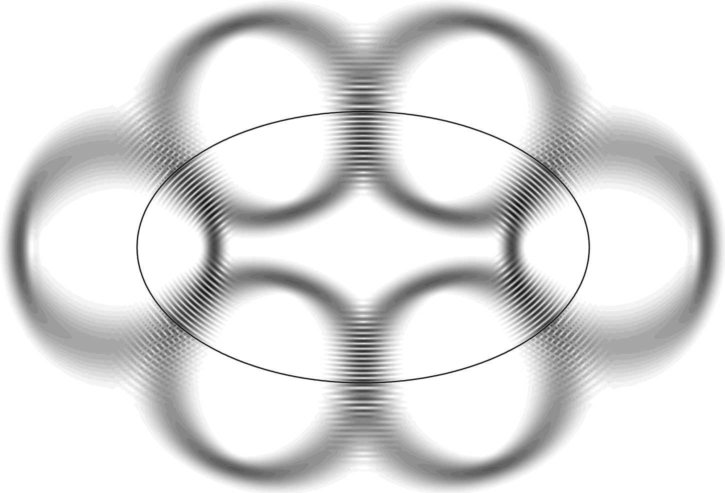

This thesis is available in electronic form at the Universitätsbibliothek München (`http://www.ub.uni-muenchen.de`) and at the author's home page (`http://www.klaus-hornberger.de`).

The title page shows correlated interior and exterior eigenstates of an elliptic billiard in the magnetic field. The two wave functions are localized along a stable pair of dual periodic orbits.

Spectral Properties of Magnetic Edge States

Dissertation der Fakultät für Physik
der Ludwig-Maximilians-Universität München

vorgelegt von Klaus Hornberger
aus München

München, den 19. Februar 2001

1. Gutachter: Priv. Doz. Dr. A. Buchleitner
2. Gutachter: Prof. Dr. W. Zwerger
Tag der mündlichen Prüfung: 17. Mai 2001

Zusammenfassung

Wir untersuchen die spektralen Eigenschaften magnetischer Randzustände, welche in den *inneren und äußeren* Quantenspektren magnetischer Billards auftreten. Zur Berechnung der Spektren erweitern wir die Randintegral-Methode auf den magnetischen Fall und allgemeine Randbedingungen. Nach der Regularisierung (hyper-)singulärer Integraloperatoren gelingt es erstmals, magnetische Billards bis in den extrem semiklassischen Bereich exakt zu quantisieren. Das Verständnis für die Ursache zunächst auftretender unphysikalischer Lösungen ermöglicht zudem die Herleitung der semiklassischen Spurformel aus den Grundgleichungen der Quantenmechanik. Um die Randzustände quantitativ zu charakterisieren, führen wir ein spektrales Maß ein. Diese *Randzustandsdiche* ermöglicht es, innere und äußere Spektren statistisch auzuwerten und semiklassisch zu beschreiben. Wir finden starke, nichttriviale *Kreuz-Korrelationen* zwischen den Quantenspektren des inneren und äußeren Problems. Ihnen liegt eine Dualität der beiden klassischen Dynamiken zugrunde. Umfangreiche numerische Studien belegen die aufgezeigten Zusammenhänge.

Abstract

We study the spectral properties of magnetic edge states, which exist in the *interior and exterior* spectra of magnetic quantum billiards. To quantize the billiards, the boundary integral method is extended to the magnetic problem and to general boundary conditions. By virtue of an analytical regularization of the (hyper-)singular integral operators, we obtain for the first time precise quantum spectra even in the extreme semiclassical regime. The insight gained into the structure of the spectral determinant enables us to derive the semiclassical trace formula for magnetic billiards from first principles. We propose a spectral measure, which quantifies the intuitive notion of edge states. This *density of edge states* allows to analyse the interior and exterior spectra statistically, and to describe them semiclassically. We find strong, non-trivial *cross-correlations* between the interior and exterior spectra. These correlations are based on a duality of the corresponding classical dynamics. Our analytical results are confirmed by extensive numerical studies.

Meinen Eltern gewidmet

This work was carried out under the guidance of Uzy Smilansky.
I am indebted to my advisor for his encouragement, confidence, and support and for the exceptional pleasure of working with him for three years, which I truly enjoyed. Many of the ideas presented here are his or arose in discussions with him.

I am also very grateful to Boris Gutkin for many helpful discussions, and to Uri Gavish, Jörn Göres, Bernard Helffer, Tsampikos Kottos, Andreas Krug, Cord Müller, Harel Primack, Peter Schlagheck, Martin Sieber, Holger Schanz, Thomas Wellens, Sandro Wimberger, and the many others whose interest and criticism contributed to this work.

Special thanks go to Andreas Buchleitner, for his care and his continuous concern in my progresses, and for a critical reading of the manuscript.

The research was carried out at the Weizmann Institute of Science, *Rehovot, and the* Max-Planck Institut für Physik komplexer Systeme, *Dresden. I am grateful to everyone in these institutes for creating a stimulating, open-minded, and truly international atmosphere it was fun to work in. Generous support by the Minerva foundation, the Minerva Center for Nonlinear Studies, and the MPG is gratefully acknowledged.*

Klaus Hornberger

Contents

1 Introduction **1**
- 1.1 Framework 1
- 1.2 Formulation of the problem and overview of the results 2
- 1.3 Structure of the thesis 3

2 Motion in the free magnetic plane **5**
- 2.1 Classical motion 5
- 2.2 Quantization 7
- 2.3 The scaling property 11
- 2.4 The free quantum propagator 13
- 2.5 The free Green function 15
  - 2.5.1 The semiclassical Green function 16
  - 2.5.2 The exact Green function 18
  - 2.5.3 Properties of the free Green function 19
  - Notes 21

3 Introducing a boundary **23**
- 3.1 Motion in a restricted domain 23
- 3.2 The classical billiard 25
  - 3.2.1 The billiard bounce map 25
  - 3.2.2 Integrable and hyperbolic billiards 26
  - 3.2.3 The interior-exterior duality 28
- 3.3 Quantum billiards 30
  - 3.3.1 General boundary conditions 30
  - 3.3.2 The quantum spectrum 31
  - 3.3.3 Asymptotic counting functions 32
- 3.4 Orbital magnetism 35

4 Quantization in the interior and the exterior **39**
- 4.1 Boundary methods 39
- 4.2 The boundary integral equations 40
  - 4.2.1 Single and double layer equations 40
  - 4.2.2 Spurious solutions and the combined operator 43
  - 4.2.3 Wave functions 45
- 4.3 The boundary operators 45
  - 4.3.1 Explicit expression for the integral kernels 45
  - 4.3.2 The hypersingular integral operator 47

4.4 Solving the integral equations . . . 48
4.5 Numerical analysis . . . 51

5 Results of the boundary integral method 55
5.1 Spectral statistics . . . 55
5.2 Wave functions in the interior and in the exterior . . . 58
5.3 General boundary conditions . . . 64

6 Semiclassical Quantization 69
6.1 The semiclassical boundary integral operators . . . 70
6.2 From boundary to map operators . . . 73
6.3 Trace formula for hyperbolic billiards . . . 76
    6.3.1 The saddle point conditions . . . 76
    6.3.2 The prefactors . . . 80
    6.3.3 Performing the trace . . . 82
    6.3.4 Geometric interpretation . . . 85
6.4 Trace formula for the integrable case . . . 87
    6.4.1 The disk billiard . . . 87
    6.4.2 Operators for the integrable map . . . 88
    6.4.3 The explicit trace formula . . . 89
    Notes . . . 92

7 Separable geometries 93
7.1 The disk billiard . . . 93
    7.1.1 Semiclassical quantization . . . 94
    7.1.2 Relation to the periodic orbit formula . . . 96
    7.1.3 Exact quantization . . . 99
7.2 The periodic line . . . 100

8 A spectral measure for edge states 105
8.1 Bulk states and edge states . . . 105
    8.1.1 A quantum criterion . . . 105
    8.1.2 The density of edge states . . . 106
8.2 The semiclassical density of edge states . . . 109
8.3 Asymptotic properties of edge and bulk states . . . 112
    8.3.1 Bulk state energies and weights . . . 112
    8.3.2 The mean edge counting function . . . 115
8.4 Edge magnetization as a spectral measure . . . 115

9 Properties of edge state spectra 119
9.1 Universal auto-correlations . . . 119
9.2 The action spectrum . . . 123
9.3 Using the edge magnetization . . . 125

10 Spectral cross correlations 129
10.1 The prediction of spectral cross correlations 129
10.2 Statistical evidence 132
10.3 The pair relation 136
10.4 Conclusions 143

Appendices 145

A Mathematical appendix 145
A.1 The stationary phase approximation 145
A.2 The singular integrals 146

B Angular momentum representation 148
B.1 Free Green function 148
B.2 The null field method 150

C The product relation of the map operators 152

D Scaled spectra 154

E Numerical evaluation of the Green function 155

List of Symbols 159

Bibliography 165

Chapter 1

Introduction

1.1 Framework

The field of *quantum chaos* tries to relate the properties of complex quantum systems to the corresponding classical motion. Its paradigm is the periodic orbit theory developed by Gutzwiller [1], Berry & Tabor [2] and many others. According to this theory, the expectation values of a quantum system are determined asymptotically by the set of classical periodic trajectories. In a common effort, nuclear, atomic, and mesoscopic physicists, as well as researchers engaged in spectral and asymptotic theory, are trying to reconcile this with other findings, such as the universality of spectral statistics, and to apply it to specific systems. For a number of books and reviews on the general subject of quantum chaos and its history, see Refs [3–10].

Looking for a model system which displays most of the generic properties of bound Hamiltonian dynamics, one is led to the *billiard* problem. Here, a point particle moves frictionless in a two-dimensional domain fenced off by a boundary. Impinging on the latter, the classical particle is reflected specularly, while the quantum wave function must satisfy a boundary condition. The classical phase space is determined by the shape of the billiard boundary, and classes of billiards are known, which generate all types of dynamics, from integrable to completely chaotic [11]. Since it is relatively easy to obtain the corresponding quantum spectra, many discoveries in the field of quantum chaos, like the universality of chaotic spectra [12], the scarring of wave functions by unstable periodic orbits [13, 14], and the existence of action correlations [15] were first made in quantum billiards.

The quantum implications of chaotic scattering, on the other hand, may be studied by considering the billiard boundary as a scattering obstacle for an outside particle. An intimate relation between the scattering problem and the interior quantization exists [16], which can be understood semiclassically, and was discovered on semiclassical grounds [17].

Although most experiments on quantum billiards are done numerically, they may be physically realized in the two-dimensional electron gas of high-mobility semiconductor heterostructures [18]. Typically, a perpendicular, homogeneous magnetic field is applied in addition, which is the experimentally easiest way to modify the billiard.

Magnetic billiards

The presence of a Lorentz force affects the classical, two-dimensional billiard dynamics. For sufficiently strong fields, closed cyclotron orbits occur, while other trajectories perform a skipping motion along the billiard boundary. Moreover, the exterior dynamics (where the billiard boundary acts as an obstacle from outside) is not a scattering problem as in the field free case but exhibits bounded skipping motion around the billiard.

The magnetic quantum spectra and wave functions reflect these classical properties. For strong fields, a separation takes place in the spectrum. Close to the energies of the Landau levels one finds *bulk states* which correspond to a free cyclotron motion of the particle. In addition, *edge states* appear which are localized at the boundary, corresponding to a skipping motion along it. Unlike the field free case, the spectrum is purely discrete also in the exterior, with accumulation points at the energies of the Landau levels.

1.2 Formulation of the problem and overview of the results

The guiding theme of this thesis is the question whether the interior and exterior quantum spectra of magnetic billiards are related. Is it possible to infer the statistical properties of one spectrum from the other? Having a pair of interior and exterior spectra at hand, can one tell whether they belong to the same billiard? In principle, these are issues of spectral theory – similar in spirit to Kac's question whether one can "hear the shape of a drum" [19] – but considerably more difficult with the magnetic field present. Our objective is to shed light upon these questions, using insights and techniques from quantum chaos.

The central observation to be made is that there exists a *duality* of the corresponding interior and exterior classical motion. For any interior periodic orbit one finds, in general, an intimately related periodic orbit of the exterior problem, and vice versa. (Strictly, this does not hold always, but under rather general conditions.) Since the set of periodic orbits determines the quantum spectrum asymptotically (by virtue of the trace formulae) one may expect that their correlation carries over to the quantum problem.

Indeed, we shall uncover strong, non-trivial cross-correlations between the quantum spectra of interior and exterior magnetic billiards. We will give evidence that they are the quantum fingerprints of the classical duality. The correlations are "non-trivial" in the sense that they are not observed by standard means. Rather, the spectra must be viewed in an appropriate way since it is specifically the *edge states* which are related.

Although the partition of the spectrum into edge states and bulk states is intuitively clear, we are not aware of an objective general criterion in the literature to distinguish edge from bulk. In particular, a strict separation of the spectrum into two types exists only in the extreme semiclassical limit. For finite $\hbar$ a gradual transition takes place between the two extremes. As a prerequisite, we therefore propose a spectral measure for edge states which provides a quantitative criterion and accounts for the existence of transitional states. We will argue that our definition is a very natural one. It renders the mean density of edge states *equal* for the interior and the exterior problems – and proportional to the circumference of the billiard. Moreover, this measure has a clear semiclassical interpretation in terms of the skipping trajectories. It facilitates the statistical and semiclassical analysis of magnetic spectra.

Large sets of exact quantum eigenvalues are needed in order to perform spectral statistics, with energies reaching far into the semiclassical regime. This is a non-trivial computational problem. To our knowledge, the exterior problem was never addressed, and the published spectra of the interior one are limited to the first few hundred eigenvalues [20–25]. Below, a method is developed which allows, for the first time, the calculation of spectra and wave functions in the interior *and* in the exterior of magnetic billiards, in particular at strong field strengths, and for high energies.

1.3 Structure of the thesis

In the next two chapters, we give a survey of the classical and quantum motion in the free magnetic plane and in magnetic billiards, respectively. Although many of the statements in **Chapter 2** are elementary, we shall present them in some detail. This allows the discussion of concepts, such as the scaling properties or the semiclassical approximation, which we refer to frequently in the remainder of the thesis. In the first part of **Chapter 3**, the classical interior-exterior duality is explained. Turning to the quantum problem, we introduce general boundary conditions and discuss the asymptotic properties of magnetic spectra. The introductory chapters conclude with the definition of a scaled edge magnetization.

In **Chapter 4**, we solve the quantization problem in the interior and exterior of arbitrary magnetic billiards by means of a boundary integral method. We explain why spurious solutions arise initially, and how they can be systematically avoided. The performance of the method is demonstrated in **Chapter 5**. Apart from wave functions in the extreme semiclassical regime, spectral statistics are presented, as far as possible with the standard spectral density.

Chapter 6 is devoted to the derivation of the semiclassical trace formula for hyperbolic and integrable magnetic billiards. We use a surface-of-section method starting from the boundary integral operators. Since the derivation is given for the first time, it will be presented in some detail, with particular consideration for the inherently non-symmetric properties of the map operators. The integrable disk billiard is quantized for a second time in **Chapter 7** making use of its separability. In combination with the result of Chapter 6, this allows the trace formula to be extended to general boundary conditions.

The spectral density of edge states is introduced in **Chapter 8**. It gives the concept of edge states a quantitative meaning and is appropriate, both in the deep quantum and in the semiclassical regime. The new measure allows spectral analysis to be performed also in the exterior. The consistency with random matrix theory is checked in **Chapter 9**, and the quantum edge state density is compared to the result of the trace formula.

In **Chapter 10** we finally identify non-trivial cross-correlations between interior and exterior edge spectra. We show that they are based on a classical duality of the periodic orbits. In order to observe them, the spectral density of edge states, or an equivalent measure like the edge magnetization, is of crucial importance.

Chapter 2

Motion in the free magnetic plane

We start by collecting a number of elementary statements on the classical and quantum motion in the magnetic plane. It allows to introduce the notation used throughout this thesis, and to set the stage for the discussion in the following chapters. The treatment of the quantum time evolution operator in Section 2.4, in particular, yields the opportunity to discuss the semiclassical approximation. In Section 2.5, the Green function of a particle in the free magnetic plane is derived, in both, its semiclassical and its exact form.

2.1 Classical motion

We consider the motion of a non-relativistic, spinless, charged particle in the two-dimensional Euclidean plane,^{1} which is subject to a magnetic field. Its Lagrangian has the form [26]

$$\mathcal{L} = \frac{m_\circ}{2}\mathbf{v}^2 + q\,\mathbf{v}\mathbf{A}(\mathbf{r})\,, \tag{2.1}$$

where $m_\circ$ and q denote mass and charge, respectively.[*] The vectors $\mathbf{r} = (x,y)^{\mathrm{T}}$ and $\mathbf{v} = \dot{\mathbf{r}}$ give the position and velocity of the particle. Both of them determine the canonical momentum

$$\mathbf{p} = \frac{\partial \mathcal{L}}{\partial \mathbf{v}} = m_\circ \mathbf{v} + q\mathbf{A}(\mathbf{r})\,. \tag{2.2}$$

The classical time evolution is given by the Lagrangian equation of motion

$$\dot{\mathbf{p}} = q\,\boldsymbol{\nabla}(\mathbf{v}\mathbf{A}(\mathbf{r}))\,. \tag{2.3}$$

Here, the magnetic field is decribed by the two-dimensional vector potential $\mathbf{A}(\mathbf{r})$. The latter must be time independent, $\partial_t \mathbf{A} = 0$, to avoid electric forces. It follows from (2.3) that the equation of motion for the velocity $\mathbf{v}$ depends only on the rotation $B = \boldsymbol{\nabla} \times \mathbf{A}$ of the vector potential. It is Newton's equation of motion

---

[*] SI units are used until the introduction of scaled, dimensionless variables in Sect. 2.3.

$$m_\circ \, \ddot{\mathbf{r}} = qB \, \boldsymbol{\nabla}(\mathbf{r} \times \mathbf{v}) \tag{2.4}$$

with the (magnetic) Lorentz force on the right side. The latter acts perpendicularly to the velocity and is proportional to the magnetic field B (the magnetic induction).

Throughout this thesis we are interested in the case of a *homogeneous* magnetic field B (with $q\,B > 0$). Equation (2.4) is then easily integrated, yielding the *cyclotron motion*

$$\begin{aligned} \mathbf{r}(t) &= \mathbf{r}(0) + \frac{1}{\omega_\mathrm{c}} \begin{pmatrix} \sin(\omega_\mathrm{c} t) & 1 - \cos(\omega_\mathrm{c} t) \\ -1 + \cos(\omega_\mathrm{c} t) & \sin(\omega_\mathrm{c} t) \end{pmatrix} \mathbf{v}(0) && (2.5) \\ &= \mathbf{r}(0) - \boldsymbol{\rho}(0) + \boldsymbol{\rho}(t) && (2.5\mathrm{a}) \end{aligned}$$

with $\mathbf{r}(0)$ and $\mathbf{v}(0)$ the initial position and velocity, respectively, and $\omega_\mathrm{c}{=}qB/m_\circ$ the cyclotron frequency. The particle moves clockwise on a circle with constant angular velocity ω_c. Below, we will need the velocity as a function of the initial and the final position, $\mathbf{r}(0)$ and $\mathbf{r}(t)$. Apart from the times which are multiples of the cyclotron period $2\pi/\omega_\mathrm{c}$, it is given by

$$\mathbf{v}(t) = \frac{\frac{1}{2}\omega_\mathrm{c}}{\sin(\frac{1}{2}\omega_\mathrm{c} t)} \begin{pmatrix} \cos(\frac{1}{2}\omega_\mathrm{c} t) & \sin(\frac{1}{2}\omega_\mathrm{c} t) \\ -\sin(\frac{1}{2}\omega_\mathrm{c} t) & \cos(\frac{1}{2}\omega_\mathrm{c} t) \end{pmatrix} (\mathbf{r}(t) - \mathbf{r}(0)) \, , \tag{2.6}$$

which follows from equation (2.5). In its second line, (2.5a), the motion is stated in terms of the radius vector,

$$\boldsymbol{\rho}(t) := \frac{1}{\omega_\mathrm{c}} \begin{pmatrix} -v_y(t) \\ v_x(t) \end{pmatrix} \, , \tag{2.7}$$

which points from the (instantaneous) center of motion to the particle position. Obviously, the center $\mathbf{c}(t) = \mathbf{r}(t) - \boldsymbol{\rho}(t)$ is a constant of the motion. To verify this in a more formal way, one may consider the classical Hamiltonian

$$\mathrm{H} = \mathbf{p}\dot{\mathbf{r}} - \mathcal{L} = \frac{1}{2m_\circ}(\mathbf{p} - q\mathbf{A}(\mathbf{r}))^2 \tag{2.8}$$

as a function of the canonically conjugate variables $\mathbf{r}$ and $\mathbf{p}$. Here, (2.2) was used to express the velocity in terms of momentum and position. A short calculation shows that the Poisson bracket vanishes indeed,

$$\frac{\mathrm{d}}{\mathrm{d}t}(\mathbf{r} - \boldsymbol{\rho}) \equiv \frac{\mathrm{d}}{\mathrm{d}t}\mathbf{c} = \{\mathrm{H}, \mathbf{c}\} = 0 \, . \tag{2.9}$$

Similarly, the energy $E := \mathrm{H}(\mathbf{r}, \mathbf{p}) = \frac{m_\circ}{2}\mathbf{v}^2$ is constant (as well as the cyclotron radius $|\boldsymbol{\rho}|$ and the kinetic angular momentum with respect to the center of motion, $\boldsymbol{\rho} \times \mathbf{v}$, which are functions thereof.) In contrast, the canonical momentum $\mathbf{p}$ itself is not a constant of the motion. It does not even have a kinetic meaning, in general, since it depends on the vector potential, cf. (2.2), which is not uniquely specified by the magnetic field. Rather, the gradient of any scalar field $\chi(\mathbf{r})$ (ie, any "gauge field") may be added to the vector potential without affecting the classical equation of motion (2.4),

$$\boldsymbol{\nabla} \times (\mathbf{A}(\mathbf{r}) + \boldsymbol{\nabla}\chi(\mathbf{r})) = \boldsymbol{\nabla} \times \mathbf{A}(\mathbf{r}) = B \, . \tag{2.10}$$

An important consequence is met in the quantum description, where the canonical momentum variable turns into a fundamental operator, leaving a mark of the choice of the vector potential on the quantum evolution. Nonetheless, according to the correspondence principle, every observable will have to be independent of the chosen gauge.

Before turning to the quantization problem, we note that the general vector potential for homogenous magnetic fields may be written in the form

$$\mathbf{A}(\mathbf{r}) = \frac{B}{2}\begin{pmatrix} -y \\ x \end{pmatrix} + \boldsymbol{\nabla}\chi(\mathbf{r}) \, . \tag{2.11}$$

The choice of χ is a matter of convenience. An important case is the *symmetric* gauge, $\chi = 0$, which distinguishes merely a point in the plane (the origin). Choosing $\chi = -\frac{B}{2}xy$, on the other hand, yields the *Landau* gauge, which distinguishes a direction (the orientation of the y-axis). These two gauges are particularly important because they turn components of the canonical momentum into constants of the motion. In the Landau case, p_x is given by the (constant) y-component of the center of motion,

$$\mathbf{A} = \mathbf{A}_{\mathrm{Lan}} \equiv B\begin{pmatrix} -y \\ 0 \end{pmatrix} \qquad \Rightarrow \qquad p_x = -m_\circ\omega_{\mathrm{c}}\, c_y \; , \tag{2.12}$$

while the symmetric gauge fixes the (canonical) angular momentum with respect to the origin, $L = \mathbf{r} \times \mathbf{p}$,

$$\mathbf{A} = \mathbf{A}_{\mathrm{sym}} \equiv \frac{B}{2}\begin{pmatrix} -y \\ x \end{pmatrix} \qquad \Rightarrow \qquad L := \mathbf{r} \times \mathbf{p} = \frac{m_\circ\omega_{\mathrm{c}}}{2}\left(|\mathbf{c}|^2 - |\boldsymbol{\rho}|^2\right) \, . \tag{2.13}$$

It is determined by the distance $|\mathbf{c}|$ of the center of motion from the origin, and the cyclotron radius $\rho = |\boldsymbol{\rho}|$.

In the course of this work, it will be important at several points to state equations in a *manifestly* gauge invariant fashion. This is done by keeping χ unspecified, and verifying that the resulting expressions do not depend on its choice. As the only restriction, χ will be assumed to be a harmonic function, ie $\boldsymbol{\nabla}^2\chi = 0$, throughout. This rules out conveniently the occurrence of singularities in χ, but keeps the essential gauge freedom. Moreover, it ensures that the vector potential (2.11) is divergence free, $\boldsymbol{\nabla}\mathbf{A} = 0$, which facilitates a number of mathematical transformations.

Turning to the quantum mechanical description, the quantum time evolution will be treated in terms of the path integral formulation in Section 2.4. Before that, we discuss the stationary solutions of the Schrödinger equation (in a specific gauge, to prove the rule stated above). This allows to discuss the spectrum and the scaling properties of the Hamiltonian straightforwardly.

2.2 Quantization

In quantum mechanics, the canonical variables $\mathbf{r}$ and $\mathbf{p}$ become observables, expressed as operators in the Hilbert space of square-integrable functions $\mathcal{L}_2(\mathbb{R}^2)$. They turn the

Hamiltonian (2.8) into an operator,

$$\mathrm{H} = \frac{1}{2m_\circ}(\mathbf{p} - q\mathbf{A}(\mathbf{r}))^2 \,, \tag{2.14}$$

whose spectrum determines the energies E of the stationary states. In position representation, $\mathbf{p} = -\mathrm{i}\hbar\boldsymbol{\nabla}$, the eigenvalue equation reads

$$\frac{1}{2m_\circ}(-\mathrm{i}\hbar\boldsymbol{\nabla} - q\mathbf{A})^2\,\psi(\mathbf{r}) = E\,\psi(\mathbf{r}) \,. \tag{2.15}$$

In addition, the solution $\psi(\mathbf{r})$ must be normalizable to qualify as a stationary quantum state.

$$\int \mathrm{d}^2\mathbf{r}\,|\psi(\mathbf{r})|^2 = 1 \tag{2.16}$$

The energy eigenstates in the magnetic plane were obtained not before 1930, when Landau published his article on orbital diamagnetism [27]. Although he used the gauge (2.12), the symmetric vector potential (2.13) will prove more convenient in the following. First, we introduce a quantum length scale

$$b := \left(\frac{2\hbar}{qB}\right)^{\frac{1}{2}} \tag{2.17}$$

and call it the magnetic length, although it *differs* from Landau's definition^2 by a factor of $\sqrt{2}$. It allows to transform position and momentum operators into dimensionless quantities, denoted by a tilde,

$$\tilde{\mathbf{r}} := \frac{\mathbf{r}}{b} \quad \text{and} \quad \tilde{\mathbf{p}} := \frac{b}{\hbar}\mathbf{p} \,, \tag{2.18}$$

In the symmetric gauge, the Hamiltonian (2.14) now assumes a particularly simple form,

$$\mathrm{H} = \hbar\omega\,\frac{1}{2}\left(\tilde{\mathbf{p}}^2 + \tilde{\mathbf{r}}^2\right) - \omega\,\hbar(\tilde{\mathbf{r}} \times \tilde{\mathbf{p}}) = \mathrm{H}_{\mathrm{osc}} - \omega\,\mathrm{L}. \tag{2.19}$$

It is given by the energy of a two-dimensional harmonic oscillator $\mathrm{H}_{\mathrm{osc}}$ minus its angular momentum $\mathrm{L} = \mathbf{r} \times \mathbf{p}$, in quanta of the same size. The oscillator eigen-frequency differs from the cyclotron frequency by a factor of 2. It is given by

$$\omega := \frac{qB}{2m_\circ} = \frac{\omega_{\mathrm{c}}}{2} \,, \tag{2.20}$$

and known from the precession of magnetic moments as the Larmor frequency. In order to construct the complete set of energy eigenstates on the magnetic plane, it is useful to consider the annihilation operators of the left- and right-circular quanta, (see, eg, [28],)

$$\hat{a}_{\binom{\mathrm{R}}{\mathrm{L}}} = \frac{1}{2}(\tilde{x} \mp \mathrm{i}\tilde{y} + \mathrm{i}(\tilde{p}_x \mp \mathrm{i}\tilde{p}_y)) \,, \tag{2.21}$$

with $[\hat{a}_{\rm L},\hat{a}^\dagger_{\rm L}] = [\hat{a}_{\rm R},\hat{a}^\dagger_{\rm R}] = 1$ as the only non-vanishing commutators. It is well known [28] that the simultaneous eigenstates of the left- and right-circular number operators $(\hat{a}^\dagger_{\rm L}\hat{a}_{\rm L})$ and $(\hat{a}^\dagger_{\rm R}\hat{a}_{\rm R})$ form a complete basis set of $\mathcal{L}_2(\mathbb{R}^2)$. An eigenstate corresponding to n left-circular and m right-circular quanta, respectively, is given by

$$|n,m\rangle = \frac{1}{\sqrt{n!\,m!}}(\hat{a}^\dagger_{\rm L})^n(\hat{a}^\dagger_{\rm R})^m|0,0\rangle\ , \tag{2.22}$$

with $n,m \in \mathbb{N}_0$. Here, $|0,0\rangle$ denotes the harmonic oscillator ground state, a Gaussian in position representation, $\langle\mathbf{r}|0,0\rangle = \exp(-\frac{1}{2}\mathbf{r}^2/b^2)/\sqrt{b^2\pi}$. Like all the states (2.22), it is square-integrable and obeys the normalization condition (2.16).

Inverting equations (2.21), the Hamiltonian of a particle in the magnetic plane may be expressed in terms of the circular operators. It assumes a form

$$\begin{aligned}\mathrm{H} = \mathrm{H}_{\rm osc} - \omega\,\tilde{L} &= \hbar\omega\,(\hat{a}^\dagger_{\rm R}\hat{a}_{\rm R} + \hat{a}^\dagger_{\rm L}\hat{a}_{\rm L} + 1) - \hbar\omega\,(\hat{a}^\dagger_{\rm R}\hat{a}_{\rm R} - \hat{a}^\dagger_{\rm L}\hat{a}_{\rm L})\\ &= \hbar\omega_{\rm c}\left(\hat{a}^\dagger_{\rm L}\hat{a}_{\rm L} + \frac{1}{2}\right)\ ,\end{aligned} \tag{2.23}$$

which depends only on the number operator of the left-circular quanta. It follows that the states (2.22) form a complete set of eigenstates of the magnetic plane. Their energies are determined by the number n of left-circular quanta, called the Landau level,

$$E = \hbar\omega_{\rm c}\left(n + \frac{1}{2}\right)\ . \tag{2.24}$$

This proves that the spectrum of H is discrete and equidistant.[*] The fact that the energy does not depend on m shows that each Landau level is infinitely degenerate (with a countable infinity.)

This degeneracy is due to the independence of the energy on the position of the center of motion. To show that the latter is indeed determined by the right-circular quanta alone, we note the operators corresponding to the classical radius vector (2.7) and the center of motion $\mathbf{c} = \mathbf{r} - \boldsymbol{\rho}$, respectively,

$$\tilde{\boldsymbol{\rho}} \equiv \frac{\boldsymbol{\rho}}{b} = \frac{1}{2}\begin{pmatrix}\hat{a}_{\rm L} + \hat{a}^\dagger_{\rm L}\\ -\mathrm{i}(\hat{a}_{\rm L} - \hat{a}^\dagger_{\rm L})\end{pmatrix} \qquad \text{and} \qquad \tilde{\mathbf{c}} \equiv \frac{\mathbf{c}}{b} = \frac{1}{2}\begin{pmatrix}\hat{a}_{\rm R} + \hat{a}^\dagger_{\rm R}\\ \mathrm{i}(\hat{a}_{\rm R} - \hat{a}^\dagger_{\rm R})\end{pmatrix}\ . \tag{2.25}$$

Here, equation (2.2) was used to express the velocity in terms of momentum and position. Clearly, $\mathbf{c}$ commutes with the Hamiltonian, like in the classical case. The components ρ_x and ρ_y, on the other hand, are not constants of the motion, although the cyclotron radius $|\boldsymbol{\rho}|$ is again fixed and determined solely by the energy. This can be seen from the squared moduli of the vectors,

$$|\tilde{\boldsymbol{\rho}}|^2 = \hat{a}^\dagger_{\rm L}\hat{a}_{\rm L} + \frac{1}{2} \qquad \text{and} \qquad |\tilde{\mathbf{c}}|^2 = \hat{a}^\dagger_{\rm R}\hat{a}_{\rm R} + \frac{1}{2}\ , \tag{2.26}$$

which contain only the number operators of left- and right-circular quanta. Consequently, the states (2.22) with fixed n and m are eigenstates of these operators. They are characterized by definite expectation values for the cyclotron radius and for the distance from the origin to the center of motion. Moreover, these stationary states are eigenvectors of the (canonical) angular momentum, obtained by the difference $|\tilde{\mathbf{c}}|^2 - |\tilde{\boldsymbol{\rho}}|^2 = L/\hbar$, in analogy to the classical result (2.13).

---

[*] For mathematical literature on the spectral properties of magnetic Schrödinger operators see [29,30].

The general eigenstate of $|\tilde{\boldsymbol{\rho}}|^2$ (with eigenvalue $n + \frac{1}{2}$) is given by a superposition of states (2.22) with different quantum numbers m. We will call any such stationary state a Landau state, within the Landau level n.

Coherent states

The states (2.22) are eigenstates of the radial components of the operators $\boldsymbol{\rho}$ and $\mathbf{c}$. Their azimuthal components are maximally uncertain. It is known from the two-dimensional harmonic oscillator that the common eigenvectors of $\hat{a}_{\mathrm{L}}$ and $\hat{a}_{\mathrm{R}}$ have the property to minimize the uncertainty product [28]. These *coherent* states are given by the superposition

$$\Big|\alpha_{\mathrm{L}};\alpha_{\mathrm{R}}\Big\rangle := \exp\left(-\frac{|\alpha_{\mathrm{L}}|^2+|\alpha_{\mathrm{R}}|^2}{2}\right)\sum_{n,m=0}^{\infty}\frac{(\alpha_{\mathrm{L}})^n(\alpha_{\mathrm{R}})^m}{\sqrt{n!m!}}\,|n,m\rangle\,, \tag{2.27}$$

with α_{L}, $\alpha_{\mathrm{R}} \in \mathbb{C}$ the associated eigenvalues. If considered in the magnetic plane, the expectation values of $\boldsymbol{\rho}$ and $\mathbf{c}$ are determined directly by these eigenvalues,

$$\begin{aligned}\Big\langle\alpha_{\mathrm{L}};\alpha_{\mathrm{R}}\Big|\boldsymbol{\rho}\Big|\alpha_{\mathrm{L}};\alpha_{\mathrm{R}}\Big\rangle &= b\begin{pmatrix}\mathrm{Re}(\alpha_{\mathrm{L}})\\ \mathrm{Im}(\alpha_{\mathrm{L}})\end{pmatrix}\\ \Big\langle\alpha_{\mathrm{L}};\alpha_{\mathrm{R}}\Big|\mathbf{c}\Big|\alpha_{\mathrm{L}};\alpha_{\mathrm{R}}\Big\rangle &= b\begin{pmatrix}\mathrm{Re}(\alpha_{\mathrm{R}})\\ -\mathrm{Im}(\alpha_{\mathrm{R}})\end{pmatrix}\,,\end{aligned} \tag{2.28}$$

as one finds immediately from equation (2.25). The corresponding uncertainties $\Delta\rho_x = \Delta\rho_y = \Delta c_x = \Delta c_y = b/2$ are minimal, indeed. Furthermore, the wave functions (2.27) remain of the coherent type as they evolve in time. From (2.23) one observes that the state at time t,

$$\mathrm{e}^{-\mathrm{i}\mathrm{H}t/\hbar}\Big|\alpha_{\mathrm{L}};\alpha_{\mathrm{R}}\Big\rangle = \mathrm{e}^{-\mathrm{i}\omega_{\mathrm{c}}t/2}\Big|\mathrm{e}^{-\mathrm{i}\omega_{\mathrm{c}}t}\alpha_{\mathrm{L}};\alpha_{\mathrm{R}}\Big\rangle\,, \tag{2.29}$$

is merely characterized by a different phase of α_{L}. It is a localized wave packet rotating with cyclotron frequency ω_{c} around the constant center of motion $\mathbf{c}$. As such it embodies the closest quantum analogy [31] to the classical motion discussed in Section 2.1.

Gauge invariance

So far, the quantum problem was discussed for the symmetric gauge (2.13) only. We will now admit an arbitrary gauge again, and consider the consequences of a finite choice of χ. Although the canonical momentum is gauge dependent, its representation as a differential operator, $\mathbf{p} = -\mathrm{i}\hbar\boldsymbol{\nabla}$, contains no dependence on the vector potential. This can be understood by the observation that the velocity operator

$$\mathbf{v} = \frac{1}{m_\circ}(\mathbf{p} - q\mathbf{A}) = \frac{\mathrm{i}}{\hbar}[\mathrm{H},\mathbf{r}] \tag{2.30}$$

undergoes a unitary transformation as one changes the gauge:

$$\frac{1}{m_\circ}\big(-\mathrm{i}\hbar\boldsymbol{\nabla} - q\mathbf{A}(\mathbf{r})\big) = \mathrm{e}^{\mathrm{i}q\chi(\mathbf{r})/\hbar}\,\frac{1}{m_\circ}\big(-\mathrm{i}\hbar\boldsymbol{\nabla} - q\mathbf{A}_{\mathrm{sym}}(\mathbf{r})\big)\,\mathrm{e}^{-\mathrm{i}q\chi(\mathbf{r})/\hbar} \tag{2.31}$$

Consequently, in order to preserve the gauge independence of the velocity expectation value, also the wave functions must be transformed unitarily as the gauge is changed. This is found immediately by applying (2.31) twice to the time dependent Schrödinger equation, at arbitrary gauge,

$$\begin{aligned} \mathrm{i}\hbar\,\partial_t|\psi_\chi\rangle &= \frac{1}{2m_\circ}(-\mathrm{i}\hbar\boldsymbol{\nabla} - q\mathbf{A})^2\,|\psi_\chi\rangle \\ &= \mathrm{e}^{\mathrm{i}q\chi(\mathbf{r})/\hbar}\,\frac{1}{2m_\circ}(-\mathrm{i}\hbar\boldsymbol{\nabla} - q\mathbf{A}_{\mathrm{sym}})^2\,\mathrm{e}^{-\mathrm{i}q\chi(\mathbf{r})/\hbar}\,|\psi_\chi\rangle\,. \end{aligned} \tag{2.32}$$

Comparing the wave function with the one of the symmetric gauge,

$$\mathrm{i}\hbar\,\partial_t|\psi_0\rangle = \frac{1}{2m_\circ}(-\mathrm{i}\hbar\boldsymbol{\nabla} - q\mathbf{A}_{\mathrm{sym}})^2\,|\psi_0\rangle\,, \tag{2.33}$$

we see that they are indeed related by a local, unitary transformation

$$|\psi_\chi\rangle = \mathrm{e}^{\mathrm{i}q\chi(\mathbf{r})/\hbar}|\psi_0\rangle \equiv \mathrm{e}^{\mathrm{i}\widetilde{\chi}(\tilde{\mathbf{r}})}|\psi_0\rangle \tag{2.34}$$

which is determined by the gauge field χ (in dimensionless units $\widetilde{\chi}(\tilde{\mathbf{r}}) := 2\chi(\mathbf{r})/(Bb^2)$). It follows that the velocity expectation value is gauge invariant. The same holds for all observables which commute with $\mathbf{r}$, due to the local nature of the transformation (2.34). As an immediate consequence, the probability density $|\psi|^2(\mathbf{r})$ and the probability flux, $\mathbf{j}(\mathbf{r})$ are also gauge-invariant. The latter may be identified from the continuity equation $\boldsymbol{\nabla}\mathbf{j} = -\partial_t|\psi|^2$, which follows from (2.32), as

$$\mathbf{j} := \mathrm{Re}(\psi^*\mathbf{v}\psi) = \frac{\hbar}{m_\circ}\,\mathrm{Im}(\psi^*\boldsymbol{\nabla}\psi) - \frac{q}{m_\circ}\mathbf{A}|\psi|^2\,. \tag{2.35}$$

Like all observables which include the gradient in position representation, it contains the vector potential explicitely to account for the gauge-dependent phase of the wave function.

2.3 The scaling property

The magnetic Schrödinger operator conventionally contains the four parameters $\hbar$, $m_\circ$, q, B, along with the energy E as the spectral variable. Due to the homogeneity of the vector potential (2.13), it is possible to reduce those to the two principal length scales which we encountered in the previous sections. Those are the cyclotron radius ρ and the magnetic length b, respectively, given by

$$\rho^2 := \frac{2m_\circ E}{q^2B^2} \qquad \text{and} \qquad b^2 := \frac{2\hbar}{qB}\,, \tag{2.36}$$

cf (2.7), (2.17). The cyclotron radius is a quantity of classical mechanics. The magnetic length, in contrast, has a pure quantum meaning. As discussed above, it determines the mean extension of a minimum uncertainty state, and vanishes as $\hbar \to 0$.

In the preceding section, we found it convenient to introduce the dimensionless variables $\tilde{\mathbf{r}} = \mathbf{r}/b$ and $\tilde{\mathbf{p}} = b\mathbf{p}/\hbar$. In fact, the homogeneity of the potential (2.13), in conjunction with the requirement $[\tilde{x}, \tilde{p}_x] = [\tilde{y}, \tilde{p}_y] = i$, leads necessarily to the magnetic length as the appropriate scale. The only freedom is a numerical factor in the definition of b. We took it such that the induced time scale $\tilde{t} = \omega t$ is given by the (classical) Larmor frequency ω, cf (2.20). It is appropriate to measure time in terms of the Larmor period $T = 2\pi/\omega$, rather than the cyclotron period $T_{\mathrm{cyc}} = \frac{1}{2}T$, because the former is the fundamental time scale of the quantum problem. It takes *two* cyclotron periods, as one observes from equation (2.29) (and more generally from the propagator (2.50)), before a wave packet returns to its initial state with correct parity.

The respective dimensionless Lagrangian, furnished with a tilde like all scaled units, reads

$$\widetilde{\mathcal{L}} = \frac{\mathcal{L}}{\hbar\omega} = \frac{1}{2}\tilde{\mathbf{v}}^2 + \tilde{\mathbf{r}} \times \tilde{\mathbf{v}} + \tilde{\mathbf{v}}\,\boldsymbol{\nabla}_{\tilde{\mathbf{r}}}\widetilde{\chi} = \frac{1}{2}\tilde{\mathbf{v}}^2 + \tilde{\mathbf{v}}\tilde{\mathbf{A}}(\tilde{\mathbf{r}}) \; . \tag{2.37}$$

It contains no parameters any more, but for the definition of the scaled gauge field,

$$\widetilde{\chi}(\tilde{\mathbf{r}}) := \frac{2}{Bb^2}\chi(b\tilde{\mathbf{r}}) \; , \tag{2.38}$$

which is not necessarily homogeneous of order two. This implies the definition of the general scaled vector potential $\tilde{\mathbf{A}}(\tilde{\mathbf{r}}) = 2\mathbf{A}(b\tilde{\mathbf{r}})/(Bb)$. The scaled Hamiltonian, given by

$$\widetilde{\mathrm{H}} = \frac{\mathrm{H}}{\hbar\omega} = \frac{1}{2}(\tilde{\mathbf{p}} - \tilde{\mathbf{A}})^2 \; , \tag{2.39}$$

shows that the proper, scaled energy reads $\widetilde{E} = E/(\hbar\omega) = 2\rho^2/b^2$. We will state the energy in terms of the spacing between Landau levels, though,

$$\nu := \frac{E}{\hbar\omega_{\mathrm{c}}} = \frac{E}{2\hbar\omega} = \frac{\rho^2}{b^2} \; , \tag{2.40}$$

and call $\nu = \tilde{E}/2$ the scaled energy, nonetheless. This way we conform with the popular convention that the Landau levels start at one half, rather than at one.

Two distinct short wave limits

Below, it will be important to distinguish the two independent short-wave limits of magnetic dynamics. From expression (2.40) one observes that the spectral variable ν can be increased by either increasing ρ at constant magnetic length b, or by decreasing b at fixed cyclotron radius ρ. The former direction is realized by raising the conventional energy at constant magnetic field. It is the standard *high-energy* limit. Here, the curvature of the classical trajectory tends to zero, which shows that in this limit the dynamical effect of the magnetic field vanishes.

On the other hand, one may increase both, the conventional energy and the field, at a fixed ratio of E/B^2, thereby keeping the cyclotron radius fixed. This way the underlying classical phase space is kept invariant, while the magnetic length tends to zero. It is a realization of the *semiclassical* limit since b^2 plays the role of $\hbar$ as the semiclassically small parameter.[3]

In order to be able to consider both limits, most equations will *not* be written in scaled variables, since they might depend on the spectral variable. Rather the formulas will be stated in terms of combinations like $\mathbf{r}/b$ so that they can be immediately replaced by scaled variables. This includes the scaled gradient $\boldsymbol{\nabla}_{\tilde{\mathbf{r}}} \equiv b\boldsymbol{\nabla}_{\mathbf{r}}$, which will be written as

$$\boldsymbol{\nabla}_{\mathbf{r}/b} := b\boldsymbol{\nabla}_{\mathbf{r}} \ . \tag{2.41}$$

This is an admittedly unusual, but consistent notation. Scaled variables will be used within calculations, if it is convenient and makes the presentation clearer. The spectral variable is always written as $E/(2\hbar\omega) = \nu$.

2.4 The free quantum propagator

We return to the Lagrangian formulation of mechanics, in order to calculate the time evolution operator $\mathrm{U}(t;0) := \exp[-\mathrm{i}\mathrm{H}t/\hbar]$ for arbitrary gauge. According to Feynman, its position representation (for $t > 0$) is given by the path integral [9, 32, 33]

$$\mathrm{U}(t,\mathbf{r};0,\mathbf{r}_0) = \int\limits_{\mathbf{q}(0)=\mathbf{r}_0}^{\mathbf{q}(t)=\mathbf{r}} \mathcal{D}[\mathbf{q}]\, \exp\left(\frac{\mathrm{i}}{\hbar} W[\mathbf{q}]\right) \ . \tag{2.42}$$

Here, the functional W attributes a classical action

$$W[\mathbf{q}] := \int_0^t \mathcal{L}(\mathbf{q}(t'), \dot{\mathbf{q}}(t'))\, \mathrm{d}t' \tag{2.43}$$

to all paths $\mathbf{q}(t')$ going from $\mathbf{r}_0$ to $\mathbf{r}$ in the given time t. (All equations are stated for a time independent Lagrangian, and the zero indicating the initial time will be omitted in the following.)

The formulation in terms of a path integral allows the calculation of the time evolution operator in a straightforward manner. Its most important advantage is that the *semiclassical* approximant of the propagator can be obtained in a transparent way. The situation is called semiclassical if $\hbar$ is small compared to the actions (2.43). In this case the dominant contributions to the path integral are represented by those paths for which the phase in (2.42) is stationary. They are solutions of the variational problem $\delta W[\mathbf{q}] = 0$ with fixed initial and final position and time. According to Hamilton's principle, these are classical trajectories. The integral is then evaluated by expanding the variations of (2.43) to second order. Provided the trajectories are isolated, one obtains the asymptotic expression of the propagator to leading order in $\hbar$ [34].

$$\mathrm{U}(t,\mathbf{r};\mathbf{r}_0) = \frac{1}{2\pi\mathrm{i}\hbar} \sum_{\mathbf{q}_{\mathrm{cl}}} \left|\det\left(-\frac{\partial^2 W[\mathbf{q}_{\mathrm{cl}}]}{\partial\mathbf{r}\partial\mathbf{r}_0}\right)\right|^{\frac{1}{2}} \exp\left(\frac{\mathrm{i}}{\hbar} W[\mathbf{q}_{\mathrm{cl}}] - \mathrm{i}\frac{\pi}{2}\nu_{\mathbf{q}_{\mathrm{cl}}}\right)\ (1 + \mathrm{O}(\hbar)) \tag{2.44}$$

It is a sum over classical trajectories $\mathbf{q}_{\mathrm{cl}}$ going from $\mathbf{r}_0$ to $\mathbf{r}$, in the given time t. The only quantum ingredient is the finite size of $\hbar$, which sets the scale of the associated classical action in the phase factor. The additional phase shift is determined by the number $\nu_{\mathbf{q}_{\rm cl}}$ of negative eigenvalues of the matrix $\big(-\partial^2 W[\mathbf{q}_{\rm cl}]/(\partial\mathbf{r}\partial\mathbf{r}_0)\big)$ [34]. The latter has a dynamical meaning [9, 33]. It is the inverse of the Jacobi field of $\mathbf{q}_{\rm cl}$, which describes the linearized deviation of classical trajectories with different initial momenta. The points of intersection of the field with the initial trajectory $\mathbf{q}_{\rm cl}$ are called focal or *conjugate*. They determine the value of $\nu_{\mathbf{q}_{\rm cl}}$ geometrically by virtue of the Morse theorem [35]. It is equal to the number of conjugate points the particle encounters on its journey (counted with their multiplicities [35]) and called the Morse index.

We are now in a position to derive the time evolution operator in the free magnetic plane. Due to the simple form of the Lagrangian (2.1), the expansion of the action functional needed in the derivation of (2.44) breaks off after the quadratic term (explaining why the motion is mimicked by a harmonic oscillator, cf eq (2.19)). In consequence, the above expression for the time evolution operator is *exact* in our case, rather than asymptotic.

In order to evaluate (2.44), the action of a classical trajectory is needed as a function of the initial position $\mathbf{r}_0$, the final one, $\mathbf{r}$, and the time of flight t. Knowing the classical motion from Section 2.1, the (scaled) action integral is easily computed,

$$\begin{aligned}\frac{1}{\hbar}W(t,\mathbf{r};\mathbf{r}_0) = \widetilde{W}(\tilde{t},\tilde{\mathbf{r}};\tilde{\mathbf{r}}_0) &= \int_0^{\tilde{t}}\left(\frac{1}{2}\tilde{\mathbf{v}}(\tilde{t}')^2 + \tilde{\mathbf{v}}(\tilde{t}')\tilde{\mathbf{A}}(\tilde{\mathbf{r}}(\tilde{t}'))\right)\mathrm{d}\tilde{t}' \\ &= \frac{1}{2}\int_0^{\tilde{t}}\tilde{\mathbf{v}}^2(\tilde{t}')\mathrm{d}\tilde{t}' + \int_{\partial Q}\tilde{\mathbf{A}}(\tilde{\mathbf{r}}')\mathrm{d}\tilde{\mathbf{r}}' + \int\limits_{\tilde{\mathbf{r}}_0\to\tilde{\mathbf{r}}}\tilde{\mathbf{A}}(\tilde{\mathbf{r}}')\,\mathrm{d}\tilde{\mathbf{r}}' \\ &= \frac{1}{2}(\tilde{\mathbf{r}}-\tilde{\mathbf{r}}_0)^2\cot(\tilde{t}) - \tilde{\mathbf{r}}\times\tilde{\mathbf{r}}_0 + \widetilde{\chi}(\tilde{\mathbf{r}}) - \widetilde{\chi}(\tilde{\mathbf{r}}_0)\,. \end{aligned} \tag{2.45}$$

Here, the action integral was split into three parts:

$$\int_0^{\tilde{t}}\tilde{\mathbf{v}}^2(\tilde{t}',\tilde{\mathbf{r}};\tilde{\mathbf{r}}_0)\,\mathrm{d}\tilde{t}' = \frac{(\tilde{\mathbf{r}}-\tilde{\mathbf{r}}_0)^2}{\sin^2(\tilde{t})}\,\frac{\tilde{t}}{2} \tag{2.46}$$

$$\int_{\partial Q}\tilde{\mathbf{A}}(\tilde{\mathbf{r}}')\,\mathrm{d}\tilde{\mathbf{r}}' = -\frac{(\tilde{\mathbf{r}}-\tilde{\mathbf{r}}_0)^2}{\sin^2(\tilde{t})}\,\frac{\tilde{t}}{2} + \frac{(\tilde{\mathbf{r}}-\tilde{\mathbf{r}}_0)^2}{2}\cot(\tilde{t}) \tag{2.47}$$

$$\int\limits_{\tilde{\mathbf{r}}_0\to\tilde{\mathbf{r}}}\tilde{\mathbf{A}}(\tilde{\mathbf{r}}')\,\mathrm{d}\tilde{\mathbf{r}}' = -\tilde{\mathbf{r}}\times\tilde{\mathbf{r}}_0 + \widetilde{\chi}(\tilde{\mathbf{r}}) - \widetilde{\chi}(\tilde{\mathbf{r}}_0) \tag{2.48}$$

In the first, the modulus of the velocity is constant. Its value (2.46) follows from (2.6). The second part was made a closed line integral, encircling a domain Q, which is defined by the trajectory and the straight line from $\tilde{\mathbf{r}}$ back to $\tilde{\mathbf{r}}_0$. By Stokes' theorem it may be transformed to an area integral over the rotation of the integrand (given by the constant magnetic field). One obtains (2.47), with the negative sign due to the clockwise (mathematically negative) sense of integration. The remaining part (2.48) is a line integral along the straight path from $\tilde{\mathbf{r}}_0$ to $\tilde{\mathbf{r}}$. Unlike the other contributions, it depends on $\tilde{\mathbf{r}}$ and $\tilde{\mathbf{r}}_0$ individually, and carries the gauge dependence.

In principle, more than one classical trajectory could connect the two points $\tilde{\mathbf{r}}$ and $\tilde{\mathbf{r}}_0$ in a given time. However, since the determinant of the matrix in (2.6) is non-zero for $\tilde{t} \neq n\pi, n = 1, 2, \ldots$, the initial velocity is uniquely specified for those times. At integer multiples of the cyclotron period, in contrast, any trajectory returns to its starting point. Excluding these instances for the time being, the time evolution operator is determined by only one trajectory. For the matrix of second derivatives one obtains

$$\det\left(\frac{\partial^2\widetilde{W}}{\partial\tilde{\mathbf{r}}\partial\tilde{\mathbf{r}}_0}\right) = \frac{1}{\sin^2(\tilde{t})}\ . \tag{2.49}$$

The determinant of its inverse has doubly degenerate zeros at $\tilde{t} = n\pi$. Hence, the Morse index reads $\nu_{\mathbf{q}_{\rm cl}} = 2[\tilde{t}/\pi]$ (with $[\cdot]$ the integer part), and one obtains immediately the time evolution operator in the free magnetic plane

$$\begin{aligned}\mathrm{U}(t,\mathbf{r};\mathbf{r}_0) =& \frac{1}{2\pi\mathrm{i}b^2}\frac{1}{\sin(\omega t)}\exp\left[\mathrm{i}\frac{(\mathbf{r}-\mathbf{r}_0)^2}{2b^2}\cot(\omega t) - \mathrm{i}\frac{\mathbf{r}\times\mathbf{r}_0}{b^2}\right] \\ &\times\exp\left[\mathrm{i}\Big(\widetilde{\chi}\Big(\frac{\mathbf{r}}{b}\Big) - \widetilde{\chi}\Big(\frac{\mathbf{r}_0}{b}\Big)\Big)\right]\ .\end{aligned} \tag{2.50}$$

As noted above, this expression is identical to the exact path integral [32, 36–38]. It is valid except for the times equal to integer multiples of the cyclotron period. At these instances the propagator is just a unit operator,

$$\begin{aligned}\lim_{\omega t\to n\pi}\mathrm{U}(t,\mathbf{r};\mathbf{r}_0) &= \lim_{\varepsilon\to 0}\frac{1}{2\pi\mathrm{i}b^2}\frac{(-)^n}{\sin(\varepsilon)}\exp\left[\mathrm{i}\frac{(\mathbf{r}-\mathbf{r}_0)^2}{2b^2}\cot(\varepsilon)\right] \\ &\qquad\times\exp\left[-\mathrm{i}\frac{\mathbf{r}\times\mathbf{r}_0}{b^2} + \mathrm{i}\widetilde{\chi}\Big(\frac{\mathbf{r}}{b}\Big) - \mathrm{i}\widetilde{\chi}\Big(\frac{\mathbf{r}_0}{b}\Big)\right] \\ &= (-)^n\,\delta\left(\frac{\mathbf{r}-\mathbf{r}_0}{b}\right)\ ,\end{aligned} \tag{2.51}$$

with a sign which is positive only after even multiples of the cyclotron period. This means that any wave function which is propagated by multiples of the Larmor period $T = 2\pi/\omega = 2T_{\rm cyc}$ returns precisely at its initial state. Equation (2.51) follows from a special representation of the two-dimensional δ-function, which is given in the appendix, cf (A.7). Note finally that the propagator (2.50) was derived for positive times $t > 0$ only. It is valid for all times, nonetheless, since it clearly obeys the unitarity relation $\mathrm{U}(-t,\mathbf{r};\mathbf{r}_0) = [\mathrm{U}(t,\mathbf{r}_0;\mathbf{r})]^*$. Furthermore, it is given for arbitrary vector potentials. The dependence on χ shows how the propagator transforms as the gauge is changed. It is consistent with the gauge dependence of the wave functions (2.34) discussed in Section 2.2.

2.5 The free Green function

We are now in a position to calculate the Green function of the free magnetic plane. It will be an important ingredient in the theory of the exact and semiclassical quantization of magnetic billiards. We define the Green function to be the Fourier transform of the free propagator

$$\mathrm{G}(E,\mathbf{r};\mathbf{r}_0) := \frac{\hbar}{2\mathrm{i}m_\circ}\lim_{\varepsilon\downarrow 0}\int_0^\infty \mathrm{U}(t,\mathbf{r};\mathbf{r}_0)\mathrm{e}^{\mathrm{i}(E+\mathrm{i}\varepsilon)t/\hbar}\,\mathrm{d}t\ . \tag{2.52}$$

As such, it is a resolvent of the Hamiltonian, ie, it obeys the inhomogeneous Schrödinger equation

$$(\mathrm{H}-E)\mathrm{G}(E,\mathbf{r};\mathbf{r}_0) = -\frac{\hbar^2}{2m_\circ}\delta(\mathbf{r}-\mathbf{r}_0)\ . \tag{2.53}$$

For later reference, we note that there exists a second, independent solution to (2.53) which differs strongly from G. We shall call it the unphysical or *irregular* Green function $\mathrm{G}^{(\mathrm{irr})}$.

One procedure to obtain the Green function is based on the observation that the differential equation (2.53) separates in radial coordinates, if the symmetric gauge is used. This way one is led to an angular momentum decomposition of G, which is of little use for our purposes. It was derived (incorrectly) in [39,40] and is summarized in Appendix B. Here, we shall perform the Fourier integral (2.52) directly. It yields the Green function in a clear-cut fashion, in Cartesian representation and arbitrary gauge. Substituting scaled variables the integral (2.52) reads

$$\begin{aligned} G_\nu(\mathbf{r};\mathbf{r}_0) &:= \mathrm{G}(2\hbar\omega\nu,\mathbf{r};\mathbf{r}_0) \\ &= \frac{-1}{4\pi}\int_0^\infty \frac{\mathrm{d}\tilde{t}}{\sin(\tilde{t})}\exp\left[\mathrm{i}\left(\frac{(\tilde{\mathbf{r}}-\tilde{\mathbf{r}}_0)^2}{2}\cot(\tilde{t}) - \tilde{\mathbf{r}}\times\tilde{\mathbf{r}}_0 + \widetilde{\chi} - \widetilde{\chi}_0 + 2\nu\tilde{t}\right)\right] \end{aligned} \tag{2.54}$$

with the abbreviations $\widetilde{\chi} := \widetilde{\chi}(\tilde{\mathbf{r}}), \widetilde{\chi}_0 := \widetilde{\chi}(\tilde{\mathbf{r}}_0)$. Here, energy ν is assumed to have an infinitesimally small positive imaginary part to ensure convergence.

Like in the case of the propagator, stating the Green function as an integral has the advantage that its semiclassical approximation can be obtained straightforwardly. This is shown in the following. The exact integration will be carried out afterwards.

2.5.1 The semiclassical Green function

The semiclassical approximation to the Green function, $\mathrm{G}_\nu^{(\mathrm{sc})}$, is obtained by performing the Fourier transform in the stationary phase approximation, which is summarized in Appendix A.1. It yields an asymptotic expansion to leading order in the semiclassically large parameter $1/b^2$. Requiring the integrand of the Fourier integral (2.54) to have a stationary phase leads to a condition

$$|\sin(\tilde{t})| \overset{!}{=} \frac{|\tilde{\mathbf{r}}-\tilde{\mathbf{r}}_0|}{2\sqrt{\nu}} \equiv \frac{|\mathbf{r}-\mathbf{r}_0|}{2\rho}\ , \tag{2.55}$$

which selects the times of flight of classical trajectories connecting the initial position $\mathbf{r}_0$ with the final point $\mathbf{r}$ at fixed energy ν. It can be satisfied only if the distance between the two points is smaller than the cyclotron diameter. If this is the case, the time derivative of the phase in (2.54) vanishes at an infinite number of (discrete) times,

$$\begin{aligned} \tilde{t}_{\mathrm{S}}^{(n)} &= \arcsin(\zeta) + n\pi\ , \\ \tilde{t}_{\mathrm{L}}^{(n)} &= \pi - \arcsin(\zeta) + n\pi\ , \qquad \text{with } n = 0,1,\dots \end{aligned} \tag{2.56}$$

The two times of flight $\tilde{t}_{\mathrm{S}}^{(0)}$ and $\tilde{t}_{\mathrm{L}}^{(0)}$ belong to the two distinct trajectories which connect the initial and the final point directly. They are "short" and "long" arcs, respectively, ie, have an arclength smaller and larger than π (cf Fig. 6.1). At times with $n > 0$

the trajectories perform in addition n complete cyclotron orbits. In (2.56), the value

$$\zeta := \frac{|\mathbf{r}-\mathbf{r}_0|}{2\rho} \tag{2.57}$$

measures the distance between the initial and the final point relative to the classical cyclotron diameter. After the Fourier transform, the trajectories entering the semiclassical Green function exhibit an action $\tilde{S} = \tilde{W} + 2\nu\tilde{t}$, which is a function of energy $\nu = \widetilde{E}/2$ rather than time. As specified by (2.56) the actions read

$$\tilde{S}^{(n)}_{\binom{\mathrm{S}}{\mathrm{L}}} = 2\pi\nu\left(\mathrm{a}_{\binom{\mathrm{S}}{\mathrm{L}}} + n\right) + \widetilde{\chi} - \widetilde{\chi}_0 \,. \tag{2.58}$$

Here, we introduced the notation

$$\begin{aligned} \mathrm{a}_\mathrm{S}(\mathbf{r};\mathbf{r}_0) &:= \frac{1}{\pi}\left(\arcsin(\zeta) + \zeta\sqrt{1-\zeta^2} - \frac{\mathbf{r}\times\mathbf{r}_0}{2\rho^2}\right) \quad \text{and} \\ \mathrm{a}_\mathrm{L}(\mathbf{r};\mathbf{r}_0) &:= \frac{1}{\pi}\left(\pi - \arcsin(\zeta) - \zeta\sqrt{1-\zeta^2} - \frac{\mathbf{r}\times\mathbf{r}_0}{2\rho^2}\right) \end{aligned} \tag{2.59}$$

for the geometric part of the action. Note that a_S and a_L depend on the initial and the final point individually, due to the term $\mathbf{r}\times\mathbf{r}_0$, which means that they are not translationally invariant. However, one observes the relation $\mathrm{a}_\mathrm{S}(\mathbf{r};\mathbf{r}_0) + \mathrm{a}_\mathrm{L}(\mathbf{r}_0;\mathbf{r}) = 1$. It follows that the (scaled) action of a closed cyclotron orbit – ie, a short arc followed by a long one – is given by $2\pi\nu$.

Conducting the stationary phase approximation (A.2), we need finally the second derivative of the phase in (2.54). It is given by $(\tilde{\mathbf{r}}-\tilde{\mathbf{r}}_0)^2\cos(\tilde{t})/\sin^3(\tilde{t})$ and at times (2.56) assumes the values $\pm 4\nu\sqrt{1-\zeta^2}/\zeta$ (where the positive sign stands for trajectories of the short type). It follows, that in the semiclassical approximation an infinite number of trajectories contributes to the Fourier integral.

$$\begin{aligned} \mathrm{G}^{(\mathrm{sc})}_\nu(\mathbf{r};\mathbf{r}_0) = \frac{-1}{4\pi}\sum_{n=0}^{\infty}(-)^n\left(\frac{\frac{\pi}{2\nu}}{\zeta\sqrt{1-\zeta^2}}\right)^{\frac{1}{2}} \Big\{ &\exp\left(2\pi\mathrm{i}\nu(\mathrm{a}_\mathrm{S}+n) + \mathrm{i}\tilde{\chi} - \mathrm{i}\tilde{\chi}_0 + \mathrm{i}\frac{\pi}{4}\right) \\ &+ \exp\left(2\pi\mathrm{i}\nu(\mathrm{a}_\mathrm{L}+n) + \mathrm{i}\tilde{\chi} - \mathrm{i}\tilde{\chi}_0 - \mathrm{i}\frac{\pi}{4}\right)\Big\} \end{aligned} \tag{2.60}$$

Fortunately, the sum over the repetitive cyclotron orbits n is of the geometric type. It converges, since ν was assumed to have a small positive imaginary part, adding a factor $(1+\mathrm{e}^{2\pi\mathrm{i}\nu})^{-1}$ which is singular at the energies of the Landau levels. The semiclassical Green function is therefore given by a sum of two contributions, belonging to the short and the long arc trajectory — the principal classical trajectories connecting $\mathbf{r}_0$ and $\mathbf{r}$:

$$\mathrm{G}^{(\mathrm{sc})}_\nu(\mathbf{r};\mathbf{r}_0) = \frac{1}{2(1+\mathrm{e}^{2\pi\mathrm{i}\nu})}\frac{1}{(2\pi\mathrm{i})^{\frac{1}{2}}}\frac{\frac{1}{2\mathrm{i}\sqrt{\nu}}}{\left(\zeta\sqrt{1-\zeta^2}\right)^{\frac{1}{2}}}\left\{\mathrm{e}^{2\pi\mathrm{i}\nu\mathrm{a}_\mathrm{S}} + \mathrm{e}^{-\mathrm{i}\frac{\pi}{2}}\mathrm{e}^{2\pi\mathrm{i}\nu\mathrm{a}_\mathrm{L}}\right\}\mathrm{e}^{\mathrm{i}(\tilde{\chi}-\tilde{\chi}_0)} \tag{2.61}$$

This form will be used in Chapter 6 for periodic orbit theory. Alternatively, one can combine the short and long arc contributions pulling out that part of the phase which was time independent in (2.54). This leads to the expression

$$\mathrm{G}_\nu^{(\mathrm{sc})}(\mathbf{r};\mathbf{r}_0) = \exp\left[-\mathrm{i}\left(\frac{\mathbf{r}\times\mathbf{r}_0}{b^2} - \tilde{\chi} + \tilde{\chi}_0\right)\right]\ \mathrm{G}_\nu^{0(\mathrm{sc})}\left(\frac{(\mathbf{r}-\mathbf{r}_0)^2}{b^2}\right)\ , \qquad (2.62)$$

with

$$\mathrm{G}_\nu^{0(\mathrm{sc})}(z) := \frac{-1}{4\pi}\,\frac{(2\pi)^{\frac{1}{2}}}{\cos(\pi\nu)}\,\frac{1}{\left[z\,(4\nu-z)\right]^{\frac{1}{4}}} \\ \times\cos\left(2\nu\left[\arcsin\left(\left(\frac{z}{4\nu}\right)^{\frac{1}{2}}\right) + \left(\frac{z}{4\nu}\left(1-\frac{z}{4\nu}\right)\right)^{\frac{1}{2}} - \frac{\pi}{2}\right] + \frac{\pi}{4}\right)\ . \qquad (2.63)$$

It shows that the Green function is given by a phase factor which contains the gauge dependence, and a *real* function, $\mathrm{G}_\nu^{0(\mathrm{sc})}$, which depends only on the distance between the initial and the final point. The exact Green function has the same property, as manifest in (2.54).

Note that the expressions (2.61) and (2.62) are defined only for separations smaller than the cyclotron diameter $|\mathbf{r}-\mathbf{r}_0| < 2\rho$. For larger distances, the semiclassical Green function vanishes by definition, since the stationary phase condition (2.55) has no solution. As the distance between the initial and the final points approaches the cyclotron diameter, the short and long arcs coalesce and are therefore no longer isolated. In this case the approximation (A.2) fails, which is indicated by the diverging prefactor of $\mathrm{G}^{(\mathrm{sc})}$, as $\zeta \to 1$. If an asymptotic expression is needed for the domain $|\mathbf{r}-\mathbf{r}_0| \gtrapprox 2\rho$, eg to describe tunnelling effects, uniform approximations [41] must be employed, as discussed in Sect. 7.2 and Appendix E.

2.5.2 The exact Green function

In [39, 40] the free magnetic Green function was derived (incorrectly) by angular momentum decomposition. A brief survey of the angular momentum treatment is given in Appendix B. In the following, we show how G_ν can be obtained by performing the Fourier transform of the time evolution operator (2.50) directly. The same expression was derived in [42] (as we have learned recently) using the separability of (2.53) in the symmetric gauge.

Like in the semiclassical case, we may separate the part of the phase in (2.54) which is not explicitely time dependent.

$$\mathrm{G}_\nu(\mathbf{r};\mathbf{r}_0) = \exp\left[-\mathrm{i}\left(\frac{\mathbf{r}\times\mathbf{r}_0}{b^2} - \tilde{\chi} + \tilde{\chi}_0\right)\right]\ \mathrm{G}_\nu^0\left(\frac{(\mathbf{r}-\mathbf{r}_0)}{b^2}\right) \qquad (2.64)$$

Now, the integral is performed exactly:

$$\begin{aligned}\mathrm{G}_\nu^0(z) &= \frac{-1}{4\pi}\int_0^\infty \frac{\mathrm{d}\tilde{t}}{\sin(\tilde{t})}\ \exp\left[\mathrm{i}\left(\frac{z}{2}\cot(\tilde{t}) + 2\nu\tilde{t}\right)\right] \\ &= \frac{-1}{4\pi}\sum_{n=0}^{\infty}\mathrm{e}^{2\pi\mathrm{i}\nu n}\int_0^\pi \frac{\mathrm{d}\tilde{t}}{\sin(n\pi+\tilde{t})}\ \exp\left[\mathrm{i}\left(\frac{z}{2}\cot(n\pi+\tilde{t}) + 2\nu\tilde{t}\right)\right]\end{aligned}$$

$$
\begin{aligned}
&= \frac{-1}{4\pi}\frac{1}{1+\mathrm{e}^{2\pi\mathrm{i}\nu}}\Bigg\{\int_0^\infty \frac{\mathrm{d}u}{\sqrt{1+u^2}}\Big(\frac{u+\mathrm{i}}{u-\mathrm{i}}\Big)^{\nu}\mathrm{e}^{\mathrm{i}zu/2} \\
&\qquad\qquad + \mathrm{e}^{2\pi\mathrm{i}\nu}\int_{-\infty}^{0} \frac{\mathrm{d}u}{\sqrt{1+u^2}}\Big(\frac{u+\mathrm{i}}{u-\mathrm{i}}\Big)^{\nu}\mathrm{e}^{\mathrm{i}zu/2}\Bigg\} \\
&= \frac{-1}{4\pi}\,\Gamma(\tfrac{1}{2}-\nu)\,\Bigg[\mathrm{e}^{-\mathrm{i}\pi(\nu-\frac{1}{2})}\,\frac{\Gamma(\frac{1}{2}+\nu)}{2\pi\mathrm{i}}\Bigg\{\int_0^{-\mathrm{i}\infty}\mathrm{d}t\,(t+1)^{\nu-\frac{1}{2}}(t-1)^{-\nu-\frac{1}{2}}\mathrm{e}^{-zt/2} \\
&\qquad\qquad + \mathrm{e}^{2\pi\mathrm{i}\nu}\int_{+\mathrm{i}\infty}^{0}\mathrm{d}t\,(t+1)^{\nu-\frac{1}{2}}(t-1)^{-\nu-\frac{1}{2}}\mathrm{e}^{-zt/2}\Bigg\}\Bigg] \\
&= \frac{-1}{4\pi}\,\Gamma(\tfrac{1}{2}-\nu)\,z^{-\frac{1}{2}}\,W_{\nu,0}(z) \qquad (2.65)
\end{aligned}
$$

Here, a logarithmic representation of the inverse cotangent was used [43; eq (4.4.31)], as well as the reflection relation of Euler's Gamma function, $\Gamma(\frac{1}{2}-\nu)\Gamma(\frac{1}{2}+\nu)\cos(\pi\nu) = \pi$. The last equality in (2.65) holds since the expression in square brackets may be deformed to the (complex conjugate of the) contour integral found in [44; eq (5.1.6)]. It gives the (real valued) *irregular Whittaker function* W [43; eq (13.1.34)] (multiplied by $z^{-\frac{1}{2}}$) in an integral representation that is valid even for positive ν.

Regularization

The function (2.65), as well as its semiclassical approximant (2.63), exhibit simple poles as the energy ν approaches the Landau levels. It is often convenient to remove these poles by considering the *regularized* version of G^0_ν,

$$
\widehat{\mathrm{G}}^0_\nu(z) := \lim_{\mu\to\nu}\cos(\pi\mu)\,\mathrm{G}^0_\mu(z)\;. \qquad (2.66)
$$

Finally, we state the regularized Green function in terms of the *irregular confluent hypergeometric function U* [43], which is more common than the Whittaker function:

$$
\widehat{\mathrm{G}}^0_\nu(z) = \frac{-1}{4\pi}\,\frac{\pi}{\Gamma(\nu+\frac{1}{2})}\,\mathrm{e}^{-z/2}\,\mathrm{U}(\tfrac{1}{2}-\nu,1;z) \qquad (2.67)
$$

2.5.3 Properties of the free Green function

Figure 2.1 displays the gauge-independent, regularized part of the exact and semiclassical Green function. As one expects, the exact Green function decays exponentially once the points are separated by a distance, $|\mathbf{r}-\mathbf{r}_0| > 2\rho$, (ie $z > 4\nu$) which cannot be traversed classically.[*] As $\mathbf{r}\to\mathbf{r}_0$, it has a logarithmic singularity (cf (2.71)) like the (complex valued) field-free Green function [45]. Our method to evaluate the free Green function numerically with high precision and efficiency is discussed in Appendix E. There, $\widehat{\mathrm{G}}^0_\nu$ is displayed at $\nu = 57.75$, as a function of $|\mathbf{r}-\mathbf{r}_0|/\rho$.

---

[*] The abovementioned independent solution of (4.2) grows exponentially beyond the classically allowed region. Its derivation is sketched in Appendix B.

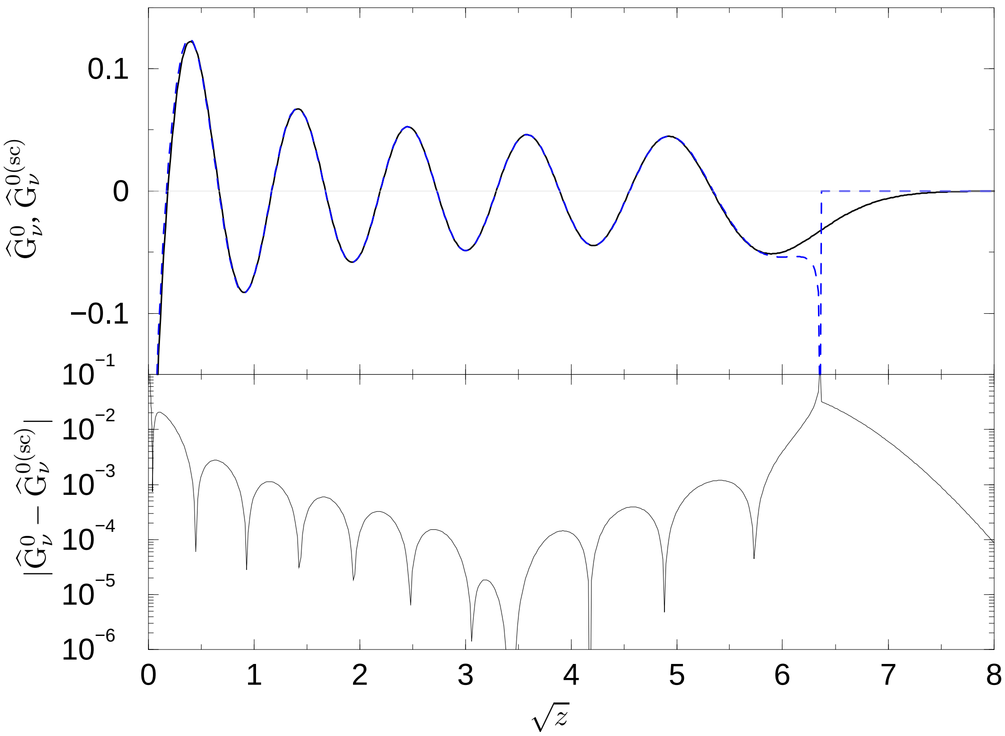

Figure 2.1: Regularized gauge-independent part of the free Green function. Top: Exact (solid line) and semiclassical (dashed line) functions $\widehat{G}^0_\nu$ at $\nu = 10.1$. Bottom: Error of the semiclassical approximation. Even at this moderate value of ν strong deviations occur only at the classical turning point $\sqrt{z} = 2\sqrt{\nu} \approx 6.36$ and at small distances. (The deviations arise since the semiclassical approximation does not account for the logarithmic singularity at $z = 0$ and the tunnelling into distances larger than the cyclotron diameter.)

Differential expressions

The gauge invariant part of the Green function has the remarkable property that its derivatives can be expressed by the function itself, at a different energy. For the regularized version one finds

$$z\frac{\mathrm{d}}{\mathrm{d}z}\widehat{G}^0_\nu(z) = -\left(\tfrac{1}{2}-\nu\right)\left(\widehat{G}^0_\nu + \widehat{G}^0_{\nu-1}\right) - \frac{z}{2}\widehat{G}^0_\nu \tag{2.68}$$

$$\begin{aligned} z^2\frac{\mathrm{d}^2}{\mathrm{d}z^2}\widehat{G}^0_\nu(z) =& \left(\tfrac{3}{2}-\nu\right)\left(\tfrac{1}{2}-\nu\right)\left(\widehat{G}^0_\nu + 2\widehat{G}^0_{\nu-1} + \widehat{G}^0_{\nu-2}\right) \\ &+ z\left(\tfrac{1}{2}-\nu\right)\left(\widehat{G}^0_\nu + \widehat{G}^0_{\nu-1}\right) + \frac{z^2}{4}\widehat{G}^0_\nu\,. \end{aligned} \tag{2.69}$$

These formulas were obtained by employing the differential properties of the confluent hypergeometric function [43].

Asymptotic behaviour

Finally, we note the behaviour of the Green function at small distances. It has a logarithmic singularity, similar to the Green function of the field-free case [45].

$$\widehat{\mathrm{G}}^0_\nu(z) = \mathrm{L}_\nu(z) + \mathrm{O}(z\log z) \qquad \text{as } z \to 0, \tag{2.70}$$

where

$$\mathrm{L}_\nu(z) := \frac{\cos(\pi\nu)}{4\pi}\big(\log(z) + \Psi(\tfrac{1}{2}+\nu) - 2\Psi(1)\big) - \frac{\sin(\pi\nu)}{4}\,. \tag{2.71}$$

Here, Ψ is the Digamma function [43]. As for the derivatives of the gauge independent part of the Green function, one finds the asymptotic expressions

$$z\frac{\mathrm{d}}{\mathrm{d}z}\widehat{\mathrm{G}}^0_\nu(z) = \frac{\cos(\pi\nu)}{4\pi}\big[1 - z\,\nu\,\big(\log(z) + \Psi(\tfrac{1}{2}-\nu) - 2\Psi(1) - 1\big)\big] + \mathrm{O}(z^2\log z)\,, \tag{2.72}$$

$$z^2\frac{\mathrm{d}^2}{\mathrm{d}z^2}\widehat{\mathrm{G}}^0_\nu(z) = -\frac{\cos(\pi\nu)}{4\pi} + \mathrm{O}(z\log z)\,, \qquad \text{as } z \to 0. \tag{2.73}$$

They were deduced from the logarithmic representation of U in terms of the regular Kummer function [43; eq. (13.6.1)]. These formulas will be needed in Section 4.4.

Notes

1. The motion on magnetic surfaces of *finite* curvature received some attention in recent years, both, in the classical [46–49] and the quantum treatment [46,47,50–52]. One motivation for introducing a non-vanishing curvature is the possibility to study the quantum spectrum of the free magnetic motion on a *compact* domain (a modular domain in the case of constant negative curvature). This has considerable mathematical advantages, since the spectrum remains discrete in the limit of vanishing field.
2. After (lengthy) deliberations, the author decided to avert from Landau's definition of the magnetic length $\ell_B = b/\sqrt{2}$. The latter is appropriate (only) for the Landau gauge (2.12). The length b, which is the appropriate scale of the symmetric gauge, proves more convenient, since it avoids the appearance of the factor 2 and $\sqrt{2}$ at various places. It gives the radius of a disk, the area $b^2\pi$ of which assumes the role of Planck's quantum, cf Eq. (3.11a). Moreover, the flux through the disk equates the "flux quantum" $\Phi_0 = h/q = B\,b^2\pi$.
3. *Scaled spectroscopy* is applied successfully in atomic physics, eg [53]. The measurement of absorption spectra in the semiclassical direction allowed in particular to extract the actions of classical periodic orbits from Rydberg spectra [54]. It should be noted that scaled spectra have some unusual mathematical features since they do not belong to one self-adjoint operator. Rather, they stem from a family of Hamilton operators parametrized by an effective value of $\hbar$ which depends on the spectral variable. As a result, the eigenfunctions are not orthogonal, although they are proper solutions of the Schrödinger equation with a real energy. More severely, the stability of spectral points with respect to changes in an external parameter known from self-adjoint operators does not hold in general.

Chapter 3

Introducing a boundary

The motion in the magnetic plane turns into a non-trivial problem, once the particle is restricted to a bounded domain.

3.1 Motion in a restricted domain

Let us assume that the particle is confined to move in a domain $\mathcal{D} \subset \mathbb{R}^2$, which is compact and singly connected. The classical equation of motion (2.4) still applies in the interior of the domain (ie, in $\mathring{\mathcal{D}}$). Here, the particle moves on arcs of constant curvature, which may at some point impinge on the boundary $\Gamma = \partial\mathcal{D}$. At these instances, the trajectories must obey the law of *specular reflection* to qualify as a classical solution. This follows directly from Hamilton's principle of requiring an extremal action, as will be shown in Sect. 6.3.1. Clearly, any trajectory which was reflected once must run into the boundary again. It follows, that the phase space is in general split up in two disjunct parts. One part consists of *skipping orbits*. Their classical motion is no longer described by a continuous Hamiltonian flow (but by a discrete map), and may range from regular (integrable) to completely chaotic (hyperbolic). It is characterized completely by the shape of the billiard and the size of the cyclotron radius. Below, in Section 3.2, we will briefly review this classical billiard problem. The remaining part of phase space describes the trivial motion on closed *cyclotron orbits*. It has a finite volume whenever the cyclotron radius is small enough to allow for a disk of radius ρ to fit into the domain. We will call the magnetic field *strong*, accordingly, if the cyclotron radius is comparable to or smaller than the size of the billiard – a criterion which is purely classical.

In the corresponding quantum problem, the eigenfunctions are required to satisfy the Schrödinger equation in the open domain $\mathring{\mathcal{D}}$, together with a boundary condition on the border line Γ (as discussed in Sect. 3.3). One observes that, at strong fields, the spectrum reflects the partitioning of the classical phase space. There are eigenstates which hardly touch the boundary, and have energies very close to the Landau levels.

They are called *bulk states*, because in the limit of strong fields they constitute the major part of the spectrum. We will see that these states are based on that part of phase space which is given by unperturbed cyclotron motion. At the same time, one finds eigenstates which are localized at the boundary. These *edge states* correspond to the skipping trajectories, and are expected to reflect the underlying billiard motion. Albeit being an effect of the boundary they may be quite significant. For instance, they typically exhibit a directed probability flux causing a large magnetic moment. This way they balance the magnetic moments of the bulk, leading to a zero mean magnetization, as discussed in Section 3.4.

The separation into edge and bulk states is intuitively clear and often used. Early studies were concerned with the surface electron states inside metals [55, 56], and after the discovery of the Quantum Hall Effect [57, 58] the notion of edge states was extensively employed to explain this phenomenon [59–64]. (In the latter problem the Hamiltonian must include an additional impurity potential.) However, the above characterization of edge states is rather vague and we are not aware of a general quantitative definition in the literature. In due course, we will propose a spectral measure, which allows to quantify the edge character of a state. Having a meaningful spectral density of edge states at our disposal, it will be worthwhile to consider the quantum problem also in the exterior.

Motion in the exterior

The *exterior* billiard problem is obtained by restricting the particle to the domain $\mathbb{R}^2 \backslash \mathcal{D}$ – henceforth called the exterior domain. From the classical point of view, there is little difference between the interior and the exterior dynamics. A particle impinging on the boundary from outside is reflected specularly and performs a skipping motion around the billiard. Like in the interior, the skipping trajectories cover a finite volume in phase space and are described by a discrete billiard bounce map. Complete cyclotron orbits, on the other hand, now exist for any ρ. The corresponding phase space volume is unbounded, because the cyclotron center may be located at an arbitrarily large distance from the billiard.

The fact that a "free particle" may not escape to infinity but is trapped on a cyclotron orbit is reflected by the exterior quantum spectrum. It is *discrete*, in marked contrast to the field-free scattering situation. The exterior quantum problem requires the stationary wave function to satisfy the Schrödinger equation in $\mathbb{R}^2 \setminus \mathring{\mathcal{D}}$, again with a boundary condition on Γ. In addition, the normalization condition (2.16) implies that the wave functions must vanish at infinity. In the absence of a boundary, the spectrum would be given by a discrete set of Landau energies, each infinitely degenerate, as shown in the preceeding chapter. The presence of a billiard lifts this degeneracy, turning each Landau level into a *spectral accumulation point*. This means, that there are infinitely many discrete eigen-energies in any finite vicinity of each Landau energy.

We shall address the general quantum problem in Section 3.3. There, the main concern will be on the boundary conditions and the average spectral behaviour, whereas the actual quantization is performed in Chapter 4. However, to prepare for the semiclassical quantization in Chapter 6, it is first necessary to take a closer look at the classical problem.

3.2 The classical billiard

Classical magnetic billiards were first examined by Robnik and Berry [65], and are still the subject of active research [49, 66–72]. In this section we collect basic results, limiting the discussion to those aspects which will be needed later on.

Parametrisation of the boundary

The classical dynamics is completely specified by the size of the cyclotron radius ρ and by the shape of the billiard. Throughout this work, the billiard boundary Γ is assumed to be smooth, so that its normals $\hat{\mathbf{n}}$ exist everywhere. We define them to point outwards (ie, into $\mathbb{R}^2 \setminus \mathcal{D}$). Keeping their orientation fixed will allow to distinguish the interior from the exterior problem. The boundary is parameterised by the arc length s,

$$\Gamma : s \in [0; \mathscr{L}] \mapsto \mathbf{r}(s) \in \mathbb{R}^2 , \tag{3.1}$$

such that the derivative yields the normalized tangent

$$\frac{\mathrm{d}\mathbf{r}(s)}{\mathrm{d}s} := \hat{\mathbf{t}}(s) = \begin{pmatrix} -n_y(s) \\ n_x(s) \end{pmatrix} . \tag{3.2}$$

We define the local curvature

$$\kappa(s_0) := 2 \lim_{s \to s_0} \frac{\big(\mathbf{r}(s) - \mathbf{r}(s_0)\big)\, \hat{\mathbf{n}}(s)}{\big(\mathbf{r}(s) - \mathbf{r}(s_0)\big)^2} \tag{3.3}$$

to be positive for convex domains. The area of the domain is denoted by $\mathscr{A}$, and $\mathscr{L}$ represents its circumference.

3.2.1 The billiard bounce map

As mentioned above, the particle's skipping motion may be described by the mapping of a Poincaré surface of section onto itself. Like in the case of field-free billiards [11, 73–75], it is natural to use the Birkhoff coordinates (s, p_s) to define the surface of section. They are given by the position on the boundary s (the curvilinear abscissa) and the (normalized) tangential component of the reflected velocity $p_s = \hat{\mathbf{v}}_0(s)\, \hat{\mathbf{t}}(s)$ at the point of reflection. The variables s and p_s are canonically conjugate in the sense described below. It is worth noting, therefore, that p_s is defined as a component of the *velocity* vector, rather than the (gauge-dependent) canonical momentum.

A point (s, p_s) in the Birkhoff phase space describes the position of incidence, and the direction of the velocity after reflection (once it is agreed on whether to consider the interior or exterior problem). Tracking the classical trajectory until its first intersection with the boundary specifies the next point of reflection s' uniquely, and p'_s follows from the law of specular reflection. Any reflected trajectory is included this way, and the complete billiard dynamics is described by the bounce map

$$\mathcal{B} : (s, p) \mapsto (s', p') \tag{3.4}$$

which maps the Poincaré surface of section $[0;\mathscr{L}] \times (-1;1)$ onto itself (in an area-preserving way.) In order to see that the map generates a discrete Hamiltonian evolution, one may look for a generating function $\mathscr{G}(s,s')$, which has the property to yield the (canonically) conjugate coordinates by differentiation,

$$p_s = -\frac{\mathrm{d}\mathscr{G}(s,s')}{\mathrm{d}s} \qquad \text{and} \qquad p'_s = \frac{\mathrm{d}\mathscr{G}(s,s')}{\mathrm{d}s'} \ . \tag{3.5}$$

The relation (3.5) is the discrete analogy to the case of continuous Hamiltonian dynamics, where the canonical momenta are similarly given by the derivative of the action. If the mixed second derivative of $\mathscr{G}$ has a definite sign the equations (3.5) may be globally inverted [75], yielding the bounce map (3.4). In the case of field free billiards, $\mathscr{G}$ is simply determined by the classical action accumulated along the trajectory between the points $\mathbf{r}(s)$ and $\mathbf{r}(s')$ [75], ie, by the distance $|\mathbf{r}(s) - \mathbf{r}(s')|$.

At this point, the magnetic billiard exhibits a peculiarity. For given initial and final points on the boundary, it allows in general for two distinct connecting trajectories. Those are the "short" and "long" arcs encountered in the preceeding chapter. It is therefore not clear, a priori, how to obtain a unique generating function for the magnetic case. In a recent article [67], Berglund and Kunz presented a "generating function", which is determined by the area between the trajectory and the boundary (together with the length of the trajectory). In the course of semiclassical quantization we will be lead to this form in a natural way (but shall argue that it is not a generating function in its proper sense).

The billiard dynamics may now be studied conveniently by investigating the properties of the map. The Poincaré surface of section plot is a simple means to get an overview on the dynamics. It is obtained by iterating the map (3.4) starting from a finite number of initial conditions. In Fig. 3.1 we show surface of section plots of an interior ellipse at different values of the the cyclotron radius. One observes the standard picture of mixed chaotic dynamics [7, 76, 77]. The trajectories either lie on invariant curves (characterizing regular motion) or cover a whole area in the surface of section (chaotic motion). Stable periodic orbits, in particular, are characterized by surrounding invariant lines ("islands of stability").

3.2.2 Integrable and hyperbolic billiards

In the field free case, the ellipse is known to be the only smooth billiard with two integrals of motion (including the circle as a special case). At finite magnetic fields, the ellipse turns chaotic – as we have just seen – except for the circle billiard. The latter exhibits the canonical angular momentum (2.13) as the second integral of the motion (if the circle is centered at the origin of the symmetric gauge). This suggests, that the circular shape yields the only integrable magnetic billiard.

The other extreme of motion is called *hyperbolic*, or displaying *hard chaos*. It is present if the stable part of phase space has zero measure, rendering almost all trajectories unstable. Hyperbolic billiards are popular, although they form a small class. Early examples of field-free billiards displaying hard chaos were given by Sinai [73] and Bunimovich [74].

Conditions for the instability of orbits in magnetic billiards are discussed in [68–70]. In his recent work [49], Gutkin applied a general hyperbolicity criterion [78] to

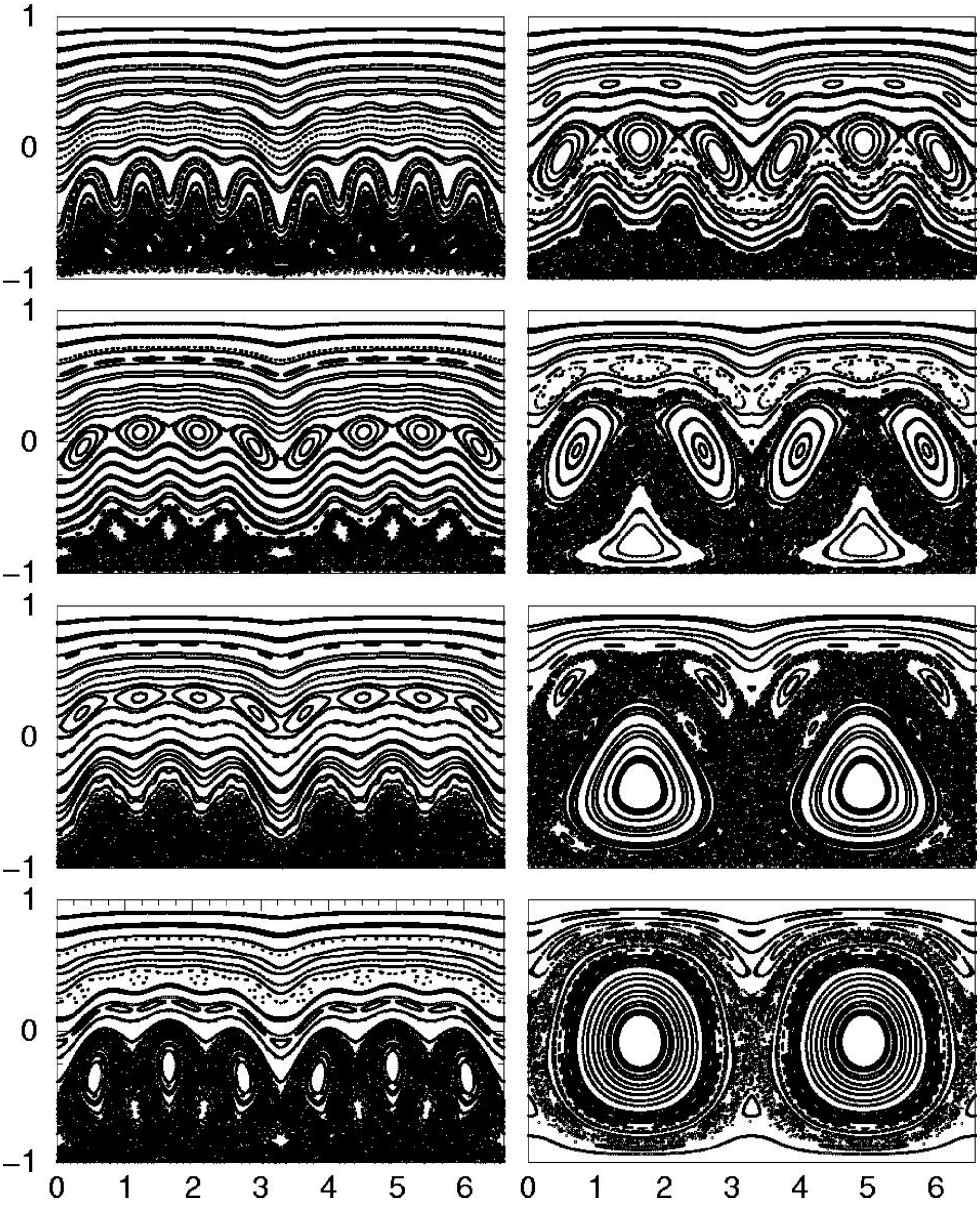

Figure 3.1: Birkhoff phase space portraits of the interior ellipse (strong eccentricity 0.8, area $\mathscr{A} = \pi$), for different values of the cyclotron radius $\rho = 0.40, 0.44, 0.50, 0.54$ (left column, top to bottom) and $\rho = 0.6, 1.0, 2.0, 10.0$ (right column, top to bottom). The motion turns (more) regular as the limit of a strong field, $\rho \to 0$, and a vanishing field, $\rho \to \infty$, is approached.

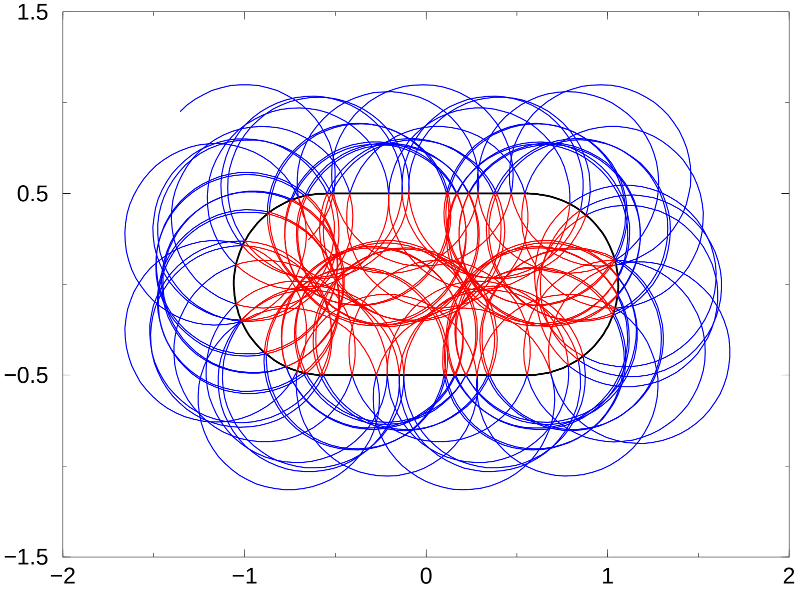

Figure 3.2: Parts of dual trajectories in the interior and exterior of a stadium-billiard at $\rho = 0.5$ (sequence of 75 reflections). The billiard shape is defined in Fig. 9.5.

construct classes of hyperbolic magnetic billiards. The critical parameter in these sets is given by the sum of the reciprocal cyclotron radius and the (local) curvature of the boundary. Hard chaos is guaranteed in these cases only for cyclotron radii above a minimum value.

Most of the billiards considered in this thesis are hyperbolic at zero field, but assume a mixed chaotic phase space at any finite cyclotron radius. An example of a billiard shape, which generates truly hyperbolic motion even at fairly strong fields, is given in the right part of Fig. 5.1.

The above statements apply equally to the interior and exterior dynamics, and there was no need to distinguish between them. This changes as we turn to the question of how the classical interior and exterior problems are related.

3.2.3 The interior-exterior duality

When comparing interior and exterior motion, the size of the cyclotron radius ρ plays a crucial role. An important situation is set up if cyclotron radius and billiard shape are such that any circle with radius ρ intersects the boundary at most twice. For convex domains, a sufficient condition is the cyclotron radius being greater than the maximum radius of curvature, or smaller than the minimum radius of curvature. However, convexity is by no means needed for the above criterion — which we shall assume to hold, for the moment.

Now consider a segment of an interior trajectory going from $\mathbf{r}(s)$ to $\mathbf{r}(s')$. The same two points are connected by a valid exterior trajectory, which travels backwards in time. Necessarily, the two arcs form a complete circle of radius ρ. (They do not intersect with the boundary, except at the points $\mathbf{r}(s)$ and $\mathbf{r}(s')$, because the above cri-

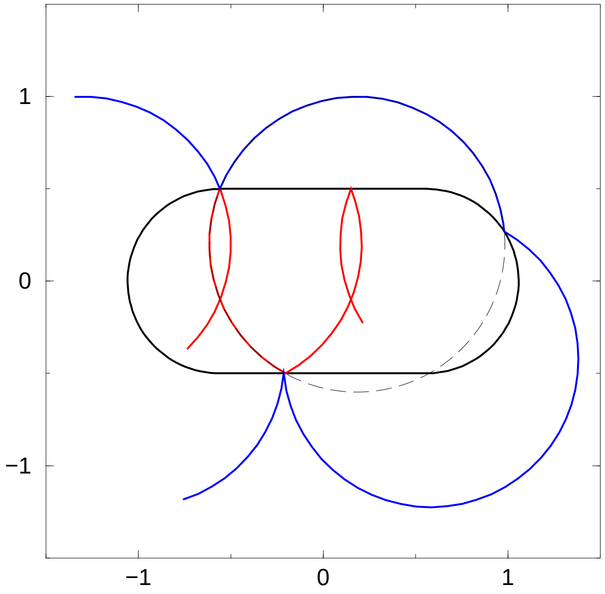

Figure 3.3: Breakdown of the duality in segments of partially corresponding trajectories (stadium of Fig. 3.2 at $\rho = 0.8$.) Only the two left (top) arcs in the interior (exterior) meet with a dual partner. The breakdown occurs because a cyclotron orbit, which is obtained by continuing the arcs (dashed line) intersects the boundary more than twice.

terion was assumed to hold.) The interior trajectory is reflected specularly and finally runs into the boundary at $\mathbf{r}(s'')$. Clearly, the time-reversed exterior trajectory obeys the same law of specular reflection, leading to the same boundary point $\mathbf{r}(s'')$. It follows that the interior dynamics and the time-reversed exterior one are described by the same Poicaré surface of section. Every interior trajectory is linked with a *dual* exterior trajectory, which travels backwards in time. We call this property the *classical duality* of interior and exterior motion. Pairs of dual trajectories are displayed in Figure 3.2 and 10.8.

As an immediate consequence of classical duality, one finds for any given interior *periodic* orbit[*] a dual periodic orbit in the exterior, and vice versa. Being periodic, both may now be thought of as running forward in time, but then with opposite orders in the sequence of reflection points. Clearly, these dual partners are intimately related. We will see that they have the same stability properties, and that the sum of their actions is an integer multiple of the action of a full cyclotron orbit (with the integer given by the number of reflections). Examples of dual periodic orbits are given in Figure 10.8 on page 140.

Figure 3.3 shows that the duality breaks down once the *duality condition* that “any circle of radius ρ intersects the boundary at most twice”, is no longer fulfilled. Typically, only a small fraction of the phase space corresponds to arcs which violate the duality condition. Fig 3.4 gives an impression of the fraction of phase space belonging to arcs whose extension intersects the boundary more than twice.

---

[*] The collection of periodic orbits is known to be dense in phase space. It plays an important role in semiclassical quantization, see Chapter 6.

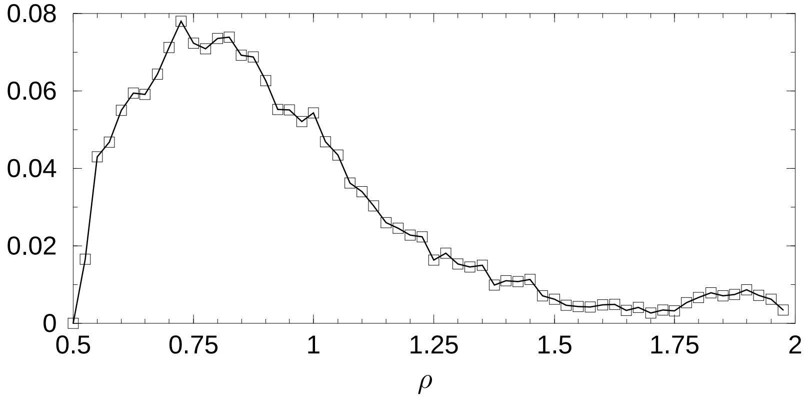

Figure 3.4: Fraction of the complete interior phase space belonging to arcs which violate the duality criterion, as a function of the cyclotron radius ρ. (Calculated for the stadium billiard in Fig. 3.2; the squares indicate the error of the statistical sampling.)

3.3 Quantum billiards

Quantizing classically chaotic billiards is a popular way to study the effects of classical chaos on quantum dynamics [79, 80]. Quantum billiards are sufficiently simple to inspire analytical studies and to permit full-scale numerical experiments. At the same time, they display most of the generic properties of Hamiltonian systems. Many discoveries in the field of quantum chaos, such as the universality of chaotic spectra [12], the scarring of wave functions by unstable periodic orbits [13, 14], and the existence of action correlations [15] were first made in these 2-dimensional model systems. When a magnetic field is applied, this is usually done to break the time-reversal symmetry, or to mimic the situation in semiconductor heterostructures.

Magnetic quantum billiards

Arguably, the earliest study of a magnetic quantum billiard was carried out by Nakamura and Thomas [20] who assert that billiards which are classically chaotic display a reduced diamagnetic susceptibility. (This was later found to be incorrect [81].) Later works are concerned with the spectral implications of the absence of time-reversal invariance [21–23]. Special geometries, such as the disk [82, 83] or, more recently, the square [25, 84, 85], received attention as well. All these studies were limited to the first few hundred eigenvalues, and only to the interior problem.

3.3.1 General boundary conditions

The mentioned works use Dirichlet boundary conditions, ie, demand the wave function to vanish on the boundary. It is the natural choice from a physical point of view, which takes the boundary as due to an infinite potential step. However, it will prove fruitful to consider slightly more general, “mixed” boundary conditions, which include the

Dirichlet choice as a special case. They are defined by the equation

$$\psi(\mathbf{r}) = \pm\frac{\lambda}{b}\big(\partial_{n/b}\psi(\mathbf{r}) - \mathrm{i}\tilde{A}_n(\mathbf{r})\psi(\mathbf{r})\big), \quad \mathbf{r}\in\Gamma\,. \tag{3.6}$$

The lower sign stands here for exterior problem. The symbols, $\partial_{n/b} := b\hat{\mathbf{n}}(\mathbf{r})\boldsymbol{\nabla}_r$ and $\tilde{A}_n = \hat{\mathbf{n}}(\mathbf{r})\tilde{\mathbf{A}}$ denote the scaled normal derivative, and the normal component of the scaled vector potential, respectively.

The "mixing" parameter λ interpolates between the two extremes, *Dirichlet*, $\lambda = 0$, and *Neumann* boundary conditions, $\lambda^{-1} = 0$. In principle, λ may be a function of the position on the boundary, but will be taken constant throughout the thesis. At non-vanishing λ, our boundary conditions (3.6) are the gauge-invariant generalisation of the mixed boundary conditions known for the Helmholtz problem [86–88]. They imply that the normal component of the current density $\tilde{\jmath}_n = \mathrm{Im}(\psi^*\partial_{n/b}\psi) - \tilde{A}_n|\psi|^2$ vanishes for any λ. (This can be noted after multiplying equation (3.6) with ψ^* and taking the imaginary part.) The resulting conservation of the probability density explains why the condition (3.6) keeps the problem self-adjoint for any λ.

The explicit appearance of the vector potential in (3.6) is needed to ensure the gauge-invariance of the boundary conditions. The fact that the definition does not depend on the gauge freedom χ is easily seen observing the gauge dependence of a general wave function (2.34).

Finally, note that λ has the dimension of a length, cancelling the dimensionality introduced by the normal derivative. The magnitude of the latter depends on the modulus $k = \sqrt{2m_\circ E}/\hbar$ of the wave vector. To account for this trivial energy dependence of the eigenstates on the boundary condition, it will be convenient (later in the semiclassical treatment) to use the dimensionless mixing parameter

$$\Lambda := k\lambda = 2\sqrt{\nu}\,\frac{\lambda}{b}\,. \tag{3.7}$$

We did not state the definition (3.6) of the boundary condition in terms of Λ because its dependence on the spectral variable ν would destroy the self-adjointness of the problem, rendering different eigenstates non-orthogonal.

A quite different type of boundary conditions for magnetic billiards was proposed recently by Akkermans *et al* [89]. It was designed specifically to be sensitive on the "chirality" of the wave functions. For the special situation of a separable problem (ie, a disk billiard) they allow to split the interior eigenspace into two subspaces with definite chirality. We will see that this is quite close to the desired separation into bulk and edge states. However, it does not work in the case of a general billiard, and the resulting spectrum has no relation to the standard Dirichlet conditions. Below, we will take a different approach to separate edge and bulk, by adjusting the spectral measure according to our needs, rather than modifying the spectrum.

3.3.2 The quantum spectrum

Unlike their field-free relatives, magnetic quantum billiards offer two independent external parameters – the cyclotron radius and the magnetic length. As discussed in Section 2.3, one must specify which one is to be fixed in order to define a quantum spectrum. In the text part of this thesis, we will state the formulas for spectral densities only for conventional high-energy spectra taken at fixed magnetic length b. This is done to avoid clumsy notation, and to minimise the danger of confusion. A summary of formulas for spectra defined in the semiclassical direction is given in Appendix D. Still, some of the numerical investigations presented below are carried out on spectra defined in the semiclassical direction. This will be clearly indicated.

The spectral staircase

The simplest function to characterize a spectrum is the *spectral staircase* (or *number counting function*), which gives the number of spectral points below the specified energy. For a set of eigenvalues $\{\nu_n\}$, it is formally defined as a sum

$$\mathrm{N}(\nu) := \sum_{n=1}^{\infty} \Theta\big(\nu - \nu_n\big) \tag{3.8}$$

over Heaviside step functions Θ. Note that N is a well-defined function only for the interior problem, because of the infinite number of exterior bulk states close to each Landau level. The spectral density is conveniently defined as the energy derivative of the counting function,

$$d(\nu) := \frac{\mathrm{d}}{\mathrm{d}\nu}\mathrm{N}(\nu) = \sum_{n=1}^{\infty} \delta(\nu - \nu_n)\ . \tag{3.9}$$

It should be understood in the sense of distributions. Formally, such a sum of Dirac δ-functions could be defined for the exterior problem as well. However, this density would be meaningful at most in a local sense, since the convolution with a generic function would diverge at all the Landau energies. Therefore, the following discussion of the smooth, asymptotic properties of magnetic spectra must be restricted to the interior problem.

3.3.3 Asymptotic counting functions

The spectral staircase is described asymptotically by the *mean number counting function* $\overline{\mathrm{N}}(\nu)$, which is uniquely defined [90]. For Dirichlet boundary conditions it is given by the asymptotic expression [91]

$$\overline{\mathrm{N}}(\nu) = \frac{\mathscr{A}}{b^2\pi}\,\nu - \frac{\mathscr{L}}{2\pi b}\,\nu^{\frac{1}{2}} + \frac{1}{6} + \mathrm{O}\big(\nu^{-\frac{1}{2}}\big)\ . \tag{3.10}$$

The expression includes only geometric quantities and the conventional wave vector $\sqrt{2m_\circ E}/\hbar = 2\sqrt{\nu}/b$, which are all *independent* of the magnetic field. The field independence of the leading order term follows immediately from Weyl's law, as we will see below. However, it is not obvious that the next two orders are identical to the field free case as well. This was proved only recently in [91], and for circular billiards in [92].

Note the hierarchy of the geometric quantities appearing in (3.10). The leading and the second term are proportional to the area and the circumference, respectively. The constant is determined* by the mean curvature $\int_\Gamma \kappa(s)\mathrm{d}s = 2\pi$. Moreover, the

---

*The constant term in (3.10) is modified if there are corners in the boundary [91].

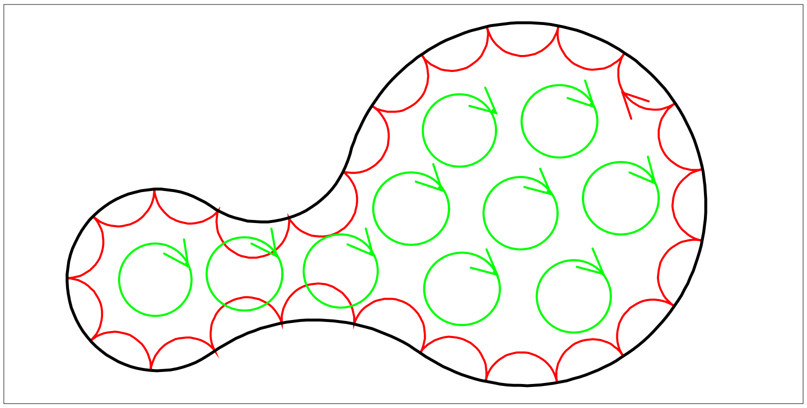

Figure 3.5: At strong magnetic fields, $\rho \ll \mathscr{L}$, the major part of the available phase space consists of complete cyclotron orbits. The skipping orbits give rise to a net current along the boundary. It has a counter-clockwise sense of orientation, in contrast to the cyclotron orbits.

higher order terms are typically proportional to higher moments of the curvature [93]. This indicates that it is reasonable to view the effect of the boundary on asymptotic quantities in a perturbative sense. The gross dependence of a general billiard is determined by the enclosed area, with the circumference as a first correction. The next modification is then given by assuming a finite mean curvature, while taking into account higher order moments of the curvature distribution would yield to higher order corrections.

Weyl's law revisited

Let us consider Weyl's law more explicitely. It states, that the number of quantum states below a given energy is determined, to leading order, by the volume of phase space, which is covered by the energy shell, divided by (a power of) Planck's quantum

$$\overline{\mathrm{N}}_{\mathrm{tot}}(\rho^2, b^2) = \frac{1}{(2\pi\hbar)^2} \iint \Theta(E - \mathrm{H})\, \mathrm{d}^2\mathbf{r}\, \mathrm{d}^2\mathbf{p} \tag{3.11}$$

$$= \frac{1}{(b^2\pi)^2} \iint \Theta\big(\rho^2 - |\boldsymbol{\rho}|^2\big)\, \mathrm{d}^2\mathbf{c}\, \mathrm{d}^2\boldsymbol{\rho}\,. \tag{3.11a}$$

This is the first term in the asymptotic expansion (3.10). Changing the integration of the canonical momentum to the velocity vector in the first line renders the phase space integral *independent* of the magnetic field (since the Jacobian is constant [94]). This shows immediately that the leading order term of the counting function (like any quantity which may be written as a phase space integral of position and velocity) cannot depend on the field strength.

In (3.11a), however, we transformed the variables of integration to the radius vector $\boldsymbol{\rho}$, cf eq (2.7), and the cyclotron center $\mathbf{c} = \mathbf{r} - \boldsymbol{\rho}$, which *do* depend on the magnetic field. As a result, the role of Planck's quantum is now played by the area $b^2\pi$.

This second form of the phase space integral has the advantage that it allows to separate the volumes of skipping and cyclotron motion. The center $\mathbf{c}$ is a constant

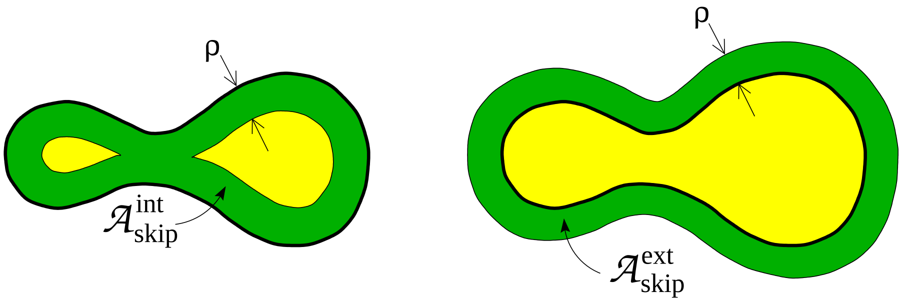
ρ
$\mathcal{A}_{\mathrm{skip}}^{\mathrm{int}}$
ρ
$\mathcal{A}_{\mathrm{skip}}^{\mathrm{ext}}$

Figure 3.6: The dark shaded region indicates the area determining the phase space volume of interior (left) and exterior (right) skipping orbits. It is given by those points of the interior and exterior domain, respectively, which have a distance less than *one* cyclotron radius ρ to the boundary.

of the motion for all cyclotron orbits. Hence, integrating only the cyclotron part of the centers one obtains the area $\mathscr{A}_{\mathrm{cyc}}(\rho)$ of the set of points in $\mathcal{D}$ with a distance from the boundary greater than ρ. Consequently, the number of quantum states which correspond to cyclotron motion is given, to leading order, by the integral

$$\overline{\mathrm{N}}_{\mathrm{cyc}}(\rho^2, b^2) = \frac{2\pi}{(b^2\pi)^2} \int_0^\rho \mathscr{A}_{\mathrm{cyc}}(\rho')\rho' \mathrm{d}\rho' \; . \tag{3.12}$$

We note from (3.10) that the total number of states reads to leading order,

$$\overline{\mathrm{N}}_{\mathrm{tot}}(\rho^2, b^2) = \frac{2\pi}{(b^2\pi)^2} \frac{\rho^2 \mathscr{A}}{2} \; . \tag{3.13}$$

Hence, the number of states associated with the skipping part of phase space can be written as an integral

$$\overline{\mathrm{N}}_{\mathrm{skip}}(\rho^2, b^2) = \overline{\mathrm{N}}_{\mathrm{tot}} - \overline{\mathrm{N}}_{\mathrm{cyc}} = \frac{2\pi}{(b^2\pi)^2} \int_0^\rho \mathscr{A}_{\mathrm{skip}}(\rho')\rho' \mathrm{d}\rho' \; , \tag{3.14}$$

involving the area $\mathscr{A}_{\mathrm{skip}}(\rho) := \mathscr{A} - \mathscr{A}_{\mathrm{cyc}}(\rho)$. By definition, this area is given by those points in the interior domain which are closer to the boundary than the cyclotron radius, cf Fig. 3.6. It determines the mean density of those states, which correspond to the skipping part of phase space.

$$\overline{d}_{\mathrm{skip}}(\nu) = \frac{\mathrm{d}}{\mathrm{d}\nu} \overline{\mathrm{N}}_{\mathrm{skip}}(\nu\, b^2, b^2) = \frac{\mathscr{A}_{\mathrm{skip}}(b\sqrt{\nu})}{b^2\pi} \tag{3.15}$$

This is a remarkably simple formula. To obtain the mean density of (interior) quantum states corresponding to the skipping motion, one merely has to divide the area $\mathscr{A}_{\mathrm{skip}}^{\mathrm{int}}$ by the Planck quantum $b^2\pi$. It should be made clear, however, that we do not yet have a criterion at our disposal, which allows for a clear distinction of edge and bulk states. Clearly, any reasonable such definition should pass the requirement of being consistent with (3.15).

Furthermore, a proper "density of edge states" will have to be well-defined also in the *exterior*. Let us therefore comment on the expected mean number of exterior states which correspond to skipping motion. By symmetry, it should be determined by the area $\mathscr{A}^{\mathrm{ext}}_{\mathrm{skip}}$ of those points in the exterior domain which are closer to the boundary than ρ. We confirmed this for the circular geometry, where the integral over the skipping part of phase space in (3.11a) can be performed explicitely. For a disk of radius R one obtains

$$\overline{\mathrm{N}}^{\mathrm{int}}_{\mathrm{skip}} = \begin{cases} \frac{4}{3}\,\frac{\mathscr{L}}{2\pi b}\,\nu^{\frac{3}{2}} - \frac{1}{2}\nu^{2} & \text{if } \sqrt{\nu}\,b < R \\ \frac{\mathscr{A}}{b^{2}\pi}\nu & \text{if } \sqrt{\nu}\,b > R \end{cases} \tag{3.16}$$

$$\overline{\mathrm{N}}^{\mathrm{ext}}_{\mathrm{skip}} = \frac{4}{3}\,\frac{\mathscr{L}}{2\pi b}\,\nu^{\frac{3}{2}} + \frac{1}{2}\nu^{2}\ , \tag{3.17}$$

for the interior and the exterior problem, respectively. Note that the interior number is determined by the area $\mathscr{A}$ of the domain once the cyclotron radius $\rho = \sqrt{\nu}\,b$ exceeds the radius R of the disk, preventing any cyclotron orbits in the interior.

At strong fields, $b \ll \rho \ll \mathscr{L}$, in contrast, it is the circumference term which dominates. Since in this case we may neglect the mean curvature, the average number of skipping states is approximately given by

$$\overline{\mathrm{N}}_{\mathrm{skip}} = \frac{4}{3}\,\frac{\mathscr{L}}{2\pi b}\,\nu^{\frac{3}{2}}\ . \tag{3.18}$$

This is the phase space estimate for a straight line with periodic boundary conditions.

We now turn to another quantity which serves to characterize interior magnetic billiards – the response of the spectrum to changes in the magnetic field. Its asymptotic properties may be related to a phase space integral as well.

3.4 Orbital magnetism

Employing the notion of *orbital magnetism* we slightly abuse a thermodynamic concept for our one-particle problem. Nonetheless, it is worthwhile to ask for the magnetic response of the billiard dynamics in the sense of statistical mechanics. Since we do not want to discuss effects of finite temperature, only microcanonical ensembles will be considered. It means that averages are performed on the energy shell in phase space, ie, among all orbits of a given cyclotron radius.

Let us first consider the classical motion along a single *periodic*[*] trajectory. Being charged, the particle constitutes an electric current, which in turn induces a magnetic moment. Will it serve to strengthen or to weaken the applied magnetic field? Clearly, the latter is true in the case of a cyclotron orbit. Here, the (scaled) magnetic moment turns negative,

$$\frac{1}{2}\int_{0}^{\tilde{T}_{\mathrm{cyc}}} \tilde{\mathbf{r}}(\tilde{t}) \times \tilde{\mathbf{v}}(\tilde{t})\,\mathrm{d}\tilde{t} = -\nu\ , \tag{3.19}$$

which shows that the cyclotronic part of phase space is *diamagnetic*. The skipping orbits, one the other hand, will in general give rise to both signs. At strong fields (if the cyclotron radius is shorter than the minimum diameter of the billiard) skipping trajectories carry a net current along the boundary. It is orientated clockwise, ie, opposite to the cyclotron orbits (see Fig. 3.5). A detailed analysis [95] shows that, in any case, a subtle cancellation mechanism between cyclotron and skipping orbits is at work, which guarantees that classically there is *no* net orbital magnetization. This is called the van Leeuwen theorem [94, 95].

---

[*] We may confine the discussion to periodic orbits, because the set of periodic orbits is known to be dense in phase space.

The statement is proved immediately by evoking the thermodynamic definition of the magnetization, as the derivative of a thermodynamic potential (the free energy or the grand canonical potential) with respect to the magnetic field. The potentials are determined by the partition sum, which is classically a phase space integral. The latter does not depend on the magnetic field for the reasons given in the preceding section [94].

Before we turn to the precise quantum definition, it should be emphasized that orbital magnetism in its proper sense is an effect of many particles at finite temperature. Assuming the temperature to be much larger than the spacing between Landau levels, $T \gg \hbar\omega_c/k_B$, Landau showed [27] that a degenerate Fermi gas exhibits a small[†] net diamagnetic response. This Landau diamagnetism is an effect of the bulk. Asymptotic corrections due to the existence of a boundary are discussed in [91, 92, 97–100].

Recently, the effect met some renewed interest, since the *geometry* of mesoscopic devices may greatly enhance orbital magnetism. Semiclassical treatments in terms of periodic orbit theory may be found in [25, 101–104]. In all these works the magnetic field was assumed to be weak, so that the bending of the trajectories could be neglected. An exception is the study of the quantum and semiclassical magnetization of the magnetic disk in [105]. A comprehensive review on the subject of orbital magnetism is given in [106].

In this work we shall use the concept of orbital magnetization merely as a means of characterizing magnetic billiards, ie, we disregard effects of impurities and finite temperature. We shall argue that it is advantageous to adopt a modified definition of orbital magnetization. In order to motivate this, we start with the conventional one.

Conventional magnetization

Given the spectrum $\{E_n\}$ at finite magnetic field B, one may conventionally define the magnetization as

$$\mathcal{M}_{\mathrm{conv}}(E,B) := -\sum_{E_n \le E} \frac{\mathrm{d}E_n}{\mathrm{d}B} = \int_0^E \mathrm{m}(E';B)\,\mathrm{d}E' \,. \tag{3.20}$$

This is the one-particle and zero-temperature limit of the standard thermodynamic definition. By means of equation (3.20) the function m is introduced, which we shall call the magnetization density,

$$\mathrm{m}(E,B) := \frac{\mathrm{d}\mathrm{N}_{\mathrm{tot}}}{\mathrm{d}B}(E,B) = -\sum_n \frac{\mathrm{d}E_n}{\mathrm{d}B}\,\delta(E-E_n) \,. \tag{3.21}$$

[†] The effect is one third of the Pauli spin paramagnetism [96].

The relation of m to the electrodynamic interpretation of the magnetization is seen once we note the derivative of the Hamilton operator (2.14) with respect to the magnetic field,

$$\frac{\mathrm{dH}}{\mathrm{d}B} = -\frac{q}{2}\,(\mathbf{r}\times\mathbf{v})_{\mathrm{sym}}\;. \tag{3.22}$$

It is the operator of the magnetic moment, where $()_{\mathrm{sym}}$ indicates the symmetrized form. It follows that the energy derivatives $\mathrm{d}E_n/\mathrm{d}B$ in eq (3.21) are given by the corresponding expectation values of the magnetic moment. Hence, the magnetization density (3.21) reads

$$\mathrm{m}(E,B) = \sum_n \frac{q}{2}\langle\psi_n|(\mathbf{r}\times\mathbf{v})_{\mathrm{sym}}|\psi_n\rangle\,\delta(E-E_n)\;. \tag{3.23}$$

The fact that the mean magnetization (density) vanishes is seen immediately from the field-independence of $\overline{\mathrm{N}}$, eq (3.10), as noted above. It follows that, at strong fields, the negative moments of (many) bulk states are balanced by the large, positive magnetic moments of relatively few edge states. This will be seen much more clearly once we modify the definition of the magnetization, such that is complies with the scaling properties of the system.

Bulk and edge magnetization

We proceed to define a scaled magnetization which has considerable advantages, compared to the conventional one. By virtue of (2.40) the spectrum $\{\nu_n\}$ depends parametrically on the magnetic length, $\nu_n = \nu_n(b^2)$. It is natural to define the *scaled magnetization density*, such that it yields the density of the scaled magnetic moment (3.25), in analogy to (3.23). Hence, one is led to the definition

$$\widetilde{\mathrm{m}}(\nu,b^2) := -\,b^2\frac{\partial\mathrm{N}}{\partial b^2} - \nu\frac{\partial\mathrm{N}}{\partial\nu} \tag{3.24}$$

$$= \sum_n \left(b^2\frac{\mathrm{d}\nu_n}{\mathrm{d}b^2} - \nu_n\right)\delta(\nu-\nu_n) \tag{3.24a}$$

$$= \sum_n \frac{1}{2}\langle\psi_n|(\tilde{\mathbf{r}}\times\tilde{\mathbf{v}})_{\mathrm{sym}}|\psi_n\rangle\,\delta(\nu-\nu_n)\;. \tag{3.24b}$$

To see that the expectation value of the scaled magnetic moment is indeed determined by a derivative of the energy with respect to the magnetic length,

$$\frac{1}{2}\langle\psi_n|(\tilde{\mathbf{r}}\times\tilde{\mathbf{v}})_{\mathrm{sym}}|\psi_n\rangle = b^2\frac{\mathrm{d}\nu_n}{\mathrm{d}b^2} - \nu_n\;, \tag{3.25}$$

one merely has to apply the appropriate differential operator to the scaled Hamiltonian. The scaled magnetization follows by integrating the density.

$$\widetilde{\mathcal{M}}(\nu,b^2) := \sum_{\nu_n\le\nu}\left(b^2\frac{\mathrm{d}\nu_n}{\mathrm{d}b^2} - \nu_n\right) = \int_0^\nu \widetilde{\mathrm{m}}(\nu',b^2)\,\mathrm{d}\nu' \tag{3.26}$$

$$= \widetilde{\mathcal{M}}_{\mathrm{edge}} + \widetilde{\mathcal{M}}_{\mathrm{bulk}} \tag{3.26a}$$

As indicated in the second line, the scaled magnetization splits up naturally into two parts, which we like to call, respectively, the *edge* magnetization,

$$\widetilde{\mathcal{M}}_{\mathrm{edge}}(\nu, b^2) := \sum_{\nu_n \leq \nu} b^2 \frac{\mathrm{d}\nu_n}{\mathrm{d}b^2} = - \int_0^{\nu} b^2 \frac{\mathrm{d}}{\mathrm{d}b^2} \mathrm{N}(\nu', b^2)\, \mathrm{d}\nu' \, , \tag{3.27}$$

and the *bulk* magnetization,

$$\widetilde{\mathcal{M}}_{\mathrm{bulk}}(\nu, b^2) := - \sum_{\nu_n \leq \nu} \nu_n = - \int_0^{\nu} \nu' \frac{\mathrm{d}}{\mathrm{d}\nu'} \mathrm{N}(\nu', b^2)\, \mathrm{d}\nu' \, . \tag{3.28}$$

This labelling is appropriate, since any Landau state (2.22) exhibits a magnetic moment $\langle n, m | \frac{1}{2}(\tilde{\mathbf{r}} \times \tilde{\mathbf{v}})_{\mathrm{sym}} | n, m \rangle = -(n + \frac{1}{2}) = -\nu$, like the classical cyclotron orbit (3.19). Each eigenstate contributes to both magnetization densities,

$$\widetilde{\mathrm{m}}_{\mathrm{edge}}(\nu, b^2) = \sum_n b^2 \frac{\mathrm{d}\nu_n}{\mathrm{d}b^2} \, \delta(\nu - \nu_n) \tag{3.29}$$

and

$$\widetilde{\mathrm{m}}_{\mathrm{bulk}}(\nu, b^2) = - \sum_n \nu_n \, \delta(\nu - \nu_n) \, . \tag{3.30}$$

The energies of bulk states lie close to the *constant* Landau levels and hardly change, as b^2 is varied. Hence, they give rise to a negligible edge contribution. Edge states, in contrast, contribute to the edge magnetization much stronger than to the bulk. This follows from the mean values of the magnetization. For the smooth edge magnetization density one finds, cf (3.10),

$$\overline{\mathrm{m}}_{\mathrm{edge}}(\nu, b^2) = -b^2 \frac{\partial \overline{\mathrm{N}}}{\partial b^2} = \frac{\mathscr{A}}{b^2 \pi} \nu - \frac{1}{2} \frac{\mathscr{L}}{2\pi b} \nu^{\frac{1}{2}} \, . \tag{3.31}$$

Remarkably, the bulk mean value assumes a form,

$$\overline{\mathrm{m}}_{\mathrm{bulk}}(\nu, b^2) = -\nu \frac{\partial \overline{\mathrm{N}}}{\partial \nu}(\nu, b^2) = -\overline{\mathrm{m}}_{\mathrm{edge}}(\nu, b^2) \, , \tag{3.32}$$

which cancels the mean edge magnetization completely. Hence, the mean (total) magnetization, $\overline{\mathcal{M}} = \overline{\mathcal{M}}_{\mathrm{edge}} + \overline{\mathcal{M}}_{\mathrm{bulk}}$ vanishes like in the conventional case. This holds strictly for any field, independently of whether or not there is a classical separation into skipping and cyclotron orbits.

The edge magnetization (3.27) defined in this section embodies a first quantity, which allows to distinguish edge states quantitatively. We emphasize that it is *observable* in a physical experiment. While the spectrum is measured in the high-energy direction, the derivative is to be taken in the semiclassical one (ie, changing b^2 at fixed cyclotron radius ρ.) This may be done by changing both, field and (Fermi) energy appropriately. This concludes the introductory part and we can start with the real work.

Chapter 4

Quantization in the interior and the exterior: The boundary integral method

In this chapter, we solve the quantization problem for interior and exterior magnetic billiards by means of a boundary integral method. It allows to obtain the spectra and wave functions of arbitrarily shaped billiard domains, and includes the general boundary conditions discussed in Section 3.3.1.

4.1 Boundary methods

As compared to the field free case, it is surprisingly difficult to obtain the quantum spectra of magnetic billiards. So far, numerical studies were limited to the interior problem and performed almost exclusively by diagonalizing the Hamiltonian [20–24]. This requires the choice and truncation of a basis, which is problematic for general billiards, where no natural magnetic basis set exists. Consequently, results were limited to the first few hundred eigenvalues (of unclear precision).

The quantum spectra of field-free billiards are usually obtained by transforming the eigenvalue problem into an integral equation of lower dimension. The corresponding integral operator is defined in terms of the free Green function, and depends only on the boundary [107–112]. This method is known to be more efficient than diagonalization by an order of magnitude [113].

It seems natural to extend these ideas to magnetic billiards. A step in this direction was taken recently by Tiago *et al* [40], who essentially propose a null-field method[*] [114] for (interior) magnetic billiards. It involves the irregular Green function (B.14) in angular momentum decomposition. A drawback of the approach is that the latter must be known for large angular momenta, which turns out to be numerically impractical. Moreover, the method does not apply for the exterior problem.

---

[*] The authors of [40] inaccurately call their scheme a “boundary integral method”.

Below, we present the boundary integral method for magnetic billiards [115]. Like in the field free case, it involves the regular Green function in position space representation. We present the method for the interior and the exterior problem, and general boundary conditions.

Outline

Two independent boundary integral equations are known for field-free billiards. In Section 4.2 we derive their magnetic analogues in a gauge-invariant formulation. It is shown that, unlike the field-free case, each of these equations yield only a necessary but not a sufficient condition for the definition of the spectra. In other words, each equation admits spurious solutions. We identify the physical origin of the latter and propose a way to avoid them, at the expense of dealing with singular (and eventually even *hypersingular* [116]) operators.

The explicit form of the integral operators is presented in Section 4.3, where we discuss the nature of the singularities as well. In Section 4.4, it is shown how the integral equations may be solved treating the singular parts of the operators analytically. This leaves the remaining problem in a form suitable for numerical treatment. Its implementation is sketched in Section 4.5, together with a discussion of the numerical convergence and the attainable accuracy.

The power of the proposed method is demonstrated in Chapter 5, where we study spectral statistics using several thousand levels and present interior and exterior wave functions in the quasi-classical regime.

4.2 The boundary integral equations

4.2.1 Single and double layer equations

The stationary eigenfunction of a magnetic billiard at energy ν is defined by the differential equation

$$\Big(\tfrac{1}{2}\big(-\mathrm{i}\boldsymbol{\nabla}_{r/b}-\tilde{\mathbf{A}}(\mathbf{r})\big)^2-2\nu\Big)\,\psi(\mathbf{r})=0\;, \tag{4.1}$$

and a specification of the wave function on the billiard boundary Γ. We shall employ the general gauge invariant boundary conditions defined in Section 3.3.1. The free Green function, G_ν, was shown to satisfy the inhomogeneous Schrödinger equation

$$\Big(\tfrac{1}{2}\big(-\mathrm{i}\boldsymbol{\nabla}_{r/b}-\tilde{\mathbf{A}}(\mathbf{r})\big)^2-2\nu\Big)\,\mathrm{G}_\nu(\mathbf{r};\mathbf{r}_0)=-\tfrac{1}{2}\,\delta\bigg(\frac{\mathbf{r}-\mathbf{r}_0}{b}\bigg)\;. \tag{4.2}$$

Our goal is to cast the quantization problem into an integral equation defined on the billiard boundary. To that end, we take the complex conjugate of (4.1) and multiply it (from the left) with G_ν. Similarly, equation (4.2) is multiplied with ψ^* and subtracted from the former expression. This way an equation is obtained,

$$\psi^*\,\boldsymbol{\nabla}^2_{r/b}\mathrm{G}_\nu-\mathrm{G}_\nu\,\boldsymbol{\nabla}^2_{r/b}\psi^*-2\mathrm{i}\,\boldsymbol{\nabla}_{r/b}\big(\tilde{\mathbf{A}}\psi^*\mathrm{G}_\nu\big)=\psi^*\,\delta\bigg(\frac{\mathbf{r}-\mathbf{r}_0}{b}\bigg)\;, \tag{4.3}$$

which has a form suitable for the Green and Gauss integral theorems. It holds everywhere in the plane, except for the boundary Γ, where the boundary condition (3.6) introduces a discontinuity in the derivative of ψ.

We start by considering the interior problem. The treatment of the exterior case is quite analogous and sketched afterwards. Choosing the initial point of the Green function away from the boundary, $\mathbf{r}_0 \in \mathbb{R}^2 \setminus \Gamma$, the integral of (4.3) over the (interior) domain $\mathcal{D}$ may be transformed to a line integral,

$$\int_\Gamma \big[\psi^* \, \partial_{n/b} \mathrm{G}_\nu - \mathrm{G}_\nu \, \partial_{n/b} \psi^* - 2\mathrm{i} \, \tilde{A}_n \, \psi^* \, \mathrm{G}_\nu \, \big] \frac{\mathrm{d}\Gamma}{b} = \left\{ \begin{array}{cl} \psi^*(\mathbf{r}_0) & \text{if } \mathbf{r}_0 \in \mathring{\mathcal{D}} \\ 0 & \text{if } \mathbf{r}_0 \in \mathbb{R}^2 \setminus \mathcal{D}. \end{array} \right. \tag{4.4}$$

It is defined on the boundary Γ (with the normal components of the vector potential and the gradient denoted as $\tilde{A}_n = \hat{\mathbf{n}}(\mathbf{r}) \tilde{\mathbf{A}}$ and $\partial_{n/b} := b \hat{\mathbf{n}}(\mathbf{r}) \boldsymbol{\nabla}_r$, respectively). Now the vector potential part of the integrand is split,

$$\begin{aligned} &\int_\Gamma \big[\psi^* \, (\partial_{n/b} \mathrm{G}_\nu - \mathrm{i} \, \tilde{A}_n \, \mathrm{G}_\nu) - \mathrm{G}_\nu \, (\partial_{n/b} \psi^* + \mathrm{i} \, \tilde{A}_n \, \psi^*)\big] \frac{\mathrm{d}\Gamma}{b} \\ &\qquad = \begin{cases} \psi^*(\mathbf{r}_0) & \text{if } \mathbf{r}_0 \in \mathring{\mathcal{D}} \\ 0 & \text{if } \mathbf{r}_0 \in \mathbb{R}^2 \setminus \mathcal{D}, \end{cases} \end{aligned} \tag{4.5}$$

which will permit a gauge invariant formulation of the boundary integral equation. We choose $\mathbf{r}_0 \in \Gamma$ and define $\mathbf{r}_0^\pm := \mathbf{r}_0 \pm \varepsilon \hat{\mathbf{n}}_0$, for small $\varepsilon > 0$. By adding the two equations in (4.5), one obtains

$$\int_\Gamma \big[\psi^* \, (\overset{\varepsilon}{\partial}_{n/b} \mathrm{G}_\nu - \mathrm{i} \, \tilde{A}_n \, \overset{\varepsilon}{\mathrm{G}}_\nu) - \overset{\varepsilon}{\mathrm{G}}_\nu \, (\partial_{n/b} \psi^* + \mathrm{i} \, \tilde{A}_n \, \psi^*))\big] \frac{\mathrm{d}\Gamma}{b} = \tfrac{1}{2} \psi^*(\mathbf{r}_0^-) \, . \tag{4.6}$$

Here, we have introduced the abbreviations $\overset{\varepsilon}{\mathrm{G}}_\nu = \frac{1}{2} \mathrm{G}_\nu(\mathbf{r}; \mathbf{r}_0^+) + \frac{1}{2} \mathrm{G}_\nu(\mathbf{r}; \mathbf{r}_0^-)$, $\overset{\varepsilon}{\partial}_{n/b} \mathrm{G}_\nu = \frac{1}{2} \partial_{n/b} \mathrm{G}_\nu(\mathbf{r}; \mathbf{r}_0^+) + \frac{1}{2} \partial_{n/b} \mathrm{G}_\nu(\mathbf{r}; \mathbf{r}_0^-)$. Equation (4.6) is true for all (sufficiently small) $\varepsilon > 0$, from which it can be concluded that the limit $\varepsilon \to 0$ exists. Moreover, by observing the asymptotic properties of the Green function (cf Sect. 2.5.3), it can be shown, that the integration and the limit $\overset{\varepsilon}{\mathrm{G}}_\nu \to \mathrm{G}_\nu$, $\overset{\varepsilon}{\partial}_{n/b} \mathrm{G}_\nu \to \partial_{n/b} \mathrm{G}_\nu$ may be interchanged. By virtue of the boundary condition (3.6) we obtain, after renaming the limiting function $u = \partial_{n/b} \psi^* + \mathrm{i} \tilde{A}_n \psi^*$, $u_0 := u(\mathbf{r}_0)$,

$$\int_\Gamma \big[\, \mathrm{G}_\nu - \frac{\lambda}{b} (\partial_{n/b} \mathrm{G}_\nu - \mathrm{i} \, \tilde{A}_n \, \mathrm{G}_\nu)\big] \, u \, \frac{\mathrm{d}\Gamma}{b} = \frac{\lambda}{b} \, (-\tfrac{1}{2} u_0) \, . \tag{4.7}$$

This is an integral equation defined on the boundary Γ.

In order to derive the corresponding equation for the exterior problem, consider a large disk $\mathcal{K}_p \supset \mathcal{D}$ of radius p, and integrate (4.3) over $\mathcal{K}_p \cap \mathring{\mathcal{D}}$. Once $\mathbf{r}_0$ lies in the vicinity of Γ, the contribution of $\partial \mathcal{K}_p$ to the boundary integral vanishes as $p \to \infty$, due to the exponential decay of the regular Green function G_ν (since $\psi \in \mathcal{L}_2(\mathbb{R}^2 \setminus \mathcal{D})$). Similar to eq (4.6), one obtains an equation

$$-\int_\Gamma \big[\psi^* (\overset{\varepsilon}{\partial}_{n/b} \mathrm{G}_\nu - \mathrm{i} \, \tilde{A}_n \, \overset{\varepsilon}{\mathrm{G}}_\nu) - \overset{\varepsilon}{\mathrm{G}}_\nu (\partial_{n/b} \psi^* + \mathrm{i} \, \tilde{A}_n \, \psi^*))\big] \frac{\mathrm{d}\Gamma}{b} = \tfrac{1}{2} \psi^*(\mathbf{r}_0^+) \, , \tag{4.8}$$

which permits the limit $\varepsilon \to 0$ to be taken before performing the integration. The resulting boundary integral equation differs from (4.7) only by a sign. In the following, we shall treat both cases simultaneously, with the convention that the upper sign stands for the interior problem, and the lower sign for the exterior one,

$$\int_\Gamma \left[\mathrm{G}_\nu \mp \frac{\lambda}{b}(\partial_{n/b}\mathrm{G}_\nu - \mathrm{i}\,\tilde{A}_n\,\mathrm{G}_\nu)\right] u\,\frac{\mathrm{d}\Gamma}{b} = \frac{\lambda}{b}\,(-\tfrac{1}{2}u_0)\;. \tag{4.9}$$

In analogy to the Helmholtz problem [107], we will refer to these equations as the *single layer equations* for the interior and the exterior domain.

The double layer equations

A second kind of boundary integral equations can be derived by applying the differential operator $(\partial_{n_0/b} + \mathrm{i}\tilde{A}_{n_0}) := \hat{\mathbf{n}}(\mathbf{r}_0)(\boldsymbol{\nabla}_{r_0/b} + \mathrm{i}\tilde{\mathbf{A}}(\mathbf{r}_0)$ on equations (4.6) and (4.8),

$$\begin{aligned}\int_\Gamma \psi^*\,(\partial_{n_0/b} + \mathrm{i}\,\tilde{A}_{n_0})(\overset{\varepsilon}{\partial}_{n/b}\mathrm{G}_\nu - \mathrm{i}\,\tilde{A}_n\,\overset{\varepsilon}{\mathrm{G}}_\nu)\frac{\mathrm{d}\Gamma}{b}&\\ - \int_\Gamma (\overset{\varepsilon}{\partial}_{n_0/b}\mathrm{G}_\nu + \mathrm{i}\,\tilde{A}_{n_0}\,\overset{\varepsilon}{\mathrm{G}}_\nu)(\partial_{n/b}\psi^* + \mathrm{i}\tilde{A}_n\psi^*)\frac{\mathrm{d}\Gamma}{b}&\\ = \pm\tfrac{1}{2}(\partial_{n_0/b} + \mathrm{i}\,\tilde{A}_{n_0})\psi^*(\mathbf{r}_\mathbf{0}^\mp)\;.&\end{aligned} \tag{4.10}$$

This equation is true for all $\varepsilon > 0$, which means that the limit $\varepsilon \to 0$ exists. As for the first integral, we may again permute the limit and the integration which yields a proper integral. Consequently, the limit of the second integral is finite, too. However, in the second integral we are not allowed to exchange the integration with taking the limit, because the limiting integrand (4.28) has a $1/(\mathbf{r} - \mathbf{r_0})^2$-singularity, which is not integrable, cf Sect. 4.3.1.

Integral operators of this kind are named *hypersingular* [116]. Similar to a Cauchy principal value integral, they are defined by taking a special limit. However, in the present case the singularity is stronger by one order. Below, in Section 4.3.2, we define which limit is to be taken. It is denoted by $⨎$ and should be read "finite part of the integral". With this concept and equation (3.6), we obtain the *double layer* equations,

$$\begin{aligned}\int_\Gamma (\partial_{n_0/b}\mathrm{G}_\nu + \mathrm{i}\,\tilde{A}_{n_0}\,\mathrm{G}_\nu)\,u\,\frac{\mathrm{d}\Gamma}{b}&\\ \mp\frac{\lambda}{b}⨎_\Gamma (\partial_{n_0/b} + \mathrm{i}\,\tilde{A}_{n_0})(\partial_{n/b}\mathrm{G}_\nu - \mathrm{i}\,\tilde{A}_n\,\mathrm{G}_\nu)\,u\,\frac{\mathrm{d}\Gamma}{b} &= \mp\tfrac{1}{2}u_0\;,\end{aligned} \tag{4.11}$$

which are again integral equations defined on the boundary Γ.

The spectral determinants

It is useful to introduce a set of integral operators (whose labels D and N indicate correspondence to pure Dirichlet or Neumann conditions):

$$\mathsf{Q}_{\mathrm{sl}}^{\mathrm{D}}[u] = \int_\Gamma \mathrm{d}\Gamma\, \mathrm{G}_\nu\, u \tag{4.12}$$

$$\mathsf{Q}_{\mathrm{sl}}^{\mathrm{N}}[u] = \int_\Gamma \frac{\mathrm{d}\Gamma}{b}(\partial_{n/b}\mathrm{G}_\nu - \mathrm{i}\,\tilde{A}_n\,\mathrm{G}_\nu)\, u \tag{4.13}$$

$$\mathsf{Q}_{\mathrm{dl}}^{\mathrm{D}}[u] = \int_\Gamma \frac{\mathrm{d}\Gamma}{b}(\partial_{n_0/b}\mathrm{G}_\nu + \mathrm{i}\,\tilde{A}_{n_0}\,\mathrm{G}_\nu)\, u \tag{4.14}$$

$$\mathsf{Q}_{\mathrm{dl}}^{\mathrm{N}}[u] = \mathop{=\!\!\!\!\!\!\!\int}_\Gamma \frac{\mathrm{d}\Gamma}{b^2}(\partial_{n_0/b} + \mathrm{i}\tilde{A}_{n_0})(\partial_{n/b}\mathrm{G}_\nu - \mathrm{i}\,\tilde{A}_n\,\mathrm{G}_\nu)\, u \tag{4.15}$$

They act in the space of square-integrable periodic functions, $u \in \mathcal{L}_2(\Gamma)$, with the period given by the circumference $\mathscr{L}$.

Nontrivial solutions of the single layer equations (4.9) and double layer equations (4.11) exist, if the corresponding Fredholm determinants vanish,

$$\det\left[\mathsf{Q}_{\mathrm{sl}}^{\mathrm{D}} \mp \lambda \mathsf{Q}_{\mathrm{sl}}^{\mathrm{N}} + \frac{\lambda}{2}\mathsf{id}\right] = 0 \qquad \text{(single layer)} \tag{4.16}$$

$$\det\left[\mathsf{Q}_{\mathrm{dl}}^{\mathrm{D}} \mp \lambda \mathsf{Q}_{\mathrm{dl}}^{\mathrm{N}} \pm \frac{1}{2}\mathsf{id}\right] = 0 \qquad \text{(double layer).} \tag{4.17}$$

These are secular equations although the explicit dependence on the spectral variable is not shown in our abbreviated notation. However, as already mentioned, each of the determinants (4.16) and (4.17) may have roots, which do not correspond to solutions of the original eigenvalue problem given by (4.1) and (3.6). For finite ε, the equations (4.6), (4.8), and (4.10) are still equivalent to the latter. They acquire additional spurious solutions only as they are transformed to boundary integral equations by the limit $\varepsilon \to 0$.

4.2.2 Spurious solutions and the combined operator

The physical origin of the redundant zeros is apparent in our gauge invariant formulation. They are proper solutions for the domain *complementary* to the one considered. This is obvious for the single layer equation with Dirichlet boundary conditions ($\lambda = 0$), where the spectral determinant does not depend on the orientation of the normals. The same is true for the double layer equation with Neumann boundary conditions ($\lambda^{-1} = 0$).

In general, the character of the spurious solutions may be summarized as follows: Independently of the boundary conditions, the *single layer* equation includes the *Dirichlet* solutions of that domain which is complementary to the one considered. Likewise, the *double layer* equation is polluted by the *Neumann* solutions of the complementary domain, irrespective of the boundary conditions employed.

This statement is easily proved by observing that the single-layer-Neumann operator and the double-layer-Dirichlet operator are *adjoint* to each other, $\mathsf{Q}_{\mathrm{sl}}^{\mathrm{N}} = (\mathsf{Q}_{\mathrm{dl}}^{\mathrm{D}})^\dagger$, while the operators $\mathsf{Q}_{\mathrm{sl}}^{\mathrm{D}}$ and $\mathsf{Q}_{\mathrm{dl}}^{\mathrm{N}}$ are self-adjoint. This is shown explicitly in the next section. Now assume that u is a complementary Dirichlet solution. In Dirac notation,

$$\begin{aligned} & \mathsf{Q}_{\mathrm{sl}}^{\mathrm{D}}|u\rangle = 0 \quad \wedge \quad \mathsf{Q}_{\mathrm{dl}}^{\mathrm{D}}|u\rangle \mp \tfrac{1}{2}|u\rangle = 0 \\ \Rightarrow \quad & \langle u|\mathsf{Q}_{\mathrm{sl}}^{\mathrm{D}} = 0 \quad \wedge \quad \langle u|\mathsf{Q}_{\mathrm{sl}}^{\mathrm{N}} \mp \tfrac{1}{2}\langle u| = 0 \, . \end{aligned} \tag{4.18}$$

Applying the dual of u to the single layer operator yields

$$\langle u|\mathsf{Q}_{\mathrm{sl}}^{\mathrm{D}} \mp \lambda \Big\{ \langle u|\mathsf{Q}_{\mathrm{sl}}^{\mathrm{N}} \mp \tfrac{1}{2}\langle u| \Big\} = 0 \, , \tag{4.19}$$

which implies that the Fredholm determinant of the single layer operator vanishes. Similarly, if u is a complementary Neumann solution,

$$\begin{aligned} & \pm\, \mathsf{Q}_{\mathrm{sl}}^{\mathrm{N}}|u\rangle + \tfrac{1}{2}|u\rangle = 0 \quad \wedge \quad \mathsf{Q}_{\mathrm{dl}}^{\mathrm{N}}|u\rangle = 0 \\ \Rightarrow \quad & \pm\, \langle u|\mathsf{Q}_{\mathrm{dl}}^{\mathrm{D}} + \tfrac{1}{2}\langle u| = 0 \quad \wedge \quad \langle u|\mathsf{Q}_{\mathrm{dl}}^{\mathrm{N}} = 0 \end{aligned} \tag{4.20}$$

then its dual satisfies the double layer equation, again for any λ,

$$\pm\Big\{ \pm\, \langle u|\mathsf{Q}_{\mathrm{dl}}^{\mathrm{D}} + \tfrac{1}{2}\langle u| \Big\} \mp \lambda \langle u|\mathsf{Q}_{\mathrm{dl}}^{\mathrm{N}} = 0 \, . \tag{4.21}$$

Since the spurious solutions are never of the same type, it is possible to dispose of them by requiring that both, the single and the double layer equations, should be satisfied by the *same* solution u. Therefore, one obtains a necessary and sufficient condition for the definition of the spectrum by considering a *combined* operator

$$\mathsf{Q}_{\mathrm{c}}^{\pm} := \left(\mathsf{Q}_{\mathrm{dl}}^{\mathrm{D}} \mp \lambda \mathsf{Q}_{\mathrm{dl}}^{\mathrm{N}} \pm \frac{1}{2}\mathsf{id} \right) + \mathrm{i}\alpha_{\mathrm{c}} \left(\mathsf{Q}_{\mathrm{sl}}^{\mathrm{D}} \mp \lambda \mathsf{Q}_{\mathrm{sl}}^{\mathrm{N}} + \frac{\lambda}{2}\mathsf{id} \right) \, . \tag{4.22}$$

It has a zero eigenvalue only if both, single and double layer operators do. In practice, the spectrum is obtained by finding the roots of the *spectral function*

$$\xi(\nu) = \det(1 - \mathsf{Q}_{\mathrm{c}}^{\pm}) \, . \tag{4.23}$$

The α_{c} in (4.22) is an arbitrary constant, in principle. Numerically, it is convenient to allow for a ν-dependence, though, to ensure that single and double layer parts are similar in size.

It is worthwhile noting that (for the interior problem) spurious solutions will not appear if one uses the irregular Green function. The reason is that the gauge-independent part of this function is *complex*, which destroys the mutual adjointness of the operators. This is why the irregular Green function had to be chosen for the null-field method [40]. For the boundary integral method, the option to use this exponentially divergent solution of (4.2) is excluded, since the corresponding operator would get arbitrarily ill-conditioned once the size of the boundary exceeds the cyclotron diameter. The exterior problem cannot even formally be solved using $\mathrm{G}_{\nu}^{(\mathrm{irr})}$ (because it has an essential singularity at the origin).

A last remark is concerned with the important case of Dirichlet boundary conditions. Here, one could as well derive a pair of boundary integral equations that are *not* gauge-invariant. (Just set $\psi = 0$ in (4.4) and consider $u = \partial_{n/b}\psi^*$.) Of course, these equations would yield the proper gauge-invariant eigen-energies of the problem. However, the energies of the additional spurious solutions would depend on the chosen gauge, and a characterization of the latter in terms of solutions of a complementary problem would not be possible.

We removed the spurious solutions from the spectral function by considering a *combined* integral operator. This is of great practical importance for numerical calculations because one is not required to calculate the eigenfunctions. Individual spurious solutions of the single and double layer operators may of course be identified, as well, by simply evaluating the corresponding wave functions.

4.2.3 Wave functions

The eigenfunctions at points off the boundary, $\psi(\mathbf{r}_0 \notin \Gamma)$, are determined by the null vectors u corresponding to the roots of the spectral determinant. From equation (4.5) we obtain immediately an integral representation of the (un-normalized) wave function,

$$\psi(\mathbf{r}_0) = \pm\Big[\int_\Gamma \frac{\mathrm{d}\Gamma}{b}\big[\pm\frac{\lambda}{b}(\partial_{n/b}\mathrm{G}_\nu - \mathrm{i}\tilde{A}_n\mathrm{G}_\nu) - \mathrm{G}_\nu\big]u\Big]^* , \tag{4.24}$$

for $\mathbf{r}_0 \notin \Gamma$. According to theory, the integral vanishes identically either in the interior or in the exterior. This is indeed confirmed by our numerical calculations, which are reported on in the next chapter.

In order to calculate the current density (2.35), the gauge invariant gradient of the wave function is needed. An integral formula is obtained from equation (4.5), after applying the differential operator $\boldsymbol{\nabla}_{r_0/b} + \mathrm{i}\tilde{\mathbf{A}}_0$,

$$\begin{aligned}\boldsymbol{\nabla}_{r_0/b}\psi(\mathbf{r}_0) - \mathrm{i}\tilde{\mathbf{A}}(\mathbf{r}_0)\psi(\mathbf{r}_0) = \pm\Big[\int_\Gamma \frac{\mathrm{d}\Gamma}{b}\big[\pm\frac{\lambda}{b}(\boldsymbol{\nabla}_{r_0/b} + \mathrm{i}\tilde{\mathbf{A}}_0)(\partial_{n/b}\mathrm{G}_\nu - \mathrm{i}\tilde{A}_n\mathrm{G}_\nu) \\ - (\boldsymbol{\nabla}_{r_0/b}\mathrm{G}_\nu + \mathrm{i}\tilde{\mathbf{A}}_0\mathrm{G}_\nu)\big]u\Big]^* .\end{aligned} \tag{4.25}$$

The densities of other observables can be obtained by similar boundary integrals.

4.3 The boundary operators

In the following, we give explicit expressions for the boundary integrals. This allows to define the "finite part integral" appearing in the double layer equation (4.11).

4.3.1 Explicit expression for the integral kernels

The integral operators (4.12) – (4.15),

$$\big(\mathsf{Q}[u]\big)(\mathbf{r}_0) = \int_\Gamma \mathrm{d}\Gamma \mathrm{q}(\mathbf{r};\mathbf{r}_0)u(\mathbf{r}) , \tag{4.26}$$

are defined by their integral kernels $\mathrm{q}(\mathbf{r};\mathbf{r}_0)$. The form of the Green function (2.64) leads to the expressions

$$\mathrm{q}_{\mathrm{sl}}^{\mathrm{D}}(\mathbf{r};\mathbf{r}_0) = \mathrm{E}(\mathbf{r};\mathbf{r}_0)\,\mathrm{G}_\nu^0(z) \tag{4.27}$$

$$\mathrm{q}_{\mathrm{sl}}^{\mathrm{N}}(\mathbf{r};\mathbf{r}_0) = \mathrm{E}(\mathbf{r};\mathbf{r}_0)\left\{ -\mathrm{i}\frac{(\mathbf{r}-\mathbf{r}_0)\times\hat{\mathbf{n}}}{b^2}\,\mathrm{G}_\nu^0(z) + 2\frac{(\mathbf{r}-\mathbf{r}_0)\,\hat{\mathbf{n}}}{(\mathbf{r}-\mathbf{r}_0)^2}\,z\frac{\mathrm{d}}{\mathrm{d}z}\mathrm{G}_\nu^0(z)\right\} \tag{4.28}$$

$$\mathrm{q}_{\mathrm{dl}}^{\mathrm{D}}(\mathbf{r};\mathbf{r}_0) = \mathrm{E}(\mathbf{r};\mathbf{r}_0)\left\{ -\mathrm{i}\frac{(\mathbf{r}-\mathbf{r}_0)\times\mathbf{n_0}}{b^2}\,\mathrm{G}_\nu^0(z) - 2\frac{(\mathbf{r}-\mathbf{r}_0)\,\hat{\mathbf{n}}_0}{(\mathbf{r}-\mathbf{r}_0)^2}\,z\frac{\mathrm{d}}{\mathrm{d}z}\mathrm{G}_\nu^0(z)\right\} \tag{4.29}$$

$$\begin{aligned}\mathrm{q}_{\mathrm{dl}}^{\mathrm{N}}(\mathbf{r};\mathbf{r}_0) = \mathrm{E}(\mathbf{r};\mathbf{r}_0)\Bigg\{ &\left(-\frac{((\mathbf{r}-\mathbf{r}_0)\times\hat{\mathbf{n}}_0)((\mathbf{r}-\mathbf{r}_0)\times\hat{\mathbf{n}})}{b^4} - \mathrm{i}\frac{\hat{\mathbf{n}}\times\hat{\mathbf{n}}_0}{b^2}\right)\mathrm{G}_\nu^0(z) \\ &+\left(-2\mathrm{i}\frac{\hat{\mathbf{n}}\times\hat{\mathbf{n}}_0}{b^2} - 2\frac{\hat{\mathbf{n}}\,\hat{\mathbf{n}}_0}{(\mathbf{r}-\mathbf{r}_0)^2}\right) z\frac{\mathrm{d}}{\mathrm{d}z}\mathrm{G}_\nu^0(z) \\ &- 4\frac{((\mathbf{r}-\mathbf{r}_0)\hat{\mathbf{n}})((\mathbf{r}-\mathbf{r}_0)\hat{\mathbf{n}}_0)}{(\mathbf{r}-\mathbf{r}_0)^4}\,z^2\frac{\mathrm{d}^2}{\mathrm{d}z^2}\mathrm{G}_\nu^0(z)\Bigg\}\,,\end{aligned} \tag{4.30}$$

with $\hat{\mathbf{n}} = \hat{\mathbf{n}}(\mathbf{r})$, $\hat{\mathbf{n}}_0 = \hat{\mathbf{n}}(\mathbf{r}_0)$, $z := (\mathbf{r}-\mathbf{r}_0)^2/b^2$, and the abbreviation

$$\mathrm{E}(\mathbf{r};\mathbf{r}_0) := \exp\left[-\mathrm{i}\left(\frac{\mathbf{r}\times\mathbf{r}_0}{b^2} - \widetilde{\chi}(\mathbf{r}) + \widetilde{\chi}(\mathbf{r_0})\right)\right] \tag{4.31}$$

for the gauge dependent part. Note that the gauge freedom χ has cancelled in the prefactors and appears in the phase only. It can be absorbed by the substitution $u(\mathbf{r}) \to \exp(+\mathrm{i}\chi(\mathbf{r}))u(\mathbf{r})$, proving the manifest gauge invariance of the boundary integral equations (4.9), (4.11). Note that expressions (4.28) and (4.29) are related by a permutation of $\mathbf{r}$ and $\mathbf{r}_0$ with subsequent complex conjugation (since G_ν^0 is real), hence the operators are the adjoints of each other. The self-adjoint nature of (4.27) and (4.30) follows likewise.

The derivatives appearing in (4.28) – (4.30) may be stated in terms of the gauge independent part of the Green function, G_ν^0, itself, at different energies ν. This is shown in Section 2.5.3, where we discuss their asymptotic properties as well. G_ν^0 displays a logarithmic singularity as $\mathbf{r} \to \mathbf{r}_0$, while the differential expressions are bounded. In that limit, most of the quotients vanish for a smooth boundary, others tend to the curvature κ_0 at the boundary point $\mathbf{r}_0$ (defined to be positive for convex domains),

$$\lim_{\mathbf{r}\to\mathbf{r}_0}\frac{(\mathbf{r}-\mathbf{r}_0)\hat{\mathbf{n}}}{(\mathbf{r}-\mathbf{r}_0)^2} = \frac{\kappa_0}{2}\,, \qquad \lim_{\mathbf{r}\to\mathbf{r}_0}\frac{(\mathbf{r}-\mathbf{r}_0)\mathbf{n_0}}{(\mathbf{r}-\mathbf{r}_0)^2} = -\frac{\kappa_0}{2}\,. \tag{4.32}$$

As a consequence, all the terms in (4.27) – (4.30) are integrable — but for the one containing the $(\hat{\mathbf{n}}\,\hat{\mathbf{n}}_0)/(\mathbf{r}-\mathbf{r}_0)^2$-singularity. The latter gives rise to the need for a finite part integral.

4.3.2 The hypersingular integral operator

For finite λ, the double-layer equation contains a hypersingular integral defined as

$$\begin{aligned}\mathsf{Q}^{\mathrm{N}}_{\mathrm{dl}}[u] = &\fint_{\Gamma} \frac{\mathrm{d}\Gamma}{b^2}(\partial_{n_0/b} + \mathrm{i}\tilde{A}_{n_0})(\partial_{n/b}\mathrm{G}_\nu - \mathrm{i}\tilde{A}_n\mathrm{G}_\nu)u \\ := &\lim_{\varepsilon\to 0}\int_{\Gamma} \frac{\mathrm{d}\Gamma}{b^2}(\partial_{n_0/b} + \mathrm{i}\tilde{A}_{n_0})(\overset{\varepsilon}{\partial}_{n/b}\mathrm{G}_\nu - \mathrm{i}\tilde{A}_n\overset{\varepsilon}{\mathrm{G}}_\nu)u\ .\end{aligned} \tag{4.33}$$

We want to replace the integrand by its limiting form. To this end the boundary is split into the part $\gamma_{c\varepsilon}$, which lies within a $(c\varepsilon)$-vicinity around $\mathbf{r}_0$ (with arbitrary constant c), and the remaining part $\Gamma_{c\varepsilon}$,

$$\begin{aligned}= \lim_{\varepsilon\to 0}\Bigg[&\int_{\Gamma_{c\varepsilon}} \frac{\mathrm{d}\Gamma}{b^2}(\partial_{n_0/b} + \mathrm{i}\tilde{A}_{n_0})(\overset{\varepsilon}{\partial}_{n/b}\mathrm{G}_\nu - \mathrm{i}\tilde{A}_n\overset{\varepsilon}{\mathrm{G}}_\nu)u \\ &+ \int_{\gamma_{c\varepsilon}} \frac{\mathrm{d}\Gamma}{b^2}(\partial_{n_0/b} + \mathrm{i}\tilde{A}_{n_0})(\overset{\varepsilon}{\partial}_{n/b}\mathrm{G}_\nu - \mathrm{i}\tilde{A}_n\overset{\varepsilon}{\mathrm{G}}_\nu)(u-u_0) \\ &+ u_0\int_{\gamma_{c\varepsilon}} \frac{\mathrm{d}\Gamma}{b^2}(\partial_{n_0/b} + \mathrm{i}\tilde{A}_{n_0})(\overset{\varepsilon}{\partial}_{n/b}\mathrm{G}_\nu - \mathrm{i}\tilde{A}_n\overset{\varepsilon}{\mathrm{G}}_\nu)\Bigg]\ ,\end{aligned} \tag{4.34}$$

with $u_0 := u(\mathbf{r}_0)$. For sufficiently small ε the boundary piece $\gamma_{c\varepsilon}$ may be replaced by its tangent and the Green function by its asymptotic expression, cf Sect. 2.5.3. This way the third integral in (4.34) may be evaluated to its contributing order,

$$\begin{aligned}&\int_{\gamma_{c\varepsilon}} \frac{\mathrm{d}\Gamma}{b^2}(\partial_{n_0/b} + \mathrm{i}\tilde{A}_{n_0})(\overset{\varepsilon}{\partial}_{n/b}\mathrm{G}_\nu - \mathrm{i}\tilde{A}_n\overset{\varepsilon}{\mathrm{G}}_\nu) \\ =&\frac{1}{4\pi}\int_{-c\varepsilon}^{c\varepsilon}\cos\Big(\frac{\mathbf{r}_0\hat{\mathbf{n}}_0}{b^2}s\Big)\cos\Big[\varepsilon\Big(\frac{\hat{\mathbf{n}}_0\times\mathbf{r}_0}{b^2}-s\Big)\Big]\Big(\frac{-2}{s^2+\varepsilon^2}+4\frac{\varepsilon^2}{(s^2+\varepsilon^2)^2}\Big)\,\mathrm{d}s \\ &+\mathrm{O}(\varepsilon^2\log\varepsilon) \\ =&\frac{1}{2\pi}\int_{-c\varepsilon}^{c\varepsilon}\mathrm{d}s\frac{\varepsilon^2-s^2}{(s^2+\varepsilon^2)^2}\ +\mathrm{O}(\varepsilon^2\log\varepsilon) = \frac{1}{\pi}\frac{1}{c\varepsilon}\frac{c^2}{c^2+1}+\mathrm{O}(\varepsilon^2\log\varepsilon) \\ \approx&\frac{1}{\pi}\frac{1}{c\varepsilon}+\mathrm{O}(\varepsilon^2\log\varepsilon)\ .\end{aligned} \tag{4.35}$$

Here, the explicit form of the integrand was obtained from (4.30) by the replacement $\mathbf{r}_0 \to \mathbf{r}_0^{\pm}$. The last approximation in (4.35) holds because c may be chosen arbitrarily large. In a similar fashion, it can be shown that the second integral in (4.34) is of order $\mathrm{O}(\varepsilon)$. In the first integral we may replace (again for large c) the integrand by its limit, because ε is small compared to $\min(|\mathbf{r}-\mathbf{r}_0|) = c\,\varepsilon$. Therefore, the limit in (4.33) may be expressed as

$$\begin{aligned}&\fint_{\Gamma} \frac{\mathrm{d}\Gamma}{b^2}(\partial_{n_0/b} + \mathrm{i}\tilde{A}_{n_0})(\partial_{n/b} - \mathrm{i}\tilde{A}_n)\mathrm{G}_\nu u \\ &\qquad = \lim_{\varepsilon\to 0}\Bigg[\int_{\Gamma_\varepsilon} \frac{\mathrm{d}\Gamma}{b^2}(\partial_{n_0/b} + \mathrm{i}\tilde{A}_{n_0})(\partial_{n/b}\mathrm{G}_\nu - \mathrm{i}\tilde{A}_n\mathrm{G}_\nu)u\ + u_0\frac{1}{\pi\varepsilon}\Bigg]\ ,\end{aligned} \tag{4.36}$$

where we replaced $c\varepsilon$ by ε. This equation defines the finite part integral. It completes the derivation of the boundary integral equations, and we may now turn to the question of how to solve them.

4.4 Solving the integral equations

As shown above, the integral equations (4.9) and (4.11) may be used to compute spectra of magnetic billiards. However, the corresponding integral kernels are not yet suitable for numerical evaluation. In this section, we show how their asymptotically singular behaviour may be separated and be treated analytically.

In the following, the *combined* integral equation as defined by (4.22) will be considered. The corresponding expressions for the pure double layer or single layer case are obtained easily by setting $\alpha_{\mathrm{c}} = 0$ or $\alpha_{\mathrm{c}}^{-1} = 0$, respectively. We also take the opportunity to *regularize* the integral equations. At the energies of the Landau levels, $\nu_N = N + \frac{1}{2}, N \in \mathbb{N}_0$, they are defined only by the limit $\nu \to \nu_N$, so far. This is because the Green function is singular at the Landau energies. These simple poles are removed by multiplying the equations with $\cos(\pi\nu)$, and taking the limiting values at ν_N, as shown in Sect. 2.5.2. This way, the Green function is replaced by its regularized version $\widehat{\mathrm{G}}{}^0_\nu$, cf eq (2.66).

For convenience, we assume λ to be constant on Γ, and parametrize the boundary according to equation (3.1). This allows to write the (regularized) integral kernel

$$\begin{aligned}\widehat{\mathrm{q}}(s,s_0) := \cos(\pi\nu)\Big[&\mathrm{q}^{\mathrm{D}}_{\mathrm{dl}}(\mathbf{r}_s;\mathbf{r}_{s_0}) + \mathrm{i}\alpha_{\mathrm{c}}\,\mathrm{q}^{\mathrm{D}}_{\mathrm{sl}}(\mathbf{r}_s;\mathbf{r}_{s_0})\\ &\mp \lambda\big(\mathrm{q}^{\mathrm{N}}_{\mathrm{dl}}(\mathbf{r}_s;\mathbf{r}_{s_0}) + \mathrm{i}\alpha_{\mathrm{c}}\,\mathrm{q}^{\mathrm{N}}_{\mathrm{sl}}(\mathbf{r}_s;\mathbf{r}_{s_0})\big)\Big]\end{aligned} \tag{4.37}$$

with $\mathbf{r}_s := \mathbf{r}(s), s \in [0;\mathscr{L}]$. After an expansion of the boundary around $\mathbf{r}(s_0)$,

$$\mathbf{r}(s) = \mathbf{r}_0 + (s-s_0)\,\hat{\mathbf{t}}_0 - \frac{\kappa_0}{2}(s-s_0)^2\,\hat{\mathbf{n}}_0 + \mathrm{O}\Big((s-s_0)^3\Big)\,, \tag{4.38}$$

one obtains, observing (4.27) — (4.30), the asymptotic behaviour for small $s' = s - s_0$,

$$\begin{aligned}\widehat{\mathrm{q}}(s_0+s',s_0) := \exp\left[-\mathrm{i}\frac{\mathbf{r}_s\times\mathbf{r}_0}{b^2}\right]\Bigg\{ &\mp\lambda\,\frac{\cos(\pi\nu)}{2\pi}\,\frac{-1}{s'^2}\\ &+\left[\mathrm{i}\frac{s'}{b^2} + \mathrm{i}\alpha_{\mathrm{c}} \mp \lambda\Big(\frac{2\nu}{b^2} - (\alpha_{\mathrm{c}} - \mathrm{i}\kappa_0)\frac{s'}{b^2}\Big)\right]\mathrm{L}_\nu\Big(\frac{s'^2}{b^2}\Big)\\ &+\left[\kappa_0 \mp \lambda\Big(-2\frac{\nu}{b^2} + \mathrm{i}\alpha_{\mathrm{c}}\kappa_0\Big)\right]\frac{\cos(\pi\nu)}{4\pi} + \mathrm{O}(s'^2\log s'^2)\Bigg\}\,.\end{aligned} \tag{4.39}$$

The necessary asymptotic expansions for the gauge-independent part of the Green function and its derivatives may be found in Section 2.5.3. The function L_ν describes the asymptotically logarithmic form of the Green function and is defined in (2.71). Note that, due to the quotient $1/s'^2$, the expansion of $z\partial_z\mathrm{G}^0$ contributes up to and including order $\mathrm{O}(s'^2\log s'^2)$. Similarly, the second order term of $\hat{\mathbf{n}}\hat{\mathbf{n}}_0 = 1 - \frac{1}{2}\kappa_0^2 s'^2 + \mathrm{O}(s'^3)$ enters with the effect of cancelling another term.

As apparent from (4.39), the singularities of the integral kernel are well described by the functions

$$\mathrm{m}(s,s_0) := \mp\lambda\,\exp\left[-\mathrm{i}\frac{\hat{\mathbf{t}}_0\times\mathbf{r}_0}{b^2}(s-s_0)\right]\,\frac{\cos(\pi\nu)}{2\pi}\,\frac{-1}{(s-s_0)^2} \tag{4.40}$$

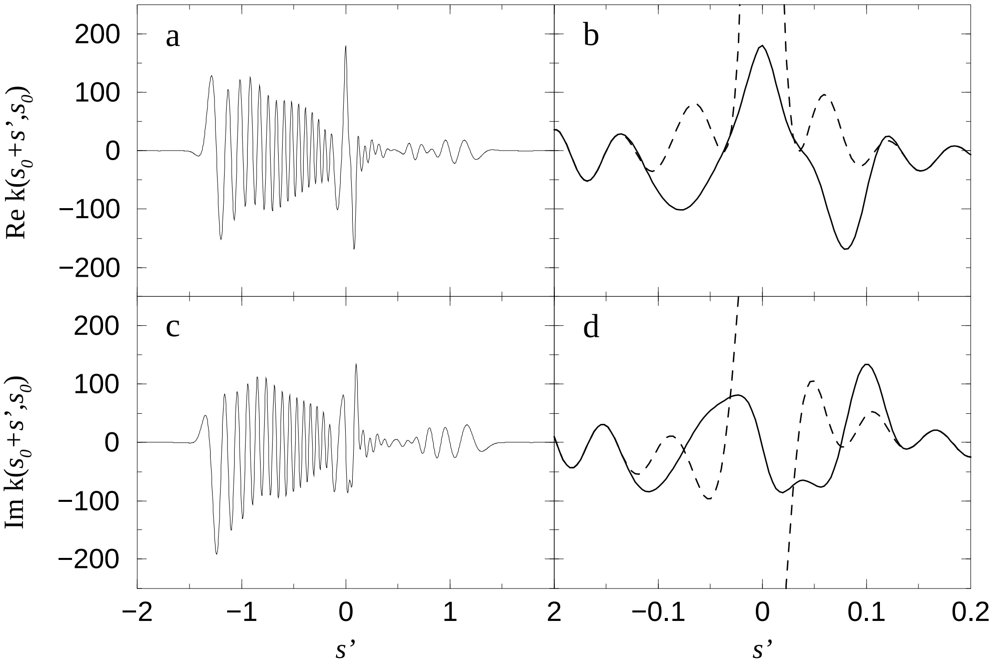

Figure 4.1: (a) Real and (c) imaginary part of the smooth combined integral kernel (4.42) for fixed s_0 and the case of Neumann boundary conditions. We choose $\rho = 0.6$ and an elliptic domain (of eccentricity 0.8 and area $\mathscr{A} = \pi$, centered on $(0.5, 0.25)$) at $\nu = 19$, corresponding to the energy of the roughly $1000\mathrm{th}$ interior eigenstate. (The boundary point $s_0 = 0$ is that of largest curvature.) The magnifications (b) and (d) around $s' = 0$ include the original singular kernel (4.37) as a dashed line.

and, for the logarithmic part,

$$\begin{aligned} \mathrm{l}(s,s_0) := \exp\left[-\mathrm{i}\frac{\hat{\mathbf{t}}_0 \times \mathbf{r}_0}{b^2}(s-s_0)\right] \mathrm{L}_\nu\left(\frac{(s-s_0)^2}{b^2}\right) \\ \times \left[\mathrm{i}\alpha_\mathrm{c} + \mathrm{i}\frac{(s-s_0)}{b^2} \mp \lambda\left(\frac{2\nu}{b^2} - (\alpha_\mathrm{c} - \mathrm{i}\kappa_0)\frac{(s-s_0)}{b^2}\right)\right] . \end{aligned} \tag{4.41}$$

It is important to include the terms of order $\mathrm{O}\big(s\log(s^2)\big)$, in order to ensure that the smooth integral kernel defined as

$$\mathrm{k}(s,s_0) := \widehat{\mathrm{q}}(s,s_0) - e(s-s_0)\left[\mathrm{l}(s,s_0) + \mathrm{m}(s,s_0)\right] \tag{4.42}$$

is differentiable at $s = s_0$ (provided the curvature is continuous). Here, $e(s')$ is a window function (with $e(0) = 1$), which smoothly switches off the singular functions for $|s'| > 0$, and vanishes beyond some small, suitably chosen σ_e. Figure 4.1 shows the smooth as well as the original kernel for a typical choice of the boundary and the energy.

The solution $u(s)$ of the boundary integral equation is periodic and may therefore be expanded in a Fourier series,

$$u(s)\,\mathrm{e}^{+\mathrm{i}\widetilde{\chi}(s)} = \sum_{\ell=-\infty}^{\infty} u_\ell\,\mathrm{e}^{2\pi\mathrm{i}\ell s/\mathscr{L}}\ . \tag{4.43}$$

As mentioned above, we include the phase due to the gauge freedom $\widetilde{\chi}$, which amounts to the choice of the symmetric gauge for the actual calculation. Within the Fourier representation, the Fredholm determinant may be written in the form

$$\det\Big[\mathrm{K}_{k\ell} + \mathrm{L}_{k\ell} + \mathrm{M}_{k\ell} - \mathscr{L}\,c\,\delta_{k\ell}\Big]_{k,\ell\in\mathbb{Z}} = 0\ , \tag{4.44}$$

with

$$c := (\mp\tfrac{1}{2} - \tfrac{1}{2}\mathrm{i}\alpha_{\mathrm{c}}\lambda)\cos(\pi\nu)\ . \tag{4.45}$$

It consists of a double Fourier integral over the smooth kernel,

$$\mathrm{K}_{k\ell} := \int_0^{\mathscr{L}}\!\!\int_0^{\mathscr{L}} \mathrm{e}^{2\pi\mathrm{i}(s\ell - s_0 k)/\mathscr{L}}\,\mathrm{k}(s,s_0)\,\mathrm{d}s_0\mathrm{d}s\ , \tag{4.46}$$

and two single Fourier integrals,

$$\mathrm{L}_{k\ell} := \int_0^{\mathscr{L}} \mathrm{e}^{2\pi\mathrm{i}s_0(\ell-k)/\mathscr{L}}\,\mathrm{L}_\ell(s_0)\,\mathrm{d}s_0\ , \tag{4.47}$$

and

$$\mathrm{M}_{k\ell} := \int_0^{\mathscr{L}} \mathrm{e}^{2\pi\mathrm{i}s_0(\ell-k)/\mathscr{L}}\,\mathrm{M}_\ell(s_0)\,\mathrm{d}s_0\ . \tag{4.48}$$

The functions $\mathrm{L}_\ell(s_0)$ and $\mathrm{M}_\ell(s_0)$ are (finite part) Fourier integrals over the asymptotic singularities (4.41) and (4.40),

$$\mathrm{L}_\ell(s_0) = \int_{-\sigma_e}^{\sigma_e} \mathrm{e}^{2\pi\mathrm{i}\ell s'/\mathscr{L}}\,e(s')\,\mathrm{l}(s_0+s';s_0)\,\mathrm{d}s'\ , \tag{4.49}$$

$$\mathrm{M}_\ell(s_0) = \neq\!\!\!\!\!\!\int_{-\sigma_e}^{\sigma_e} \mathrm{e}^{2\pi\mathrm{i}\ell s'/\mathscr{L}}\,e(s')\,\mathrm{m}(s_0+s',s_0)\,\mathrm{d}s'\ . \tag{4.50}$$

They may be calculated *analytically*, for a suitable window function $e(s)$, yielding smooth functions of s_0. In Appendix A.2 the results can be found for

$$e(s) := \cos^2\!\Big(\frac{\pi}{2}\,\frac{s}{\sigma_e}\Big)\,\big(\Theta(s-\sigma_e) - \Theta(s+\sigma_e)\big)\ , \tag{4.51}$$

with Θ the Heaviside step function. With this choice of the window function the integrals (4.49) and (4.50) are given in terms of elementary functions, and are easily evaluated. Having treated the (hyper-)singular features of the boundary integrals analytically, the remaining problem can be solved efficiently by numerical means.

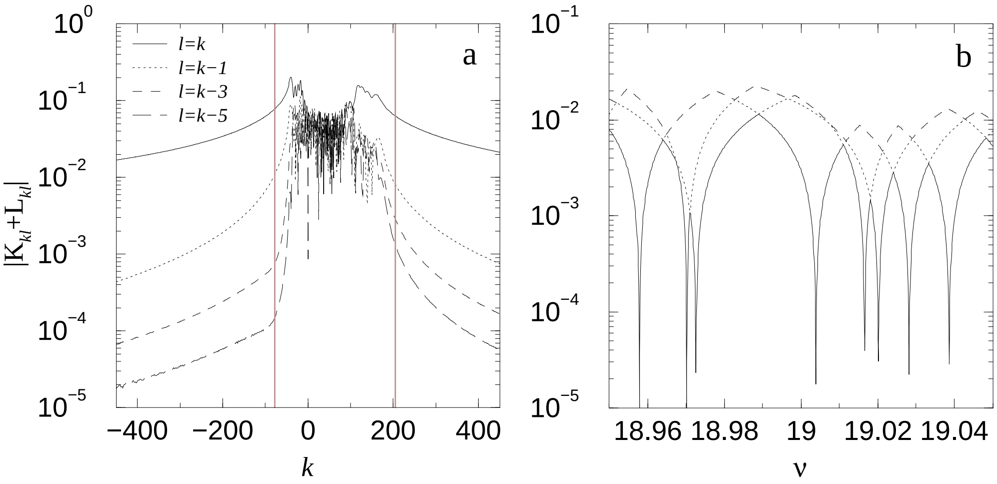

Figure 4.2: (a) Matrix $\mathrm{K}_{k\ell} + \mathrm{L}_{k\ell}$ corresponding to the same choice of parameters as in Fig. 4.1, for Dirichlet boundary conditions (where $\mathrm{M}_{k\ell} = 0$). Shown are the absolute values of the matrix elements along its diagonal and neighbouring diagonals on a logarithmic scale. Apart from the diagonal, appreciable values of the matrix $\mathrm{K}_{k\ell} + \mathrm{L}_{k\ell} - \mathscr{L}\, c\, \delta_{k\ell}$ are localized within a sub-block which allows safe truncation. The vertical lines indicate the typical size after truncation. (b) The three smallest singular values of the matrix around $\nu = 19$ (at constant $\rho = 0.6$ corresponding to roughly the 1000th eigenvalue). The minima of the smallest singular value (solid line) determine the spectrum to a high accuracy.

4.5 Numerical analysis

In the following, we briefly describe some aspects of the numerical treatment and discuss the question of numerical accuracy.

The evaluation of the remaining Fourier integrals (4.46) - (4.48) must be performed numerically. Since the integrands are well-behaved, this may be done by dividing the boundary into N equidistant pieces and approximating the integrand at each one by its value at the mid-point. The summations can be performed by a Fast-Fourier algorithm. For large enough N, this simple method is more effective than any attempt to evaluate the highly oscillatory integrals (4.46) – (4.48) by more sophisticated schemes.

Due to the Fourier representation, the resulting large $N \times N$ matrix has a partly diagonal structure, cf Fig. 4.2(a). There are off-diagonal elements of appreciable value only within a sub-block the size of which is independent of N. Outside of the sub-block, essentially only the diagonal elements are occupied (the values decay rapidly as one leaves the diagonal.) It is the *bulk* wave functions which are given by the null vectors corresponding to the latter diagonal Fourier components. These components do not contribute to the other states, since they are not coupled to them. As a consequence, the restriction of the matrix to the above-mentioned sub-block at most removes bulk states, if they exist, out of the numerically calculated spectrum, *without* affecting other states. Generically, one is not particularly interested in these states whose energies are exponentially close to the Landau levels. Since the spectrum is modified at most in a well-controlled way, it is permissible to truncate the matrix to a smaller size $N_{\rm trunc}$.(Nonetheless, the described method yields precise bulk energies, as long as their exponentially small distance to the Landau energies is resolvable within the numerical precision, cf Fig. 4.2 (b).)

A small complication arises in the case of finite λ. Due to the hypersingular part, the diagonal Fourier elements increase linearly as $|\ell| \to \infty$, cf (A.12). The above statements apply in this case after dividing the matrix (4.44) column-wise by the asymptotic factor

$$\left[\left(\frac{\langle \hat{\mathbf{t}}_0 \times \mathbf{r}_0 \rangle}{b^2} - 2\pi \frac{\ell}{\mathscr{L}} \right)^2 + \left(\frac{\mathrm{Si}(\pi)}{\sigma_e} \right)^2 \right]^{1/2} . \tag{4.52}$$

Here, $\langle \hat{\mathbf{t}}_0 \times \mathbf{r}_0 \rangle$ is the average (the $0^{\rm th}$ Fourier component) of the function $\hat{\mathbf{t}}(s_0) \times \mathbf{r}(s_0)$ defined on the boundary.

The calculation of the spectrum amounts to finding (all) the roots of the complex-valued determinant (4.44) in a given energy range. Numerically, this is the most expensive task, scaling as $N^3_{\rm trunc}$. Since the computation of the determinant tends to be unstable around its zeros, it is more advantageous to employ a singular-value decomposition of the matrix which is stable in any case [117]. The vanishing of a singular value indicates a defective rank of its matrix. Due to roundoff errors these non-negative quantities are always greater than zero. However, the spectral points are very well defined by the sharp minima of the lowest singular value as a function of ν, cf Figure 4.2(b). The detection of near degeneracies is made appreciably easier if one monitors the next smallest singular values, as well.

In order to calculate the probability densities and current distributions away from the boundary, one may evaluate the integral representations (4.24) and (4.25). Since the integrands are not singular for $\mathbf{r}_0 \notin \Gamma$, the integrals may be approximated by a discrete sum over the N boundary elements without further ado. The densities of other observables can be obtained by similar boundary integrals.

Convergence and accuracy

Careful numerical tests indicate that the precision of the calculated spectra and wave functions is determined almost exclusively by the dimension N of the initial matrix. In Figure 4.3(a) we show how the energies converge exponentially as N increases. At the same time, the calculated spectra are found to be numerically invariant with respect to other parameters such as $\alpha_{\rm c}$, σ_e, $N_{\rm trunc}$, and in particular the location of the origin.

Reasonable choices for $\alpha_{\rm c}$ and σ_e are $\alpha_{\rm c} = \sqrt{\nu}/b$ and $\sigma_e = b$. The location and size of the sub-block is best determined by summing over the moduli of the matrix elements in each column. The resulting spectra are independent of $N_{\rm trunc}$, provided it exceeds a critical value. Here, the position of the origin is relevant, because the calculation of the spectral determinant (4.44), in particular its analytical parts, must be performed in a specific gauge. The choice in favour of the symmetric gauge is made in (4.43) where the remaining gauge freedom χ is absorbed into the solution vector. As a consequence of the resulting distinction of the origin, the spectral determinant is no longer translationally invariant.

As a result, the *size* of the truncated matrix depends on the choice of the origin. For example, the values in Fig. 4.3(a) belong to an ellipse centered at the origin. With an

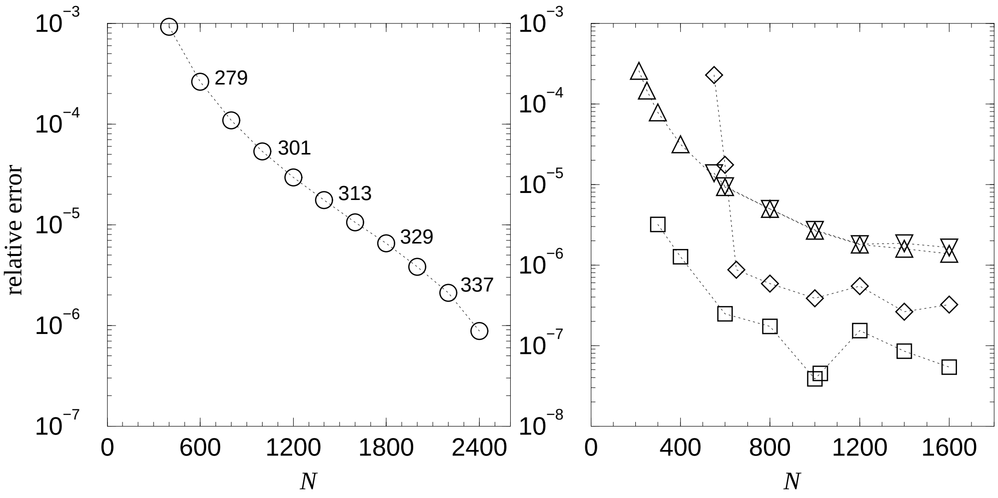

Figure 4.3: Errors of the 1000th interior eigenvalue at $\rho = 0.6$ as a function of the boundary discretization N. (a) Approximate relative error for the elliptic domain of Fig. 4.2(b) (the Dirichlet state closest to $\nu = 19$). Here, the energy for $N = 2600$ was taken as reference. The numbers indicate the matrix dimension after truncation which determines the numerical effort. They increase only weakly with N. (b) Exact relative error of the *exterior Neumann* energies of a typical edge state ($\triangle, \bigtriangledown$) and a typical bulk state ($\square, \diamondsuit$), as a function of N. Here, we use a *circular domain* (of area $\mathscr{A} = \pi$) which allows to determine the exact energies ($\nu_{\mathrm{edge}} \simeq 19.0294509$, $\nu_{\mathrm{bulk}} \simeq 19.4816851$) independently. The center of the domain is placed at the origin ($\triangle, \square$) and at the point (3,0) ($\bigtriangledown, \diamondsuit$), respectively. One observes that the displacement does not affect the error of the edge state, but increases the error of the bulk state energy systematically. (Note that the graphs do not have the same scale.)

ellipse displaced by the vector $(2,1)^{\mathrm{T}}$ one obtains the same relative errors for $N = 600$ and $N = 2400$ (not shown, one would not see a difference) with truncation sizes larger by 50%. In order to minimize the numerical effort it is therefore advantageous to choose the origin in the center of the domain considered.

The fact that bulk states are more strongly affected by the truncation is seen in Fig. 4.3(b), where exterior Neumann states of a circular domain are compared after displacement by 3 radii. Since the disk is a separable problem, we can check here against the exact energies (obtained as the roots of a special function, cf Sect. 7.1) Note that the calculation of the hypersingular integral introduces no additional error.

The only precise published calculations for a non-trivial shape known to us are the results of Tiago *et al*, who give the first twenty Dirichlet levels for an ellipse of eccentricity 0.8 and area $\mathscr{A} = \pi$ at constant $b^2 = 2/25$ (missing one symmetry class!). Our method is able to confirm their results to *all* given seven digits (apart from occasional differences in the last digit by one). For reference, we note the energy of the approximately *one-thousandth* state (the one closest to $\nu = 80$), which we calculate to be $\nu \simeq 79.9362(6)$. The expected error is less than 0.1% of the mean level spacing.

Chapter 5

Results of the boundary integral method

In the following, we demonstrate the performance of the boundary integral method by exhibiting some numerical results on magnetic billiards, which have been inaccessible by other methods.

5.1 Spectral statistics

We start by applying some of the standard tools of spectral statistics to large data sets of interior spectral points. The spectra are expected to reproduce the features of Random Matrix Theory (RMT), if the underlying classical motion displays hard chaos. Therefore, we define the spectra of this section in the semiclassical direction $b \to 0$, keeping the cyclotron radius ρ constant. This way we ensure that the classical dynamics are hyperbolic throughout the spectral intervals considered.

We consider the two domains described in Fig. 5.1. One is an asymmetric version of the Bunimovich stadium billiard ($r_1 = 0.75$, $r_2 = 0.25$, $\mathscr{A} = 5.39724$). In the magnetic field, its dynamics is free of unitary symmetries but exhibits an anti-unitary one (time reversal and reflection at $y = 0$). The skittle shape, in contrast, (made up of the arcs of four symmetrically touching circles, $r_1 = 1.0$, $r_2 = 0.5$, $\mathscr{A} = 4.33969$) does not display any symmetry. We chose it, because it generates hyperbolic classical motion even for small cyclotron radii $\rho > 1$ [49]. (The asymmetric stadium could not be proven to be strictly hyperbolic, but any possibly integrable part in phase space is much smaller than the uncertainty product, $(b^2\pi)^2$, throughout the considered spectral interval.)

We calculated 5300 and 7300 consecutive interior Dirichlet eigenvalues at $\rho = 1.2$, for the asymmetric stadium and the skittle shaped domain, respectively. It should be noted, that states of much higher ordinal number can be computed at little cost with the boundary integral method. The time consuming task is rather to find *all* energies, including the near-degenerate ones, in a given interval.

A quantity which indicates faithfully whether spectral points were missed is the

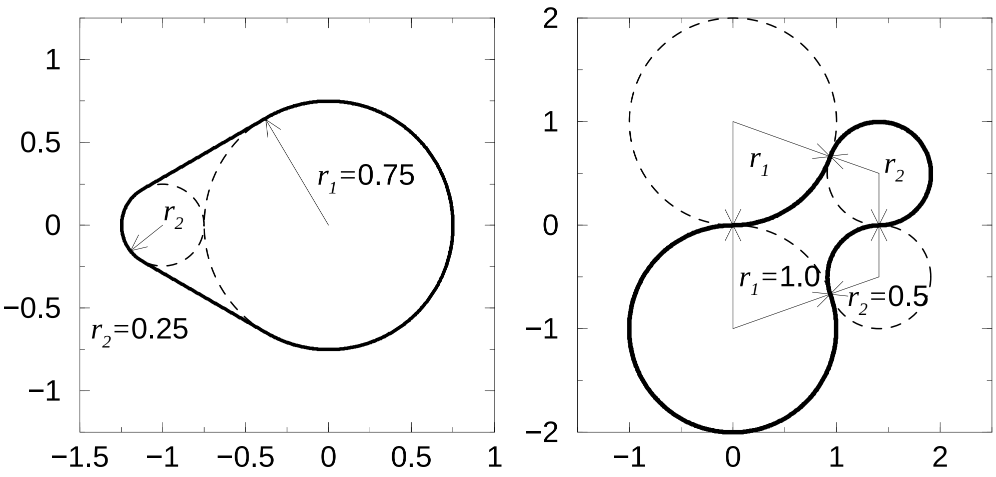

Figure 5.1: Definition of domain boundaries considered in Chapter 5. The magnetic dynamics in the asymmetric stadium (left) exhibits an anti-unitary symmetry, but no unitary one. In contrast, the skittle shaped domain (right) is free of any symmetry. It generates *hyperbolic* classical motion for $\rho > 1$, ie even for strong magnetic fields.

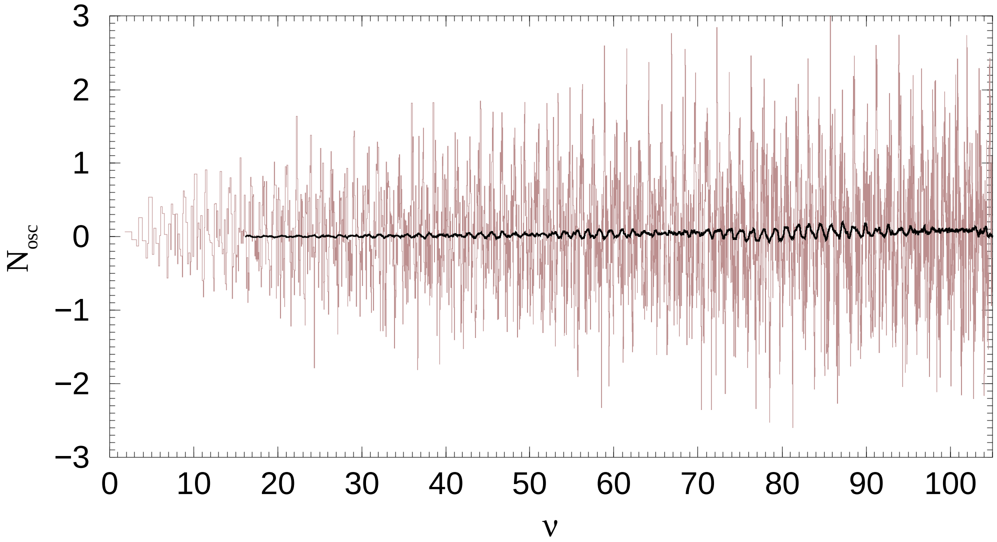

Figure 5.2: Fluctuating part of the spectral staircase in the asymmetric stadium at $\rho = 1.2$. The displayed range contains the first 5000 points of the interior spectrum, with the heavy line a running average over 250 neighbouring points. If a spectral point was missed in the calculation the curve would show a distinct step by one.

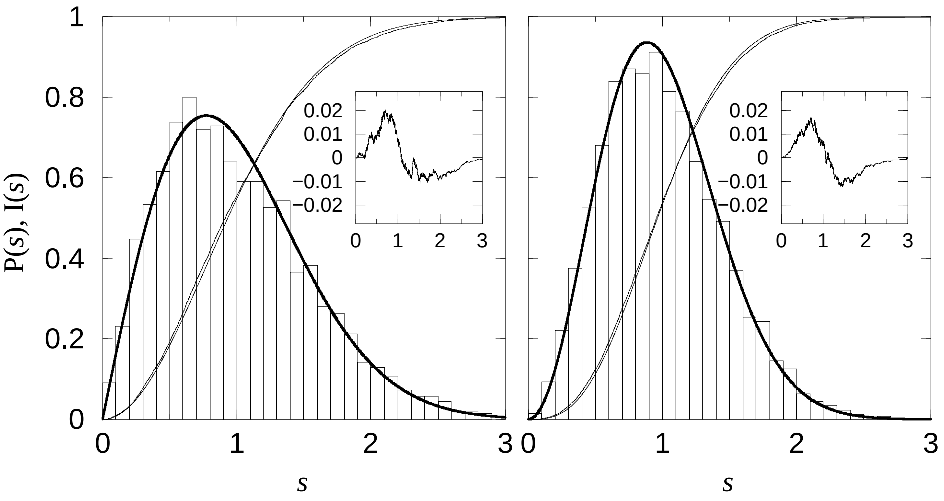

Figure 5.3: Nearest neighbour distributions of the asymmetric stadium (left) and of the skittle shaped domain (right), at $\rho = 1.2$. The histograms should be compared to GOE and GUE predictions of Random Matrix Theory, respectively (heavy lines.) The monotonic lines give the corresponding cumulative quantities. Their differences are reported in the insets.

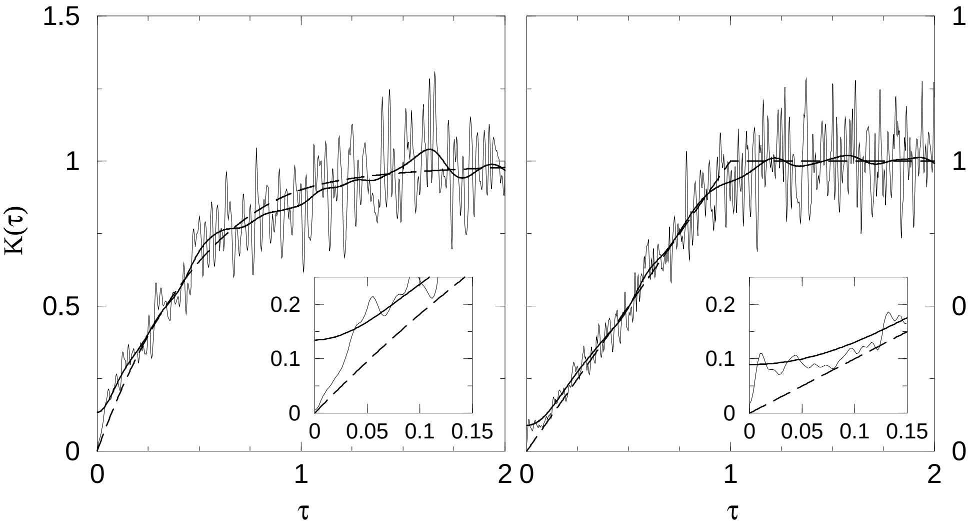

Figure 5.4: Spectral form factor of the asymmetric stadium (left) and the skittle shaped domain (right), based on 5300 and 7300 spectral points, respectively. The heavy lines display the same data after stronger spectral averaging. The random matrix result for the Gaussian Orthogonal and the Gaussian Unitary Ensemble, respectively, is indicated by the dashed lines. The insets show the regions of small τ.

fluctuating part $\mathrm{N}^{(\rho)}_{\mathrm{osc}}(\nu) = \mathrm{N}^{(\rho)}(\nu) - \overline{\mathrm{N}}^{(\rho)}(\nu)$ of the spectral counting function. It is defined in terms of the mean staircase, which is given, for fixed ρ, in equation (D.1). Figure 5.2 displays $\mathrm{N}^{(\rho)}_{\mathrm{osc}}$ for the asymmetric stadium proving that the spectrum is complete. A similar result is obtained for the skittle shaped domain (not shown).

The large spectral intervals at hand allow for the direct calculation of some of the popular statistical functions. Due to the underlying classical chaos and the symmetry properties mentioned above, one expects the statistics of the Gaussian Orthogonal Ensemble (GOE) for the asymmetric stadium, and of the Gaussian Unitary Ensemble (GUE) for the skittle. Figure 5.3 shows the distributions of nearest neighbours $P(s)$ of the unfolded[*] spectra. Indeed, one finds excellent agreement with Random Matrix Theory. The differences between the numerical and the RMT cumulative functions $I(s) = \int_0^s P(s')\mathrm{d}s'$ stay below 2% (ie, below the error of Wigner's surmise [118]).

A function which characterizes the spectrum much more sensitively than $P(s)$ is the form factor $K(\tau)$, ie, the (spectrally averaged) Fourier transform of the two-point autocorrelation function of the spectral density [119,120]. Figure 5.4 gives the spectral form factor together with the RMT results. We find very good agreement. One would expect systematic deviations at small τ, due to the contributions of single short periodic orbits. These cannot be resolved with the present size of the spectral interval, though. Since most other popular spectral measures, such as Dyson's Δ_3 statistic, are functions of the form factor, there is no need to present them here.

Thie good agreement with RMT is not only a consequence of the large spectral intervals the statistics are based on. It is equally important that the spectra are defined at fixed classical dynamics. Had we calculated the spectra at fixed field, they would have been based on a classical phase space that transforms from a near-integrable, time-invariance-broken structure, to a hyperbolic time-invariant one as ρ increases with energy. This transformation of spectral statistics from GOE to GUE as the field is increased was studied in [21–23].

5.2 Wave functions in the interior and in the exterior

We proceed to present a selection of stationary wave functions calculated in the semiclassical regime. We start with those of the skittle shaped domain choosing again $\rho = 1.2$. This ensures that the corresponding classical skipping motion is hyperbolic in the interior, as well as in the exterior.

The skittle

Figure 5.5(a) shows the density plot of a typical interior wave function around the one-thousandth eigenstate. As expected for a classically ergodic system, it spreads out throughout the whole domain. Occasionally, one may also find *bouncing-ball* modes, ie wave functions localized on a manifold of marginally stable periodic orbits. One such wave function is given in Fig. 5.5(b). It belongs to a family of 2-orbits.

A typical *exterior* wave function with an energy close to that of Fig. 5.5(a) is displayed in the middle row of Figure 5.5, at the same scale (c), and at a larger scale (d). One observes that in the vicinity of the boundary it behaves similar to an interior

---

[*] The spectra are transformed to unit density; see also the discussion in Sect. 9.1.

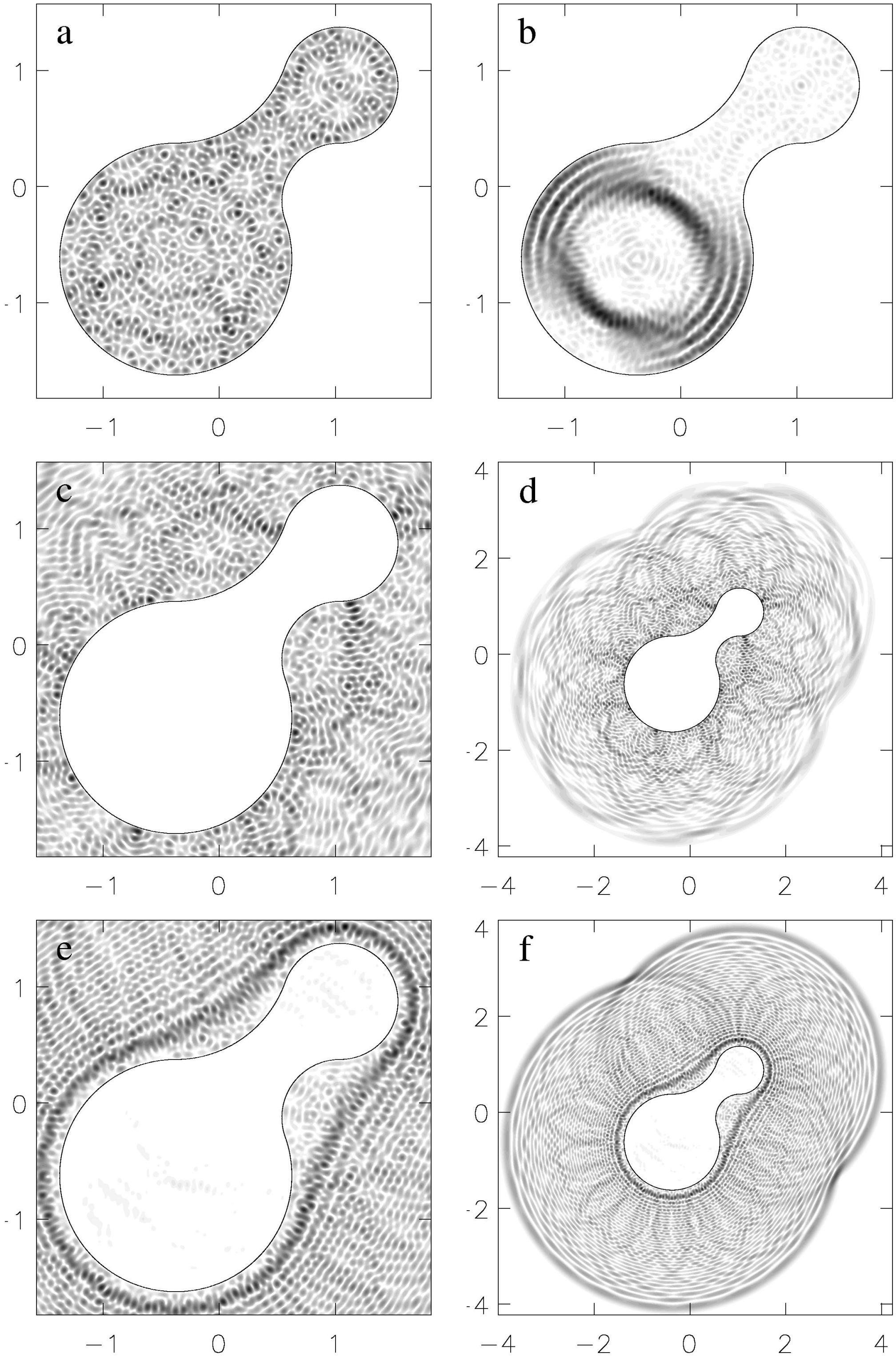

Figure 5.5: Interior and exterior wave functions of the skittle shape at $\rho = 1.2$, around the one-thousandth interior eigenstate. The plotted shade is proportional to $|\psi|$, the thin lines indicate the boundary Γ. Energies: (a) $\nu \simeq 32.98804$, (b) $\nu \simeq 33.12033$, (c,d) $\nu \simeq 32.84740$, (e,f) $\nu \simeq 32.50073$.

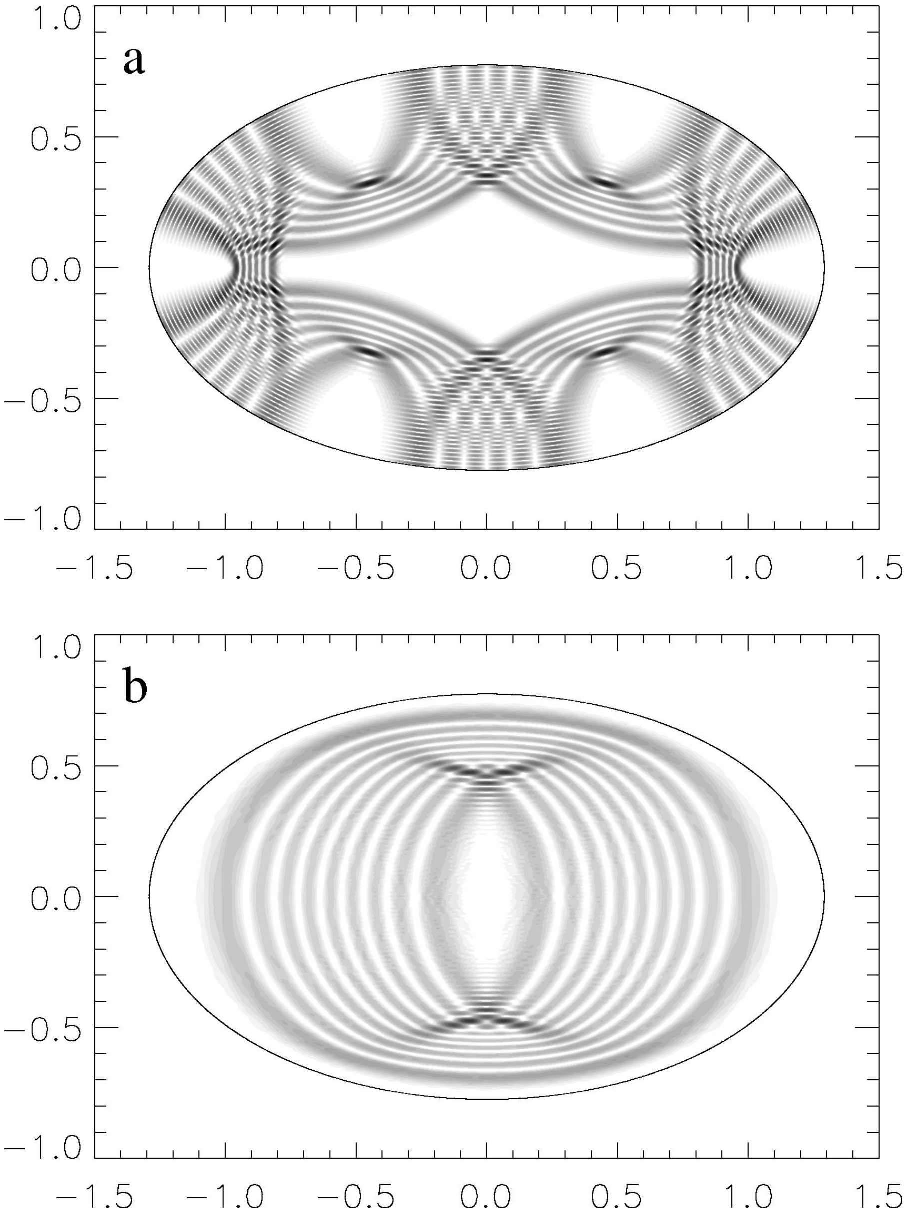

Figure 5.6: Wave functions (a,b) and current distributions (c,d) in an elliptic domain at $\rho = 0.6$, around the ten-thousandth interior eigenstate.

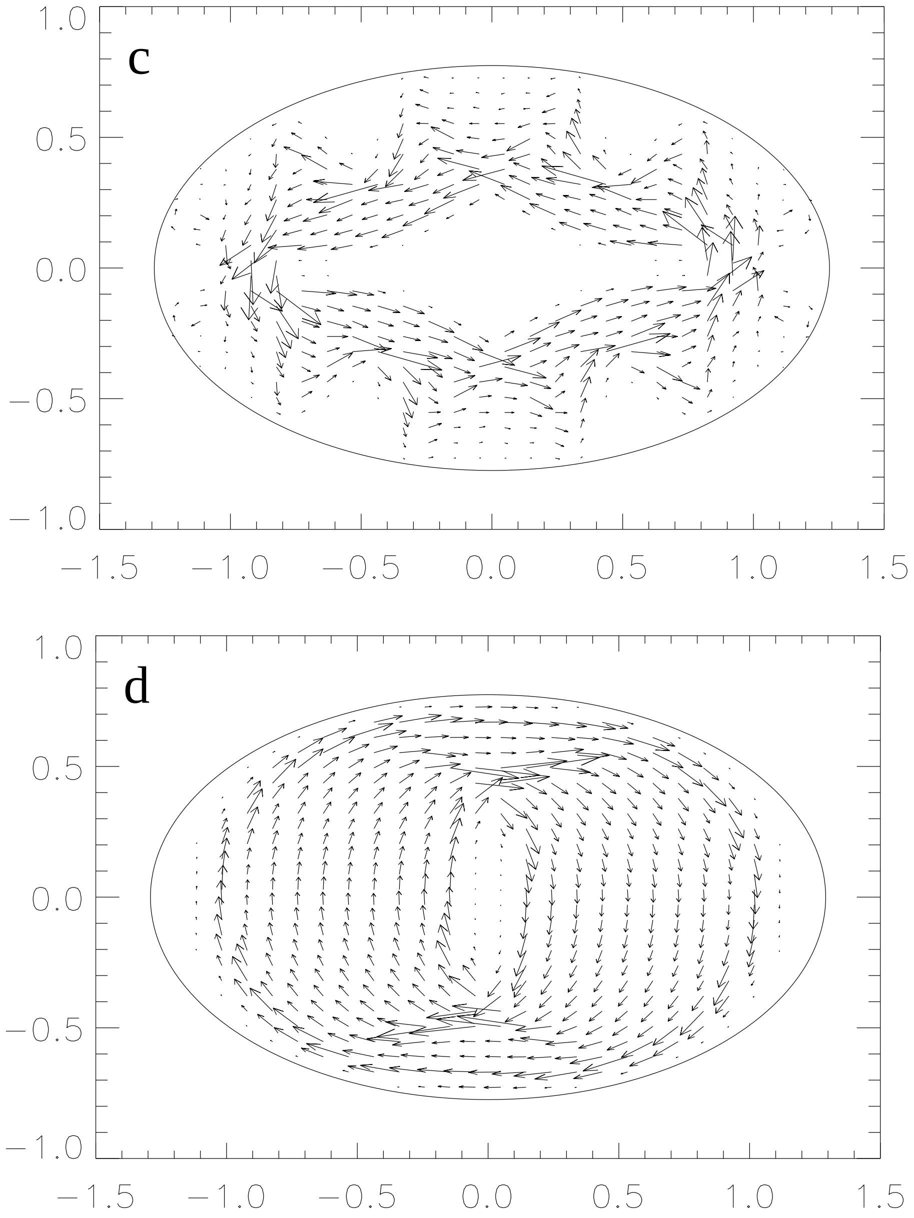

Figure 5.6: (continued) The energies of the states are $\nu \simeq 60.06026$ (a,c) and $\nu \simeq 60.50030$ (b,d).

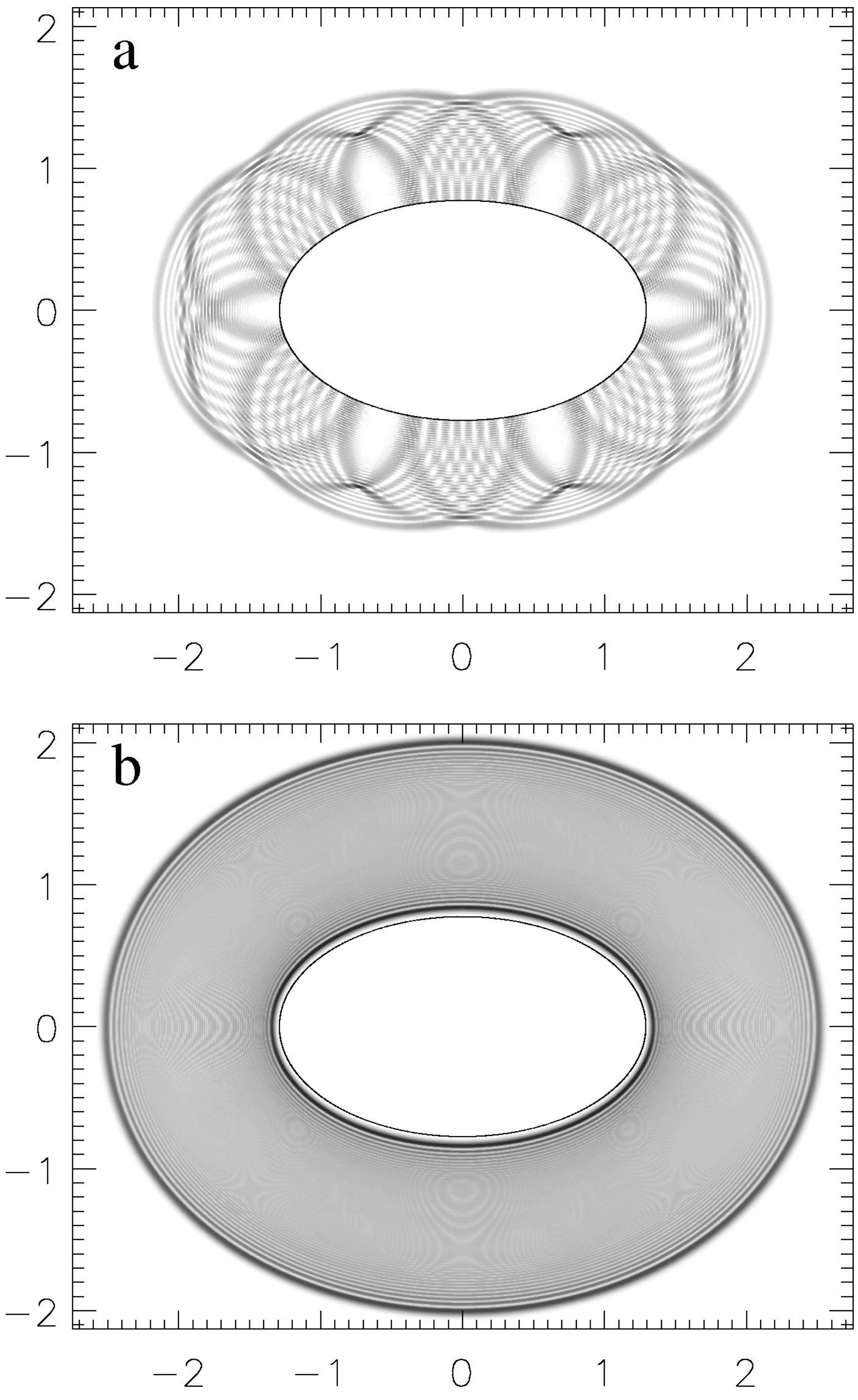

Figure 5.7: Exterior wave functions (a,b) and current distributions (c,d) at $\rho = 0.6$ and at similar energies as in Fig. 5.6, $\nu \simeq 60.13634$ (a,c) and $\nu \simeq 60.50049$ (b,d).

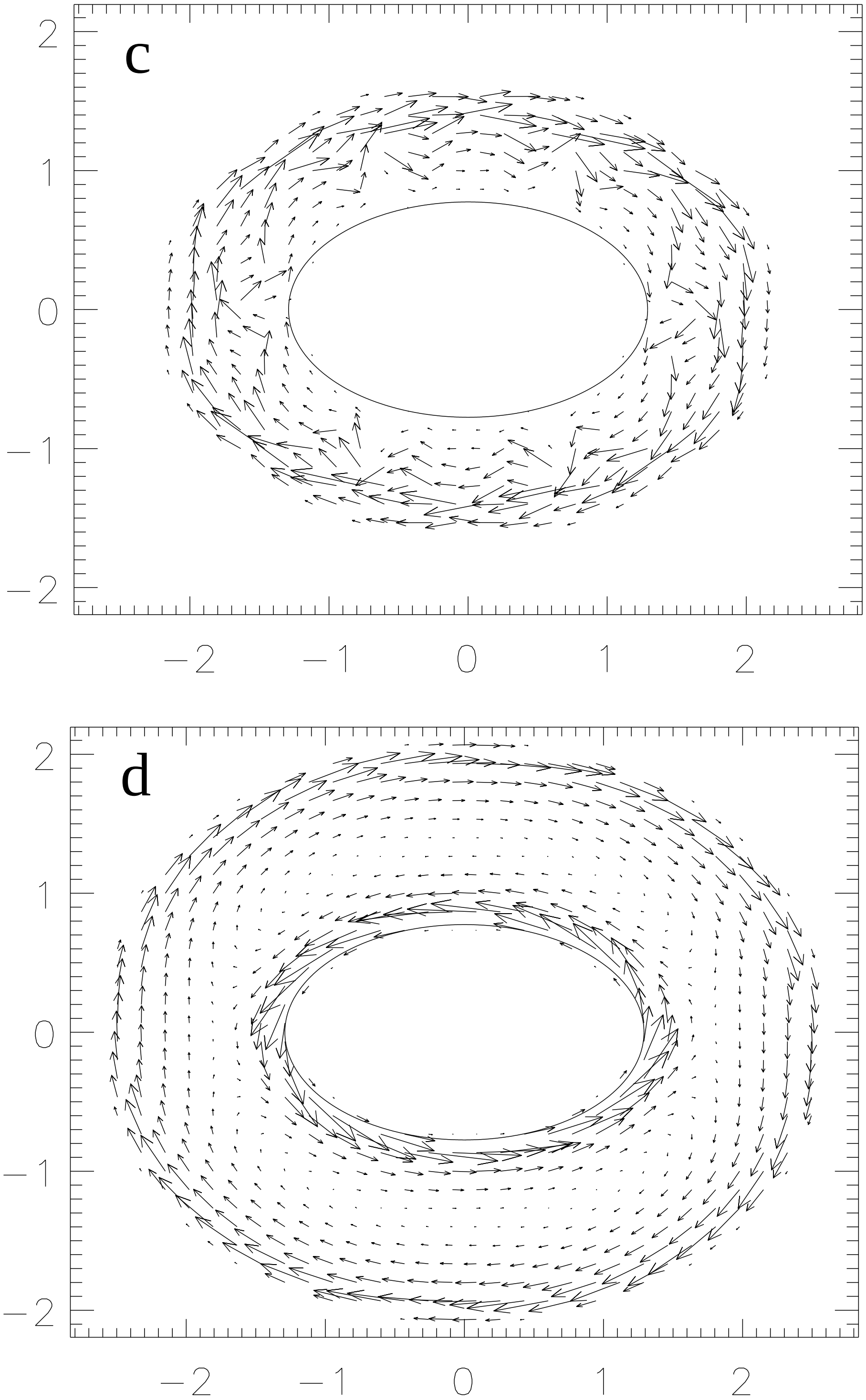

Figure 5.7: (continued) [The image in part (b) has been blurred to reduce Moiré patterns when printed with finite resolution. It should show only concentric elliptic strips.]

function. On a larger scale, the wave function decays after a distance smaller than two cyclotron radii. In this region circular structures are faintly visible, with the radius of the classical cyclotron motion.

The bottom row of Figure 5.5 shows a quite different exterior state with an energy close to that of a Landau level. It is a bulk state. A typical feature is the fact that there are no large amplitudes close to the boundary. Rather, one finds a ring of increased amplitude encircling the domain. Another ring surrounds the domain at a distance of 2ρ. This double-ring structure moves outwards as one goes through the series of states with energies increasingly close to the Landau levels. Semiclassically, it can be understood as being made up of a superposition of cyclotron orbits. This becomes even more clear in the following where we consider a more symmetric shape of the boundary.

The ellipse

For the second set of wave functions we choose an elliptic domain (of eccentricity 0.8 and area π), at a small cyclotron radius $\rho = 0.6$. The classical dynamics is mixed chaotic in this case [65], cf Fig. 3.1. Going to the extreme semiclassical limit – the ten-thousandth interior eigenstate – we expect the wave functions to mimic the structures of the underlying classical phase space. Indeed, Figure 5.6(a) displays a wave function which is localized along a stable interior 6×6-orbit. Note that the wave nature of the eigenstate is still visible at points where the trajectory intersects with itself. Since ρ is small enough to allow for closed cyclotron orbits fitting into the ellipse, we find bulk states also in the interior, see Fig. 5.6(b) for an example. Again it is semiclassically described by a superposition of closed cyclotron orbits. This can be seen clearly from the current distributions which are given in the right column of Fig. 5.6 for the edge state (c) and the bulk state (d), respectively. Here, the length of the arrows is proportional to the amplitude of the current density.

Similar semiclassical states can also be found in the exterior, as displayed in Figure 5.7. The edge state, Fig. 5.7(a), is distinguished from a typical bulk state, cf. Fig. 5.7(b), by the finite current it carries around the domain. In contrast, the bulk state with its counter-running current densities has no net current along the boundary, cf. Fig. 5.7(c) and Fig. 5.7(d). We emphasize that all the wave functions and current distributions shown above are calculated throughout the entire displayed area. They turn out to be *numerically* zero in the complementary domains, as expected from the theory.

5.3 General boundary conditions

The Neumann ground state

So far, we only considered Dirichlet conditions. They are the natural choice from a physical point of view. The Neumann boundary conditions, $\Lambda^{-1} = 0$, are occasionally employed in spectral theory [30]. They have the advantage that the ground state energy lies below the first Landau level, which facilitates its mathematical analysis. Here, we are able to observe the manifestation of a recent theorem of spectral theory [121]. It states that the Neumann ground state of a magnetic billiard is *exponentially localized*

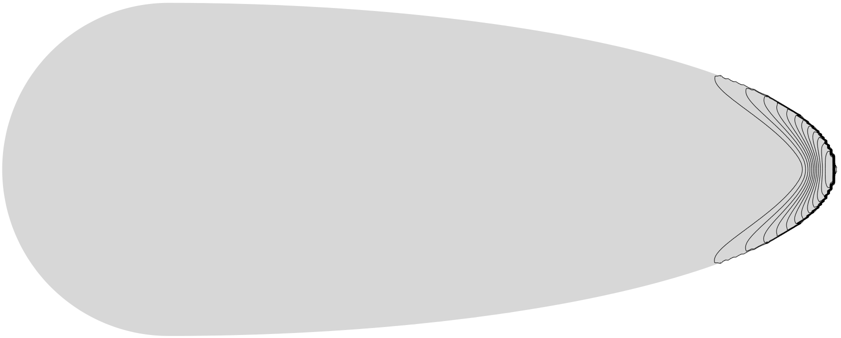

Figure 5.8: Contour plot of the ground state wave function (absolute value) for *Neumann* boundary conditions and strong field, $b = 0.05$, $\nu \simeq 0.2763$. The wave function is *localized* at the boundary point of maximum curvature, as predicted by a recent theorem [121]. The billiard domain is given by the union of a half-circle and a half-ellipse (shaded region).

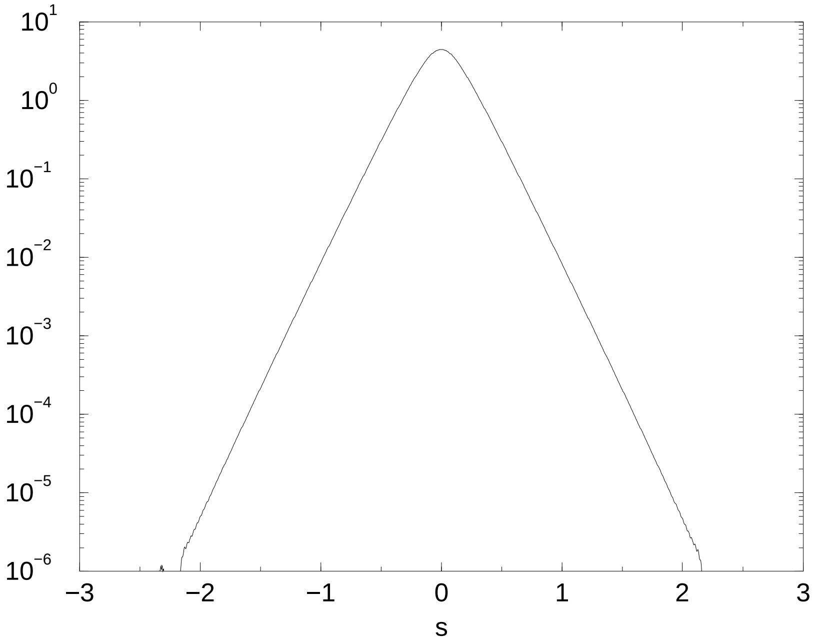

Figure 5.9: Boundary values of the ground state wave function of Fig. 5.8. As predicted in [121], it is *exponentially* localized at the point $s = 0$ of maximum curvature.

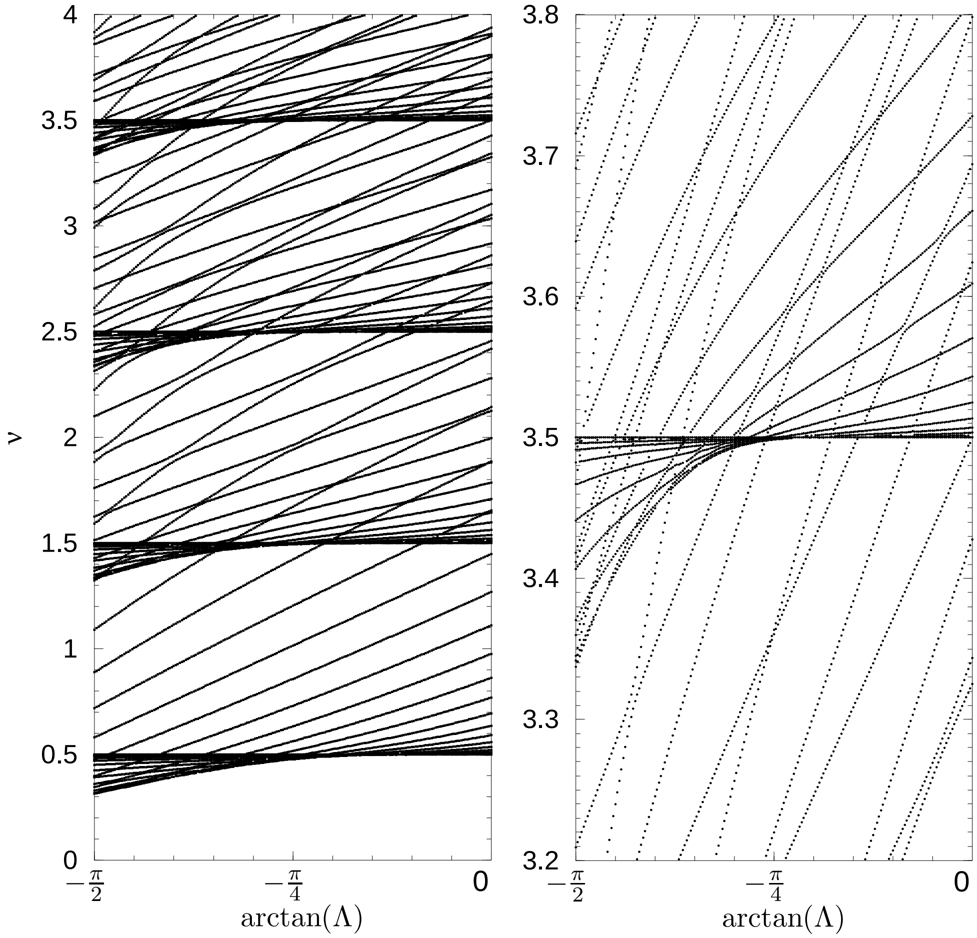

Figure 5.10: The parametric dependence of the *exterior* spectrum on the boundary condition (for the asymmetric stadium, ie $\mathscr{L} = 5.39724$, at fixed $b = 0.25$). The parameter Λ interpolates between Neumann ($\arctan \Lambda = -\frac{\pi}{2}$) and Dirichlet ($\arctan \Lambda = 0$) boundary conditions. The right graph shows details around the forth Landau level.

around the boundary point of maximum curvature. In order to deal with a unique boundary point of maximum curvature we choose the union of a half-circle and a half-ellipse (with half-axes $\breve{a} = 2, \breve{b} = 0.5$) as billiard boundary. Choosing a magnetic length of $b = 0.05$ (which corresponds to a very strong field), we find the ground state energy $\nu = 0.2763$. The Figures 5.8 and 5.9 display the ground state wave function in the billiard and on the boundary, respectively. Indeed, one observes an exponential localization over six orders of magnitude.

Parametric dependence on the mixing parameter

As a last point, we show the parametric dependence of a spectrum on the type of boundary conditions. Figure 5.10 presents the *exterior* spectrum of the asymmetric stadium as a function of the scaled mixing parameter $\Lambda \in (-\infty, 0]$, cf (3.7). It is chosen negative to ensure that the transformation from Neumann ($\Lambda = -\infty$) to Dirichlet ($\Lambda = 0$) boundary conditions is continuous. For positive Λ this would not be the case, which is a restriction similar to the one for the field free case [88]. (The $\arctan$ function is used in Fig. 5.10 to transform the infinite range of Λ into a bounded interval.)

The energies clustering around the Landau levels $\nu = N + \frac{1}{2}, N \in \mathbb{N}_0$ belong to bulk states. One observes that they are lifted from the Landau levels to higher energies at Dirichlet boundary conditions, whereas in the Neumann case they are shifted to smaller energies. A semiclassical theory which describes the exponential approach of the bulk states to the Landau levels and their transition as a function of Λ will be described in Sects. 7.2 and 8.3.1. We will come back to Fig. 5.10 not only there, but also in Chapter 8, when we define the edge state density.

Chapter 6

Semiclassical Quantization

In Chapter 4, the boundary integral equations were found to yield an efficient method to obtain the exact quantum spectrum of magnetic billiards. It will be shown in the following, that the same equations are as important for semiclassical quantization. They serve as the starting point for the derivation of the semiclassical periodic orbit formulas.

Periodic orbit formulae for magnetic billiards

The celebrated trace formulas of Gutzwiller [1,34] and Berry & Tabor [2,122] allow to quantize systems semiclassically in terms of their classical motion. They were derived assuming a continuous Hamiltonian flow. The corresponding formulas for field free billiards are known to exhibit additional phase factors which account for the discontinuity at the billiard boundary.

In order to prove that the same is true for magnetic billiards, we shall explain *how* the corresponding trace formulas are obtained from first principles. To our knowledge, no such derivation has been published for magnetic billiards, yet. The natural approach is to follow the lines of Balian and Bloch's treatment of field-free billiards [123], in analogy to the surface-of-section method [124] and the scattering approach [125] for non-magnetic systems. Those attempts *failed* so far, due to the appearance of an abundance of unphysical "ghost" orbits which could not be handled. To resolve this problem, we take advantage of the analysis performed in Chapter 4. There, it was found that the boundary integral equations allow for spurious solutions which belong to a particular complementary problem. We will show that the semiclassical spectral determinant can be factorized, accordingly, into an interior and exterior part. Each of them leads to a trace formula incorporating only the physical periodic orbits in the appropriate domain.

Outline

Like in the field-free case [123–127] the semiclassical quantization will be based on the double layer boundary integral equation. The main complication arising at finite magnetic field – apart from the spurious solutions – is the inherently asymmetric form of the respective integral kernel. The latter is not simply related to the semiclassically unitary operator derived from the generating function of the map, unlike the case of field-free billiards [75].

In Section 6.1, we deduce the semiclassical approximants to the boundary integral operators of Chapter 4. After that, in Sect. 6.2, special map operators are introduced which allow to transform the spectral function of the double-layer boundary integral equation. As a result, the number counting function is given in terms of the traces of powers of the map operators.

These traces are evaluated semiclassically in Section 6.3 assuming hyperbolic (ie, purely chaotic) skipping motion. We show why only classically allowed, skipping periodic orbits contribute, and how their stability properties enter. The section concludes with the trace formula for the density of states and the magnetization density. In Section 6.4, the traces are evaluated assuming integrable dynamics. As a result, we obtain the explicit periodic orbit formula for the spectral density of states in the magnetic disk billiard.

6.1 The semiclassical boundary integral operators

In section 4.3 the boundary integral operators were defined in terms of the free Green function and derivatives thereof. To obtain the semiclassical approximations of the operators, one simply replaces the Green function by its approximant. The latter is an asymptotic expression to leading order in the semiclassically small parameter ν^{-1}, which was derived in Sect. 2.5.1. To remain at a consistent level of approximation, the derivatives appearing in the single-layer Neumann and the double-layer operators (4.13) – (4.15) are to be evaluated to the same leading order. This means in practise, that only the phase of the Green function (2.61) must be differentiated (but not the amplitudes). Accordingly, in the remainder of this thesis all equalities involving semiclassical quantities are understood to be semiclassical in the sense that they are correct (only) to leading order in ν^{-1}.

In order to obtain expressions which have a semiclassically intuitive and useful form, it will be important to use that representation (2.61) which contains the actions of the short and long arcs separately.[*] We found the geometric parts of the corresponding scaled actions (2.59) to be given by

$$\mathrm{a_S}(\mathbf{r};\mathbf{r}_0) = \frac{1}{\pi}\left(\arcsin\left(\frac{|\mathbf{r}-\mathbf{r}_0|}{2\rho}\right) + \frac{|\mathbf{r}-\mathbf{r}_0|}{2\rho}\sqrt{1-\left(\frac{\mathbf{r}-\mathbf{r}_0}{2\rho}\right)^2} - \frac{\mathbf{r}\times\mathbf{r}_0}{2\rho^2}\right) \tag{6.1}$$

and

$$\mathrm{a_L}(\mathbf{r};\mathbf{r}_0) = 1 - \mathrm{a_S}(\mathbf{r}_0;\mathbf{r}) \, . \tag{6.2}$$

---

[*] At this point, the reader may wish to refresh his or her memory on the ingredients to the semiclassical Green function as discussed in Sect. 2.5.1.

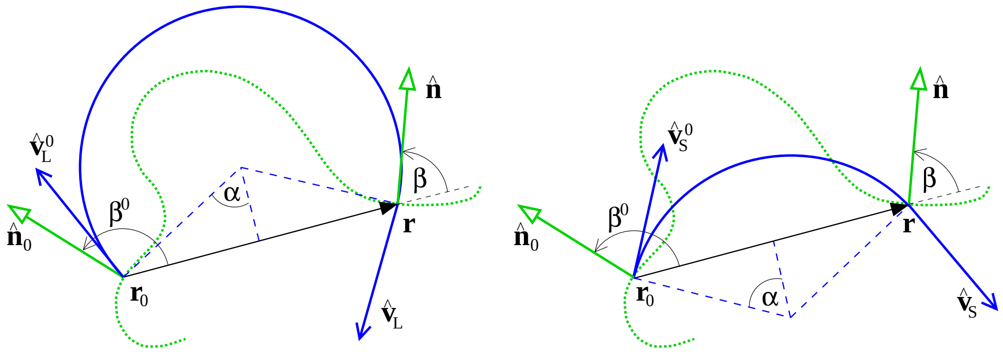

Figure 6.1: The angles α, β^0, and β are defined with respect the vector $\mathbf{r}-\mathbf{r}_0$ connecting the initial and the final point. They measure its length, and the relative direction of the boundary normals, respectively. These quantities do not depend on the type of the arc (left: long, right: short), unlike the relative direction of the initial and the final velocities $\hat{\mathbf{v}}^0$ and $\hat{\mathbf{v}}$. The latter may be expressed in terms of α, β^0, and β, cf eq (6.7). (The dotted line indicates the billiard boundary.)

As a first step, we note their gradients with respect to the initial and the final points.

$$\nabla_{\mathbf{r}_0} \mathrm{a}_{\left(\begin{smallmatrix}\mathrm{S}\\ \mathrm{L}\end{smallmatrix}\right)}(\mathbf{r};\mathbf{r}_0) = \frac{1}{\pi\rho}\left(\mp\frac{\mathbf{r}-\mathbf{r}_0}{|\mathbf{r}-\mathbf{r}_0|}\sqrt{1-\left(\frac{\mathbf{r}-\mathbf{r}_0}{2\rho}\right)^2}-\frac{1}{2\rho}\begin{pmatrix}-y\\ x\end{pmatrix}\right) \tag{6.3}$$

$$\nabla_{\mathbf{r}} \mathrm{a}_{\left(\begin{smallmatrix}\mathrm{S}\\ \mathrm{L}\end{smallmatrix}\right)}(\mathbf{r};\mathbf{r}_0) = \frac{1}{\pi\rho}\left(\pm\frac{\mathbf{r}-\mathbf{r}_0}{|\mathbf{r}-\mathbf{r}_0|}\sqrt{1-\left(\frac{\mathbf{r}-\mathbf{r}_0}{2\rho}\right)^2}+\frac{1}{2\rho}\begin{pmatrix}-y_0\\ x_0\end{pmatrix}\right) \tag{6.4}$$

Here, the upper and lower signs of the first summands stand for the short arc and long arc contribution, respectively. In the following, it will be useful to state the distance between the initial and the final point in terms of the positive angle

$$\alpha(\mathbf{r};\mathbf{r}_0) := \arcsin\left(\frac{|\mathbf{r}-\mathbf{r}_0|}{2\rho}\right) . \tag{6.5}$$

In addition, the direction of the normal vectors at the initial and the final points will be measured by their (signed) angles with respect to the distance vector connecting the two points.

$$\beta(\mathbf{r};\mathbf{r}_0) := \sphericalangle(\hat{\mathbf{n}};\mathbf{r}-\mathbf{r}_0) \qquad \beta^0(\mathbf{r};\mathbf{r}_0) := \sphericalangle(\hat{\mathbf{n}}_0;\mathbf{r}-\mathbf{r}_0) \tag{6.6}$$

Now consider the classical arcs connecting the initial and the final points. They define the direction of the classical velocities at the points of reflection and incidence, see Figure 6.1 for a sketch of the situation. The angles (6.5) and (6.6) allow to describe the direction of the velocities. For the normal components, one finds

$$\begin{aligned} \hat{\mathbf{v}}_{\mathrm{S}}\,\hat{\mathbf{n}} &= \cos(\beta+\alpha) & \hat{\mathbf{v}}_{\mathrm{S}}^{0}\,\hat{\mathbf{n}}_0 &= \cos(\beta^0-\alpha) \\ \hat{\mathbf{v}}_{\mathrm{L}}\,\hat{\mathbf{n}} &= -\cos(\beta-\alpha) & \hat{\mathbf{v}}_{\mathrm{L}}^{0}\,\hat{\mathbf{n}}_0 &= -\cos(\beta^0+\alpha) \end{aligned} \tag{6.7}$$

for short and long arcs, respectively. (Here, the velocity at the initial point of the arc is denoted with a zero superscript, and the hats indicate that the velocity vectors are normalized.)

The semiclassical Dirichlet operators

We proceed to calculate the semiclassical approximation[1]to the kernel of the double layer Dirichlet operator (4.14) by inserting (2.61). For the short arc term one has to evaluate the gauge invariant derivative

$$\begin{aligned}\partial_{n_0/b}[2\pi\mathrm{i}\nu\mathrm{a}_\mathrm{S} - \tilde{\chi}_0] + \mathrm{i}\tilde{A}_{n_0} &= 2\mathrm{i}\sqrt{\nu}\left(-\frac{(\mathbf{r}-\mathbf{r}_0)\,\hat{\mathbf{n}}_0}{|\mathbf{r}-\mathbf{r}_0|}\cos(\alpha) - \frac{(\mathbf{r}-\mathbf{r}_0)\times\hat{\mathbf{n}}_0}{2\rho}\right)\\ &= 2\mathrm{i}\sqrt{\nu}\left(-\cos(\beta^0)\cos(\alpha) - \sin(\beta^0)\sin(\alpha)\right)\\ &= -2\mathrm{i}\sqrt{\nu}\,\cos(\beta^0-\alpha) = -2\mathrm{i}\sqrt{\nu}\,(\hat{\mathbf{v}}^0_\mathrm{S}\,\hat{\mathbf{n}}_0)\,, \qquad (6.8)\end{aligned}$$

where we used eqs (6.3) and (6.7). Apart from the sign, it is given by the normal component of the classical velocity after reflection, since $2\sqrt{\nu}$ is the magnitude of the scaled velocity. Note, that $(\hat{\mathbf{v}}^0_\mathrm{S}\,\hat{\mathbf{n}}_0)$ is a non-symmetric function of the initial and the final point, and depends on the energy through α. For long arc term, one obtains the analogous expression

$$\partial_{n_0/b}[2\pi\mathrm{i}\nu\mathrm{a}_\mathrm{L} - \tilde{\chi}_0] + \mathrm{i}\tilde{A}_{n_0} = +2\mathrm{i}\sqrt{\nu}\,\cos(\beta^0+\alpha) = -2\mathrm{i}\sqrt{\nu}\,(\hat{\mathbf{v}}^0_\mathrm{L}\,\hat{\mathbf{n}}_0)\,. \qquad (6.9)$$

It follows that the semiclassical approximation of the double-layer Dirichlet kernel (4.29) can be stated in a particularly simple form,

$$\begin{aligned}\mathrm{q}^{\mathrm{D(sc)}}_{\mathrm{dl}}(\mathbf{r};\mathbf{r}_0) &:= \partial_{n_0/b}\mathrm{G}^{(\mathrm{sc})}_\nu + \mathrm{i}\tilde{A}_{n_0}\mathrm{G}^{(\mathrm{sc})}_\nu = \frac{1}{2(1+\mathrm{e}^{2\pi\mathrm{i}\nu})}\,\frac{1}{(2\pi\mathrm{i})^{\frac{1}{2}}}\,\mathrm{e}^{\mathrm{i}(\tilde{\chi}-\tilde{\chi}_0)}\\ &\times\left\{\frac{-\hat{\mathbf{v}}^0_\mathrm{S}\,\hat{\mathbf{n}}_0}{(\sin\alpha\cos\alpha)^{\frac{1}{2}}}\,\mathrm{e}^{2\pi\mathrm{i}\nu\mathrm{a}_\mathrm{S}} + \mathrm{e}^{-\mathrm{i}\frac{\pi}{2}}\,\frac{-\hat{\mathbf{v}}^0_\mathrm{L}\,\hat{\mathbf{n}}_0}{(\sin\alpha\cos\alpha)^{\frac{1}{2}}}\,\mathrm{e}^{2\pi\mathrm{i}\nu\mathrm{a}_\mathrm{L}}\right\}\,. \qquad (6.10)\end{aligned}$$

It will be an important ingredient in the derivation of the trace formulas. For completeness, we note that the semiclassical single-layer Dirichlet kernel is simply given by the semiclassical Green function itself, $\mathrm{q}^{\mathrm{D(sc)}}_{\mathrm{sl}}(\mathbf{r};\mathbf{r}_0) := \mathrm{G}^{(\mathrm{sc})}_\nu$, as an immediate consequence of (4.12).

The semiclassical Neumann operators

The kernels of the single- and double layer Neumann operators, eqs (4.13) and (4.15), involve gauge invariant gradients with respect to the final point of the Green function. One finds

$$\partial_{n/b}[2\pi\mathrm{i}\nu\mathrm{a}_\mathrm{S} + \tilde{\chi}] - \mathrm{i}\tilde{A}_n = +2\mathrm{i}\sqrt{\nu}\,\cos(\beta+\alpha) = +2\mathrm{i}\sqrt{\nu}\,(\hat{\mathbf{v}}_\mathrm{S}\,\hat{\mathbf{n}})\,, \qquad (6.11)$$

$$\partial_{n/b}[2\pi\mathrm{i}\nu\mathrm{a}_\mathrm{L} + \tilde{\chi}] - \mathrm{i}\tilde{A}_n = -2\mathrm{i}\sqrt{\nu}\,\cos(\beta-\alpha) = +2\mathrm{i}\sqrt{\nu}\,(\hat{\mathbf{v}}_\mathrm{L}\,\hat{\mathbf{n}})\,, \qquad (6.12)$$

similar to eqs (6.8) and (6.9). It follows that the semiclassical single-layer Neumann kernels assumes the form (compared to eq (4.28))

$$\mathrm{q}_{\mathrm{sl}}^{\mathrm{N(sc)}}(\mathbf{r};\mathbf{r}_0) := \partial_{n/b}\mathrm{G}_{\nu}^{\mathrm{(sc)}} - \mathrm{i}\tilde{A}_n\mathrm{G}_{\nu}^{\mathrm{(sc)}} = \frac{1}{2(1+\mathrm{e}^{2\pi\mathrm{i}\nu})}\,\frac{1}{(2\pi\mathrm{i})^{\frac{1}{2}}}\,\mathrm{e}^{\mathrm{i}(\tilde{\chi}-\tilde{\chi}_0)}$$
$$\times\left\{\frac{+\hat{\mathbf{v}}_{\mathrm{S}}\,\hat{\mathbf{n}}}{(\sin\alpha\cos\alpha)^{\frac{1}{2}}}\,\mathrm{e}^{2\pi\mathrm{i}\nu a_{\mathrm{S}}} + \mathrm{e}^{-\mathrm{i}\frac{\pi}{2}}\,\frac{+\hat{\mathbf{v}}_{\mathrm{L}}\,\hat{\mathbf{n}}}{(\sin\alpha\cos\alpha)^{\frac{1}{2}}}\,\mathrm{e}^{2\pi\mathrm{i}\nu a_{\mathrm{L}}}\right\}\ . \tag{6.13}$$

It is worth noting, how the mutual adjointness of the operators (4.28) and (4.29) shows up in the semiclassical case. By permuting $\mathbf{r}$ and $\mathbf{r}_0$ the prefactors of the short and long arc terms change their roles,

$$(\hat{\mathbf{v}}_{\mathrm{S}}\,\hat{\mathbf{n}}) \equiv \hat{\mathbf{v}}_{\mathrm{S}}(\mathbf{r};\mathbf{r}_0)\,\hat{\mathbf{n}}(\mathbf{r}) = \hat{\mathbf{v}}_{\mathrm{L}}^{0}(\mathbf{r}_0;\mathbf{r})\,\hat{\mathbf{n}}(\mathbf{r}_0) \equiv (\hat{\mathbf{v}}_{\mathrm{L}}^{0}\,\hat{\mathbf{n}}_0)^{\dagger}\ , \tag{6.14}$$

and likewise $(\hat{\mathbf{v}}_{\mathrm{L}}\,\hat{\mathbf{n}}) = (\hat{\mathbf{v}}_{\mathrm{S}}^{0}\,\hat{\mathbf{n}}_0)^{\dagger}$. As for the phases, it is the factor $(1+\mathrm{e}^{2\pi\mathrm{i}\nu})^{-1}$ whose conjugation provides the term $\mathrm{e}^{2\pi\mathrm{i}\nu}$ needed in conjunction with the relation (6.2) to prove the mutual adjointness.

The kernel of the semiclassical double-layer Neumann operator follows from applying the gauge invariant derivative (6.11) to the single-layer Dirichlet expression (6.10), cf eq (4.15). One obtains

$$\mathrm{q}_{\mathrm{dl}}^{\mathrm{N(sc)}}(\mathbf{r};\mathbf{r}_0) := (\partial_{n_0/b} + \mathrm{i}\tilde{A}_{n_0})(\partial_{n/b}\mathrm{G}_{\nu}^{\mathrm{(sc)}} - \mathrm{i}\tilde{A}_n\mathrm{G}_{\nu}^{\mathrm{(sc)}})$$
$$= \frac{1}{2(1+\mathrm{e}^{2\pi\mathrm{i}\nu})}\,\frac{2\mathrm{i}\sqrt{\nu}}{(2\pi\mathrm{i})^{\frac{1}{2}}}\,\mathrm{e}^{\mathrm{i}(\tilde{\chi}-\tilde{\chi}_0)}$$
$$\times\left\{\frac{-(\hat{\mathbf{v}}_{\mathrm{S}}^{0}\,\hat{\mathbf{n}}_0)(\hat{\mathbf{v}}_{\mathrm{S}}\,\hat{\mathbf{n}})}{(\sin\alpha\cos\alpha)^{\frac{1}{2}}}\,\mathrm{e}^{2\pi\mathrm{i}\nu a_{\mathrm{S}}} + \mathrm{e}^{-\mathrm{i}\frac{\pi}{2}}\,\frac{-(\hat{\mathbf{v}}_{\mathrm{L}}^{0}\,\hat{\mathbf{n}}_0)(\hat{\mathbf{v}}_{\mathrm{L}}\,\hat{\mathbf{n}})}{(\sin\alpha\cos\alpha)^{\frac{1}{2}}}\,\mathrm{e}^{2\pi\mathrm{i}\nu a_{\mathrm{L}}}\right\}\ . \tag{6.15}$$

Like the exact kernel (4.30) this semiclassical version is self-adjoint. This follows again from the observation that the two summands simply change roles when the adjoint operator is formed.

6.2 From boundary to map operators

Let us now consider the semiclassical double-layer equation for Dirichlet boundary conditions in more detail. As known from Chapter 4, the corresponding Fredholm determinant (4.17) is a spectral function. Its roots yield the Dirichlet spectrum of the domain considered, conjoint with the Neumann spectrum of the complementary domain.

In general, the fluctuating part of the number counting function, $\mathrm{N}_{\mathrm{osc}} = \mathrm{N} - \overline{\mathrm{N}}$ is obtained from a spectral function by taking the imaginary part of its logarithm, cf eg [128]. Employing the semiclassical expression (6.10) we get from eq (4.17)

$$-\frac{1}{\pi}\,\mathrm{Im}\log\det\left[\frac{1}{2} \pm \mathsf{Q}_{\mathrm{dl}}^{\mathrm{D(sc)}}\right]$$
$$= -\frac{1}{\pi}\,\mathrm{Im}\log\det\left[\frac{1}{2(1+\mathrm{e}^{2\pi\mathrm{i}\nu})}\right] - \frac{1}{\pi}\,\mathrm{Im}\log\det\left[1+\mathrm{e}^{2\pi\mathrm{i}\nu} \pm \mathsf{P}\right]\ . \tag{6.16}$$

Here, the determinant was split into two parts. This was done to reflect the the partitioning of the corresponding classical phase space into cyclotron orbits (which are detached from the boundary) and skipping trajectories, cf Sect. 3.1. In the first part of the sum (6.16), the determinant does not depend on the boundary. The diagonal operator is *singular* at the energies $\nu_N = N + \frac{1}{2}, N \in \mathbb{N}_0$ of the Landau levels, and represents semiclassically the contribution of the bulk states to the number counting function. This part is infinite at ν_N, corresponding to the infinite number of degenerate bulk states found in the exterior at each Landau level. (The exponentially small lifting of the degeneracy observed in the exact spectrum is not seen here, since the semiclassical Green function (2.62) does not describe tunneling effects.)

The map operators

As will become clear in the following, the second part in (6.16) gives the contribution of the *skipping* trajectories to the number counting function. It is described by the *map* operator P, defined as[2]

$$\mathsf{P} := 2(1 + \mathrm{e}^{2\pi \mathrm{i}\nu})\, \mathsf{Q}_{\mathrm{dl}}^{\mathrm{D}\,(\mathrm{sc})} \,. \tag{6.17}$$

We will show that it can be related to the classical billiard map (3.4) describing the motion of skipping trajectories.

Equation (6.16) suggests that the fluctuating part of the number counting function may formally be split, $\mathrm{N}_{\mathrm{osc}} = \mathrm{N}_{\mathrm{osc}}^{\mathrm{cycl}} + \mathrm{N}_{\mathrm{osc}}^{\mathrm{skip}}$, into parts which correspond to the bulk states and the edge states, respectively. Strictly speaking, $\mathrm{N}_{\mathrm{osc}}^{\mathrm{cycl}}$ is not a well-defined quantity. We shall disregard this contribution of the bulk states, for the time being, postponing a rigorous justification to Chapter 8 (where the spectral measure will be adjusted to remove the bulk states). The relevant contribution to the fluctuating number counting function is given by the part $\mathrm{N}_{\mathrm{osc}}^{\mathrm{skip}}$ which is due to the skipping motion,

$$\mathrm{N}_{\mathrm{osc}}^{\mathrm{skip}} = -\frac{1}{\pi}\, \mathrm{Im} \log \det \left[1 + \mathrm{e}^{2\pi \mathrm{i}\nu} \pm \mathsf{P} \right] \,. \tag{6.18}$$

Here, the upper sign stands for the interior problem, like in Chapter 4. The map operator P consists of a short arc and a long arc term. It is advantageous to split it accordingly,

$$\mathsf{P} = \mathsf{P}_{\mathrm{S}} + \mathsf{P}_{\mathrm{L}} \,, \tag{6.19}$$

with the corresponding integral kernels given by

$$\mathrm{p}_{\mathrm{S}}(s, s_0) := \frac{1}{(2\pi \mathrm{i})^{\frac{1}{2}}}\, \frac{-\hat{\mathbf{v}}_{\mathrm{S}}^{0}\, \hat{\mathbf{n}}_0}{(\sin(\alpha) \cos(\alpha))^{\frac{1}{2}}}\, \mathrm{e}^{2\pi \mathrm{i}\nu \mathrm{a}_{\mathrm{S}}}\, \mathrm{e}^{\mathrm{i}\tilde{\chi} - \mathrm{i}\tilde{\chi}_0} \tag{6.20}$$

and

$$\mathrm{p}_{\mathrm{L}}(s, s_0) := \frac{1}{(2\pi \mathrm{i})^{\frac{1}{2}}}\, \frac{-\hat{\mathbf{v}}_{\mathrm{L}}^{0}\, \hat{\mathbf{n}}_0}{(\sin(\alpha) \cos(\alpha))^{\frac{1}{2}}}\, \mathrm{e}^{-\mathrm{i}\frac{\pi}{2}}\, \mathrm{e}^{2\pi \mathrm{i}\nu \mathrm{a}_{\mathrm{L}}}\, \mathrm{e}^{\mathrm{i}\tilde{\chi} - \mathrm{i}\tilde{\chi}_0} \,, \tag{6.21}$$

cf eq (6.10) with $\mathbf{r} = \mathbf{r}(s), \mathbf{r}_0 = \mathbf{r}(s_0)$. In the standard procedure to obtain a trace formula one would now make use of the identity $\log \det = \operatorname{tr} \log$ [129] in equation

(6.18), and evaluate the trace of powers of the operator (6.19) in stationary phase approximation. However, unlike the case of field-free billiards the corresponding saddle point condition selects classical periodic orbits in the interior *and* in the exterior. This could be expected from the fact that the double-layer equation allows for solutions in the complementary domain. What is worse, an abundance of saddle-point configurations arises which do not have a physical meaning at all. In order to avoid these severe difficulties, it is vital to be able to write the spectral function (6.18) as a product, such that each factor yields the spectrum in either the interior or the exterior domain.

Factorising the determinant

To facilitate the factorization of the determinant (6.18), we split the short and long arc operators once more, $\mathsf{P}_\mathrm{S} = \mathsf{P}_\mathrm{S}^\mathrm{int} - \mathsf{P}_\mathrm{S}^\mathrm{ext}$ and $\mathsf{P}_\mathrm{L} = \mathsf{P}_\mathrm{L}^\mathrm{int} - \mathsf{P}_\mathrm{L}^\mathrm{ext}$. Ultimately, the parts labelled by “int”and “ext” should exclusively account for the motion in the interior and in the exterior, respectively. To that end, the splitting is defined by the signs of the prefactors of the integral kernels, which are functions of the initial and the final points.

$$\begin{aligned}
\mathrm{p}_\mathrm{S}^\mathrm{int}(s,s_0) &:= \Theta(-\hat{\mathbf{n}}_0\hat{\mathbf{v}}_\mathrm{S}^0)\,\mathrm{p}_\mathrm{S}(s,s_0) \qquad & \mathrm{p}_\mathrm{L}^\mathrm{int}(s,s_0) &:= \Theta(-\hat{\mathbf{n}}_0\hat{\mathbf{v}}_\mathrm{L}^0)\,\mathrm{p}_\mathrm{L}(s,s_0) \\
\mathrm{p}_\mathrm{S}^\mathrm{ext}(s,s_0) &:= -\Theta(\hat{\mathbf{n}}_0\hat{\mathbf{v}}_\mathrm{S}^0)\,\mathrm{p}_\mathrm{S}(s,s_0) \qquad & \mathrm{p}_\mathrm{L}^\mathrm{ext}(s,s_0) &:= -\Theta(\hat{\mathbf{n}}_0\hat{\mathbf{v}}_\mathrm{L}^0)\,\mathrm{p}_\mathrm{L}(s,s_0)
\end{aligned} \tag{6.22}$$

(The minus sign in front of the exterior kernels is introduced for convenience.) According to the definitions (6.22), the “interior” part of the operators vanishes whenever the initial and the final points have positions such that the corresponding classical arc points into the exterior domain, and vice versa. This crucial property is embodied in the operator equations

$$\mathsf{P}_\mathrm{S}^\mathrm{int}\,\mathsf{P}_\mathrm{L}^\mathrm{ext} + \mathsf{P}_\mathrm{L}^\mathrm{int}\,\mathsf{P}_\mathrm{S}^\mathrm{ext} = -\,\mathrm{e}^{2\pi\mathrm{i}\nu}\,\mathsf{id} \tag{6.23}$$

and

$$\mathsf{P}_\mathrm{S}^\mathrm{int}\,\mathsf{P}_\mathrm{S}^\mathrm{ext} + \mathsf{P}_\mathrm{L}^\mathrm{int}\,\mathsf{P}_\mathrm{L}^\mathrm{ext} = 0\,, \tag{6.24}$$

which are derived in Appendix C. With their help, it follows immediately that the determinant in eq (6.18) factorizes into an interior and exterior part.

$$\begin{aligned}
\mathrm{N}_\mathrm{osc}^\mathrm{skip} &= -\frac{1}{\pi}\,\mathrm{Im}\log\det\left[1 + \mathrm{e}^{2\pi\mathrm{i}\nu} \pm \left(\mathsf{P}_\mathrm{S}^\mathrm{int} - \mathsf{P}_\mathrm{S}^\mathrm{ext} + \mathsf{P}_\mathrm{L}^\mathrm{int} - \mathsf{P}_\mathrm{L}^\mathrm{ext}\right)\right] && (6.25) \\
&= -\frac{1}{\pi}\,\mathrm{Im}\log\det\left[\Big(1 \pm \left(\mathsf{P}_\mathrm{S}^\mathrm{int} + \mathsf{P}_\mathrm{L}^\mathrm{int}\right)\Big)\Big(1 \mp \left(\mathsf{P}_\mathrm{S}^\mathrm{ext} + \mathsf{P}_\mathrm{L}^\mathrm{ext}\right)\Big)\right] && (6.25\mathrm{a}) \\
&= -\frac{1}{\pi}\,\mathrm{Im}\,\mathrm{tr}\log\left[1 \pm \left(\mathsf{P}_\mathrm{S}^\mathrm{int} + \mathsf{P}_\mathrm{L}^\mathrm{int}\right)\right] - \frac{1}{\pi}\,\mathrm{Im}\,\mathrm{tr}\log\left[1 \mp \left(\mathsf{P}_\mathrm{S}^\mathrm{ext} + \mathsf{P}_\mathrm{L}^\mathrm{ext}\right)\right] \\
&= \frac{1}{\pi}\,\mathrm{Im}\sum_{n=1}^{\infty}\frac{(\mp)^n}{n}\,\mathrm{tr}\left[\left(\mathsf{P}_\mathrm{S}^\mathrm{int} + \mathsf{P}_\mathrm{L}^\mathrm{int}\right)^n\right] + \frac{1}{\pi}\,\mathrm{Im}\sum_{n=1}^{\infty}\frac{(\pm)^n}{n}\,\mathrm{tr}\left[\left(\mathsf{P}_\mathrm{S}^\mathrm{ext} + \mathsf{P}_\mathrm{L}^\mathrm{ext}\right)^n\right] \\
& && (6.25\mathrm{b})
\end{aligned}$$

Here we merely replaced the term $\mathrm{e}^{2\pi\mathrm{i}\nu}$ in (6.25) by the operators (6.23), and included (6.24). Then the identity $\log\det = \mathrm{tr}\log$ [129] was used, together with the Taylor expansion of the logarithm. The result is a sum of traces which contain only powers of operators of either the interior or the exterior type.

We shall show in the following that the first sum in (6.25b) yields the interior semiclassical Dirichlet (Neumann) spectrum, for the upper (lower) sign. Accordingly, the second sum gives the exterior semiclassical spectrum for Neumann or Dirichlet, repectively. This is in complete agreement with the finding of Section 4.2.2, that the double layer Dirichlet equation includes the Neumann solutions of the complementary domain.

6.3 Trace formula for hyperbolic billiards

In order to obtain the periodic orbit formula we can now follow the lines of the derivation of the trace formula for field free billiards [110, 123, 124, 126–128, 130–132]. Starting with the interior case, the trace in (6.25b) amounts to an n-dimensional integral of the form

$$
\begin{aligned}
\mathrm{tr}\big[(\mathsf{P}_{\mathrm{S}}^{\mathrm{int}} + \mathsf{P}_{\mathrm{L}}^{\mathrm{int}})^n\big] &= \int \frac{\mathrm{d}s_1 \ldots \mathrm{d}s_n}{b^n} \left(\mathrm{p}_{\mathrm{S}}^{\mathrm{int}} + \mathrm{p}_{\mathrm{L}}^{\mathrm{int}}\right)(s_2, s_1) \cdots \left(\mathrm{p}_{\mathrm{S}}^{\mathrm{int}} + \mathrm{p}_{\mathrm{L}}^{\mathrm{int}}\right)(s_1, s_n) \\
= \frac{1}{(2\pi\mathrm{i})^{n/2}} &\int \frac{\mathrm{d}s_1 \ldots \mathrm{d}s_n}{b^n} \, \exp\Big(\mathrm{i} \sum_{j=1}^{n} (\widetilde{\chi}(s_{j+1}) - \widetilde{\chi}(s_j))\Big) \qquad (6.26) \\
&\times \prod_{j=1}^{n} \Bigg[\frac{-(\hat{\mathbf{v}}_{\mathrm{S}}^0 \hat{\mathbf{n}}_0)_j \, \Theta\big(-(\hat{\mathbf{v}}_{\mathrm{S}}^0 \hat{\mathbf{n}}_0)_j\big)}{\big(\sin(\alpha_j)\cos(\alpha_j)\big)^{\frac{1}{2}}} \exp\Big(2\pi\mathrm{i}\nu \mathrm{a}_{\mathrm{S}}(s_{j+1}; s_j)\Big) \\
&\qquad + \frac{-(\hat{\mathbf{v}}_{\mathrm{L}}^0 \hat{\mathbf{n}}_0)_j \, \Theta\big(-(\hat{\mathbf{v}}_{\mathrm{L}}^0 \hat{\mathbf{n}}_0)_j\big)}{\big(\sin(\alpha_j)\cos(\alpha_j)\big)^{\frac{1}{2}}} \exp\Big(2\pi\mathrm{i}\nu \mathrm{a}_{\mathrm{L}}(s_{j+1}; s_j) - \mathrm{i}\frac{\pi}{2}\Big) \Bigg] .
\end{aligned}
$$

Here, the abbreviation $(\hat{\mathbf{v}}^0 \hat{\mathbf{n}}_0)_j := \hat{\mathbf{v}}^0(\mathbf{r}(s_{j+1}); \mathbf{r}(s_j)) \, \hat{\mathbf{n}}(\mathbf{r}(s_j))$ was used, together with (6.28), and the convention $s_0 \equiv s_n$. Note, that the gauge dependent factor (involving the $\widetilde{\chi}(s_j)$) vanishes identically, as a consequence of the cyclic permutability of the integration variables. This renders the trace (6.26) a gauge invariant quantity. It will now be evaluated to leading semiclassical order, by the stationary phase approximation (A.3).

6.3.1 The saddle point conditions

For each of the 2^n integrands in (6.26) the condition of a stationary phase leads to n saddle point equations

$$
\frac{\mathrm{d}}{\mathrm{d}s_j} \Big[2\pi\nu \mathrm{a}_{\eta_j}(s_j; s_{j-1}) + 2\pi\nu \mathrm{a}_{\eta_{j+1}}(s_{j+1}; s_j) \Big] \overset{!}{=} 0 \, , \quad j \in \{1, \ldots, n\} \, . \qquad (6.27)
$$

Here, the indices $\eta_j \in \{\mathrm{S}, \mathrm{L}\}$ account for the 2^n different sequences of short and long arc operators under the trace. We shall treat all these equations simultaneously, noting for any solution $\underline{s}$ of (6.27) not only the configuration of saddle points, but also the corresponding sequence of types of arcs, $\underline{s} = ((s_1, \eta_1), .., (s_n, \eta_n))$.

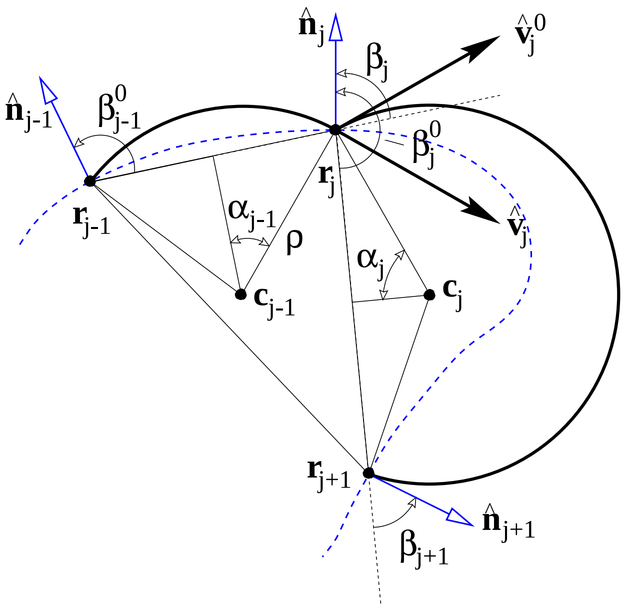

Figure 6.2: The angles entering the jth saddle point condition. (The dashed line indicates the boundary.)

$\hat{\mathbf{n}}_j\,\hat{\mathbf{v}}^0_{\mathrm{S}\,j} = +\cos(\beta^0_j - \alpha_j)$	$\hat{\mathbf{t}}_j\,\hat{\mathbf{v}}^0_{\mathrm{S}\,j} = -\sin(\beta^0_j - \alpha_j)$
$\hat{\mathbf{n}}_j\,\hat{\mathbf{v}}^0_{\mathrm{L}\,j} = -\cos(\beta^0_j + \alpha_j)$	$\hat{\mathbf{t}}_j\,\hat{\mathbf{v}}^0_{\mathrm{L}\,j} = +\sin(\beta^0_j + \alpha_j)$
$\hat{\mathbf{n}}_j\,\hat{\mathbf{v}}_{\mathrm{S}\,j} = +\cos(\beta_j + \alpha_{j-1})$	$\hat{\mathbf{t}}_j\,\hat{\mathbf{v}}_{\mathrm{S}\,j} = -\sin(\beta_j + \alpha_{j-1})$
$\hat{\mathbf{n}}_j\,\hat{\mathbf{v}}_{\mathrm{L}\,j} = -\cos(\beta_j - \alpha_{j-1})$	$\hat{\mathbf{t}}_j\,\hat{\mathbf{v}}_{\mathrm{L}\,j} = +\sin(\beta_j - \alpha_{j-1})$

Table 6.1: Components of the incident and reflected velocities. For the geometrical interpretation, see Fig. 6.2.

In order to obtain a geometric interpretation of the saddle point conditions, we fix the positions $\mathbf{r}_j := \mathbf{r}(s_j)$, and extend the selection of the angles (6.5) and (6.6) to a sequence of n points.

$$\alpha_j := \arcsin\left(\frac{|\mathbf{r}_{j+1} - \mathbf{r}_j|}{2\rho}\right) \tag{6.28}$$

and

$$\beta^0_j := \sphericalangle(\hat{\mathbf{n}}_j; \mathbf{r}_{j+1} - \mathbf{r}_j) \qquad \beta_{j+1} := \sphericalangle(\hat{\mathbf{n}}_{j+1}; \mathbf{r}_{j+1} - \mathbf{r}_j)\ . \tag{6.29}$$

This definition implies

$$\begin{aligned}
\cos(\beta_j) &= \frac{(\mathbf{r}_j - \mathbf{r}_{j-1})\,\hat{\mathbf{n}}_j}{|\mathbf{r}_j - \mathbf{r}_{j-1}|} \qquad & \sin(\beta_j) &= \frac{(\mathbf{r}_j - \mathbf{r}_{j-1}) \times \hat{\mathbf{n}}_j}{|\mathbf{r}_j - \mathbf{r}_{j-1}|} \\
\cos(\beta_j^0) &= \frac{(\mathbf{r}_{j+1} - \mathbf{r}_j)\,\hat{\mathbf{n}}_j}{|\mathbf{r}_{j+1} - \mathbf{r}_j|} \qquad & \sin(\beta_j^0) &= \frac{(\mathbf{r}_{j+1} - \mathbf{r}_j) \times \hat{\mathbf{n}}_j}{|\mathbf{r}_{j+1} - \mathbf{r}_j|}\ ,
\end{aligned} \tag{6.30}$$

as well as

$$\cos(\beta_{j+1} - \beta_j^0) = \hat{\mathbf{n}}_j\,\hat{\mathbf{n}}_{j+1} \qquad \sin(\beta_{j+1} - \beta_j^0) = \hat{\mathbf{n}}_j \times \hat{\mathbf{n}}_{j+1}\ . \tag{6.31}$$

Again, α_j determines the angles of the incident and the reflected velocity vectors with respect to the direction given by $\mathbf{r}_{j+1} - \mathbf{r}_j$. It follows that the normal and tangential components of the velocity are given by the expressions in Table 6.1. They allow to state the derivative of the action with respect to the arc length s along the boundary (cf eq (3.1)) in a particularly convenient form:

$$\begin{aligned}
\frac{\mathrm{d}}{\mathrm{d}s_j}\mathrm{a_S}(s_j; s_{j-1}) &= \frac{1}{\pi}\left(2\sqrt{1-\left(\frac{\mathbf{r}_j - \mathbf{r}_{j-1}}{2\rho}\right)^2}\,\frac{(\mathbf{r}_j - \mathbf{r}_{j-1})\hat{\mathbf{t}}_j}{|\mathbf{r}_j - \mathbf{r}_{j-1}|2\rho} - \frac{\hat{\mathbf{t}}_j \times \mathbf{r}_{j-1}}{2\rho^2}\right) \\
&= \frac{1}{\pi\rho}\left(\cos(\alpha_{j-1})\frac{\hat{\mathbf{n}}_j \times (\mathbf{r}_j - \mathbf{r}_{j-1})}{|\mathbf{r}_j - \mathbf{r}_{j-1}|} + \frac{\mathbf{r}_{j-1}\,\hat{\mathbf{n}}_j}{2\rho}\right) \\
&= \frac{1}{\pi\rho}\left(-\cos(\alpha_{j-1})\sin(\beta_j) + \frac{\mathbf{r}_{j-1}\,\hat{\mathbf{n}}_j}{2\rho}\right)
\end{aligned} \tag{6.32}$$

Similarly, one finds

$$\frac{\mathrm{d}}{\mathrm{d}s_j}\mathrm{a_S}(s_{j+1}; s_j) = \frac{1}{\pi\rho}\left(+\cos(\alpha_j)\sin(\beta_j^0) - \frac{\mathbf{r}_{j+1}\,\hat{\mathbf{n}}_j}{2\rho}\right) \tag{6.33}$$

$$\frac{\mathrm{d}}{\mathrm{d}s_j}\mathrm{a_L}(s_j; s_{j-1}) = \frac{1}{\pi\rho}\left(+\cos(\alpha_{j-1})\sin(\beta_j) + \frac{\mathbf{r}_{j-1}\,\hat{\mathbf{n}}_j}{2\rho}\right) \tag{6.33a}$$

$$\frac{\mathrm{d}}{\mathrm{d}s_j}\mathrm{a_L}(s_{j+1}; s_j) = \frac{1}{\pi\rho}\left(-\cos(\alpha_j)\sin(\beta_j^0) - \frac{\mathbf{r}_{j+1}\,\hat{\mathbf{n}}_j}{2\rho}\right)\ . \tag{6.33b}$$

As a result, one obtains an explicit expression for the jth saddle point condition in terms of the vectors $\mathbf{r}_{j-1}, \mathbf{r}_j, \mathbf{r}_{j+1}$, and $\hat{\mathbf{n}}_j$. Naturally, the condition depends on the type of the two operators involved.

$$\frac{(\mathbf{r}_{j+1} - \mathbf{r}_{j-1})\,\hat{\mathbf{n}}_j}{2\rho} = \begin{cases}
-\sin(\beta_j)\cos(\alpha_{j-1}) + \sin(\beta_j^0)\cos(\alpha_j) & \text{if } (\eta_{j-1}, \eta_j) = (\mathrm{S}, \mathrm{S}) \\
-\sin(\beta_j)\cos(\alpha_{j-1}) - \sin(\beta_j^0)\cos(\alpha_j) & \text{if } (\eta_{j-1}, \eta_j) = (\mathrm{S}, \mathrm{L}) \\
+\sin(\beta_j)\cos(\alpha_{j-1}) + \sin(\beta_j^0)\cos(\alpha_j) & \text{if } (\eta_{j-1}, \eta_j) = (\mathrm{L}, \mathrm{S}) \\
+\sin(\beta_j)\cos(\alpha_{j-1}) - \sin(\beta_j^0)\cos(\alpha_j) & \text{if } (\eta_{j-1}, \eta_j) = (\mathrm{L}, \mathrm{L}).
\end{cases} \tag{6.34}$$

Note that the left hand side of this equation can be written in terms of the angles appearing on the right side, after simply adding and subtracting the expression $(\mathbf{r}_j\,\hat{\mathbf{n}}_j)/(2\rho)$.

$$\frac{(\mathbf{r}_{j+1} - \mathbf{r}_j)\,\hat{\mathbf{n}}_j}{2\rho} + \frac{(\mathbf{r}_j - \mathbf{r}_{j-1})\,\hat{\mathbf{n}}_j}{2\rho} = \cos(\beta_j^0)\sin(\alpha_j) + \cos(\beta_j)\sin(\alpha_{j-1}) \tag{6.35}$$

Combining the last two equations, the saddle point condition assumes a form,

$$\begin{aligned}
\sin(\beta_j + \alpha_{j-1}) &= \sin(\beta_j^0 - \alpha_j) && \text{if } (\eta_{j-1}, \eta_j) = (\mathrm{S}, \mathrm{S}) \\
\sin(\beta_j + \alpha_{j-1}) &= -\sin(\beta_j^0 + \alpha_j) && \text{if } (\eta_{j-1}, \eta_j) = (\mathrm{S}, \mathrm{L}) \\
\sin(\beta_j - \alpha_{j-1}) &= -\sin(\beta_j^0 - \alpha_j) && \text{if } (\eta_{j-1}, \eta_j) = (\mathrm{L}, \mathrm{S}) \\
\sin(\beta_j - \alpha_{j-1}) &= \sin(\beta_j^0 + \alpha_j) && \text{if } (\eta_{j-1}, \eta_j) = (\mathrm{L}, \mathrm{L}) ,
\end{aligned} \tag{6.36}$$

which should be compared to the expressions in Table 6.1 for the components of the classical velocities. One observes that the equations (6.36) simply amount to the condition

$$\hat{\mathbf{t}}_j \, \hat{\mathbf{v}}_{\eta_j \, j} = \hat{\mathbf{t}}_j \, \hat{\mathbf{v}}^0_{\eta_j \, j} , \tag{6.37}$$

for $j = 1, \ldots n$, and any $\eta_j \in \{\mathrm{S}, \mathrm{L}\}$. It means that the tangential component of the classical velocities which correspond to the saddle point configuration $\underline{s}$ are continuous in the point of reflection. Since the modulus of the velocity is a constant of the motion, the trajectory is either continuous in this point, or the normal component changes its sign. In the first case the trajectory penetrates the boundary, which we call an unphysical solution. In the second case, the trajectory corresponding to the saddle point configuration obeys the law of *specular reflection* in $\mathbf{r}_j$.

From the fact that (6.37) must be satisfied simultaneously at the n points $\mathbf{r}_j$, it follows that any saddle point configuration corresponds to a closed, periodic orbit. However, by no means is this orbit necessarily a physically allowed classical trajectory. Figure 6.3 sketches the two different types of saddle point configurations which appear in magnetic billiards. Here, we choose $n = 5$, hence the saddle points correspond to periodic orbits of period 5. Clearly, both of them are unphysical trajectories. The one on the top features a specular reflection at $\mathbf{r}_2$. Then, the boundary is penetrated at $\mathbf{r}_3$, giving rise to a full cyclotron loop. After one more reflection – this time from the exterior – at $\mathbf{r}_4 = \mathbf{r}_2$, the trajectory arrives at its initial point. It performs one more cyclotron orbit, without even displaying a boundary point at $\mathbf{r}_2$. This saddle point is a legitimate solution to (6.37), belonging to a dense and two-dimensional set of stationary points (since the boundary points $\mathbf{r}_1$ and $\mathbf{r}_2$ may be shifted independently without changing the picture.) However, it has no relation to a physical periodic orbit whatsoever.

The saddle point shown on the bottom part of Fig. 6.3, on the other hand, does exhibit the boundary points of a physical periodic orbit (with period 4.) Nonetheless, the depicted trajectory is unphysical, since it leaves the interior domain, performing a cyclotron loop between the third and forth boundary points. Obviously, there is an infinite number of these unphysical saddle points attached to any proper, physical periodic orbit. They merely dress the original orbit with additional cyclotron loops. It might be expected that these unphysical contributions can be re-summed, leaving behind only the contributions of physical periodic orbits of the interior and exterior problem. However, this is a virtually impossible task, due to its combinatorial nature in conjunction with a number of ambiguities. A saddle point configuration may, for example, incorporate an interior and and exterior periodic orbit at the same time, leaving the question undetermined whether to assign the contribution to the interior or to the exterior problem.

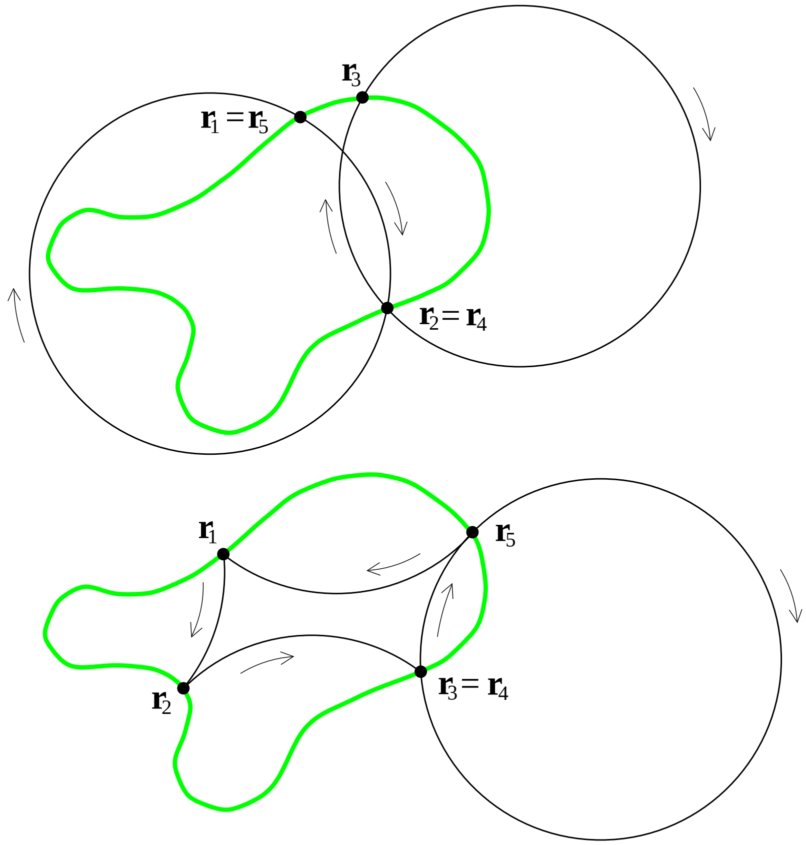
$\mathbf{r}_1 = \mathbf{r}_5$
$\mathbf{r}_3$
$\mathbf{r}_2 = \mathbf{r}_4$
$\mathbf{r}_1$
$\mathbf{r}_5$
$\mathbf{r}_2$
$\mathbf{r}_3 = \mathbf{r}_4$

Figure 6.3: Typical saddle point configurations appearing in the semiclassical evaluation of the trace (6.26). Both correspond to unphysical trajectories. The upper configuration has no relation to an orbit of the classical problem, while the lower one corresponds to a physical trajectory which is dressed by an additional cyclotron loop.

These problems are resolved immediately by the above splitting of the operator in interior and exterior types. Here, it is the Heaviside functions introduced by the splitting which guarantee that only those saddle points contribute for which the corresponding classical trajectory is directed into the correct domain at *each* point of reflection. As a consequence, the unphysical solutions discussed above are *erased* from the sum. The remaining saddle points will be denoted by $\gamma_{\rm int}^{(n)}$ and $\gamma_{\rm ext}^{(n)}$, respectively. They correspond to the periodic orbits of period n, found in the classical interior and exterior billiard problem.[3]

6.3.2 The prefactors

The next step is to transform the prefactors in the trace integral (6.26) in a suitable way. Eventually they should combine with the determinant of the matrix of action derivatives which will be introduced by the stationary phase approximation (A.3). The resulting expression should then be given in terms of the physical properties of the attributed periodic orbit $\gamma^{(n)}$.

We start with the evaluation of the mixed derivatives of the actions in terms of the angles (6.28), (6.29) characterising the jth part of the trajectory. If the arc is of the short type one obtains the formula

$$\begin{aligned}\frac{\mathrm{d}^2}{\mathrm{d}s_j\mathrm{d}s_{j+1}}\,\mathrm{a_S}(s_{j+1},s_j) &= \frac{1}{\pi\rho}\frac{\mathrm{d}}{\mathrm{d}s_{j+1}}\left(\cos(\alpha_j)\sin(\beta_j^0)-\frac{\mathbf{r}_{j+1}\,\hat{\mathbf{n}}_j}{2\rho}\right)\\ &= \frac{1}{2\pi\rho^2}\Big(\tan(\alpha_j)\sin(\beta_{j+1})\sin(\beta_j^0)\\ &\qquad -\cot(\alpha_j)\cos(\beta_{j+1})\cos(\beta_j^0)+\sin(\beta_{j+1}-\beta_j^0)\Big)\\ &= \frac{-1}{2\pi\rho^2}\,\frac{\cos(\beta_j^0-\alpha_j)\cos(\beta_{j+1}+\alpha_j)}{\sin(\alpha_j)\cos(\alpha_j)}\\ &= \frac{-1}{2\pi\rho^2}\,\frac{(\hat{\mathbf{v}}^0_{\mathrm{S}\,j}\hat{\mathbf{n}}_j)(\hat{\mathbf{v}}_{\mathrm{S}\,j+1}\hat{\mathbf{n}}_{j+1})}{\sin(\alpha_j)\cos(\alpha_j)}\;. \end{aligned} \tag{6.38}$$

Here, the expressions given in (6.33) and Tab. 6.1 were employed, as well as the formulas

$$\begin{aligned}\frac{\mathrm{d}}{\mathrm{d}s_{j+1}}\cos(\alpha_j) &= -\sin(\alpha_j)\,\frac{\mathrm{d}}{\mathrm{d}s_{j+1}}\arcsin\left(\frac{|\mathbf{r}_{j+1}-\mathbf{r}_j|}{2\rho}\right)\\ &= \frac{-1}{2\rho}\,\frac{\sin(\alpha_j)}{\cos(\alpha_j)}\,\frac{(\mathbf{r}_{j+1}-\mathbf{r}_j)\,\hat{\mathbf{t}}_{j+1}}{|\mathbf{r}_{j+1}-\mathbf{r}_j|}\\ &= \frac{1}{2\rho}\tan(\alpha_j)\sin(\beta_{j+1}) \end{aligned} \tag{6.39}$$

and

$$\begin{aligned}\frac{\mathrm{d}}{\mathrm{d}s_{j+1}}\sin(\beta_j^0) &= \frac{\mathrm{d}}{\mathrm{d}s_{j+1}}\left[\frac{(\mathbf{r}_{j+1}-\mathbf{r}_j)\times\hat{\mathbf{n}}_j}{|\mathbf{r}_{j+1}-\mathbf{r}_j|}\right]\\ &= \frac{\hat{\mathbf{t}}_{j+1}\times\hat{\mathbf{n}}_j}{|\mathbf{r}_{j+1}-\mathbf{r}_j|}-\frac{(\mathbf{r}_{j+1}-\mathbf{r}_j)\times\hat{\mathbf{n}}_j}{|\mathbf{r}_{j+1}-\mathbf{r}_j|}\,\frac{(\mathbf{r}_{j+1}-\mathbf{r}_j)\,\hat{\mathbf{t}}_{j+1}}{(\mathbf{r}_{j+1}-\mathbf{r}_j)^2}\\ &= \frac{-1}{2\rho}\,\frac{\cos(\beta_{j+1})\cos(\beta_j^0)}{\sin(\alpha_j)}\;. \end{aligned} \tag{6.40}$$

Hence, the mixed derivative (6.38) is essentially determined by the normal components of the velocities at the initial and the final point of the corresponding arc. Note that this expression is manifestly *positive*, if the arc is part of a physical trajectory, meaning that it lies either in the interior or in the exterior at both points (see also Fig. 6.2).

If the jth part of the action corresponds to a long arc, one obtains in a similar fashion

$$\begin{aligned}\frac{\mathrm{d}^2}{\mathrm{d}s_j\mathrm{d}s_{j+1}}\,\mathrm{a_L}(s_{j+1},s_j) &= \frac{1}{2\pi\rho^2}\,\frac{\cos(\beta_j^0+\alpha_j)\cos(\beta_{j+1}-\alpha_j)}{\sin(\alpha_j)\cos(\alpha_j)}\\ &= \frac{1}{2\pi\rho^2}\,\frac{(\hat{\mathbf{v}}^0_{\mathrm{L}\,j}\hat{\mathbf{n}}_j)(\hat{\mathbf{v}}_{\mathrm{L}\,j+1}\hat{\mathbf{n}}_{j+1})}{\sin(\alpha_j)\cos(\alpha_j)}\;. \end{aligned} \tag{6.41}$$

The form of this formula is analogous to (6.38), except for the difference in sign. It follows that equation (6.41) is manifestly *negative* if the angles α_j, β_j^0, and β_{j+1}

describe a segment of a physical trajectory — again due to the change in the orientation of the velocity vector.

The mixed derivatives (6.38) and (6.41) allow to transform the product under the trace integral (6.26) into a symmetrised expression. For a given saddle point $\gamma^{(n)}$, we denote the geometric part of the total action by

$$\mathrm{A}(\gamma^{(n)}) := \sum_{j=1}^{n} \mathrm{a}_{\eta_j}(s_{j+1}, s_j) \ , \tag{6.42}$$

cf (6.1), (6.2). In addition, the number of *long* arcs appearing in $\gamma^{(n)}$ will be called ℓ_γ. The product under trace integral (6.26) can now be stated in terms of $\mathrm{A}(\gamma^{(n)})$ and ℓ_γ. For the interior operators, it assumes the form

$$\mathrm{e}^{2\pi\mathrm{i}\nu\mathrm{A}(\gamma^{(n)}_{\mathrm{int}})}\ \mathrm{e}^{-\mathrm{i}\frac{\pi}{2}\ell_\gamma} \prod_{j=1}^{n} \frac{-(\hat{\mathbf{v}}^0_{\eta_j}\hat{\mathbf{n}}_0)_j}{\big(\sin(\alpha_j)\cos(\alpha_j)\big)^{\frac{1}{2}}} \tag{6.43}$$

$$= \frac{\prod_{j=1}^{n}\Big((\hat{\mathbf{v}}^0_{\{\eta_j\,j\}}\hat{\mathbf{n}}_j)(\hat{\mathbf{v}}^0_{\{\eta_{j+1}\,j+1\}}\hat{\mathbf{n}}_{j+1})\Big)^{\frac{1}{2}}}{\prod_{j=1}^{n}(\sin(\alpha_j)\cos(\alpha_j))^{\frac{1}{2}}}\ \mathrm{e}^{-\mathrm{i}\frac{\pi}{2}\ell_\gamma}\ \mathrm{e}^{2\pi\mathrm{i}\nu\mathrm{A}(\gamma^{(n)}_{\mathrm{int}})} \tag{6.43a}$$

$$= \frac{\prod_{j=1}^{n}\Big(-(\hat{\mathbf{v}}^0_{\{\eta_j\,j\}}\hat{\mathbf{n}}_j)(\hat{\mathbf{v}}_{\{\eta_{j+1}\,j+1\}}\hat{\mathbf{n}}_{j+1})\Big)^{\frac{1}{2}}}{\prod_{j=1}^{n}(\sin(\alpha_j)\cos(\alpha_j))^{\frac{1}{2}}}\ \mathrm{e}^{-\mathrm{i}\frac{\pi}{2}\ell_\gamma}\ \mathrm{e}^{2\pi\mathrm{i}\nu\mathrm{A}(\gamma^{(n)}_{\mathrm{int}})} \tag{6.43b}$$

$$= \prod_{j=1}^{n}\left(2\pi\rho^2\frac{\mathrm{d}^2\mathrm{a}_{\eta_j}(s_{j+1}, s_j)}{\mathrm{d}s_j\mathrm{d}s_{j+1}}\right)^{\frac{1}{2}}\ \mathrm{e}^{\mathrm{i}\frac{\pi}{2}(\ell_\gamma-\ell_\gamma)}\ \mathrm{e}^{2\pi\mathrm{i}\nu\mathrm{A}(\gamma^{(n)}_{\mathrm{int}})} \tag{6.43c}$$

$$= (2\pi)^{\frac{n}{2}} \prod_{j=1}^{n}\left|\rho^2\frac{\mathrm{d}^2\mathrm{A}(\gamma^{(n)}_{\mathrm{int}})}{\mathrm{d}s_j\mathrm{d}s_{j+1}}\right|^{\frac{1}{2}}\ \mathrm{e}^{-\mathrm{i}\frac{\pi}{2}\ell_\gamma}\ \mathrm{e}^{2\pi\mathrm{i}\nu\mathrm{A}(\gamma^{(n)}_{\mathrm{int}})}\ . \tag{6.43d}$$

Here, we used several times the fact that the saddle point configurations described by $\gamma^{(n)}_{\mathrm{int}}$ correspond to physical, interior periodic orbit with n reflections. First, we noted the positivity of the factor $-(\hat{\mathbf{v}}^0_{\eta_j}\hat{\mathbf{n}}_0)_j$, to write it as a product of square roots (and shifted one index by one). Second, the reflection condition

$$(\hat{\mathbf{v}}^0_{\{\eta_j\,j\}}\hat{\mathbf{n}}_j) = -(\hat{\mathbf{v}}_{\{\eta_j\,j\}}\hat{\mathbf{n}}_j) \tag{6.44}$$

was employed to get from (6.43a) to (6.43b). As a result, the prefactors are symmetric in s_j and s_{j+1}, which allows to state them in terms of the mixed derivatives of the classical action. Finally, given the sign of each factor in (6.43d), the sign of the product can be taken out. It is $(-)^{\ell_\gamma}$, due to the ℓ_γ long arcs in $\gamma^{(n)}$.

Upon evaluating the trace of the exterior operators, one is led to the *same* expression (6.43d), with $\gamma^{(n)}_{\mathrm{int}}$ replaced by $\gamma^{(n)}_{\mathrm{ext}}$. This is because the additional sign in the definition (6.22) of the exterior operators cancels the change in the orientation of the normals relative to the velocity vectors.

6.3.3 Performing the trace

Now, once we succeeded to write the prefactors as mixed derivatives of the action in (6.43d) we can follow the standard procedure to derive the semiclassical trace formula.

ρ	cyclotron radius ($\rho > 0$)	(2.36)
α	relative distance of the initial and the final point ($0 \leq \alpha \leq \frac{\pi}{2}$)	(6.5)
β^0	relative direction of normal at the initial point ($0 \leq \beta^0 < 2\pi$)	(6.6)
β	relative direction of normal at final point ($0 \leq \beta < 2\pi$)	(6.6)
$\mathrm{a_S}$, $\mathrm{a_L}$	geometric part of the action of a short (long) arc	(6.1)
γ, $\gamma^{(n)}$	physical periodic orbit (with n reflections)	page 80
$\mathrm{A}(\gamma)$	geometric part of the action of the periodic orbit γ	(6.42)
n_γ (r_γ)	number of reflections (repetitions) in γ	page 83
μ_γ	Maslov index (number of conjugate points in γ)	page 83
$\mathrm{M}(\gamma)$	stability matrix of γ	(6.46)

Table 6.2: Important geometric quantities

We apply the stationary phase approximation to the n-dimensional trace integral. The contributing saddle points will be assumed to be isolated. This amounts to the assumption that the corresponding classical billiard dynamics is *hyperbolic* [4]. The contrary case of an integrable system will be treated afterwards.

Combining eqs (6.26) and (6.43), together with (A.3), yields

$$\begin{aligned}
\mathrm{tr}\big[\big(\mathsf{P}_\mathrm{S}^\mathrm{int} + \mathsf{P}_\mathrm{L}^\mathrm{int}\big)^n\big] &= \int \prod_{j=1}^{n} \big[\big(\mathrm{p}_\mathrm{S}^\mathrm{int} + \mathrm{p}_\mathrm{L}^\mathrm{int}\big)(s_{j+1}, s_j)\big] \, \frac{\mathrm{d}s_1 \ldots \mathrm{d}s_n}{b^n} \\
&= \sum_{\gamma \in \left\{\gamma_\mathrm{int}^{(n)}\right\}} \frac{n}{r_\gamma} \, \frac{1}{\rho^n} \, \frac{\prod_{j=1}^{n} \left| \rho^2 \frac{\partial^2 \mathrm{A}(\gamma)}{\partial s_j \partial s_{j+1}} \right|^{\frac{1}{2}}}{\left| \det \left(\frac{\partial^2 \mathrm{A}(\gamma)}{\partial s_k \partial s_l} \right)_{k,l} \right|^{\frac{1}{2}}} \, \mathrm{e}^{2\pi \mathrm{i} \nu \mathrm{A}(\gamma)} \, \mathrm{e}^{-\mathrm{i}\frac{\pi}{2}(\ell_\gamma + \nu_\gamma)} \\
&= \sum_{\gamma \in \left\{\gamma_\mathrm{int}^{(n)}\right\}} \frac{n}{r_\gamma} \, \frac{1}{|\,\mathrm{tr}(\mathrm{M}(\gamma) - 2|^{\frac{1}{2}}} \, \mathrm{e}^{2\pi \mathrm{i} \nu \mathrm{A}(\gamma)} \, \mathrm{e}^{-\mathrm{i}\frac{\pi}{2}\mu_\gamma} \, . \qquad (6.45)
\end{aligned}$$

The factor n/r_γ is appears because the sum is taken over all n-periodic orbits of the interior billiard, rather than over all contributing saddle points. Each n-periodic orbit (with repetition number r_γ) corresponds to n/r_γ distinct saddle points $\underline{s}$, which are related by a cyclic shift of their components. For the last equality in (6.45), we used once more the fact that $\gamma_\mathrm{int}^{(n)}$ is a classical periodic orbit of a billiard problem. This implies a general relation between the derivatives of the generating function of the billiard map $\mathrm{A}(\gamma^{(n)})$ and the stability matrix $\mathrm{M}(\gamma^{(n)})$ [127],

$$\det \left[\left(\frac{\partial^2 \mathrm{A}(\gamma^{(n)})}{\partial s_k \partial s_l} \right)_{k,l} \right] = (-)^n \big[\,\mathrm{tr}\,\mathrm{M}(\gamma^{(n)}) - 2\big] \prod_{j=1}^{n} \frac{\partial^2 \mathrm{A}(\gamma^{(n)})}{\partial s_j \partial s_{j-1}} \, . \qquad (6.46)$$

Its modulus was taken to arrive at (6.45). The integer $\mu_\gamma := \ell_\gamma + \nu_\gamma$ denotes the total number of conjugate points. Here, ν_γ is given by the number of negative eigenvalues of the determinant in the dominator. It counts those conjugate points along the trajectory, which are due to the focusing and defocusing effect of the boundary. The remaining, trivial conjugate points, which show up at each long arc (after an angle of π), are taken into account by ℓ_γ.

For later reference, let us mention that the dual partner orbit of $\gamma^{(n)}$, denoted as $\overline{\gamma}^{(n)}$, has

$$\mu_{\overline{\gamma}} = 2n - \mu_\gamma \tag{6.47}$$

conjugate points (if it exists at all). As discussed in Section 3.2.3, the dual orbits consists of the arcs complementary to those of $\gamma^{(n)}$, and has opposite orientation. From (6.2), we find $\mathrm{A}(\overline{\gamma}^{(n)}) = n - \mathrm{A}(\gamma^{(n)})$, and it follows that $\nu_{\overline{\gamma}} = n - \nu_\gamma$, since every element of the matrix of second derivatives in (6.45) is multiplied by (-1). By definition, we have $\ell_{\overline{\gamma}} = n - \ell_\gamma$, what leads to equation (6.47). Note also that the stabilities of dual periodic orbits are equal, $\operatorname{tr}\mathrm{M}(\overline{\gamma}) = \operatorname{tr}\mathrm{M}(\gamma)$, which follows from equation (6.46).

The trace formula for the spectral counting function

Inserting the expression for the trace (6.45) into (6.25b) we obtain the first part of the fluctuating number counting function $\mathrm{N}_{\mathrm{osc}}^{\mathrm{skip}} = \mathrm{N}_{\mathrm{osc}}^{\mathrm{skip(int)}} + \mathrm{N}_{\mathrm{osc}}^{\mathrm{skip(ext)}}$:

$$\begin{aligned}
\mathrm{N}_{\mathrm{osc}}^{\mathrm{skip(int)}} &:= \frac{1}{\pi}\,\mathrm{Im}\sum_{n=1}^{\infty}\frac{(\mp)^n}{n}\,\operatorname{tr}\big[\big(\mathsf{P}_{\mathrm{S}}^{\mathrm{int}} + \mathsf{P}_{\mathrm{L}}^{\mathrm{int}}\big)^n\big] && (6.48)\\
&= \frac{1}{\pi}\,\mathrm{Im}\sum_{n=1}^{\infty}\sum_{\gamma\in\{\gamma_{\mathrm{int}}^{(n)}\}}\frac{(\mp)^n}{r_\gamma}\frac{1}{\big|\operatorname{tr}\mathrm{M}(\gamma)-2\big|^{\frac{1}{2}}}\,\mathrm{e}^{2\pi\mathrm{i}\nu\mathrm{A}(\gamma)-\mathrm{i}\frac{\pi}{2}\mu_\gamma}\\
&= \frac{1}{\pi}\sum_{\gamma\in\{\gamma_{\mathrm{int}}\}}\frac{(\mp)^{n_\gamma}}{r_\gamma\,\big|\operatorname{tr}\mathrm{M}(\gamma)-2\big|^{\frac{1}{2}}}\,\sin\Big(2\pi\nu\mathrm{A}(\gamma)-\frac{\pi}{2}\mu_\gamma\Big) && (6.48a)
\end{aligned}$$

It is naturally associated with the *interior* problem, since the sum finally includes all periodic orbits $\{\gamma_{\mathrm{int}}\}$ of the interior billiard problem (with n_γ the number of reflections). Like in (6.18), (6.25b) the upper and lower signs in eq (6.48) refer to the interior and exterior choice, respectively, of the original spectral problem.

The second part of the number counting function (6.25b) includes the trace over powers of the exterior operators. In complete analogy to the treatment above, one obtains a periodic orbit sum like equation (6.45). As the only difference, the sum is over all the periodic orbits γ_{ext} of the *exterior* classical billiard map. Hence, the exterior part of the fluctuating number counting function is given by a periodic orbit sum,

$$\begin{aligned}
\mathrm{N}_{\mathrm{osc}}^{\mathrm{skip(ext)}} &:= \frac{1}{\pi}\,\mathrm{Im}\sum_{n=1}^{\infty}\frac{(\pm)^n}{n}\,\operatorname{tr}\big[\big(\mathsf{P}_{\mathrm{S}}^{\mathrm{ext}} + \mathsf{P}_{\mathrm{L}}^{\mathrm{ext}}\big)^n\big] && (6.49)\\
&= \frac{1}{\pi}\sum_{\gamma\in\{\gamma_{\mathrm{ext}}\}}\frac{(\pm)^{n_\gamma}}{r_\gamma\,\big|\operatorname{tr}\mathrm{M}(\gamma)-2\big|^{\frac{1}{2}}}\,\sin\Big(2\pi\nu\mathrm{A}(\gamma)-\frac{\pi}{2}\mu_\gamma\Big) && (6.49a)
\end{aligned}$$

which differs formally from (6.48a) only by a sign $(-)^{n_\gamma}$ in each periodic orbit contribution. This is readily explained. From the theory of non-magnetic quantum billiards, it is well known [88], that the trace formulae for Dirichlet and Neumann boundary conditions differ only by a phase: At Dirichlet boundary conditions, there exists a phase shift of π for each reflection along the periodic orbit, which is absent in the Neumann case. The same is true for magnetic quantum billiards, as evident from equations (6.48a) and (6.49a). Those were obtained from the Dirichlet double-layer equation, which was shown to be polluted by the Neumann spectrum of the complementary domain, cf Sect. 4.2.2. Indeed, equations (6.48a) and (6.49a) exhibit a Dirichlet factor $(-)^{n_\gamma}$ for the periodic orbits in the original domain, while the trajectories in the complementary domain do not get an additional phase.

Hence, for either the interior or the exterior Dirichlet problem the fluctuating number function is given by

$$\mathrm{N}_{\mathrm{osc}}^{\mathrm{skip}}(\nu) = \frac{1}{\pi}\sum_{\gamma} \frac{1}{r_\gamma \left| \operatorname{tr}\mathrm{M}(\gamma) - 2\right|^{\frac{1}{2}}} \sin\Big(2\pi\nu\mathrm{A}(\gamma) - \pi n_\gamma - \frac{\pi}{2}\mu_\gamma\Big) \ , \tag{6.50}$$

where the sum is over all periodic orbits in the respective domain.

6.3.4 Geometric interpretation

Let us briefly discuss the geometric meaning of the scaled action of a trajectory. We start with the observation, that the actions of short and long arcs are given by *identical* expressions, once the parameter

$$\sigma_j := \frac{(\mathbf{r}_{j+1} - \mathbf{c}_j) \times (\mathbf{r}_{j+1} - \mathbf{r}_j)}{\rho\, |\mathbf{r}_{j+1} - \mathbf{r}_j|} = \begin{cases} -\cos(\alpha_j) & \text{if “short” arc} \\ +\cos(\alpha_j) & \text{if “long” arc,} \end{cases} \tag{6.51}$$

is introduced to describe the j-th arc. Unlike the angle α_j (6.28), it is not just a function of $\mathbf{r}_j$ and $\mathbf{r}_{j+1}$, but it contains information on the *type* of the arc, through its sign: σ_j is negative for short arcs, and positive for long ones. The geometric parts of the actions of short and long arcs, (6.1) and (6.2), now assume the common form

$$\mathrm{a}(\mathbf{r}_{j+1};\mathbf{r}_j) = \frac{1}{\pi}\left(\frac{\pi}{2} + \arcsin(\sigma_j) - \sigma_j\sqrt{1-\sigma_j^2} - \frac{\mathbf{r}_{j+1}\times\mathbf{r}_j}{2\rho^2}\right) \ , \tag{6.52}$$

which is a remarkable simplification.[*] It allows to show immediately that a periodic orbit γ (of period n) exhibits a geometric action (6.42)

$$\mathrm{A}(\gamma^{(n)}) = \sum_{j=1}^{n} \mathrm{a}(\mathbf{r}_{j+1},\mathbf{r}_j) = \frac{\rho\,\mathscr{L}_\gamma \pm \mathscr{A}_\gamma}{\rho^2\pi} \ , \tag{6.53}$$

which is given by the length of the trajectory,

$$\mathscr{L}_\gamma := \rho\sum_{j=1}^{n}(\pi + 2\arcsin(\sigma_j)) \tag{6.54}$$

$$= \rho\,\frac{\mathrm{d}}{\mathrm{d}\nu}\big[2\pi\nu\mathrm{A}(\gamma^{(n)})\big] \ , \tag{6.54a}$$

---

[*] The derivation of the trace formulas would have been considerably more complicated, had we introduced this parametrization earlier.

and the enclosed area,

$$\mathscr{A}_\gamma := \mathscr{A}_\gamma^{\text{poly}} \mp \sum_{j=1}^{n} \left(\frac{\pi}{2} + \arcsin(\sigma_j) + \sigma_j \sqrt{1 - \sigma_j^2} \right) \rho^2 \,. \tag{6.55}$$

Here, $\mathscr{A}_\gamma^{\text{poly}}$ is the area of the polygon defined by the points of reflection $\{\mathbf{r}_j\}$, and each of the summands in (6.55) is equal to the area enclosed by the j-th arc, and the cord connecting its initial and final points, cf eq (2.47). (Hence, overlapping parts of the enclosed area are counted according to their multiplicity.)

In Chapter 3, we mentioned the generating function $\mathscr{G}(s, s')$ for the skipping motion in magnetic billiards, cf eq (3.5). In Ref. [67] it was taken to depend on the area enclosed by the trajectory and the billiard *boundary*, along with the length of the trajectory. Since the billiard area $\mathscr{A}$ – like any constant – may be added to the generating function without changing the dynamics, we arrive at the same quantity (for periodic orbits). However, for given initial and final points the enclosed area depends on the type of the arc, ie, $\mathscr{G}$ is not uniquely specified by s and s' alone. Since additional information is required, it is not a generating function in its proper sense.

Density of skipping states

Equation (6.54a) follows, bearing in mind that ρ and σ_i are functions of ν, cf (2.40). It illustrates the fact that the excursion time of a trajectory is given by the derivative of its action with respect to energy. Using the proper scaled energy $\widetilde{E} = 2\nu$ (cf the discussion of (2.40)), we obtain the scaled time of flight τ_γ of the periodic orbit,

$$\tau_\gamma = \frac{\mathrm{d}}{\mathrm{d}(2\nu)} \left[2\pi\nu \mathrm{A}(\gamma^{(n)}) \right] = \sum_{j=1}^{n} \left(\frac{\pi}{2} + \arcsin(\sigma_j) \right) \,. \tag{6.56}$$

The formula for the fluctuating part of the density of skipping states (3.15) follows by taking the derivative of the number counting function (6.50) with respect to ν,

$$d_{\text{osc}}^{\text{skip}}(\nu) = \frac{2}{\pi} \sum_\gamma \frac{\tau_\gamma}{r_\gamma \left| \operatorname{tr} \mathrm{M}(\gamma) - 2 \right|^{\frac{1}{2}}} \cos\left(2\pi\nu \mathrm{A}(\gamma) - \pi n_\gamma - \frac{\pi}{2} \mu_\gamma \right) \,. \tag{6.57}$$

It must be emphasized, however, that the applicability of this expression is rather restricted. It is valid only for the interior billiard at fields which are weak enough that no cyclotron orbit fits into the domain. In the opposite case, the attempt to include the cyclotron contributions "by hand" yields unsatisfactory results [83]. (This is due to the fact that orbits which are almost detached from the boundary are no longer isolated; moreover, the semiclassically large parameter ν would enter with a different power in the integrable cyclotron part.) Since we are interested in strong field effects, equation (6.57) will not be used in the following.

Magnetization density

Another derivative of the action occurs in the definition of the scaled magnetization density (3.24) which was discussed in Sect. 3.4. We find that it is determined by the area $\mathscr{A}_\gamma$ enclosed by the trajectory (6.55),

$$\left(-b^2\frac{\mathrm{d}}{\mathrm{d}b^2}-\nu\frac{\mathrm{d}}{\mathrm{d}\nu}\right)\Big[2\pi\nu\mathrm{A}(\gamma)\Big]=\pm\frac{2}{b^2}\mathscr{A}_\gamma\;. \tag{6.58}$$

The semiclassical expression for the fluctuating part of the scaled magnetization density is obtained by applying (6.58) to the trace formula for $\mathrm{N}_{\mathrm{osc}}$, cf eq (3.24). Assuming that all periodic orbits are isolated and of the skipping type we find

$$\widetilde{\mathrm{m}}^{\mathrm{osc}}(\nu)=\pm 2\sum_\gamma\frac{\mathscr{A}_\gamma/(b^2\pi)}{r_\gamma\left|\,\mathrm{tr}\,\mathrm{M}(\gamma)-2\right|^{\frac{1}{2}}}\;\cos\Big(2\pi\nu\mathrm{A}(\gamma)-\pi n_\gamma-\frac{\pi}{2}\mu_\gamma\Big)\;. \tag{6.59}$$

Hence, compared to the density of skipping states (6.57), each periodic orbit contribution to the scaled magnetization density includes the enclosed area in units of $b^2\pi$, ie, the magnetic moment of the classical orbit, rather than the scaled time of flight. Again, the expression (6.59) is only applicable for the interior problem at weak fields. The corresponding, less intuitive semiclassical expression for the *conventional* magnetization at weak fields may be found in [81].

6.4 Trace formula for the integrable case

In the previous section, the classical billiard map was assumed to be hyperbolic. We now shift to the other extreme – systems with an integrable bounce map. In fact, only one type of magnetic billiard is known which exhibits integrable motion. It is the disk billiard, whose boundary is given by a circle of radius R.

6.4.1 The disk billiard

The periodic orbit formula for the density of states in the interior of the magnetic disk was derived recently by Blaschke *et al* [83]. These authors used the trace formula by Creagh and Littlejohn [133] to account for the continuous circular symmetry of the disk.

In the following, we derive the trace formula starting from the boundary integral equation, ie, from first principles. This demonstrates how the integrable case is treated in the framework of the boundary map operators and yields an explicit formula in a straightforward manner. Moreover, the exterior case is easily included in our treatment.

Fortunately, many results of the last section apply. In particular, the factorization of the spectral function (6.25) does not depend on the type of motion, so we can start directly with the equations (6.48) and (6.49) for the interior and the exterior counting functions. However, the trace of powers of the map operators cannot be evaluated like in the hyperbolic case, since the periodic orbits are not isolated but appear in continuous families [122].

The classical motion is governed by one parameter. It is the ratio

$$\Gamma_{\mathrm{d}}:=\frac{R}{\rho} \tag{6.60}$$

between the radius of the disk and the cyclotron radius. For *weak* fields $\Gamma_{\mathrm{d}}<1$, any two points on the boundary can be connected in the interior only by short arcs, and in the exterior (only) by long ones. The field is *strong*, $\Gamma_{\rm d} > 1$, if complete cyclotron orbits fit into the interior. The skipping motion then displays both types of arcs in the interior and exterior, and two points on the boundary are then no longer necessarily connected by an arc.

It is advantageous to use the polar angles $\varphi = s/R$ as the coordinates for explicit formulas. To be definite, we shall choose the angles always such, that adjacent points differ at most by π. Simple geometry tells that the positive angle α,[*] as defined in (6.5), obeys

$$\sin(\alpha) = \Gamma_{\rm d} \sin\left(\frac{|\varphi - \varphi_0|}{2}\right) . \tag{6.61}$$

Moreover, we note the relation

$$\frac{1}{2}\Gamma_{\rm d}^2 \, |\sin(\varphi - \varphi_0)| \;\gtrless\; \sin(\alpha)\cos(\alpha) \quad \text{for} \quad \Gamma_{\rm d} \;\gtrless\; 1 \tag{6.62}$$

which is needed in proving almost all the equations below. Finally, geometry tells that the normal components of the reflected velocities are given by

$$-\hat{\mathbf{v}}^0_{\binom{\rm S}{\rm L}} \, \hat{\mathbf{n}}_0 = \frac{1}{\Gamma_{\rm d}} \left(\frac{1}{2}\Gamma_{\rm d}^2 \sin(\varphi - \varphi_0) \pm \sin(\alpha)\cos(\alpha) \right) , \tag{6.63}$$

for the short arc and long arc, respectively. They allow to state explicitely the prefactors of the map operators (6.20) and (6.21), in terms of the angle increment $\varphi - \varphi_0$.

6.4.2 Operators for the integrable map

Upon choosing the symmetric gauge, $\chi = 0$, one finds that the actions of short and long arcs are merely functions of the difference of the initial and the final coordinate,[†]

$$\mathrm{a_S}(\varphi - \varphi_0) := \mathrm{a_S}(R\varphi; R\varphi_0) = \frac{1}{\pi} \left(\alpha + \sin(\alpha)\cos(\alpha) + \tfrac{1}{2}\Gamma_{\rm d}^2 \sin(\varphi - \varphi_0) \right) , \tag{6.64}$$

and likewise $\mathrm{a_L}(\varphi - \varphi_0) := \mathrm{a_L}(R\varphi; R\varphi_0) = 1 - \mathrm{a_S}(\varphi_0 - \varphi)$. This reflects the integrability of the classical motion.

For the special case of the disk billiard, the map operators can be related directly to the magnetic generalisation of the T operator [124] (cf Note 2 on page 92). Following [124], we define two operators, $\mathsf{T}_{\rm S}$ and $\mathsf{T}_{\rm L}$, entirely in terms of the actions of a short and long arc, $\eta \in \{\rm S, L\}$, respectively, with kernels

$$\mathrm{t}_\eta(\varphi; \varphi_0) := \frac{1}{(2\pi \mathrm{i})^{\frac{1}{2}}} \left(\frac{\mathrm{d}^2(2\pi\nu \mathrm{a}_\eta)}{\mathrm{d}\varphi \, \mathrm{d}\varphi_0}(\varphi - \varphi_0) \right)^{\frac{1}{2}} \mathrm{e}^{2\pi \mathrm{i}\nu \mathrm{a}_\eta} . \tag{6.65}$$

---

[*] For the sake of clarity we use α (6.5) rather than σ (6.51) in this section.

[†] At arbitrary gauge the actions depend on both coordinates individually, and the canonical momentum is not a constant of the motion.

Evaluating the mixed second derivatives of the actions, one finds that they may be stated in a form

$$\frac{\mathrm{d}^2 \mathrm{a_S}}{\mathrm{d}\varphi\,\mathrm{d}\varphi_0}(\varphi-\varphi_0) = \frac{1}{2\pi}\,\frac{(\sin(\alpha)\cos(\alpha)+\frac{1}{2}\Gamma_\mathrm{d}^2\sin(\varphi-\varphi_0))^2}{\sin(\alpha)\cos(\alpha)} \tag{6.66}$$

$$\frac{\mathrm{d}^2 \mathrm{a_L}}{\mathrm{d}\varphi\,\mathrm{d}\varphi_0}(\varphi-\varphi_0) = -\frac{1}{2\pi}\,\frac{(\sin(\alpha)\cos(\alpha)-\frac{1}{2}\Gamma_\mathrm{d}^2\sin(\varphi-\varphi_0))^2}{\sin(\alpha)\cos(\alpha)} \tag{6.67}$$

which allows the direct comparison with equation (6.63). It follows that the operators $\mathsf{P}_\mathrm{S}^\mathrm{int}$ and $\mathsf{P}_\mathrm{S}^\mathrm{ext}$ (cf eq (6.22)) are given essentially in terms of T_S.

$$\mathrm{p}_\mathrm{S}^\mathrm{int}(R\varphi, R\varphi_0) = \mathrm{t_S}\,(\varphi;\varphi_0)\;\frac{b}{R}\begin{cases}\Theta(\varphi-\varphi_0) & \text{if } \Gamma_\mathrm{d}>1\\ 1 & \text{if } \Gamma_\mathrm{d}<1\end{cases} \tag{6.68}$$

$$\mathrm{p}_\mathrm{S}^\mathrm{ext}(R\varphi, R\varphi_0) = \mathrm{t_S}\,(\varphi;\varphi_0)\;\frac{b}{R}\begin{cases}\Theta(\varphi_0-\varphi) & \text{if } \Gamma_\mathrm{d}>1\\ 0 & \text{if } \Gamma_\mathrm{d}<1\end{cases} \tag{6.69}$$

They vanish whenever there is no classically allowed trajectory connecting the initial and the final point in the considered domain. Similarly, the operators $\mathsf{P}_\mathrm{L}^\mathrm{int}$ and $\mathsf{P}_\mathrm{L}^\mathrm{ext}$ are given as restrictions of T_L.

$$\mathrm{p}_\mathrm{L}^\mathrm{int}(R\varphi, R\varphi_0) = -\mathrm{t_L}\,(\varphi;\varphi_0)\;\frac{b}{R}\begin{cases}\Theta(\varphi-\varphi_0) & \text{if } \Gamma_\mathrm{d}>1\\ 0 & \text{if } \Gamma_\mathrm{d}<1\end{cases} \tag{6.70}$$

$$\mathrm{p}_\mathrm{L}^\mathrm{ext}(R\varphi, R\varphi_0) = -\mathrm{t_L}\,(\varphi;\varphi_0)\;\frac{b}{R}\begin{cases}\Theta(\varphi_0-\varphi) & \text{if } \Gamma_\mathrm{d}>1\\ 1 & \text{if } \Gamma_\mathrm{d}<1\end{cases} \tag{6.71}$$

Here we assume $|\varphi-\varphi_0|\le\pi$, as throughout this section.

6.4.3 The explicit trace formula

To obtain a semiclassical expression for the number counting function, we start by calculating the kernel of the Nth power $(\mathsf{P}_\mathrm{S}^\mathrm{int}+\mathsf{P}_\mathrm{L}^\mathrm{int})^N$, at coinciding initial and final point s_0. It is given by a $(N-1)$-dimensional integral,

$$\left(\mathrm{p}_\mathrm{S}^\mathrm{int}+\mathrm{p}_\mathrm{L}^\mathrm{int}\right)^N(s_0,s_0) = \int\prod_{j=1}^{N}\left[(\mathrm{p}_\mathrm{S}^\mathrm{int}+\mathrm{p}_\mathrm{L}^\mathrm{int})(s_j,s_{j-1})\right]\frac{\mathrm{d}s_1\ldots\mathrm{d}s_{N-1}}{b^{N-1}} \tag{6.72}$$

with *fixed* $s_N\equiv s_0$. This integral may be evaluated by the stationary phase method. For the same reason as above (Sect. 6.3.1), only the saddle points contribute, which correspond to a physically allowed trajectory. However, they are now required to start and end at the point s_0. Each saddle point is characterized by the constant angular increment $\Delta\varphi\in\mathcal{P}^N$, the jth component given by

$$\varphi_j = \varphi_0 + j\,\Delta\varphi\,,\qquad j=0,\ldots,N-1\,. \tag{6.73}$$

For given N, there is a finite number of possible increments

$$\mathcal{P}_\mathrm{int}^N = \begin{cases}+2\pi\frac{M}{N}; & M=1,2,\ldots M_\mathrm{max} \quad \text{if } \Gamma_\mathrm{d}>1\\ \pm2\pi\frac{M}{N}; & M=1,2,\ldots M_\mathrm{max} \quad \text{if } \Gamma_\mathrm{d}<1.\end{cases} \tag{6.74}$$

Here, the second index M has the meaning of a winding number.[‡] It gives the number of times the trajectory encircles the origin. The maximum value is given by

$$M_{\max} = \begin{cases} [\arcsin(1/\Gamma_{\mathrm{d}})\, N/\pi] & \text{if } \Gamma_{\mathrm{d}} > 1 \\ [N/2] & \text{if } \Gamma_{\mathrm{d}} < 1, \end{cases} \tag{6.75}$$

where $[\cdot]$ indicates the integer part. The stationary phase approximation (A.3) brings about a $(N-1)$-dimensional matrix of second derivatives. Its determinant is easily calculated, since the difference between adjacent angles is constant:

$$\begin{aligned} \det\left(\frac{\partial^2 \sum \mathrm{a}(\varphi_{j+1}-\varphi_j)}{\partial\varphi_k \partial\varphi_l}\right)_{k,l=1\ldots N-1} &= \left(\mathrm{a}''(\Delta\varphi)\right)^{N-1} \det \begin{pmatrix} 2 & -1 & & 0 \\ -1 & \ddots & \ddots & \\ & \ddots & \ddots & -1 \\ 0 & & -1 & 2 \end{pmatrix} \\ &= N \left(\mathrm{a}''(\Delta\varphi)\right)^{N-1} \end{aligned} \tag{6.76}$$

The number of negative eigenvalues is $\nu_{\mathsf{A}} = 0$ or $\nu_{\mathsf{A}} = N-1$, respectively, for positive or negative sign of $\mathrm{a}''(\Delta\varphi)$ (ie, for long or short arcs).

Taking the square-root of (6.76) cancels all but one of the prefactors in the integrand of eq (6.72). Altogether, the kernel $\left(\mathrm{p}_{\mathrm{S}}^{\mathrm{int}} + \mathrm{p}_{\mathrm{L}}^{\mathrm{int}}\right)^N (s_0, s_0)$, is given by

$$\begin{aligned} \frac{1}{(2\pi\mathrm{i})^{\frac{1}{2}}} \frac{1}{\sqrt{N}} \frac{b}{R} \sum_{\Delta\varphi\in\mathcal{P}_{\mathrm{int}}^N} \Bigg\{ &\left|\frac{\mathrm{d}^2(2\pi\nu \mathrm{a}_{\mathrm{S}}(\Delta\varphi))}{\mathrm{d}\varphi^2}\right|^{\frac{1}{2}} \mathrm{e}^{N 2\pi\mathrm{i}\nu\mathrm{a}_{\mathrm{S}}(\Delta\varphi) - \mathrm{i}\frac{\pi}{2}(N-1)} \\ &+ \left|\frac{\mathrm{d}^2(2\pi\nu \mathrm{a}_{\mathrm{L}}(\Delta\varphi))}{\mathrm{d}\varphi^2}\right|^{\frac{1}{2}} \mathrm{e}^{N 2\pi\mathrm{i}\nu\mathrm{a}_{\mathrm{L}}(\Delta\varphi) - \mathrm{i}\frac{\pi}{2}N}\, \Theta(\Gamma_{\mathrm{d}} - 1) \Bigg\}. \end{aligned} \tag{6.77}$$

It is a sum over all *families* of interior periodic orbits, where each family is represented by the orbit starting at s_0.

The nth power of the *exterior* operators, $(\mathsf{P}_{\mathrm{S}}^{\mathrm{ext}} + \mathsf{P}_{\mathrm{L}}^{\mathrm{ext}})^N$, assumes the same form, except for the Heaviside function, which appears in the short arc term of the sum. Naturally, the summation is now over the exterior periodic orbit families, the respective increments given by the set

$$\mathcal{P}_{\mathrm{ext}}^N = \begin{cases} -2\pi\frac{M}{N}; & M = 1, 2, \ldots M_{\max} \quad \text{if } \Gamma_{\mathrm{d}} > 1 \\ \pm 2\pi\frac{M}{N}; & M = 1, 2, \ldots M_{\max} \quad \text{if } \Gamma_{\mathrm{d}} < 1\,. \end{cases} \tag{6.78}$$

As the last step in forming the trace $\mathrm{tr}\{(\mathsf{P}_{\mathrm{S}}^{\mathrm{int}} + \mathsf{P}_{\mathrm{L}}^{\mathrm{int}})^N\}$ we have to integrate s_0. Since the expression (6.77) does not depend on s_0, this simply adds the factor $2\pi R/b$.

It follows that for the magnetic disk, the fluctuating number function due to the skipping orbits (6.48) assumes the form

---

[‡] We use capital letters for the indices N, M in this section, to avoid confusion with the radial and angular momentum quantum numbers, cf (7.12).

$$\begin{aligned}\mathrm{N}_{\mathrm{osc}}^{\mathrm{skip(int)}} = &\left(\frac{2\nu}{\pi}\right)^{\frac{1}{2}} \sum_{N=2}^{\infty} \frac{1}{N^{3/2}} \sum_{\Delta\varphi\in\mathcal{P}_{\mathrm{int}}^{N}} \Bigg\{ \\ &\frac{\frac{1}{2}\Gamma_{\mathrm{d}}^2 \sin(\Delta\varphi) + \sin(\alpha)\cos(\alpha)}{(\sin(\alpha)\cos(\alpha))^{\frac{1}{2}}} \sin\left(2\pi\nu N\, \mathrm{a_S}(\Delta\varphi) + N\frac{\pi}{2} + \frac{\pi}{4}\right) \\ &+ \frac{\frac{1}{2}\Gamma_{\mathrm{d}}^2 \sin(\Delta\varphi) - \sin(\alpha)\cos(\alpha)}{(\sin(\alpha)\cos(\alpha))^{\frac{1}{2}}} \sin\left(2\pi\nu N\, \mathrm{a_L}(\Delta\varphi) + N\frac{\pi}{2} - \frac{\pi}{4}\right) \Theta(\Gamma_{\mathrm{d}} - 1) \Bigg\},\end{aligned} \tag{6.79}$$

with $\alpha \equiv \arcsin(\Gamma_{\mathrm{d}} \sin(|\Delta\varphi|/2))$. Analogously, the periodic orbit sum for the exterior problem is given by

$$\begin{aligned}\mathrm{N}_{\mathrm{osc}}^{\mathrm{skip(ext)}} = &\left(\frac{2\nu}{\pi}\right)^{\frac{1}{2}} \sum_{N=2}^{\infty} \frac{1}{N^{3/2}} \sum_{\Delta\varphi\in\mathcal{P}_{\mathrm{ext}}^{N}} \Bigg\{ \\ &- \frac{\sin(\alpha)\cos(\alpha) + \frac{1}{2}\Gamma_{\mathrm{d}}^2 \sin(\Delta\varphi)}{(\sin(\alpha)\cos(\alpha))^{\frac{1}{2}}} \sin\left(2\pi\nu N\, \mathrm{a_S}(\Delta\varphi) + N\frac{\pi}{2} + \frac{\pi}{4}\right) \Theta(\Gamma_{\mathrm{d}} - 1) \\ &+ \frac{\sin(\alpha)\cos(\alpha) - \frac{1}{2}\Gamma_{\mathrm{d}}^2 \sin(\Delta\varphi)}{(\sin(\alpha)\cos(\alpha))^{\frac{1}{2}}} \sin\left(2\pi\nu N\, \mathrm{a_L}(\Delta\varphi) + N\frac{\pi}{2} - \frac{\pi}{4}\right) \Bigg\}.\end{aligned} \tag{6.80}$$

The conventional density of states

The semiclassical expression for the density of states is obtained by taking the derivative of the number function with respect to the energy. In order to compare with the result of Blaschke *et al* , which is in units of the conventional energy E, we have to take the derivative

$$\frac{\mathrm{d}}{\mathrm{d}E} = \frac{1}{E}\left(\nu\frac{\mathrm{d}}{\mathrm{d}\nu} - \frac{1}{2}\Gamma_{\mathrm{d}}\frac{\mathrm{d}}{\mathrm{d}\Gamma_{\mathrm{d}}}\right) . \tag{6.81}$$

Applying this differential to (6.79) yields the fluctuating part of the density for the interior problem

$$\begin{aligned}d_{\mathrm{osc}}^{\mathrm{skip(int)}}(E) = &\frac{1}{E}\frac{(2\nu)^{\frac{3}{2}}}{\pi^{\frac{1}{2}}} \sum_{N=2}^{\infty} \sum_{\Delta\varphi\in\mathcal{P}_{\mathrm{int}}^{N}} \frac{1}{\sqrt{N}} \\ \times &\left\{ \alpha\, \frac{\frac{1}{2}\Gamma_{\mathrm{d}}^2 \sin(\Delta\varphi) + \sin(\alpha)\cos(\alpha)}{(\sin(\alpha)\cos(\alpha))^{\frac{1}{2}}} \cos\left(2\pi\nu N\, \mathrm{a_S}(\Delta\varphi) + N\frac{\pi}{2} + \frac{\pi}{4}\right) \right. \\ &\left. + \frac{\pi - \alpha}{\Theta(\Gamma_{\mathrm{d}} - 1)}\, \frac{\frac{1}{2}\Gamma_{\mathrm{d}}^2 \sin(\Delta\varphi) - \sin(\alpha)\cos(\alpha)}{(\sin(\alpha)\cos(\alpha))^{\frac{1}{2}}} \cos\left(2\pi\nu N\, \mathrm{a_L}(\Delta\varphi) + N\frac{\pi}{2} - \frac{\pi}{4}\right) \right\} .\end{aligned} \tag{6.82}$$

This periodic orbit formula is identical to the result in [83]. It approximates the quantum spectrum of the interior magnetic disk only for weak fields $\Gamma_{\mathrm{d}} < 1$, when all trajectories are of the skipping type. For strong fields, $\Gamma_{\mathrm{d}} > 1$, complete cyclotron orbits occur in the interior. One may wish to include them by hand into the periodic orbit sum, to account for their contribution to the total number counting function. However, it was shown in [83] that energies close to the Landau levels cannot be reproduced this way. Rather than trying to refine the semiclassical approximation, we shall define a new spectral density of edge states below, which will resolve the problem of bulk contributions.

Notes

1. The semiclassical operators derived in Section 6.1 allow to compute spectra within a "semiquantum" approximation, by means of the boundary integral method of Chapter 4. One merely has to replace the exact kernels (4.27) – (4.30) by their approximants (2.62), (6.10), (6.13), (6.15) and calculate the respective determinants numerically without further approximation. As an advantage of this scheme, it applies irrespective of the type of classical motion (including mixed chaotic dynamics). However, it should *not* be regarded as a proper semiclassical quantization, since the degree of approximation is not consistent throughout the calculation. To be consistent, also the determinant must be evaluated to leading order in ν (as performed in Sections 6.3 and 6.4).
2. The operator P is *not* identical – albeit similar – to the standard map operator defined in terms of the generating function $\mathscr{G}$ of the classical map [75],

$$\mathsf{S} = -\frac{1}{(2\pi \mathrm{i})^{\frac{1}{2}}} \left(\frac{\partial^2 \mathscr{G}}{\partial s \partial s_0} \right)^{\frac{1}{2}} \mathrm{e}^{\mathrm{i}\mathscr{G}} \,, \tag{6.83}$$

   which is the analogy of Bogomolny's transfer operator T [124]. The fact that P consists of two distinct parts, cf (6.19) is no even the main difference. Rather, it is the inherent asymmetry in the coordinates s, s_0, which introduces the most difficulties compared to the field-free treatment. (The prefactors cannot in general be stated as mixed derivatives of the relevant phase.) Moreover, the parts P_η are not semiclassically unitary, but satisfy equation (6.23).
3. Strictly speaking, the set of saddle points $\gamma^{(n)}$ which are directed into the correct domain at each point of reflection still includes the so-called ghost orbits. These are periodic orbits which leave (and necessarily re-enter) the proper domain without exhibiting a component of the saddle point (ie, a point of reflection) when leaving it. The left side of Fig. 6.4 shows the situation. Like in the case of non-magnetic billiards [123], these saddle points do finally not contribute to the sum over the traces. This is because for any ghost orbit of period n one finds another of period $n + 1$, with an additional boundary point at the position of re-entrance (right side of Fig. 6.4). These two contributions differ by a factor (-1) due to the additional boundary point and therefore cancel. (The orbits having a component of the saddle point at the the place of exit do not contribute due to the vanishing of one Heaviside function (6.22), as discussed above.)

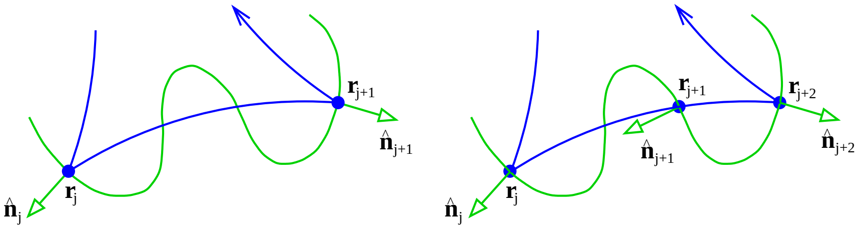

Figure 6.4: Sketch of an interior ghost orbit. (The normals are pointing outwards.)

Chapter 7

Separable geometries

In this chapter, the disk billiard is quantized semiclassically for a second time, using the separability of the quantum problem. This permits to examine the effect of general boundary conditions on the trace formula. In the second part, a model system is introduced which allows to study the transition of edge states to bulk states asymptotically.

7.1 The disk billiard

The disk is an exception among the magnetic billiards, as the only shape which exhibits integrable dynamics. The exact and semiclassical quantization procedures presented in Chapters 4 and 6 do of course apply in the case of the magnetic disk. Nonetheless, we shall briefly discuss the quantization based on the separability of the problem. This way closed expressions for the spectral functions may be obtained, which allow the derivation of explicit formulas for important quantities, such as the magnetization. Moreover, formulating the connection of the semiclassical spectral function to the periodic orbit formula of Sect. 6.4, allows the trace formula to be extended to general boundary conditions.

We take the boundary to be a circle of radius R which is centered on the origin. In the symmetric gauge, $\chi = 0$, this ensures that the canonical angular momentum is conserved. Hence, the eigenstates are characterized by the quantum number

$$m = \frac{L}{\hbar} = \frac{c^2 - \rho^2}{b^2} \,. \tag{7.1}$$

In the second equality the scaled angular momentum is stated in terms of the radial distance c of the center of motion, cf (2.13). Along with the cyclotron radius ρ, the latter determines whether the classical motion is of the skipping type. This is the case for $R-\rho < c < R+\rho$. Hence, a quantum state (of energy ν) corresponds to classically skipping motion if its angular momentum quantum number m is bounded from above and below by

$$m_{\max} = \widetilde{R}^2 + 2\sqrt{\nu}\widetilde{R} \tag{7.2}$$

and

$$m_{\min} = \max\left(\widetilde{R}^2 - 2\sqrt{\nu}\widetilde{R}, -\nu\right) \;, \tag{7.2a}$$

respectively. Here, the scaled radius $\widetilde{R} := R/b$ enters as the only external parameter.

We start with the traditional Bohr-Sommerfeld quantization method, and proceed to discuss its relation to the periodic orbit formula of Sect. 6.4. The exact quantization in terms of special functions will be treated afterwards.

7.1.1 Semiclassical quantization

Using polar coordinates (r, ϑ), the ansatz

$$\psi(r,\vartheta) = \frac{\varphi(r/b)}{\sqrt{r/b}}\,\mathrm{e}^{\mathrm{i}m\vartheta} \tag{7.3}$$

transforms equation (4.1) into the form of a one-dimensional Schrödinger equation for the radial function $\varphi(\tilde{r})$.

$$-\frac{1}{4}\varphi''(\tilde{r}) + \left(\frac{1}{4}\frac{(\tilde{r}^2 - m)^2 - \frac{1}{4}}{\tilde{r}^2} - \nu\right)\varphi(\tilde{r}) = 0 \tag{7.4}$$

It may be solved to leading order in b^2 using the standard WKB technique, see eg [41, 134].

The semiclassical wave function

It follows that in the energetically allowed region the resulting semiclassical wave function has the form

$$\psi^{(\mathrm{sc})}(r,\vartheta) = \mathcal{N}_{\mathrm{disk}}\,\frac{\cos\left(\Phi^{\mathrm{int/ext}}_{\mathrm{disk}}(\nu, m, \frac{r}{b}) - \frac{\pi}{4}\right)}{\left(4\nu\frac{r}{b} - \left((\frac{r}{b})^2 - m\right)^2\right)^{\frac{1}{4}}}\,\mathrm{e}^{\mathrm{i}m\vartheta} \;. \tag{7.5}$$

Here, the phases $\Phi^{\mathrm{int}}_{\mathrm{disk}}$ and $\Phi^{\mathrm{ext}}_{\mathrm{disk}}$ are obtained by an integration starting at the interior and exterior classical turning points of the radial motion, respectively.

$$\begin{aligned}\Phi^{\mathrm{int}}_{\mathrm{disk}}(\nu, m, \tilde{r}) = \frac{1}{2}\sqrt{4\nu\tilde{r}^2 - (\tilde{r}^2 - m)^2} - (\nu + \frac{m}{2})\arctan\left(\frac{2\nu + m - \tilde{r}^2}{\sqrt{4\nu\tilde{r}^2 - (\tilde{r}^2 - m)^2}}\right)\\ - \frac{m}{2}\arctan\left(\frac{(2\nu + m)\tilde{r}^2 - m^2}{m\sqrt{4\nu\tilde{r}^2 - (\tilde{r}^2 - m)^2}}\right) + \frac{\pi}{2}\left(\nu + \frac{m - |m|}{2}\right)\end{aligned} \tag{7.6}$$

and

$$\Phi^{\mathrm{ext}}_{\mathrm{disk}}(\nu, m, \tilde{r}) = \pi\left(\nu + \frac{m - |m|}{2}\right) - \Phi^{\mathrm{int}}_{\mathrm{disk}}(\nu, m, \tilde{r}) \;. \tag{7.7}$$

As for the normalization factor $\mathcal{N}_{\text{disk}}$, we find [134]

$$(\mathcal{N}_{\text{disk}})^{-2} := \frac{\pi^2}{4} \mp \frac{\pi}{2} \arctan\left(\frac{2\nu + m - \widetilde{R}^2}{\sqrt{4\nu\widetilde{R}^2 - (\widetilde{R}^2 - m)^2}} \right) , \tag{7.8}$$

where the upper sign stands for the interior problem (like throughout this chapter).

A spectral function

Allowing for general boundary conditions (3.6) at the disk radius $r = R$, we obtain the quantization condition

$$\begin{aligned} &\pm \cot\big(\Phi_{\text{disk}}^{\text{int/ext}}(\nu, m, \widetilde{R}) - \frac{\pi}{4}\big) \\ &= -\frac{(\pm\Lambda)\left(4\nu\widetilde{R}^2 - (\widetilde{R}^2 - m)^2\right)^{\frac{3}{2}}}{2\sqrt{\nu}\widetilde{R}\big(4\nu\widetilde{R}^2 - (\widetilde{R}^2 - m)^2\big) + (\pm\Lambda)\widetilde{R}^2\big(2\nu + m - \widetilde{R}^2\big)} . \end{aligned} \tag{7.9}$$

The boundary condition enters on the right side through the dimensionless[*] mixing parameter Λ, cf (3.7). It vanishes for Dirichlet boundary conditions. In order to transform the dependence on the boundary condition into a *phase shift* α_Λ, we define

$$\alpha_\Lambda(\nu, m, \widetilde{R}) := \arctan\left(\frac{(\pm\Lambda)\left(4\nu\widetilde{R}^2 - (\widetilde{R}^2 - m)^2\right)^{\frac{3}{2}}}{2\sqrt{\nu}\widetilde{R}\big(4\nu\widetilde{R}^2 - (\widetilde{R}^2 - m)^2\big) + (\pm\Lambda)\,\widetilde{R}^2\big(2\nu + m - \widetilde{R}^2\big)} \right) \tag{7.10}$$

The semiclassical quantization condition (7.9) is then readily brought into a form,

$$\cos\left(\Phi_{\text{disk}}^{\text{int/ext}}(\nu, m, \widetilde{R}) \mp \alpha_\Lambda(\nu, m, \widetilde{R}) - \frac{\pi}{4}\right) = 0 , \tag{7.11}$$

which allows to state a spectral function ξ in terms of two quantum numbers, the number of radial nodes n, and the angular momentum m,

$$\xi_{\text{disk}}^{(\text{sc})}\left(\nu; n, m, \Lambda, \frac{R}{b}\right) := \Phi_{\text{disk}}^{\text{int/ext}}\left(\nu, m, \frac{R}{b}\right) \mp \alpha_\Lambda\left(\nu, m, \frac{R}{b}\right) - \left(n + \frac{3}{4}\right)\pi , \tag{7.12}$$

with $n \in \mathbb{N}_0, m_{\min} \leq m \leq m_{\max}$, cf (7.2). Its zero in ν yields the semiclassical energy of a state with given radial and angular quantum numbers n and m. Although the energies are defined implicitly by (7.12), the spectral function allows for explicit formulas for the infinitesimal change of the energies as an external parameter is varied. Calculating the derivative of the energy with respect to the boundary mixing parameter at Dirichlet boundary conditions ($\Lambda = 0$), we obtain

$$\left.\frac{\mathrm{d}\nu}{\mathrm{d}\Lambda}\right|_{\Lambda=0} = -\frac{\frac{\mathrm{d}}{\mathrm{d}\Lambda}\xi_{\text{disk}}^{(\text{sc})}}{\frac{\mathrm{d}}{\mathrm{d}\nu}\xi_{\text{disk}}^{(\text{sc})}} = \frac{\sqrt{1 - \frac{(\widetilde{R}^2 - m)^2}{4\nu\widetilde{R}^2}}}{\frac{\pi}{2} \mp \arctan\left(\frac{2\nu + m - \widetilde{R}^2}{\sqrt{4\nu\widetilde{R}^2 - (\widetilde{R}^2 - m)^2}}\right)} . \tag{7.13}$$

---

[*] The dimensionless mixing parameter (3.7) is introduced for convenience. Strictly, it is not an independent variable but should be replaced by $2\sqrt{\nu}\lambda/b$ everywhere (to avoid energy dependent boundary conditions). This distinction does not matter, ultimately, since we are only interested in the derivatives at $\Lambda = 0$, cf (7.13), (8.1).

This short formula is further compressed below and needed soon.

The magnetic moment

It was shown in Sect. 3.4 that the scaled magnetic moment of a quantum state in the magnetic billiard is essentially determined by the derivative of its energy with respect to the magnetic length, cf equation (3.25). From the semiclassical spectral function (7.12) we find

$$b^2\,\frac{\mathrm{d}\nu}{\mathrm{d}b^2} = -\frac{b^2\,\frac{\mathrm{d}}{\mathrm{d}b^2}\xi^{(\mathrm{sc})}_{\mathrm{disk}}}{\frac{\mathrm{d}}{\mathrm{d}\nu}\xi^{(\mathrm{sc})}_{\mathrm{disk}}} = \pm\frac{1}{2}\,\frac{\sqrt{4\nu\widetilde{R}^2-(\widetilde{R}^2-m)^2}}{\frac{\pi}{2}\mp\arctan\left(\frac{2\nu+m-\widetilde{R}^2}{\sqrt{4\nu\widetilde{R}^2-(\widetilde{R}^2-m)^2}}\right)}\,. \tag{7.14}$$

Alternatively, the expectation value may be calculated directly, using the semiclassical wave function (7.5). We obtain indeed, after lengthy transformations,

$$\begin{aligned}\frac{1}{2}\langle\psi^{(\mathrm{sc})}|(\tilde{\mathbf{r}}\times\tilde{\mathbf{v}})_{\mathrm{sym}}|\psi^{(\mathrm{sc})}\rangle &= \int\mathrm{Im}\left[\psi^{*}_{(\mathrm{sc})}(\partial_\vartheta-\mathrm{i}\,\tilde{r}^2)\psi^{(\mathrm{sc})}\right]\mathrm{d}\vartheta\,\tilde{r}\,\mathrm{d}\tilde{r}\\ &= \pm\frac{1}{2}\,\frac{\sqrt{4\nu\widetilde{R}^2-(\widetilde{R}^2-m)^2}}{\frac{\pi}{2}\mp\arctan\left(\frac{2\nu+m-\widetilde{R}^2}{\sqrt{4\nu\widetilde{R}^2-(\widetilde{R}^2-m)^2}}\right)}-\nu\,,\end{aligned} \tag{7.15}$$

in complete agreement with (3.25). In the above radial integration (which is limited by the disk radius and the interior or exterior turning point, respectively), the strongly fluctuating $\cos^2$-term was replaced by its mean. The fact that the exact relation (3.25) is reproduced shows that this approximation is consistent with the semiclassical one.

The bulk states

States with angular momenta beyond the bounds given by (7.2) are not included in the spectral function (7.12). Classically, they correspond to cyclotron motion. The semiclassical energies of these bulk states are determined by the condition that the two wave functions (7.5) defined from the interior and exterior turning points must match. They are given by the Landau energies $\nu = n + \frac{1}{2}$, and the wave functions are readily shown to exhibit a magnetic moment of $-\nu$. (Exponential corrections to the bulk energy are discussed in Sect. 8.3.1)

7.1.2 Relation to the periodic orbit formula

The semiclassical quantization method discussed above amounts to the traditional Bohr-Sommerfeld rule for separable systems. It is based on the *quantizing tori*, ie, those invariant manifolds in phase space whose *scaled* actions are integers. This should be contrasted to the periodic orbit formula for the magnetic disk derived in Sect. 6.4. The latter is a sum over the *rational tori*, whose *classical* frequencies are commensurate [122]. In order to sketch, how the trace formula is connected to the

Bohr-Sommerfeld quantization, we follow the work of Berry and Tabor [2] who derived the trace formula for general integrable systems. In particular, this allows us to show how the trace formula is modified if one allows for general boundary conditions (3.6).

The semiclassical spectrum is given by the energies $\nu(n,m)$, which are implicitly defined as the roots of $\xi^{(\mathrm{sc})}_{\mathrm{disk}}$. We may write the spectral density as a sum over the two quantum numbers,

$$\begin{aligned} d(\nu_0) &= \sum_{n,m} \delta\big(\nu_0 - \nu(n,m)\big) \\ &= \overline{d}(\nu_0) + \sum_{N,M=-\infty}^{\infty} \int \mathrm{e}^{2\pi\mathrm{i}(Nn+Mm)} \delta\big(\nu(n,m)-\nu_0\big)\, \mathrm{d}n\, \mathrm{d}m \\ &= \overline{d}(\nu_0) + \sum_{N,M=-\infty}^{\infty} \int \left|\frac{\mathrm{d}n}{\mathrm{d}\nu}\right| \mathrm{e}^{2\pi\mathrm{i}(Nn(\nu_0,m)+Mm)}\, \mathrm{d}m\,, \end{aligned} \tag{7.16}$$

where the Poisson summation formula (eg [135]) was employed to transform the sum into an integral. (Boundary corrections which are to higher order in ν are neglected.) The sum excludes the term with $N = M = 0$, which yields the mean density $\overline{d}$. Upon integrating n, the δ-function selects the (real valued) "number" of radial nodes, which is known explicitely from above.

$$n(\nu_0, m) = \frac{1}{\pi}\Big(\Phi^{\mathrm{int/ext}}_{\mathrm{disk}}(\nu_0, m, \widetilde{R}) \mp \alpha_\Lambda(\nu, m, \widetilde{R}) - \frac{3\pi}{4}\Big) \tag{7.17}$$

We evaluate the remaining integral in the stationary phase approximation. The phase shift α_Λ should be neglected in the saddle point condition

$$-2\frac{\mathrm{d}}{\mathrm{d}m}\big[\Phi^{\mathrm{int/ext}}_{\mathrm{disk}} \mp \alpha_\Lambda\big] \overset{!}{=} 2\pi\frac{M}{N} \equiv \Delta\varphi \tag{7.18}$$

since Φ is of order ν (while α_Λ is of order 1). A detailed calculation shows, that the angles $\Delta\varphi$ selected by (7.18) are indeed given by the sets $\mathcal{P}^N_{\mathrm{int/ext}}$ defined in (6.74) and (6.78) (modulo 2π). It is now convenient to characterize the corresponding skipping trajectories by the signed sine of the angle of incidence

$$\varepsilon := \frac{c^2 - R^2 - \rho^2}{2R\rho} = \hat{\mathbf{n}} \times \hat{\mathbf{v}}\,, \tag{7.19}$$

such that the former quantum number m is given by the (real) value

$$m = \widetilde{R}^2 + 2\sqrt{\nu}\widetilde{R}\,\varepsilon\,. \tag{7.20}$$

One finds, after a lengthy calculation, that

$$\begin{aligned} 2\Phi^{\mathrm{int/ext}}_{\mathrm{disk}} + \frac{M}{N}2\pi m &= \pi\nu + 2\nu\arcsin(\sigma) - 2\nu\sigma\sqrt{1-\sigma^2} + \widetilde{R}^2\sin(\Delta\varphi) \\ &= 2\pi\nu\,\mathrm{a} \end{aligned} \tag{7.21}$$

with $\sigma = \mp(\varepsilon R + \rho)/c$ defined in (6.51), and "a" the geometric action (6.52) of one arc. Transforming the summation in (7.16) to positive N we obtain, observing (A.2),

$$d_{\text{osc}}^{\text{skip}}(\nu_0) = \frac{2}{\sqrt{\pi}} \sum_{\substack{N\in\mathbb{N},M\in\mathbb{Z}: \\ \Delta\varphi=2\pi\frac{M}{N}\in\mathcal{P}^N_{\text{int/ext}}}} \frac{1}{N^{\frac{1}{2}}} \frac{\frac{\mathrm{d}}{\mathrm{d}\nu}\Phi_{\text{disk}}^{\text{int/ext}}}{\left|\frac{\mathrm{d}^2}{\mathrm{d}m^2}\Phi_{\text{disk}}^{\text{int/ext}}\right|^{\frac{1}{2}}} \\ \times \cos\left(N2\pi\nu a + N\frac{\pi}{2} + \frac{\pi}{4}\operatorname{sgn}\left(N\partial_m^2\Phi_{\text{disk}}^{\text{int/ext}}\right) \mp 2N\alpha_\Lambda\right) . \tag{7.22}$$

We note the derivatives

$$\frac{\mathrm{d}^2}{\mathrm{d}m^2}\Phi_{\text{disk}}^{\text{int/ext}} = -\frac{1}{2\widetilde{R}\tilde{c}} \frac{\sigma}{\sqrt{1-\varepsilon^2}} \tag{7.23}$$

and

$$\frac{\mathrm{d}}{\mathrm{d}\nu}\Phi_{\text{disk}}^{\text{int/ext}} = \frac{\pi}{2} + \arcsin(\sigma) = \frac{1}{2}\frac{\mathrm{d}}{\mathrm{d}\nu}\big(2\pi\nu a\big) . \tag{7.24}$$

The last equality allows to integrate the spectral density immediately. It yields the oscillatory part of the number counting function,

$$\mathrm{N}_{\text{osc}}^{\text{skip}}(\nu_0) = \left(\frac{2\nu}{\pi}\right)^{\frac{1}{2}} \sum_{N=2}^{\infty} \sum_{\Delta\varphi\in\mathcal{P}^N} \frac{1}{N^{\frac{3}{2}}} \frac{\left(\frac{Rc}{\rho^2}\sqrt{1-\varepsilon^2}\sqrt{1-\sigma^2}\right)^{\frac{1}{2}}}{\left|\sigma\sqrt{1-\sigma^2}\right|^{\frac{1}{2}}} \\ \times \sin\left(2\pi\nu a N + \frac{\pi}{2}N + \frac{\pi}{4}\operatorname{sgn}(\sigma) \mp 2N\alpha_\Lambda\right) , \tag{7.25}$$

which may be compared to the trace formulas (6.79) and (6.80) obtained from the boundary integral equations. The agreement of the prefactors follows after a tedious discrimination of the various cases (interior/exterior, short/long arcs, and $R \gtrless \rho$.) As the only difference compared to the Dirichlet result of Section 6.4, we observe the non-vanishing phase factor $\mp 2N\alpha_\Lambda$ for finite Λ.

The effect of general boundary conditions

This result suggests that, compared to Dirichlet boundary conditions, the only effect of a finite mixing parameter is the appearance of an additional *phase shift* at every point of reflection,

$$\mp 2\alpha_\Lambda = -2\arctan\left(\Lambda\frac{\sqrt{1-\varepsilon^2}}{1 \pm \Lambda\frac{1}{4\nu}\frac{\rho/R+\varepsilon}{1-\varepsilon^2}}\right) \tag{7.26}$$

$$= -2\arctan\Big(\Lambda\sqrt{1-\varepsilon^2}\Big) + \mathrm{O}(\Lambda^2) , \qquad \text{as } \Lambda \to 0. \tag{7.26a}$$

Here, we stated (7.10) in terms of the geometry of the periodic orbit, cf (7.19), and of ν. One might be tempted to "generalise" the result (7.26) to arbitrarily shaped billiards, by replacing the disk radius R by the radius of curvature at the point of reflection. However, the phase shift at a point of zero curvature (which is given below) is not reproduced correctly this way. Only the limiting expression for small Λ, cf (7.26a), matches with its zero curvature analogue. The latter is determined merely by the (unsigned) angle of incidence with respect to the normal at the point of reflection,

$$\sqrt{1-\varepsilon^2} = |\hat{\mathbf{n}}\,\hat{\mathbf{v}}|\,. \tag{7.27}$$

This form coincides with the non-magnetic result [88]. This generality suggests that at small Λ any billiard exhibits the additional phase (7.26a) at the points of reflection.

All what will be needed below, fortunately, is this dependence to first order in Λ. It shows up in the derivative (7.13) which we may now write in terms of the geometric quantities ε and σ, cf (7.19) and (6.51). It assumes a particularly simple form,

$$\left.\frac{\mathrm{d}\nu}{\mathrm{d}\Lambda}\right|_{\Lambda=0} = \frac{\sqrt{1-\varepsilon^2}}{\frac{\pi}{2}+\arcsin(\sigma)}\,. \tag{7.28}$$

The remainder of this chapter is of a more technical nature and may be skipped at a first reading.

7.1.3 Exact quantization

The exact solutions of the Schrödinger equation in symmetric gauge are given in Appendix B, cf eqs (B.6) and (B.7). At fixed angular momentum m, the interior and exterior wave functions of the disk are specified uniquely by their behaviour at the origin and at infinity, respectively. Since in the interior the wave function (for energy ν) must be regular at the origin, it has the form

$$\psi_m(r,\vartheta) = \mathcal{N}_{\text{int}}\,\mathrm{e}^{\mathrm{i}m\vartheta}\left(\frac{r}{b}\right)^{|m|}\mathrm{e}^{-\frac{r^2}{2b^2}}\;{}_1\mathrm{F}_1\Big(\frac{1}{2}-\nu+\frac{|m|-m}{2},1+|m|;\frac{r^2}{b^2}\Big)\,. \tag{7.29}$$

For the exterior wave function, which vanishes at infinity, we have

$$\psi_m(r,\vartheta) = \mathcal{N}_{\text{ext}}\,\mathrm{e}^{\mathrm{i}m\vartheta}\left(\frac{r}{b}\right)^{|m|}\mathrm{e}^{-\frac{r^2}{2b^2}}\,\mathrm{U}\Big(\frac{1}{2}-\nu+\frac{|m|-m}{2},1+|m|;\frac{r^2}{b^2}\Big)\,. \tag{7.30}$$

Here, ${}_1\mathrm{F}_1$ and U are the regular and irregular confluent hypergeometric function, respectively [43]. Upon applying the general boundary conditions (3.6) at the disk radius $r=R$, we obtain the spectral functions

$$\begin{aligned}\xi_{\text{disk}}\Big(\nu;m,\Lambda,\frac{R}{b}\Big) = {}&\Big[\sqrt{\nu}+(\pm\Lambda)\Big(\frac{R}{2b}-\frac{|m|b}{2R}\Big)\Big]K\Big(\frac{1}{2}-\nu+\frac{|m|-m}{2},1+|m|;\frac{R^2}{b^2}\Big)\\ &-(\pm\Lambda)\frac{R}{b}\,\partial_3K\Big(\frac{1}{2}-\nu+\frac{|m|-m}{2},1+|m|;\frac{R^2}{b^2}\Big)\end{aligned} \tag{7.31}$$

with

$$K(a,b;z) = \begin{cases}{}_1\mathrm{F}_1(a,b;z) & \text{for interior problem}\\ \mathrm{U}(a,b;z) & \text{for exterior problem.}\end{cases} \tag{7.32}$$

Unlike the semiclassical case (7.12), one cannot predetermine the radial quantum number here, but has to search for all zeros at given angular quantum number m. The derivatives of the energies with respect to external parameters are given explicitely by derivatives of the spectral function, like in the semiclassical case. For variations in the boundary condition we find

$$\left.\frac{\mathrm{d}\nu}{\mathrm{d}\Lambda}\right|_{\Lambda=0} = \mp\frac{R}{\sqrt{\nu}b}\,\frac{\partial_3 K}{\partial_1 K} \tag{7.33}$$

with the arguments of K like above. Similarly, the derivative with respect to the magnetic length if given by the quotient

$$b^2\frac{\mathrm{d}\nu}{\mathrm{d}b^2} = -\frac{R^2}{b^2}\,\frac{\partial_3 K}{\partial_1 K}\,. \tag{7.34}$$

Note the relation

$$b^2\frac{\mathrm{d}\nu}{\mathrm{d}b^2} = \pm\sqrt{\nu}\,\frac{R}{b}\,\left.\frac{\mathrm{d}\nu}{\mathrm{d}\Lambda}\right|_{\Lambda=0}\,, \tag{7.35}$$

which holds in the semiclassical case as well.

As already mentioned, out results on the magnetic disk are relevant for other shapes, because the general billiard may be considered a disk to leading order neglecting variations in the curvature. One further step of neglect would disregard even the mean curvature.

7.2 The periodic line

In order to remove the effects of a a finite curvature let us deform the boundary Γ to a straight line of length $\mathscr{L}$. In addition to the mixed boundary conditions along the straight line, we prescribe periodic boundary conditions at the end points of the line and perpendicular to Γ. This is clearly no longer a billiard problem in its proper sense. In particular, there is no distinction between an interior and an exterior problem. Nonetheless, the classical and quantum problem is well-defined, with a discrete quantum spectrum. This simple system will allow to discuss the asymptotics of bulk and edge states in a straightforward fashion, cf Sect. 8.3.

The problem is separable in the Landau gauge, eq (2.12), and may be solved analogous to the disk above. Now, it is the *longitudinal* canonical momentum (ie, the transverse component of the scaled center of motion), which is the second constant of the motion. It is quantized,

$$\frac{c_y}{b} = \frac{\pi b}{\mathscr{L}}m\,, \tag{7.36}$$

with integer m (taking the boundary as the x-axis.) The transverse part φ of the wave function obeys the equation

$$\varphi''(z) + \big(\nu - \frac{1}{4}z^2\big)\varphi(z) = 0\,, \tag{7.37}$$

with $z := 2(y - c_y)/b$. The semiclassical and exact solutions yield spectral functions, like above. We shall give only the results.

Semiclassical quantization

For given longitudinal and transverse quantum numbers, m and n, the semiclassical energies of skipping states are determined by the roots of the spectral function

$$\begin{aligned}\xi^{(\mathrm{sc})}_{\mathrm{line}}\Big(\nu; n, m, \Lambda, \frac{\mathscr{L}}{b}\Big) = \nu \left[\frac{\pi}{2} + \arcsin\Big(\frac{\pi m}{\sqrt{\nu}}\frac{b}{\mathscr{L}}\Big) + \Big(\frac{\pi m}{\sqrt{\nu}}\frac{b}{\mathscr{L}}\Big)\Big[1 - \Big(\frac{\pi m}{\sqrt{\nu}}\frac{b}{\mathscr{L}}\Big)^2\Big]^{\frac{1}{2}}\right] \\ - \alpha^{\mathrm{line}}_{\Lambda}\Big(\nu, m, \frac{\mathscr{L}}{b}\Big) - \pi\Big(n + \frac{3}{4}\Big)\,, \qquad (7.38)\end{aligned}$$

with the phase shift

$$\alpha^{\mathrm{line}}_{\Lambda}\Big(\nu, m, \widetilde{\mathscr{L}}\Big) = \arctan\left(\Lambda\Big[1 - \Big(\frac{\pi m}{\sqrt{\nu}\widetilde{\mathscr{L}}}\Big)^2\Big]^{\frac{1}{2}}\right) \qquad (7.39)$$

being determined by the boundary condition Λ.

Exact quantization

Equation (7.37) is solved by the parabolic cylinder functions. It follows that the exact spectral function has the form

$$\begin{aligned}\xi_{\mathrm{line}}\Big(\nu; m, \Lambda, \frac{\mathscr{L}}{b}\Big) = \mathrm{D}_{\nu-\frac{1}{2}}\Big(-2\pi m\frac{b}{\mathscr{L}}\Big) + \Lambda\Big[\pi m\frac{b}{\mathscr{L}}\mathrm{D}_{\nu-\frac{1}{2}}\Big(-2\pi m\frac{b}{\mathscr{L}}\Big) \\ + \frac{1}{\sqrt{\nu}}\,\mathrm{D}_{\nu+\frac{1}{2}}\Big(-2\pi m\frac{b}{\mathscr{L}}\Big)\Big]\,, \qquad (7.40)\end{aligned}$$

where D_k is Whittaker's form of the regular parabolic cylinder function [43].

The uniform approximation

As a last point, we are interested in a semiclassical description of the situation when the corresponding classical trajectory is just detached from the boundary. Since the WKB approximation of the wave function fails close to the classical turning points, we have to resort to a uniform approximation, see eg [41]. It yields the asymptotic wave function in the whole region around one classical turning point, $z_\nu = -2\sqrt{\nu}$, in terms of the (action) integral

$$\begin{aligned}w(z) &:= \left|\int_{z_\nu}^{z}\Big|\nu - \frac{1}{4}z'^2\Big|^{\frac{1}{2}}\,\mathrm{d}z'\right| \qquad (7.41)\\ &= \begin{cases}\nu\left[\frac{1}{2}\sinh\Big(2\,\mathrm{arccos}\Big(\frac{z}{z_\nu}\Big)\Big) - \mathrm{arccos}\Big(\frac{z}{z_\nu}\Big)\right] & \text{if } z < -2\sqrt{\nu}\\ \nu\left[\frac{\pi}{2} + \arcsin\Big(\frac{z}{2\sqrt{\nu}}\Big) + \Big(\frac{z}{2\sqrt{\nu}}\Big)\sqrt{1 - \Big(\frac{z}{2\sqrt{\nu}}\Big)^2}\,\right] & \text{if } -2\sqrt{\nu} < z < 2\sqrt{\nu},\end{cases}\end{aligned}$$

which we define to be positive for any z. In uniform approximation, the two independent solutions of (7.37) are given (for $-\infty < z < 2\sqrt{\nu}$) in terms of the Airy functions [43]

$$\varphi_1(z) = \mathcal{N}\,\frac{\big(w(z)\big)^{\frac{1}{6}}}{|\nu - \frac{1}{4}z^2|^{\frac{1}{4}}}\,\mathrm{Ai}\Big(-\,\mathrm{sgn}(z - z_\nu)\Big(\frac{3}{2}w(z)\Big)^{\frac{2}{3}}\Big) \qquad (7.42)$$

and

$$\varphi_2(z) = \mathcal{N}\, \frac{\big(w(z)\big)^{\frac{1}{6}}}{|\nu - \frac{1}{4}z^2|^{\frac{1}{4}}}\, \mathrm{Bi}\Big(-\operatorname{sgn}(z - z_\nu)\Big(\frac{3}{2}w(z)\Big)^{\frac{2}{3}}\Big)\ . \tag{7.43}$$

The general solution may be parametrized by an angle $\alpha_u \in [-\frac{\pi}{2}; \frac{\pi}{2}]$.

$$\varphi(z) = \cos(\alpha_u)\, \varphi_1(z) - \sin(\alpha_u)\, \varphi_2(z) \tag{7.44}$$

This form is particularly convenient. By virtue of the asymptotic expansions of the Airy functions [43], we regain the WKB wave functions in both, the energetically forbidden region,

$$\psi(z) \sim \frac{1}{(\frac{1}{4}z^2 - \nu)^{\frac{1}{2}}} \left(\frac{1}{2}\cos(\alpha_u)\, \mathrm{e}^{-w(z)} - \sin(\alpha_u)\, \mathrm{e}^{w(z)}\right) \qquad (z \ll z_\nu,) \tag{7.45}$$

and in the energetically allowed one,

$$\psi(z) \sim \frac{1}{(\nu - \frac{1}{4}z^2)^{\frac{1}{2}}} \cos\Big(w(z) - \frac{\pi}{4} - \alpha_u\Big) \qquad (z \gg z_\nu.)\ . \tag{7.46}$$

Note the factor one-half in (7.45), which arises in a non-trivial fashion when connecting the WKB solutions of the two regions [41].

The eigenfunctions turn into bulk states, once the longitudinal quantum number m is large enough to leave the boundary in the energetically forbidden region,

$$q_m := \frac{\pi b m}{\mathscr{L}\sqrt{\nu}} = \frac{z}{z_\nu} > 1\ . \tag{7.47}$$

From the uniform approximation (7.42), (7.44) we find that in this case the angle α_u is determined by the ratio

$$\tan(\alpha_u) = \frac{\mathrm{Ai}\left((\frac{3}{2}w)^{\frac{2}{3}}\right) - \Lambda\sqrt{q_m^2 - 1}\,\mathrm{Ai}'\left((\frac{3}{2}w)^{\frac{2}{3}}\right)}{\mathrm{Bi}\left((\frac{3}{2}w)^{\frac{2}{3}}\right) - \Lambda\sqrt{q_m^2 - 1}\,\mathrm{Bi}'\left((\frac{3}{2}w)^{\frac{2}{3}}\right)}\ . \tag{7.48}$$

By comparing the asymptotic expression (7.46) of the wave function in the allowed region with that of a Landau state (which has no phase shift), one obtains the energy shift $\Delta\nu$ compared to the Landau energy,

$$\Delta\nu(m, \Lambda) = \frac{1}{\pi} \arctan\left(\frac{\mathrm{Ai}\left((\frac{3}{2}w)^{\frac{2}{3}}\right) - \Lambda\sqrt{q_m^2 - 1}\,\mathrm{Ai}'\left((\frac{3}{2}w)^{\frac{2}{3}}\right)}{\mathrm{Bi}\left((\frac{3}{2}w)^{\frac{2}{3}}\right) - \Lambda\sqrt{q_m^2 - 1}\,\mathrm{Bi}'\left((\frac{3}{2}w)^{\frac{2}{3}}\right)}\right)\ . \tag{7.49}$$

Figure 7.1 shows the energy shifts for the forth Landau level as a function of the boundary mixing parameter. Here, the value of $\mathscr{L}/b$ was chosen to correspond to the situation of Fig. 5.10. We observe that the bulk state behaviour is reproduced qualitatively even at this low Landau level. A quantitative comparison of the bulk energy shifts (7.49) with a quantum spectrum is given in Sect. 8.3.1.

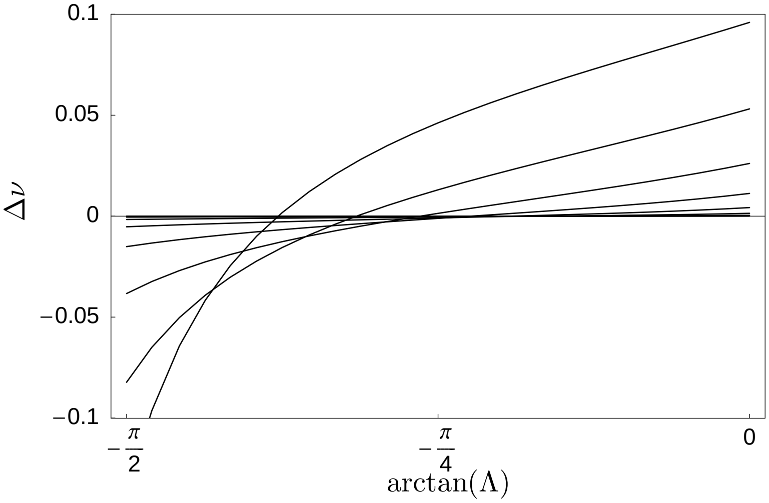

Figure 7.1: Energy shifts of the bulk states (7.49) for the forth Landau level and values ($\mathscr{L} = 5.39724$, $b = 0.25$, $m = 14 \;\ldots\; 20$) which allow the comparison with the right part of Fig. 5.10. As m is increased, the energy shifts $\Delta\nu$ turn exponentially small, cf (8.11), (and the boundary mixing parameter, for which there is no energy shift, approaches the Neumann condition).

For quantum numbers m which put the boundary into the energetically allowed region ($|q_m| < 1$), the angle α_u is semiclassically given by the phase shift (7.39) obtained above. For these states, the energy derivative with respect to Λ reads

$$\left.\frac{\mathrm{d}\nu}{\mathrm{d}\Lambda}\right|_{\Lambda=0} = \frac{\sqrt{1-q_m^2}}{\frac{\pi}{2} + \arcsin(q_m)} \; . \tag{7.50}$$

It coincides with the limiting expression of a large disk if we set $|\mathbf{c}| = R + c_y$ in (7.28), (7.19) and let $R \to \infty$.

Chapter 8

A spectral measure for edge states

In this chapter, a spectral measure for edge states is introduced. We discuss its asymptotically smooth form and its semiclassical interpretation. The edge magnetization is shown to provide an alternative, essentially equivalent measure.

8.1 Bulk states and edge states

8.1.1 A quantum criterion

The intuition which leads us to propose a quantitative criterion for edge states may be acquired from Figure 5.10 on page 66. It displays an *exterior* spectrum as a function of the boundary mixing parameter Λ (3.7). One observes that the (infinitely many) states which accumulate near the Landau levels are hardly affected by changes of the boundary condition. Clearly, these are *bulk states*. The extreme insensitivity of their energies with respect to Λ is explained by the fact, that bulk wave functions are not localized at the the boundary. They merely touch it with an (exponentially) small tail, giving rise to (exponentially) small energy shifts, as discussed in Sect. 8.3.1.

Other states depend strongly on Λ because they are localized at the boundary. They are naturally associated with *edge states*. The fact that states may have a transitional nature, as well, can be seen in the right part of Figure 5.10. One observes a sequence of bulk states which originate from the Landau level and gradually turn into edge states, with a strong dependence on the boundary. This indicates that any attempt to split the spectrum into two distinct parts, edge and bulk, would be inappropriate, because states of an ambivalent nature do exist.

In any case, it is the *slope* in the level diagram Fig. 5.10 which provides a quantitative criterion on the degree to which a state is of the edge type. We therefore propose to characterize each Dirichlet eigenstate $|\psi_n\rangle$ by the (positive) derivative of its energy ν_n with respect to the boundary mixing parameter at Dirichlet boundary conditions

$\Lambda = 0$,

$$w_n := \left.\frac{\mathrm{d}\nu_n}{\mathrm{d}\Lambda}\right|_{\Lambda=0} \equiv \frac{b}{2\sqrt{\nu}} \left.\frac{\mathrm{d}\nu_n}{\mathrm{d}\lambda}\right|_{\lambda=0} . \tag{8.1}$$

Along with the Dirichlet energies ν_n, these quantum weights w_n form the *edge spectrum* $\{(\nu_n, w_n)\}$.

In Figures 8.1 and 8.2 we show the *interior* and *exterior* edge spectra of the disk billiard at strong magnetic field on a linear and a logarithmic scale, respectively. One observes that the weights succeed to segregate edge states, with large w_n, from the bulk states. The latter – an infinite number in the exterior case – accumulate at the Landau levels $\nu = N + \frac{1}{2}, N \in \mathbb{N}_0$, with vanishingly small weights. There is a sequence of transitional states emanating from each Landau level, which gradually turn into edge states. (The spectra were obtained from eqs (7.31) and (7.33).)

Since the disk billiard offers a second quantum number, we can compare our characterization of edge states with a classical criterion. As shown above, a state corresponds classically to skipping motion if the angular momentum quantum number lies within the bounds given by (7.2). Those states in Figs. 8.1 and 8.2 indicated by a full dot have constants of the motion which belong to a skipping trajectory, while the others are represented by an open dot. We observe that the classical criterion complies with our picture, but argue that a continuous characterization of the states by means of the weights is more appropriate. This is the more so, as a second quantum number does not exist for shapes other than the disk.

The exterior edge spectrum of an *elliptic* billiard is given, accordingly, in Figure 8.3. It has the same area $\mathscr{A}$ and magnetic length b as the disk of Fig. 8.1 (bottom). Comparing the spectra we observe that they resemble in their gross features. In particular, the bulk states behave very similarly. However, there are additional structures showing up in the distribution of the weights of edge states. These can be related to features of the classical (mixed chaotic) phase space, as will be shown below.

The real advantage of the weights lies in the fact that they allow us to propose a meaningful spectral measure for the edge states of interior and exterior billiards.

8.1.2 The density of edge states

We define the *density of edge states* such that, compared to the standard density, each δ-contribution of an energy ν_n is *weighted* individually by the slope given in (8.1),

$$d_{\mathrm{edge}}(\nu) := \sum_{n=1}^{\infty} w_n \, \delta(\nu - \nu_n) \tag{8.2}$$

This definition applies equally for the interior and the exterior problem. In the exterior case, the sum extends formally over the infinite, near degenerate bulk states. However, the rapid decay of their weights ensures, that a well-defined mean density exists in the exterior, as shown below. It is *equal* to the interior one, to leading order, and given by

$$\overline{d}_{\mathrm{edge}}(\nu) = \frac{\mathscr{L}}{2\pi b} \nu^{\frac{1}{2}} \mp \frac{1}{2} . \tag{8.3}$$

Hence, the leading order term is proportional to the *circumference* $\mathscr{L}$ of the billiard, rather than its area. This is precisely what one expects of the quasi one-dimensional

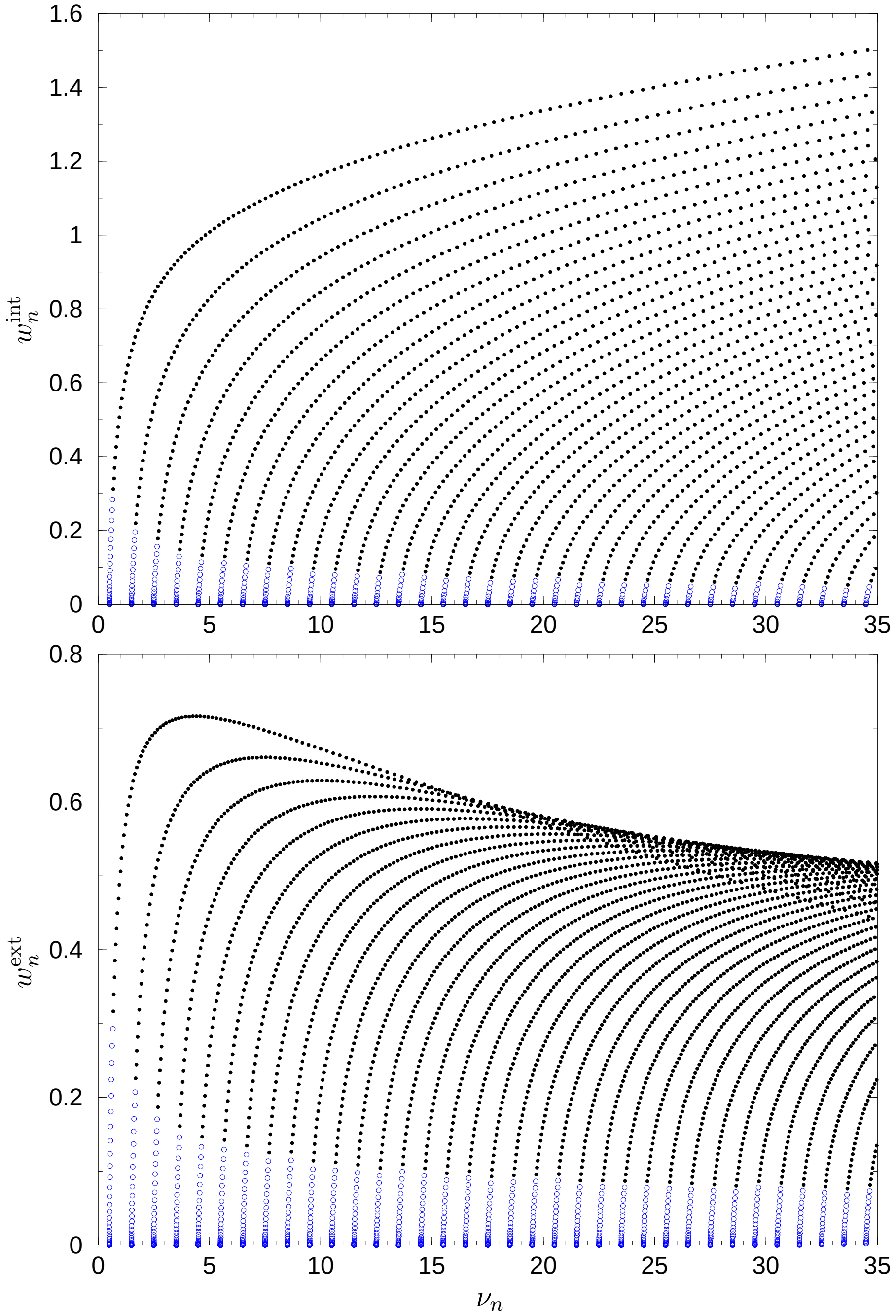

Figure 8.1: Weighted spectra of the interior (top) and exterior (bottom) magnetic disk (area $\mathscr{A} = \pi, b = 0.1$). Each point (open and filled) corresponds to an eigenstate $|\psi_n\rangle$ with the energy ν_n given by the abscissa. The ordinate indicates the attributed quantum weight w_n defined in eq (8.1). It serves to distinguish edge states (with large w_n) from bulk states. The latter accumulate at the Landau levels $\nu = N+\frac{1}{2}, N \in \mathbb{N}$, and are characterized by vanishingly small weights w_n. A sequence of transitional states emanates from each Landau level and connects with the edge states. As an alternative criterion, the angular momentum quantum number allows to decide whether the state corresponds classically to skipping motion (filled points) or cyclotron motion (open points), cf eq (7.2).

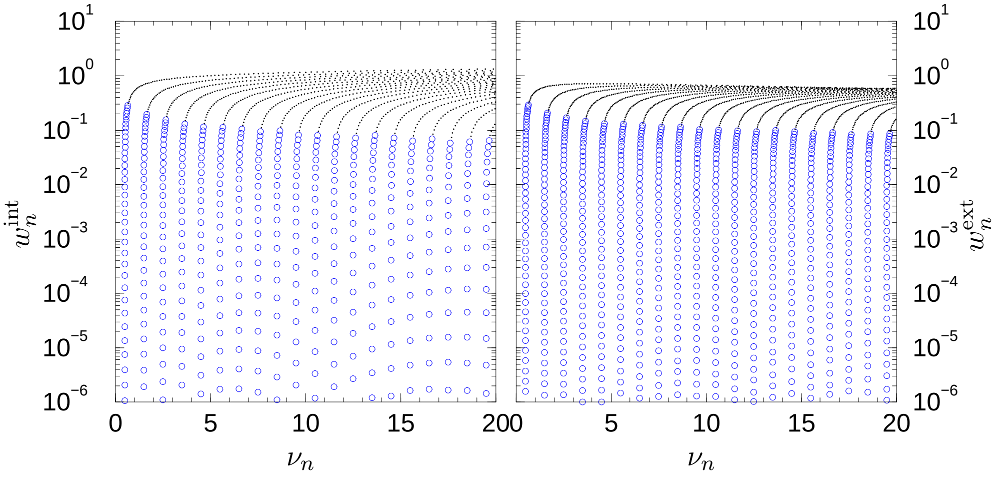

Figure 8.2: Weighted spectra of the interior (left) and exterior (right) magnetic disk on a logarithmic scale to highlight the bulk states. (Same data as in Fig. 8.1.)

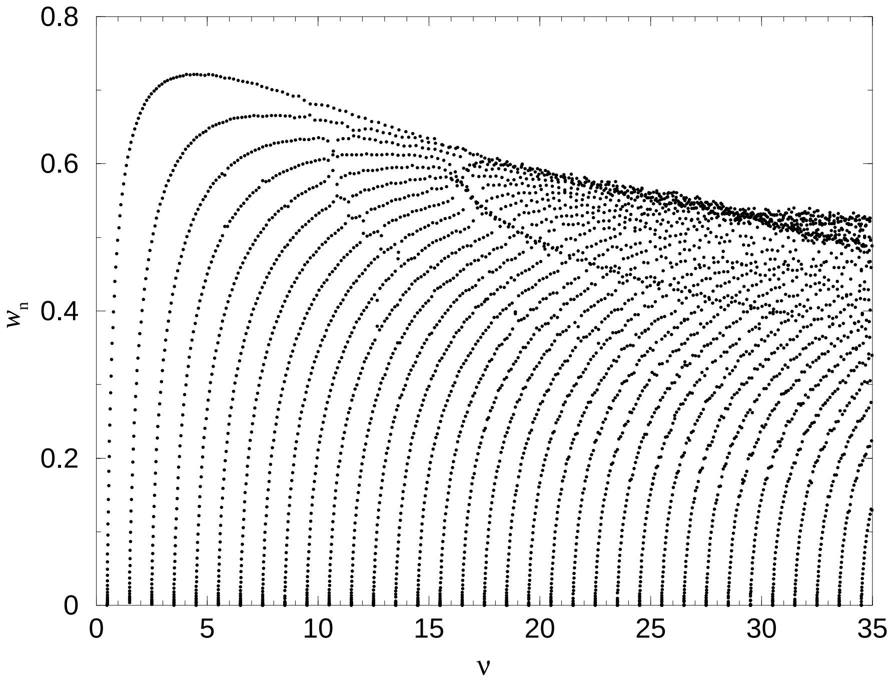

Figure 8.3: Weighted spectrum of the *exterior* ellipse billiard (with eccentricity 0.8, area $\mathscr{A} = \pi$, magnetic length $b = 0.1$). It should be compared to the exterior disk, Fig. 8.1 (bottom). While the bulk states are very similar, one observes that the edge weights no longer lie on smooth curves but tend to cluster. These structures can be related to the classical (mixed chaotic) phase space, as discussed below.

edge states. The second order term may be related to the mean curvature, as discussed below. (The upper sign stands for the interior problem.)

Let us now turn to the integrated quantity, in order to judge whether this spectral measure succeeds to filter the edge states out of the spectrum.

Counting functions

Integrating the edge density we obtain the *edge state counting function*

$$\mathrm{N}_{\mathrm{edge}}(\nu) := \int_0^\nu d_{\mathrm{edge}}(\nu')\,\mathrm{d}\nu' = \sum_{n=1}^{\infty} w_n\,\Theta(\nu-\nu_n). \tag{8.4}$$

which is a *weighted* staircase. Again, the sum formally includes the bulk states. We expect their contribution to be effectively eliminated by the rapid decay of the weights.

Since the rapid decay of the bulk weights should eliminate the contribution of the bulk, we expect the edge state counting function to bear no marks of the Landau levels. The smooth part of the edge state counting function is given by

$$\overline{\mathrm{N}}_{\mathrm{edge}}(\nu) = \frac{2}{3}\frac{\mathscr{L}}{2\pi b}\nu^{\frac{3}{2}} \mp \frac{1}{2}\nu \quad + \mathrm{O}(1)\ . \tag{8.5}$$

Note that, to leading order, this exhibits the same functional dependence as the phase space estimate of the skipping states in the periodic line problem (3.18) — with an additional prefactor of $\frac{1}{2}$ as the only difference.

In Figure 8.4 we compare the various spectral counting functions of the magnetic disk spectra given in Fig. 8.1. Curve (a) shows the *total* number of states in the interior. It exhibits steps at the Landau levels. In the exterior, a total counting function does not exist, but the angular momentum criterion (7.2) allows to count the exterior states of the *skipping* type, see curve (b). The corresponding number of interior skipping states is indicated by curve (c). As one expects, these two counting functions do hardly exhibit steps, but they have rather different values. In contrast, the weighted exterior and interior edge state counting functions, curves (d) and (e), respectively, follow the same mean values to leading order, which is consistent with (8.5). At the same time, they do not show marks of the Landau levels.

This is seen more clearly in Figure 8.5 which shows the fluctuating part of the edge state counting function,

$$\mathrm{N}^{\mathrm{osc}}_{\mathrm{edge}}(\nu) = \mathrm{N}_{\mathrm{edge}}(\nu) - \overline{\mathrm{N}}_{\mathrm{edge}}(\nu)\ , \tag{8.6}$$

for the exterior ellipse spectrum displayed in Fig. 8.3. One observes that the infinitely many bulk states around each Landau level do not leave marks in the edge counting function, apart from the first few Landau energies.

The semiclassical formulas for the oscillatory part of the edge state density and for the edge state counting function are given in the next section. They only involve periodic orbits of the skipping type.

8.2 The semiclassical density of edge states

While the standard spectral density (3.9) is given by the derivative of the number counting function N with respect to energy, the edge state density (8.2) may be formally

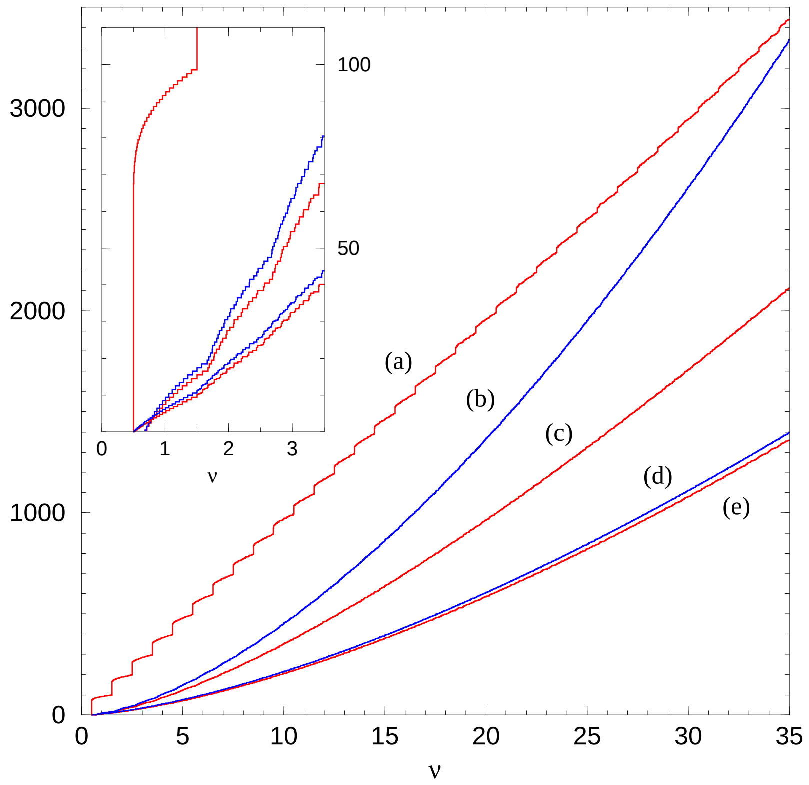

Figure 8.4: Spectral counting functions for the magnetic disk ($R/b = 10$). (a) Total number of interior states. (b,c) Number of exterior (b) and interior (c) skipping states (according to the angular momentum criterion). (d,e) Weighted number of edge states for the exterior (d) and interior (e) problem. On average, the curves are well reproduced by the smooth counting functions, eqs (3.10), (3.17), (3.16), (8.5), respectively (not shown). The inset gives the counting functions for the first four Landau levels. The small kinks in $\mathrm{N}_{\mathrm{skip}}$ and $\mathrm{N}_{\mathrm{edge}}$ are no longer present at larger energies.

defined as the derivative with respect to Λ, at Dirichlet boundary conditions ($\Lambda = 0$),

$$\begin{aligned} d_{\mathrm{edge}}(\nu) &= -\left.\frac{\mathrm{dN}(\nu)}{\mathrm{d}\Lambda}\right|_{\Lambda=0} \equiv -\frac{b}{2\sqrt{\nu}}\left.\frac{\mathrm{dN}(\nu)}{\mathrm{d}\lambda}\right|_{\lambda=0} \\ &= \sum_{n=1}^{\infty} w_n\,\delta(\nu-\nu_n)\,. \end{aligned} \tag{8.7}$$

Hence, the periodic orbit expression of the oscillatory part of the state density is deduced immediately, once we have the semiclassical formula for $\mathrm{N}_{\mathrm{osc}}$ at hand. For the time being, we restrict ourselves to hyperbolic systems. Combining the results of Chapters 6 and 7 (eqs (6.50), (7.26a), and (7.27)), the number of states based on the

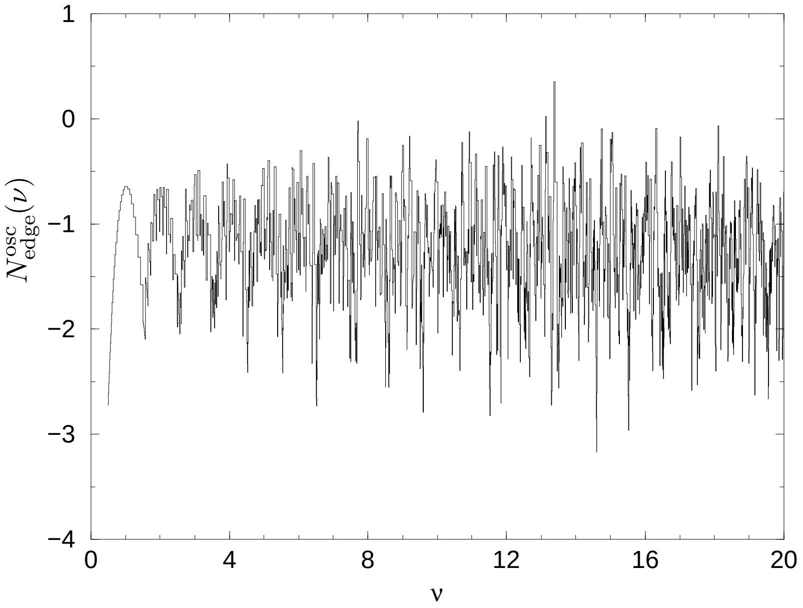

Figure 8.5: Oscillatory part of the edge state counting function for the *exterior* ellipse, cf Fig. 8.3. Apart from the first few Landau levels, it bears no marks of the bulk states. (The unknown constant part of $\overline{\rm N}_{\rm edge}$ was not subtracted.)

skipping part of phase space is given by

$$\mathrm{N}_{\rm osc}^{\rm skip}(\nu;\Lambda) = \frac{1}{\pi}\sum_{\gamma}\frac{(-)^{n_\gamma}}{r_\gamma \left|\,\mathrm{tr}\,\mathrm{M}(\gamma)-2\right|^{\frac{1}{2}}} \times \sin\left(2\pi\nu\mathrm{A}(\gamma) - \frac{\pi}{2}\mu_\gamma - 2\Lambda\sum_{j=1}^{n_\gamma}|\hat{\mathbf{n}}_j\hat{\mathbf{v}}_j|\right) + \mathrm{O}(\Lambda^2)\ . \tag{8.8}$$

Compared to (6.50), the leading order dependence on Λ is included, as discussed in Sect. 7.1.2. (See Tables 6.1 and 6.2 for the definition of the various quantities in (8.8).) Since the semiclassical bulk states do not depend on the boundary condition, their contribution vanishes when taking the derivative. One obtains the semiclassical trace formula for the edge state density at Dirichlet boundary conditions, cf (8.7),

$$d_{\rm edge}^{\rm osc}(\nu) = \frac{2}{\pi}\sum_{\gamma}\frac{\sum_{j=1}^{n_\gamma}|\hat{\mathbf{n}}_j\hat{\mathbf{v}}_j|}{r_\gamma \left|\,\mathrm{tr}\,\mathrm{M}(\gamma)-2\right|^{\frac{1}{2}}}\cos\left(2\pi\nu\mathrm{A}(\gamma) - \pi n_\gamma - \frac{\pi}{2}\mu_\gamma\right)\ . \tag{8.9}$$

In contrast, the unweighted density of states (6.57) was obtained by taking the derivative with respect to the energy ν. It exhibits the scaled time of flight τ_γ, cf eq (6.56), in the denominator. Hence, compared to the expression for the standard spectral density the periodic orbit sum (8.9) differs only by an additional prefactor

$$w_\gamma = \frac{\sum_{j=1}^{n_\gamma}|\hat{\mathbf{n}}_j\hat{\mathbf{v}}_j|}{\tau_\gamma}\ . \tag{8.10}$$

It attributes an individual *classical weight* to each skipping periodic orbit. The classical weights are given by the time averaged value for the normal component of the velocity $|\hat{\mathbf{n}}\,\hat{\mathbf{v}}|$ at the points of reflection, and vanish for cyclotron orbits.

Similar to the quantum weights, the w_γ lead to a gradual transition from edge to bulk contributions. In the limit of a "grazing" trajectory of many short arcs, variations in the curvature of the boundary may be neglected and the classical weights w_γ approach a value of unity. In the opposite case of an orbit which is almost detached from the boundary, the weights vanish since the cosines approach zero at a finite time of flight in the denominator of (8.10). In contrast, the periodic orbit expression for the standard density of states would contain the contribution of cyclotron orbits (with a different order in $\hbar$) and would suffer divergencies at almost detached orbits [83].

It is instructive to compare the distributions of quantum and classical weights. Unlike the quantum weights (8.1) attributed to each eigenvalue, the classical weights (8.10) are a property of the (periodic) orbits. In Fig. 8.6 we compare the phase space distribution of classical weights to the corresponding weighted quantum spectrum. The data were obtained for the interior elliptic billiard, and are given in both cases as a function of the classical cyclotron radius ρ. The distribution of classical weights $p(w_\gamma)$ was approximated numerically by the histogram over a finite number of trajectories taken uniformly from phase space. Remarkably, one observes that the characteristic features of both distributions coincide. This shows that the quantum weights may be considered the expectation values of an observable which has a classical limit, ie, they measure a classical property. This holds in spite of the fact that the w_n are defined in terms of the boundary condition, which has no classical analogy.

The particular bifurcating structures in Fig. 8.6 are due to stable periodic orbits, surrounded by locally integrable regions in phase space. At the bifurcation points, periodic orbits $\gamma^{(n)}$ with a given number of reflections n_γ exhibit the smallest possible cyclotron radius ($n_\gamma = 6$ in the case of the rightmost structure). As the cyclotron radius increases, the orbits turn into pairs with either longer or shorter arcs. (Some of the corresponding integrable parts of phase space may be identified in the space portraits in Fig. 3.1, left column.)

8.3 Asymptotic properties of edge and bulk states

We proceed to briefly discuss the leading order behaviour of the bulk energies, and the smooth part of the edge counting function. In both cases, the boundary is treated in the perturbative sense alluded to in Sect. 3.3.3. We therefore substitute it by the periodic line of Sect. 7.2, and expect that the finite curvature of billiard boundaries leads to higher order corrections only.

8.3.1 Bulk state energies and weights

The energy shift of a bulk state for general boundary condition is already given in equation (7.49). An asymptotic expansion, which amounts to the WKB approximation

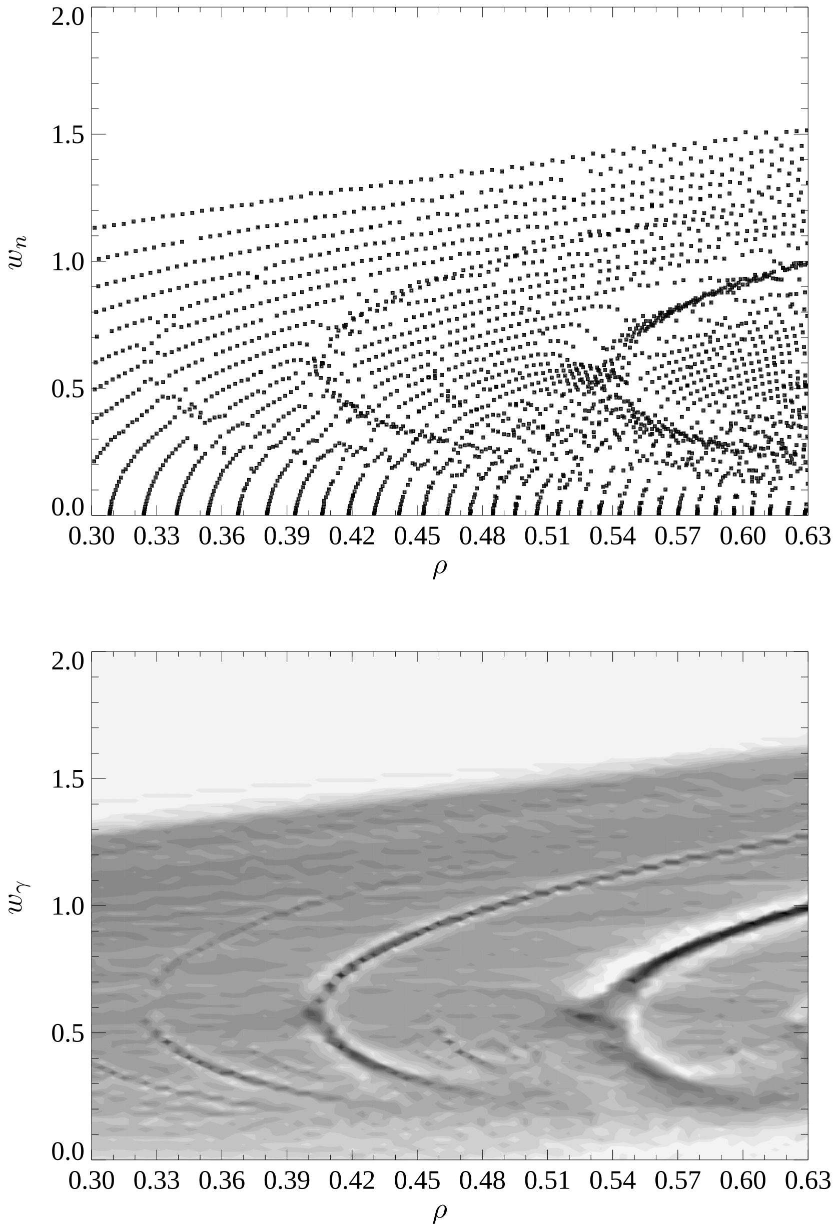

Figure 8.6: Weighted edge spectrum (8.2) (top) and phase space distribution of the classical weights (8.10) (bottom) for the interior ellipse. To ease comparison, also the quantum spectrum (calculated at constant $b = 0.1$, as in Fig. 8.3) is given in terms of the classical cyclotron radius ($\rho = b \times \sqrt{\nu}$.) One observes that the quantum weights tend to mimic the structures in the distribution of classical weights (which are due to stable islands in phase space, cf Fig. 3.1).

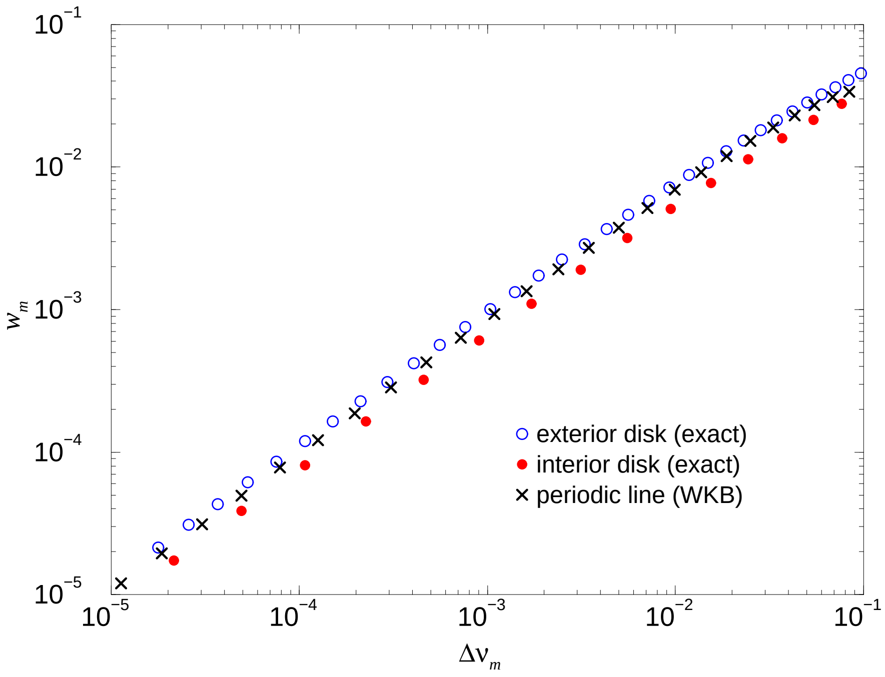

Figure 8.7: Bulk state energy shifts $\Delta\nu_n$, and weights w_n, for the magnetic disk ($R/b = 15.0111$) at the 50th Landau level (on a double-logarithmic scale). The interior (●) and exterior (○) bulks states are approximated by the periodic line (×), cf (8.11) and (8.12).

in the energetically forbidden region, yields the expressions

$$\Delta\nu_m \simeq \frac{1}{2\pi}\exp\Big(-2\nu\big(q_m\sqrt{q_m^2-1}-\log\big(q_m+\sqrt{q_m^2-1}\big)\big)\Big) \tag{8.11}$$

$$\sim \frac{1}{2\pi}\left(\frac{2\pi bm}{\mathscr{L}(N+\frac{1}{2})^{\frac{1}{2}}}\right)^{2N+1}\exp\left(N+\frac{1}{2}-2\Big(\frac{\pi bm}{\mathscr{L}}\Big)^2\right) \quad \text{as } m\to\infty\,, \tag{8.11a}$$

with N the Landau level, and q_m defined in (7.47). We observe that the bulk state energies approach the Landau levels exponentially fast (indeed, like a Gaussian) as the integer m increases — ie, as the distance of the cyclotron center from the boundary grows.

The weights of bulk states follow likewise, by taking the derivative of (7.49). Essentially, they decay as fast, as the shifts of the bulk energies.

$$w_m \simeq 2\left(\frac{\pi^2b^2m^2}{\mathscr{L}^2(N+\frac{1}{2})}-1\right)^{\frac{1}{2}}\Delta\nu_m \tag{8.12}$$

In Figure 8.7 we show (exact) bulk state energies and weights in a double-logarithmic representation. They belong to the interior and exterior disk at $R/b = 15.0111$, and to the 50th Landau level. The crosses give the zero curvature estimates according to eqs (8.11) and (8.12). One observes that the asymptotic weights and the spacing between the asymptotic energies match approximately the exact values, and lie between the those of the finite curvature case. Individual bulk states are not yet reproduced by the straight line approximation.

8.3.2 The mean edge counting function

As a second application, the periodic line allows to derive the leading term of the mean edge state counting function (8.5) in a straightforward manner. We simply identify the transverse quantum number n as a partial counting function for states with fixed quantum number m. An explicit formula for n, which includes the dependence on Λ follows from $\xi^{(\mathrm{sc})}_{\mathrm{line}} = 0$, cf eq (7.38). The sum

$$\mathrm{N}_{\mathrm{skip}}(\nu, \Lambda) = \sum_{m} n(m, \Lambda) \tag{8.13}$$

yields the total number of states corresponding to skipping motion. Taking the derivative with respect to Λ and replacing the summation by an integral, we obtain the leading order of the smooth edge state density,

$$\begin{aligned} \overline{d}_{\mathrm{edge}}(\nu) &= -\frac{\mathrm{d}\overline{\mathrm{N}}_{\mathrm{skip}}(\nu;\Lambda)}{\mathrm{d}\Lambda}\bigg|_{\Lambda=0} = \frac{1}{\pi}\int_{-\sqrt{\nu}}^{\sqrt{\nu}} \left(1-\frac{\tilde{c}_y^2}{\nu}\right)^{\frac{1}{2}} \frac{\mathscr{L}\,\mathrm{d}\tilde{c}_y}{\pi b} + \mathrm{O}(1) \\ &= \frac{\mathscr{L}}{2\pi b}\sqrt{\nu} + \mathrm{O}(1)\,. \end{aligned} \tag{8.14}$$

An analogous calculation for the disc billiard leads to the *same* expression. The second order term in (8.3) cannot obtained this way. We will deduce it in the next section by relating the quantum weights of the disk to the magnetic moments of the states.

8.4 Edge magnetization as a spectral measure

The edge magnetization (3.27) discussed in Section 3.4 is in many respects similar to $\mathrm{N}_{\mathrm{edge}}$. It was defined, for interior billiards, as

$$\widetilde{\mathcal{M}}_{\mathrm{edge}}(\nu) = \sum_{n=1}^{\infty} u_n\, \Theta(\nu - \nu_n)\,. \tag{8.15}$$

Like the edge counting function, this is a weighted staircase. The magnetic weights are given by a derivative with respect to the magnetic length rather than Λ,

$$u_n := b^2 \frac{\mathrm{d}\nu_n}{\mathrm{d}b^2}\,. \tag{8.16}$$

As discussed in Sect. 3.4, the bulk states are contributing to (8.15) merely to a negligible degree. Hence, it is reasonable to extend the definition of the edge magnetization to the exterior problem. As one expects, the exterior edge magnetization turns negative. Moreover, it has a *finite* mean, given by

$$\overline{\mathcal{M}}_{\mathrm{edge}}(\nu) = \pm\frac{1}{2}\,\frac{\mathscr{A}}{b^2\pi}\nu^2 - \frac{1}{3}\,\frac{\mathscr{L}}{2\pi b}\nu^{\frac{3}{2}}\,. \tag{8.17}$$

The interior case (upper sign) follows from eq (3.31), while the exterior one is suggested by symmetry and confirmed empirically. Hence, like in the case of the edge counting function, the moduli of the mean interior and exterior edge magnetizations are equal to leading order.

This suggests to take the edge magnetization as an alternative spectral measure for the edge states. The role of d_{edge} is taken over by the edge magnetization density (3.29)

$$\widetilde{\mathrm{m}}_{\mathrm{edge}}(\nu) = \sum_{n=1}^{\infty} u_n \, \delta(\nu - \nu_n) \tag{8.18}$$

which is a sequence of weighted δ-functions, like in eq (8.2). (To obtain a positive measure in the exterior case, one should of course change the sign of the u_n.)

In order to measure the edge magnetization spectrum, field and energy must be controlled, but the boundary condition is fixed at Dirichlet. This is an experimental advantage. As a disadvantage, the leading order of the edge magnetization is determined by the area of the billiard, rather than by its circumference. It indicates that with this measure the one-dimensional character of the edge states is not accounted for to the same degree as by d_{edge}. However, we shall see that is does a good job in suppressing the bulk contributions. Moreover, both spectral measures, d_{edge} and $\widetilde{\mathrm{m}}_{\mathrm{edge}}$ are *equivalent* in the case of a disk billiard. This is seen from equation (7.35), which yields the exact relation

$$u_n = \pm\sqrt{\nu}\,\frac{R}{b}\,w_n \, . \tag{8.19}$$

It is as surprising as fortuitous, and does not hold for general billiard shapes. Nonetheless, this relation allows to deduce the second, constant term of the mean edge state density (8.3) by comparison with the smooth edge magnetization density (3.31). Being the next order after the circumference term, it should be considered as due to the mean curvature, which is equal for all connected boundaries, $\int_\Gamma \kappa(s)\mathrm{d}s = \pm 2\pi$ (according to the Gauss-Bonnet theorem). Since the edge magnetization spectra of the disk differ from the edge spectra shown in Fig. 8.1 only by a geometric transformation (8.19), we shall not display them here.

Semiclassical edge magnetization

The semiclassical periodic orbit formula for the complete magnetization density is given in (6.59). Likewise, one finds that $\widetilde{\mathrm{m}}^{\mathrm{osc}}_{\mathrm{edge}}$ is given by the trace formula for the standard density, with each periodic orbit weighted individually by

$$\begin{aligned} u_\gamma &:= -\,\frac{b^2 \dfrac{\mathrm{d}}{\mathrm{d}b^2}\big[2\pi\nu \mathrm{A}(\gamma)\big]}{\dfrac{\mathrm{d}}{\mathrm{d}\nu}\big[2\pi\nu \mathrm{A}(\gamma)\big]} = \nu\,\frac{\sum_{j=1}^{n_\gamma}\Big(-\sigma_j\sqrt{1-\sigma_j^2} - \dfrac{\mathbf{r}_{j+1}\times\mathbf{r}_j}{2\rho^2}\Big)}{\sum_{j=1}^{n_\gamma}\Big(\dfrac{\pi}{2} + \arcsin(\sigma_j)\Big)} \\ &= \nu\,\frac{\pm 2\mathscr{A}_\gamma + \rho\mathscr{L}_\gamma}{\rho\mathscr{L}_\gamma} \, , \end{aligned} \tag{8.20}$$

see eqs (6.54a) and (6.58). Like in the case of w_γ, the weights u_γ vanish as trajectories get almost detached from the boundary (since the numerator approaches $\pm 2\mathscr{A}$, while $\mathscr{L}_\gamma \to \infty$).

Equipped with a well-defined spectral density and the corresponding trace formula, we can now proceed with a statistical and semiclassical study of edge state spectra. We shall not only consider the statistics within of a given edge state spectrum (Chapter 9), but also cross correlations between different, classically related spectra in Chapter 10.

Chapter 9

Properties of edge state spectra

We apply the spectral measures discussed in the previous chapter to analyse interior and exterior edge spectra statistically, and to compare them to the results of the periodic orbit theory.

9.1 Universal auto-correlations

One of the central goals in the study of quantum chaos is to understand how the statistical properties of the quantum spectrum reflect the nature of the underlying classical dynamics. We extend this line of research to magnetic billiards, by making use of the spectral measure of edge states introduced in the previous chapter. It was constructed to focus on the non-trivial part of phase space, which is determined by the billiard boundary map (3.4).

We want to show that edge spectra of both, interior and exterior magnetic billiards, display the universal characteristics of random matrix theory (RMT), provided the corresponding skipping motion is hyperbolic. Our quantity of choice to characterize spectral features is the form factor $K(\tau)$ which is sensitive to correlations beyond the mean level spacing [118]. The standard form factor was already used in Chapter 5 to qualify unweighted spectra of interior billiards. For edge spectra it is readily defined in terms of the 2-point autocorrelation function of the edge density,

$$R_{\nu_0}(\nu) = \int d_{\mathrm{edge}}^{\mathrm{osc}}\Big(\nu' + \frac{\nu}{2}\Big)\, d_{\mathrm{edge}}^{\mathrm{osc}}\Big(\nu' - \frac{\nu}{2}\Big)\, g_1(\nu' - \nu_0)\, \mathrm{d}\nu' \; . \tag{9.1}$$

Here, we included a normalized Gaussian window function g_1 to pick up a spectral interval centered at ν_0.

Before comparison to RMT, it is necessary to remove the trivially system-dependent properties of the spectrum by “unfolding” it [118]. This is a transformation of the spectral density which renders it dimensionless and of unit density. Dealing with a *weighted* spectrum the unfolding procedure must transform both, the energies and the weights. The natural choice involves the smooth edge state counting function $\overline{\mathrm{N}}_{\mathrm{edge}}$ and the average weight $\langle w^2\rangle/\langle w\rangle$ in the spectral interval considered:

$$\check{\nu}_n := \frac{\langle w\rangle}{\langle w^2\rangle}\,\overline{\mathrm{N}}_{\mathrm{edge}}(\nu_n) \qquad \text{and} \qquad \check{w}_n := \frac{\langle w\rangle}{\langle w^2\rangle}\, w_n \ . \tag{9.2}$$

Here, the first and second moments of the weights,

$$\langle w\rangle = \sum_{n=1}^{\infty} w_n \; g(\overline{\mathrm{N}}_{\mathrm{edge}}(\nu_n) - \check{\nu}_0) \tag{9.3}$$

and

$$\langle w^2\rangle = \sum_{n=1}^{\infty} w_n^2 \; g(\overline{\mathrm{N}}_{\mathrm{edge}}(\nu_n) - \check{\nu}_0) \ , \tag{9.4}$$

are taken locally in the spectrum in terms of the window function g (a normalized Gaussian of width σ_g.) As a result of this unfolding, both the weights and the weighted density have unit mean.

Since we are dealing with a discrete spectrum, the form factor must be averaged to be well-defined. The standard procedure is to take the spectral average over non-overlapping parts of the spectrum,

$$K(\tau) = \left\langle \int \mathrm{e}^{2\pi\mathrm{i}\check{\nu}\tau} R_{\check{\nu}_0}(\check{\nu})\, g_2(\check{\nu})\, \mathrm{d}\check{\nu} \right\rangle_{\check{\nu}_0} \tag{9.5}$$

as indicated by the triangular brackets. According to the spectral ergodicity hypothesis [136] this should be equivalent to an ensemble average for hyperbolic systems.

If we choose the widths of the Gaussians g_1 and g_2 as $\sigma_g/\sqrt{2}$ and $\sigma_g\sqrt{2}$, respectively, the Fourier transform of the autocorrelation function leads directly to the power spectrum. The form factor is then given by the *weighted* sum

$$K(\tau) = \left\langle \frac{2\sqrt{2\pi}\sigma}{\langle w^2\rangle} \left| \sum_{n=1}^{\infty} \check{w}_n\, \mathrm{e}^{2\pi\mathrm{i}(\check{\nu}_n - \check{\nu}_0)\tau} g(\check{\nu}_n - \check{\nu}_0) - \hat{g}(\tau) \right|^2 \right\rangle_{\check{\nu}_0} , \tag{9.6}$$

where the Fourier transform of g is denoted by $\hat{g}$.

In Figure 9.1 we show the form factors for the interior (top) and exterior (bottom) edge state spectra for the asymmetric stadium (left) and skittle (right) billiard, respectively. The spectra were obtained in the semiclassical direction, at fixed $\rho = 1.2$, ie, for the same situation as in Fig. 5.4. (This was done to ensure that the corresponding interior and exterior skipping motion is essentially hyperbolic, as discussed in Sect. 5.1 — see Appendix D for the definition of the edge state density at fixed ρ.)

We observe that the interior form factors follow the RMT prediction of the Gaussian Orthogonal and Gaussian Unitary Ensembles, respectively, as expected from the specific symmetry properties of the Hamiltonians. In the interior case, this is not surprising. To ensure hyperbolicity, the value of ρ had to be chosen large, such that the phase space consists only of skipping trajectories which cover it ergodicly. As a consequence, one expects that all *interior* states are edge states to an equal degree. Indeed,

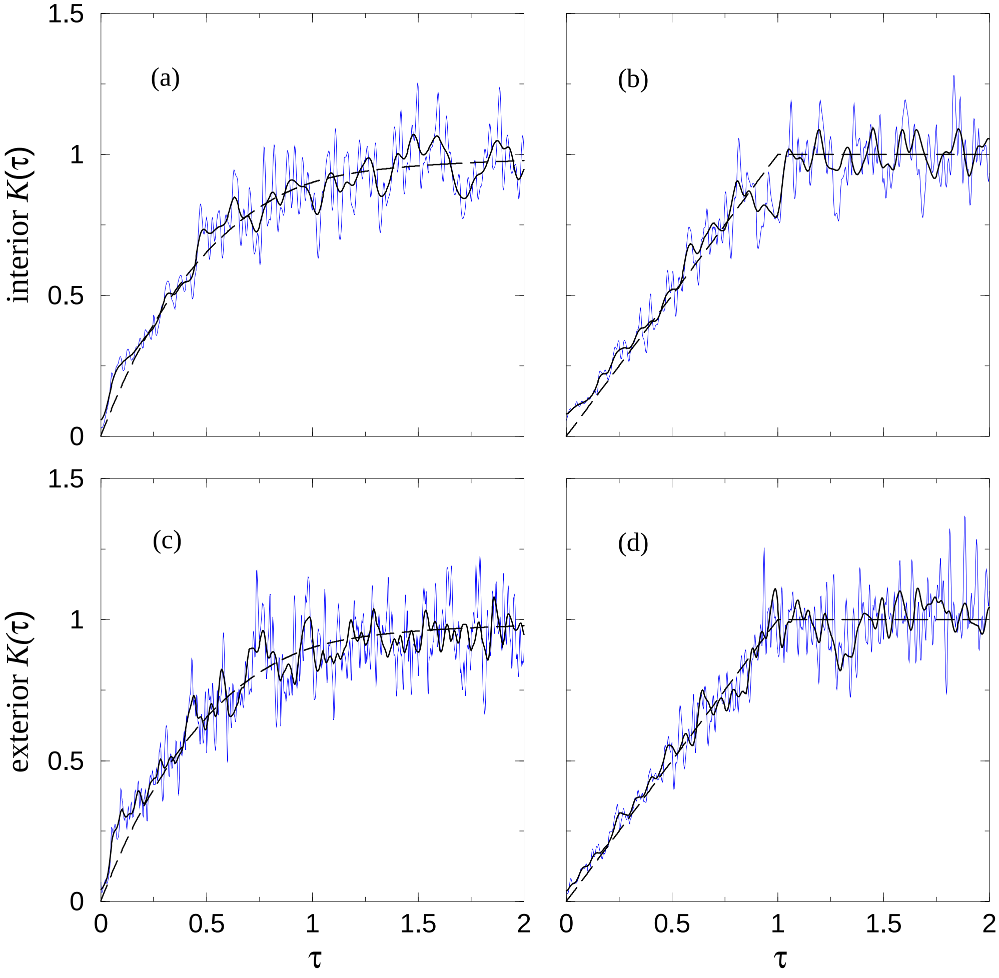

Figure 9.1: Form factors (9.6) of the interior (a,b) and exterior (c,d) edge state spectra for the asymmetric stadium (a,c) and skittle (b,d) billiard, at $\rho = 1.2$. The shapes are defined in Fig. 5.1. The functions follow the RMT predictions of the GOE and GUE ensembles [118], respectively (dashed lines). The heavy lines correspond to stronger spectral averaging than the thin lines ($\sigma_g = 10$ and $\sigma_g = 3$, respectively.)

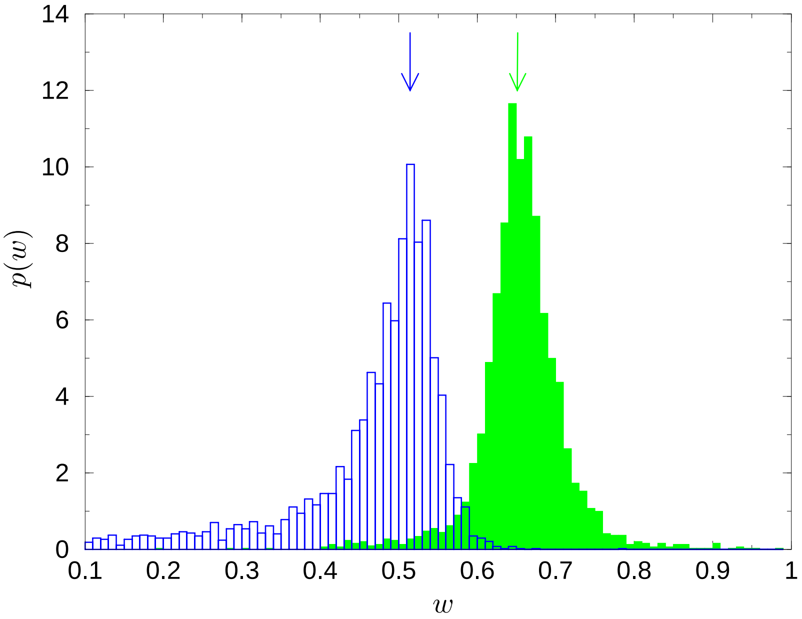

Figure 9.2: Distribution of the quantum weights $w_n > 0.1$ of the interior (shaded) and exterior (transparent) skittle spectrum at $\rho = 1.2$. The histograms display peaks whose positions are well reproduced by the phase space estimates (9.7) and (9.8) (indicated by the arrows). Unlike the interior case, the exterior distribution shows a tail due to the transitional states which ranges to the small weights. (For normalization, (bulk) states with weights smaller than 0.1 had to be disregarded.)

the interior weights are distributed narrowly around a mean value $\overline{w}$, given by the ratio of weighted and unweighted mean densities,

$$\overline{w} = \frac{\overline{d}^{(\rho)}_{\text{edge}}(\nu)}{\overline{d}^{(\rho)}_{\text{tot}}(\nu)} = \frac{\mathscr{L}\rho}{4\mathscr{A}} \,, \tag{9.7}$$

as can be observed from the filled histogram in Fig. 9.2. The weights provide not much additional information in this case, which explains why $K(\tau)$ reproduces the RMT prediction, like in the unweighted case.

In contrast, the standard form factor – like any other standard statistical function – does not even exist for the exterior spectrum, which is dominated by infinitely many bulk states. Nonetheless, viewing the exterior spectrum in an appropriate way, by means of the edge state density, we find that it closely obeys the predictions of random matrix theory (bottom row of Fig. 5.4.) This way, a crucial test for the appropriateness of the new spectral measure is passed. The quantum weights succeed to filter out *selectively* the relevant edge states, which in turn exhibit the universal characteristics expected for chaotic motion.

The distribution of the exterior weights is given by the transparent histogram in Figure 9.2. Here, we disregarded (bulk) states with small weights. One observes that the distribution of large weights is peaked, like in the interior case. Again, the peak

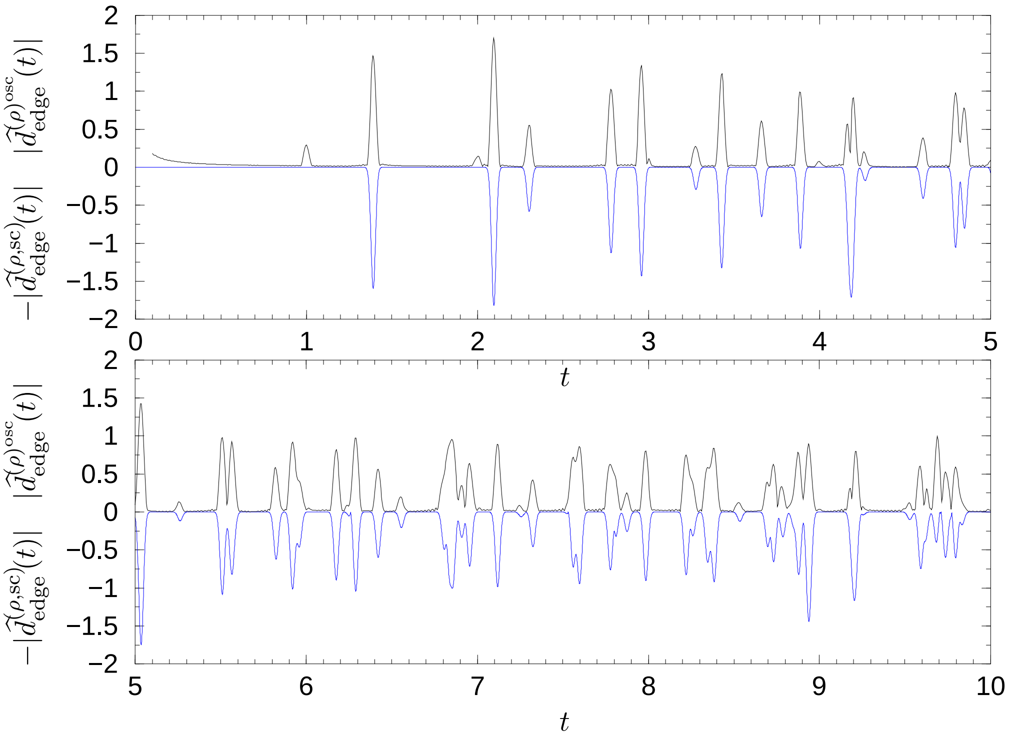

Figure 9.3: Action spectrum of the exterior disk at $\rho = 2R$. The positive values give the Fourier transform (9.10) of the exterior edge density (absolute values). The positions of the peaks are well reproduced by the trace formula (9.9) (negative values) – except for the small peaks at integer t, which are remnants of the bulk states. The peak heights match well in most cases; they are expected to fit better if a spectral interval larger than $\nu \in [0; 48]$ is used.

position is well described by the ratio of weighted and unweighted densities,

$$\overline{w} = \frac{\overline{d}^{(\rho)}_{\mathrm{edge}}(\nu)}{\overline{d}^{(\rho)}_{\mathrm{skip}}(\nu)} \simeq \frac{\mathscr{L}\rho}{2\mathscr{A}^{\mathrm{ext}}_{\mathrm{skip}}(\rho)}\,, \tag{9.8}$$

with the mean unweighted density now given by the phase space estimate (3.15) of skipping states. Unlike the interior case, the distribution has a tail of transitional states which ranges to the infinitely many bulk states with small weights.

9.2 The action spectrum

We turn from the statistical analysis of edge spectra to their semiclassical description. Here, the main purpose is to show that the trace formula for the edge state density – which rates each periodic orbit with a classical weight – succeeds in approximating the exact edge spectrum.

We choose the disk billiard for which an explicit periodic orbit formula is readily obtained from equation (7.25). For the exterior case and $\Gamma_{\mathrm{d}} = R/\rho < 1$ we find, cf

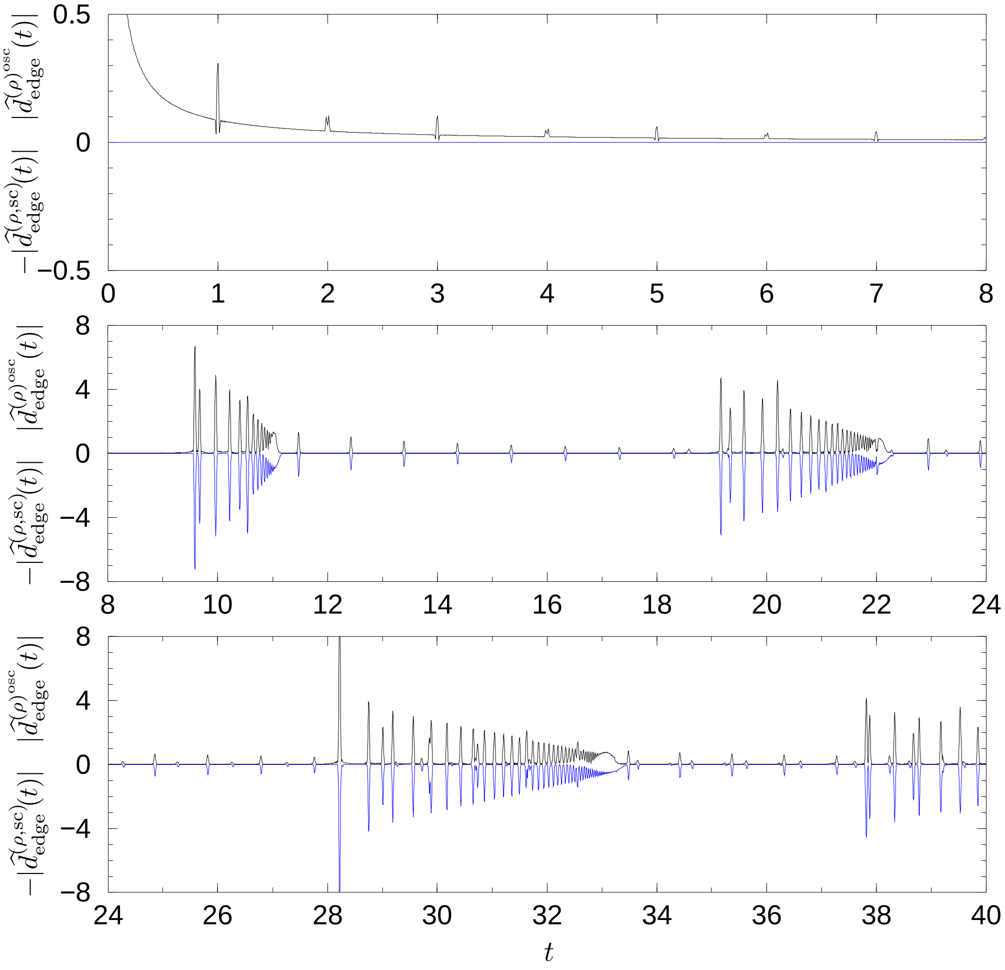

Figure 9.4: Action spectrum of the interior disk at a cyclotron radius $\rho = 0.4 \times R$ small enough to allow for bulk states. The Fourier transform (9.10) of the interior edge density (positive values, $\nu \in [0; 60]$) is well reproduced by the trace formula (negative values). Note that in the top part, which shows the remnant peaks of bulk contributions, the y-axis has a different scale.

(8.7)

$$d_{\text{edge}}^{\text{osc}}(\nu) = \left(\frac{2\nu}{\pi}\right)^{\frac{1}{2}} \sum_{N=2}^{\infty} \frac{2}{N^{1/2}} \sum_{\Delta\varphi \in \mathcal{P}_{\text{ext}}^{N}} \left|\sin\left(\alpha - \frac{\Delta\varphi}{2}\right)\right| \tag{9.9}$$
$$\times \frac{\sin(\alpha)\cos(\alpha) - \frac{1}{2}\Gamma_{\text{d}}^{2}\sin(\Delta\varphi)}{(\sin(\alpha)\cos(\alpha))^{\frac{1}{2}}} \cos\left(2\pi\nu N \, \mathrm{a}_{\text{L}}(\Delta\varphi) + N\frac{\pi}{2} - \frac{\pi}{4}\right) ,$$

with α defined by equation (6.61). (The term $|\sin(\alpha - \frac{\Delta\varphi}{2})|$ corresponds to the normal component of the velocity, $|\hat{\mathbf{n}}\,\hat{\mathbf{v}}|$, in (8.9).) Moreover, the exact quantum spectrum of the disk is calculated (relatively) easily in terms of the roots of special functions, cf Sect. 7.1.3. We obtained spectral intervals large enough to allow the Fourier transformation of the spectral densities,

$$\widehat{d_{\text{edge}}^{\text{osc}}}(t) = \int \mathrm{e}^{2\pi\mathrm{i}\nu t} d_{\text{edge}}^{\text{osc}}(\nu)\, h(\nu - \nu_0)\, \mathrm{d}\nu \,, \tag{9.10}$$

to resolve the classical actions t of the underlying periodic orbits. (The function h is a suitable window centered on the midpoint ν_0 of the spectral interval.) This *action spectrum* may be readily compared to the semiclassical prediction based on (9.9).

Like in the previous section, it is convenient to take the spectrum in the semiclassical direction, at constant ρ. (See appendix D for a summary on the edge state density defined at fixed classical dynamics.) In Figure 9.3 we display the action spectrum for the *exterior* disk at a cyclotron radius $\rho = 2R$ larger than the radius R of the disk (positive values). The corresponding prediction of the trace formula (9.9) is given by the negative values. One observes that the peak positions match very well with the predictions of semiclassical theory. The only exception are the small peaks at integer actions, which are not reproduced semiclassically. They may be considered remnants of the infinite number of bulk states. The peak heights are well reproduced most of the time, except if two peaks overlap too strongly. These deviations are expected to decrease as a larger spectral interval is used, leading to smaller widths of the peaks.

This is seen in Figure 9.4 where we present the exact and semiclassical action spectra of the interior magnetic disk – based on a large spectral interval ($\nu \in [0; 60]$ at $\rho = 0.4 \times R$). Here the cyclotron radius was chosen small enough to allow for bulk states in the interior. One observes again that the latter are very efficiently suppressed in the action spectrum giving rise only to the small peaks at integer values (shown in the top part of Fig. 9.4). In the Fourier transform of the unweighted density, in contrast, the bulk states obliterate the edge contributions and not a single action is resolved (not shown).

In conclusion, we find that the the semiclassical trace formula succeeds in reproducing the quantum edge state density. It does so by weighting each periodic orbit contribution with a classical weight which vanishes for cyclotron orbits. This removes the bulk contributions analogous to (and consistent with) the quantum weights of the edge state density.

9.3 Using the edge magnetization

Finally, let us demonstrate that the edge magnetization (8.18) as discussed in Section 8.4 may serve as a spectral measure for edge states as well.

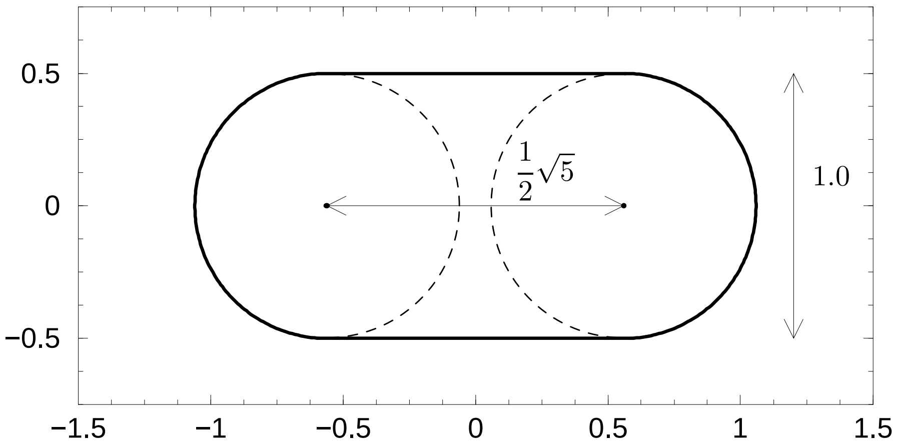

Figure 9.5: Definition of the Bunimovich stadium used in Sect. 9.3 and Chapter 10.

Choosing the Bunimovich stadium billiard (defined in Fig. 9.5), we calculated the interior and exterior magnetization spectrum in the high-energy direction, at $b = 0.2$. The selected spectral interval $\nu \in [100; 135]$ corresponds to large cyclotron radii $\rho = 2 \ldots 2.32$ giving rise to essentially hyperbolic classical motion (ie, although there are small integrable parts in phase space, their combined area is much smaller than the uncertainty product $(b^2\pi)^2$). Quantum mechanically, the problem exhibits one unitary and one anti-unitary symmetry (rotation by π and reflection at one axis, respectively). Hence, the spectrum decomposes into two symmetry classes – a feature which will be needed in the next chapter – while each class should obey the characteristics of the Gaussian Orthogonal Ensemble [118].

The weighted spectra are shown in Figure 9.6. Note that the weights are very different in magnitude, although they lead to the same average edge magnetization (8.17). This is explained by the different areas $\mathscr{A}_{\text{skip}}$ of the interior and exterior skipping motion since the mean weight is asymptotically determined by

$$\overline{u} = \frac{\overline{\mathrm{m}}_{\text{edge}}(\nu)}{\overline{d}_{\text{edge}}(\nu)} \simeq \frac{\mathscr{A}}{\mathscr{A}_{\text{skip}}(\rho = \sqrt{\nu}b)}\,\nu\,, \tag{9.11}$$

cf eqs (3.31) and (8.3). The center in the distributions of the magnetization weights is indeed well characterized by the value of $\overline{u}$ (similar to Fig. 9.2, not shown). Moreover, equation (9.11) indicates that it is reasonable to account for the gross energy dependence of the magnetization weights u_n by dividing them by the energies ν_n. The counting function then has the same leading order energy dependence as the edge state counting function (8.5).

Figure 9.7 presents the form factor of the exterior magnetization spectrum. It was calculated analogous to the expression (9.5) in Section 9.1, except that only energies within the same symmetry class were taken. As one expects, the form factors follows the GOE prediction (dashed line). This indicates that the magnetization weights (8.16) succeed to filter the bulk states consistently, similar to the edge state weights (8.1).

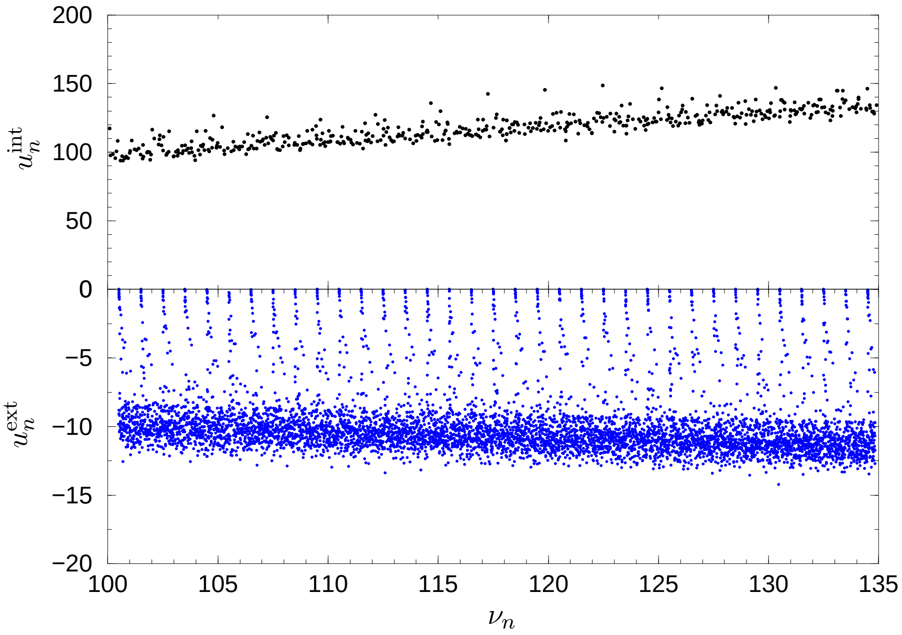

Figure 9.6: Edge magnetization spectrum of the stadium billiard at $b = 0.2$ and high energy. Although the mean values of the magnetic weights differ strongly in the interior (top) and exterior (bottom) the absolute value of the average edge magnetizations are equal to leading order, cf (8.17). The classical cyclotron radius corresponding to this part of the spectrum is large, $\rho \in [2; 2.32]$, giving rise to essentially hyperbolic classical motion.

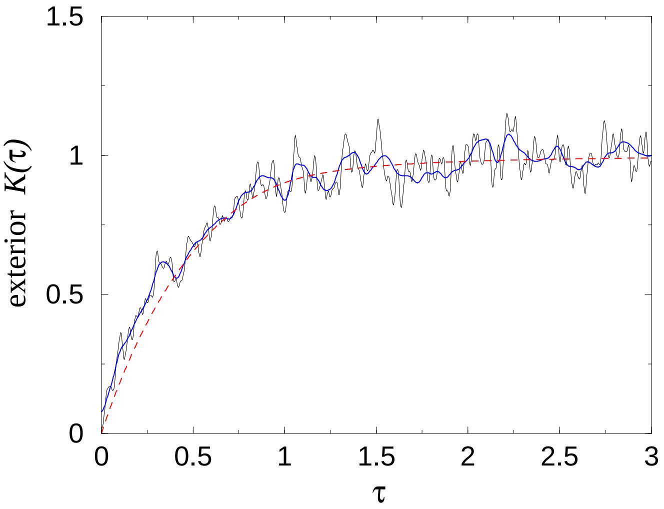

Figure 9.7: Form factor of the exterior Bunimovich stadium (Fig. 9.5) computed from the edge magnetization spectrum shown in Fig. 9.6, bottom part.

Chapter 10

Spectral cross correlations

In the previous chapter we have seen that interior and exterior edge spectra display the same universal statistics if the underlying classical motion is chaotic. It will be shown in the following that a much more intimate relation exists between the interior and the exterior spectra. It is generated by the classical duality of periodic orbits discussed in Section 3.2.

10.1 The prediction of spectral cross correlations

In order to unravel the connection between interior and exterior edge state energies, a special cross-correlation function is needed. It not only involves the Dirichlet energies of the edge states, but also relies on the information provided by their weights.

The cross correlation function

As the first step to obtain the appropriate correlator, we *formally* extend the definition of the edge state density to finite boundary mixing parameters Λ.

$$d_{\mathrm{edge}}(\nu;\Lambda) := -\frac{\mathrm{d}}{\mathrm{d}\Lambda}\mathrm{N}(\nu;\Lambda) \qquad (10.1)$$

The dependence of the spectral density on Λ will be needed only in the vicinity of the Dirichlet boundary condition, $\Lambda = 0$, (3.6), where an expansion to first order in Λ is allowed. The spectral density (10.1) can then be written only in terms of the Dirichlet energies and Dirichlet weights,

$$\begin{aligned} d_{\mathrm{edge}}(\nu;\Lambda) &= \sum_{n=1}^{\infty} \frac{\mathrm{d}\nu_n}{\mathrm{d}\Lambda}(\Lambda)\, \delta\big(\nu - \nu_n(\lambda)\big) \\ &\simeq \sum_{n=1}^{\infty} \frac{\mathrm{d}\nu_n}{\mathrm{d}\Lambda}(0)\, \delta\Big(\nu - \nu_n(0) - \Lambda\, \frac{\mathrm{d}\nu_n}{\mathrm{d}\Lambda}(0)\Big) \\ &= \sum_{n=1}^{\infty} \delta\Big(\frac{\nu - \nu_n}{w_n} - \Lambda\Big)\ , \end{aligned} \tag{10.2}$$

which follows from (8.1) and the properties of the δ-function. The cross-correlation function is now defined as an integral over energy and boundary parameter

$$C(\nu_0) = \iint d_{\mathrm{int}}^{\mathrm{osc}}(\nu;\Lambda)\, d_{\mathrm{ext}}^{\mathrm{osc}}(\nu;-\Lambda)\, h(\Lambda)\, g(\nu-\nu_0)\, \mathrm{d}\Lambda\, \mathrm{d}\nu\ , \tag{10.3}$$

with normalized Gaussian window functions h and g. Here, h serves to restrict the integration over Λ to the range where the linear approximation in (10.2) is valid and may have a width of order one. The function g, on the other hand, is needed since the spectra are discrete. It selects a narrow energy interval centered around the energy ν_0 and should have the width of a few effective nearest neighbour spacings.

Inserting expression (10.2), the cross-correlation function turns into a double sum over the interior and exterior edge spectrum,

$$C(\nu_0) = \sum_{i,j=1}^{\infty} \frac{w_i w_j'}{w_i + w_j'}\, g\left(\frac{\dfrac{\nu_i - \nu_0}{w_i} - \dfrac{\nu_0 - \nu_j'}{w_j'}}{\dfrac{1}{w_i} + \dfrac{1}{w_j'}}\right) h\left(\frac{\nu_i - \nu_j'}{w_i + w_j'}\right) - C_{\mathrm{bg}}\ , \tag{10.4}$$

where the primes label the exterior energies and weights, for the sake of brevity.

The important point to note is that due to the small width of g only a few pairs of interior and exterior spectral points will contribute appreciably at a given ν_0. It is the pairs with equal *weighted distances* from the left and right, respectively, to the reference energy ν_0. Here, the energy differences are scaled individually by the reciprocal weight attached to each spectral point. The function h, in contrast, limits the absolute energy distance. Note also that the prefactor in (10.4) ensures that those pairs which include one bulk state do not contribute to the sum.

The term C_{bg} in (10.4) subtracts the background. It is approximated by

$$C_{\mathrm{bg}} \simeq \overline{d}_{\mathrm{edge}}(\nu_0) \left(\sum_{i=1}^{\infty} h\Big(\frac{\nu_i - \nu_0}{w_i}\Big) + \sum_{j=1}^{\infty} h\Big(\frac{\nu_j' - \nu_0}{w_j'}\Big) - \overline{d}_{\mathrm{edge}}(\nu_0) \right)\ , \tag{10.5}$$

if we neglect the width of g and disregard the fact that the interior and exterior mean edge densities differ in the higher order terms.

The semiclassical correlator

We turn now to the semiclassical evaluation of the correlation function using the periodic orbit formula (8.9) discussed in Section 8.2. One obtains a double sum over the skipping interior and exterior periodic orbits:

$$\begin{aligned}C(\nu_0) = \int \mathrm{d}\nu\, g(\nu-\nu_0)\ \frac{2}{\pi^2}\sum_{\gamma,\gamma'} &\frac{w_\gamma\,\tau_\gamma}{r_\gamma\,|\operatorname{tr}\mathrm{M}(\gamma)-2|^{\frac{1}{2}}}\ \frac{w_{\gamma'}\,\tau_{\gamma'}}{r_{\gamma'}\,|\operatorname{tr}\mathrm{M}(\gamma')-2|^{\frac{1}{2}}}\\ \times\Bigg\{ &\cos\Big(2\pi\nu\big(\mathrm{A}(\gamma)+\mathrm{A}(\gamma')\big)-\pi(n_\gamma+n_{\gamma'})-\frac{\pi}{2}(\mu_\gamma+\mu_{\gamma'})\Big)\\ &\times\ \hat{h}\Big(\frac{1}{\pi}\sum_{j=1}^{n_\gamma}|\hat{\mathbf{n}}_j\hat{\mathbf{v}}_j| - \frac{1}{\pi}\sum_{j=1}^{n_{\gamma'}}|\hat{\mathbf{n}}'_j\hat{\mathbf{v}}'_j|\Big)\\ &+\cos\Big(2\pi\nu\big(\mathrm{A}(\gamma)-\mathrm{A}(\gamma')\big)-\pi(n_\gamma-n_{\gamma'})-\frac{\pi}{2}(\mu_\gamma-\mu_{\gamma'})\Big)\\ &\times\ \hat{h}\Big(\frac{1}{\pi}\sum_{j=1}^{n_\gamma}|\hat{\mathbf{n}}_j\hat{\mathbf{v}}_j| + \frac{1}{\pi}\sum_{j=1}^{n_{\gamma'}}|\hat{\mathbf{n}}'_j\hat{\mathbf{v}}'_j|\Big)\Bigg\}\end{aligned} \tag{10.6}$$

Here, $\hat{h}$ is the Fourier transform of the window function h, and the exterior quantities are again marked with a prime. The width of $\hat{h}$ is small compared to the sum over $|\hat{\mathbf{n}}_j\hat{\mathbf{v}}_j|$ (which is of order n_γ). As a result, the second term in the curly brackets of (10.6) is suppressed. In the first term of equation (10.6), $\hat{h}$ reduces the sum effectively to those pairs with approximately equal sums of angles of incidence $\sum_j|\hat{\mathbf{n}}_j\hat{\mathbf{v}}_j| = \sum_j|\hat{\mathbf{n}}'_j\hat{\mathbf{v}}'_j|$. It is the dual pairs of periodic orbits discussed in Section 3.2.3 which have this property. Hence, the only systematic contribution to the correlator will come from these pairs. In Sect. 6.3.3 we discussed the relations between γ and its dual partner orbit $\overline{\gamma}$, which may be summarized as

$$\begin{array}{rclrcl} \mathrm{A}(\gamma)+\mathrm{A}(\overline{\gamma}) &=& n_\gamma = n_{\overline{\gamma}} & r_{\overline{\gamma}} &=& r_\gamma \\ \operatorname{tr}\mathrm{M}(\overline{\gamma}) &=& \operatorname{tr}\mathrm{M}(\gamma) & \mu_{\overline{\gamma}} &=& 2n_\gamma-\mu_\gamma \\ |\hat{\mathbf{n}}_j\hat{\mathbf{v}}_j|_{(\overline{\gamma})} &=& |\hat{\mathbf{n}}_{j-n_\gamma}\hat{\mathbf{v}}_{j-n_\gamma}|_{(\gamma)} & w_{\overline{\gamma}}\,\tau_{\overline{\gamma}} &=& w_\gamma\,\tau_\gamma\ . \end{array} \tag{10.7}$$

If we retain only the contributions of dual pairs, the cross-correlation function simplifies to a single sum over interior (or exterior) periodic orbits. Assuming global duality we obtain

$$C(\nu_0) = \frac{2}{\pi^2}\sum_\gamma \frac{w_\gamma^2\,\tau_\gamma^2}{r_\gamma^2\,|\operatorname{tr}\mathrm{M}(\gamma)-2|}\cos(2\pi n_\gamma(\nu_0-\tfrac{1}{2}))\ \hat{g}(n_\gamma)\ . \tag{10.8}$$

The restriction of the double sum (10.6) to the dual pairs is tantamount to the *diagonal approximation* used in the semiclassical evaluation of the autocorrelation function [119]. In present case, the actions of the chosen pairs of periodic orbits complement each other, while in the usual diagonal approximation it is the resonant terms, $\mathrm{A}(\gamma)-\mathrm{A}(\gamma')=0$, which give the dominant “diagonal” contribution.

In deriving (10.8), the energy dependence of the amplitudes of the trace formula could be neglected since the variation of the energy was assumed to be small on the classical scale in (10.3). If ν_0 is taken large (i.e. we are in the semiclassical regime of the spectrum) the classical quantities in (10.8) will hardly change as ν_0 is varied. By grouping together the contributions from all the periodic orbits with the same number of reflections n_γ we obtain

$$C(\nu_0) = \sum_{n=n_{\min}}^{\infty} f(n)\,\hat{g}(n)\,\cos(2\pi n(\nu_0 - \tfrac{1}{2}))\,, \tag{10.9}$$

with

$$f(n) = \frac{2}{\pi^2} \sum_{\gamma : n_\gamma = n} \frac{w_\gamma^2\,\tau_\gamma^2}{r_\gamma^2\,|\,\mathrm{tr}\,\mathrm{M}(\gamma) - 2|}\,. \tag{10.10}$$

Assuming ergodicity, the weighted sum over classical n-orbits (10.10) can be calculated as a phase space average. For large n it takes on the universal value $f(n) = n/8$. At the same time, the number of reflections n_γ is geometrically bounded from bellow, $n \geq n_{\min}$, for a given cyclotron radius. Hence,

$$f(n) = \begin{cases} 0 & \text{for } n < n_{\min} \\ \frac{1}{8}n & \text{as } n \gg n_{\min}\,. \end{cases} \tag{10.11}$$

Equation (10.9) makes a clear prediction on the form of the cross-correlation function. Even if the classical dynamics changes slowly as ν_0 is varied, the infinite sum (10.9) will be appreciable only at energies $\nu_0 = N + \frac{1}{2}$, $N \in \mathbb{N}_0$, where the cosine terms are stationary. We therefore expect the cross-correlation function to display pronounced, equidistant peaks at large energies. These peaks are a direct manifestation of the existence of dual orbits. Their positions are expected to coincide with the Landau levels (although they have nothing to do with bulk states).

This prediction is not restricted to purely chaotic dynamics, although the bouncing map was assumed to be hyperbolic, so far. For the (integrable) disk one obtains a completely analogous result. The function $f(n)$ is not universal in this case, but the prediction remains that $C(\nu_0)$ is peaked at the energies of the Landau levels. The statement carries over to generic magnetic billiards, if we are allowed to approximate a mixed chaotic system by a union of non-overlapping hyperbolic and integrable phase space domains.

10.2 Statistical evidence

In Figure 10.1 we show the cross-correlation function (10.4) for the ellipse billiard at magnetic length $b = 0.1$. It was calculated from the edge spectra shown in Figures 8.3 and 8.6. The corresponding classical dynamics is generic (mixed chaotic) and there is a strict, one-to-one correspondence between the interior and the exterior classical dynamics up to $\nu = 21.6$. Beyond this energy, when the cyclotron radius is greater than the minimum radius of curvature, the classical duality still holds in a substantial part of phase space.

One observes that $C(\nu_0)$ is strongly fluctuating, and displays pronounced, equidistant peaks at energies $\nu_0 = N + \frac{1}{2}$. In Figure 10.2 we focus on these dominant structures by plotting the cross-correlation function in terms of $\nu_{\text{shift}} = \nu_0 (\mathrm{mod}\ 1)$ around one half. To check that this clear signal is not an artefact or due to the accumulation of bulk states, we make use of the fact that the spectra of the ellipse decompose into

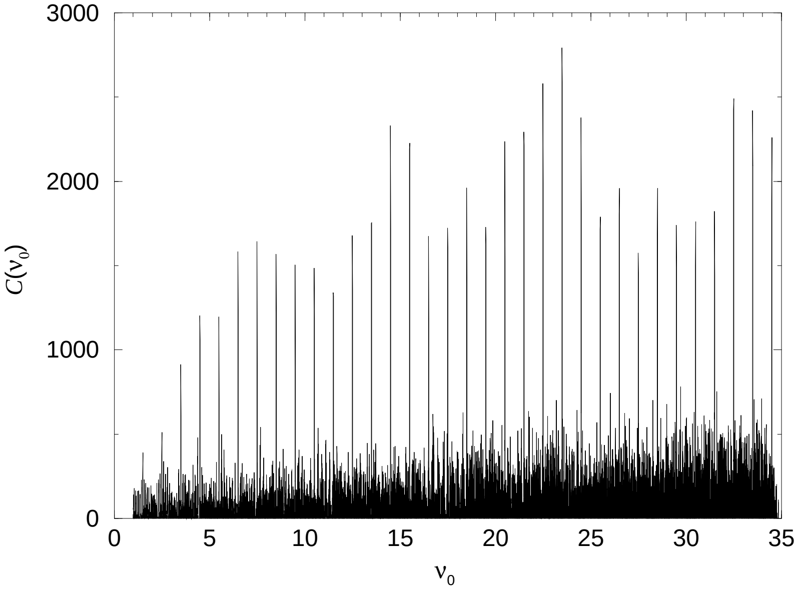

Figure 10.1: Cross-correlation function (10.4) for the elliptic billiard (eccentricity $\varepsilon = 0.8$, $b = 0.1$, $\sigma_g = 0.001$, $\sigma_h = 1$, positive part). The pronounced peaks at $\nu_0 = N + \frac{1}{2}$, $N \in \mathbb{N}_0$, indicate the existence of non-trivial correlations between interior and exterior edge states. (The figure remains unchanged if one removes all bulk states from the sum (10.4) by imposing a threshold on w_n; not shown.)

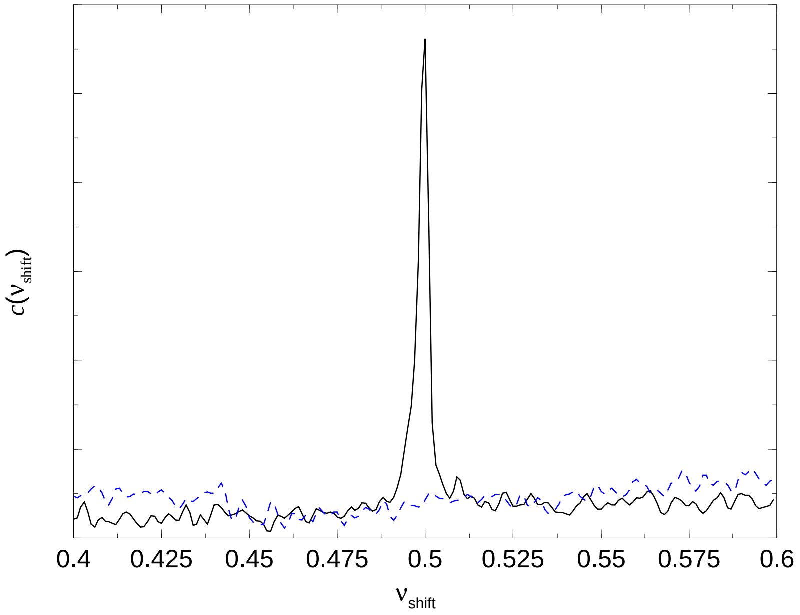

Figure 10.2: Cross-correlation function of Fig. 10.1, summed over integer shifts of the argument, $c(\nu_{\text{shift}}) = \sum_n C(n + \nu_{\text{shift}})$. In the double sum (10.4) the energies were taken within the same symmetry class (solid line) and between different symmetry classes (dotted line.)

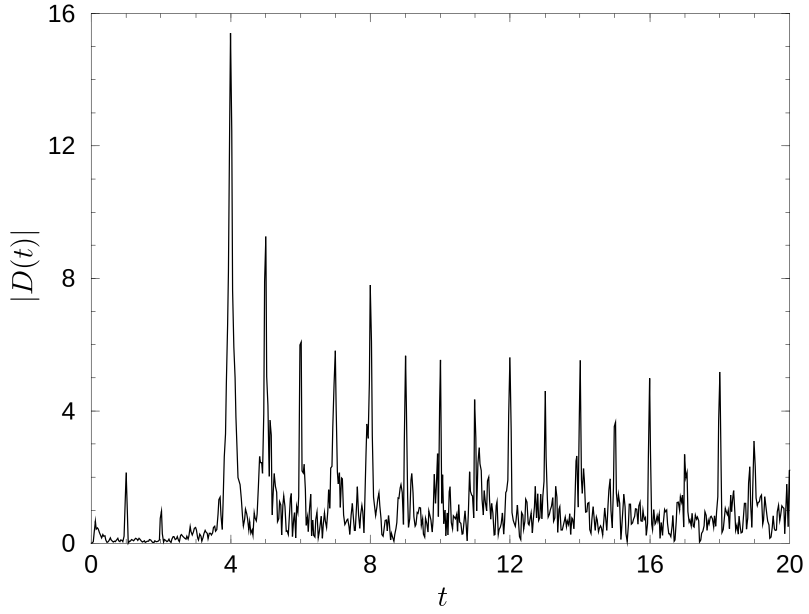

Figure 10.3: Fourier transformation $D(t)$, eq (10.13), of the cross-correlation function $C(\nu_0)$ given in Fig. 10.1 (absolute value). The peaks at integer t correspond to the combined actions of dual periodic orbits ($\sigma_g = 5\times\ 10^{-4}$, $\sigma_h = 4$.) The fact that the peaks are substantial starting from $n_{\min} = 4$ clearly proves the classical origin of the cross correlations.

two symmetry classes. The semiclassical prediction for the cross correlation between exterior and interior spectra with different symmetries is derived in a similar fashion as (10.9). However, now we have

$$f(n) = \frac{2}{\pi^2} \sum_{\gamma : n_\gamma = n} (-)^{s_\gamma} \frac{w_\gamma^2\, \tau_\gamma^2}{r_\gamma^2\, |\,\mathrm{tr}\,\mathrm{M}(\gamma) - 2|}\ , \tag{10.12}$$

where s_γ counts the number of times the periodic orbit γ crosses the symmetry line [137]. Since s_γ will be even or odd with equal probability for a given n, the terms cancel on average, and no correlation signal is expected. This is clearly supported by the numerical results shown as a dashed line in Figure 10.2.

Action cross correlations

Next, we consider the Fourier transform of the cross-correlation function (10.3), which highlights its fluctuating part. The semiclassical theory predicts a sequence of equidistant δ-spikes at integer values,

$$D(t) = \int C(\nu_0)\, \mathrm{e}^{-2\pi \mathrm{i} \nu_0 t} \mathrm{d}\nu_0 = \frac{1}{2} \sum_{n=n_{\min}}^{\infty} (-)^n f(n)\, \hat{g}(n)\, \delta(n-t)\ . \tag{10.13}$$

They correspond to the sums of the actions of dual pairs, which complement each other to integer values, starting from the minimal number of reflections $n_{\min}$.

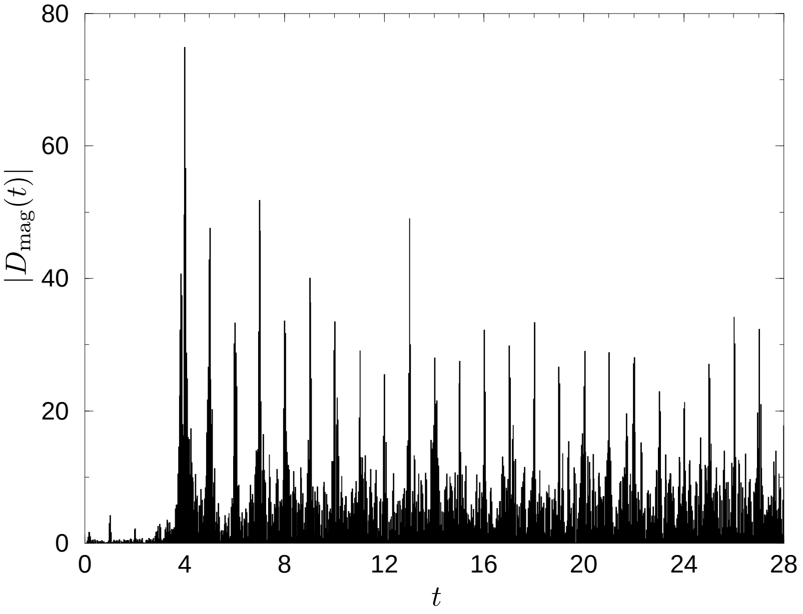

Figure 10.4: Fourier transform of the cross correlation function (10.14) defined in terms of the edge magnetization density. The graph should be compared to Fig. 10.3. It shows that also the edge magnetization density $\widetilde{\mathrm{m}}_{\mathrm{edge}}$ permits to unravel the cross correlations. ($\sigma_g = 5 \times 10^{-4}$, $\sigma_h = 0.5$)

The absolute value of $D(t)$, calculated for the same spectrum as Fig. 10.1, is shown in Figure 10.3. In this case, the periodic orbits of the de-symmetrised ellipse have at least $n_{\mathrm{min}} = 4$ reflections. One observes that $|D(t)|$ displays distinct spikes at integer values.[*] As predicted by the semiclassical theory, the dominant peaks start at $n_{\mathrm{min}} = 4$, which is a clear proof for the classical origin of the edge state correlations.

The tiny peaks at $t = 1, 2, 3$ vanish if one decreases the width of the window function g (which in turn deteriorates the statistical significance of the result). They are due to the remnant contributions of the bulk states, and disappear if one removes the bulk states from the correlator sum by setting a threshold on the weights (not shown; the remaining peaks would not change by this procedure).

Using the edge magnetization

Let us turn to the question whether the correlation is also seen if one uses the (unsigned) edge magnetization density (8.18) as the spectral measure. The latter has the advantage of being easier to measure, both numerically and in experiments, since one does not have to change the boundary conditions. The theoretical treatment is analogous to the above, with the correlation function now involving an integration over the variation in (the square of) the magnetic length, δb^2, rather than the boundary condition:

---

[*] The real parts of the peaks have signs $(-)^n$, as expected from eq (10.10); not shown.

$$C_{\mathrm{mag}}(\nu_0) = -\iint \widetilde{\mathrm{m}}_{\mathrm{edge}}^{\mathrm{osc(int)}}(\nu; b^2+\delta b^2)\, \widetilde{\mathrm{m}}_{\mathrm{edge}}^{\mathrm{osc(ext)}}(\nu; b^2+\delta b^2) \times h\Big(\frac{\delta b^2}{b^2}\Big)\, g(\nu-\nu_0)\, \frac{\mathrm{d}(\delta b^2)\,\mathrm{d}\nu}{b^2} \ . \tag{10.14}$$

The minus sign accounts for the fact that the edge magnetization of the exterior problem is negative. The linear expansion of the dependence of the energies on b^2 yields a double sum like eq (10.4), with the edge weights (8.1) replaced by the moduli of the magnetization weights (8.16). Semiclassically, the integration over δb^2 selects those pairs of interior and exterior orbits which satisfy

$$u_\gamma\, \tau_\gamma = -u_{\gamma'}\, \tau_{\gamma'} \ , \tag{10.15}$$

which is again the *dual* pairs. (This is seen from eqs (8.20) and (6.56), since the signs of the σ_j, eq (6.51), and the order of the points of reflection $\mathbf{r}_j$ are reversed as one goes from an orbit to its dual.) We repeated the calculation of the cross-correlation function of the ellipse spectrum, using the edge magnetization density as the spectral measure. The resulting function exhibits peaks at the Landau energies similar to Fig. 10.1 (not shown.) Its Fourier transform is given in Figure 10.4. This shows that the edge magnetization density $\widetilde{\mathrm{m}}_{\mathrm{edge}}$ succeeds to unravel the cross correlations, similar to the edge density d_{edge}.

The hyperbolic case

The ellipse spectrum considered so far exhibits generic, mixed chaotic dynamics, with relatively large integrable parts in phase space. As the last point, we demonstrate that the correlations do exist also in a system which is (essentially) hyperbolic. We take the spectrum of the stadium billiard defined in Fig. 9.5 and use the edge magnetization as the spectral density.

As discussed in Chapter 9, the spectral interval shown in Fig. 9.6 corresponds to cyclotron radii large enough to guarantee that the corresponding classical dynamics is essentially hyperbolic (ie, the integrable parts of phase space are much smaller than $(b^2\pi)^2$). Figure 10.5 gives the corresponding cross-correlation function. Like in Fig. 10.2 the variable is plotted modulo one in order to focus attention on the peaks. Again, we observe a clear cross-correlation signal for pairs within the same symmetry class (solid line) while the reference calculation from different symmetry classes shows no peak (dashed line).

10.3 The pair relation

The peaks in $C(\nu_0)$ were attributed to the complementarity of the actions of dual orbits. Quantum mechanically, their occurrence implies that there exists a pairwise relation between individual interior and exterior edge states. This follows from the discussion of the quantum correlator (10.4) above. We have noted that pairs of edge energies contribute only if they have the same weighted distance to the reference energy from

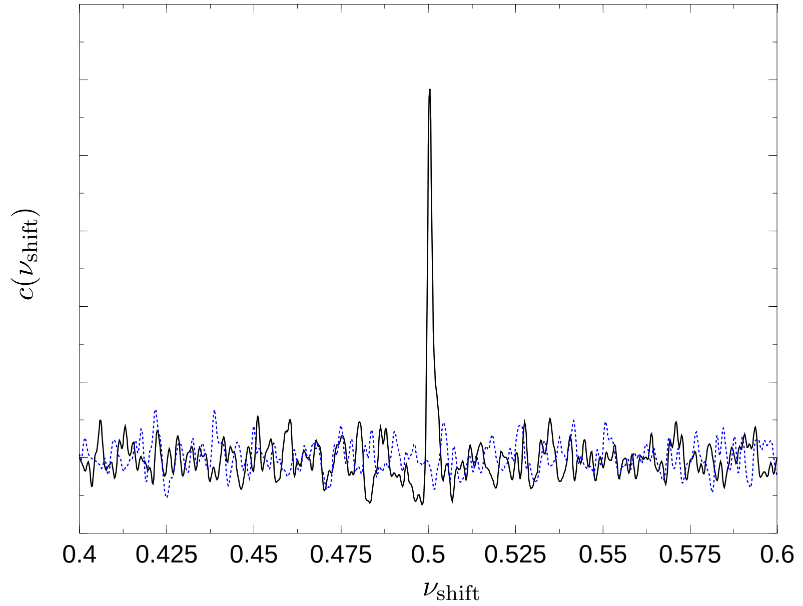

Figure 10.5: Cross-correlation summed over integer shifts of the argument like in Fig. 10.2. The data belongs to the stadium billiard in Fig. 9.6 ($\nu = 100 - 135$, $\sigma_g = 5 \times 10^{-4}$, $\sigma_h = 0.2$, using the edge magnetization density (8.18).) A clear cross-correlation exists between energies of the same symmetry class (full line), while there is no signal if the energies are taken from different symmetry classes (dotted line.)

the left and right, respectively. Since the peaks appear at $\nu_0 = N + \frac{1}{2}$, the interior energies ν_i and exterior energies ν'_j must appear in pairs, such that, according to (10.4)

$$\frac{\nu_i - (N - \frac{1}{2})}{w_i} \cong \frac{(N - \frac{1}{2}) - \nu'_j}{w'_j} \qquad (10.16)$$

with integer N. Although this is not an exact relation, it will be the more precise the larger and the closer the two energies are, since the semiclassical approximation (8.9) and the linearization (10.2) then hold the better.

The information provided by the ratio of the individual quantum weights plays a crucial role in unravelling this pair correlation. It explains why standard correlation functions, which involve unweighted densities, do not show any signal, in general. Moreover, the fact that the quantum weights enter reciprocally in (10.16) explains how a pairwise relation between interior and exterior states can exist in spite of different local unweighted densities. It is consistent with the mean edge densities (8.3) being equal in the interior and exterior.[*]

It should be mentioned that the relation (10.16) can be deduced also from the semiclassical relation between the P operators of dual maps, cf Sect. 6.2, without invoking

---

[*] Using the edge magnetization weights (8.19) we obtain the same picture, which implies that the individual ratios of the edge and the magnetization weights are approximately equal. This is indeed observed numerically.

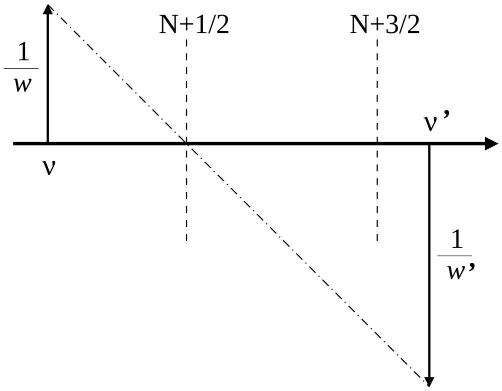

Figure 10.6: For every correlated pair of interior and exterior edge energies, ν and ν', there exists a Landau level $N + \frac{1}{2}$ such that the distances – scaled individually by the reciprocal quantum weights, w and w' – coincide.

Pair	ν_n	w_n	$\frac{\nu_n - \nu_0}{w_n}$	$\frac{\nu_0 - \nu'_n}{w'_n}$	w'_n	ν'_n
top	32.5367	0.826	0.0445	0.0444	0.506	32.4775
middle	33.5248	0.489	0.0507	0.0501	0.533	33.4733
bottom	32.5082	0.286	0.0288	0.0248	0.508	32.4874

Table 10.1: Energies and weights of the correlated pairs in Fig. 10.7, with the primes indicating exterior states.

periodic orbit theory. This will be discussed elsewhere [138]. It shows that the pairwise cross-correlation is a generic semiclassical feature of dual magnetic billiards, and is not related to the type of the classical motion.

For a given interior edge state it is of course not known, a priori, which is the associated Landau level $N + \frac{1}{2}$ and the exterior weight. Therefore, even in an asymptotic sense it is not possible to infer an edge spectrum given the complementary one, using the relation (10.16). However, having an interior and exterior edge spectrum available, one can clearly decide whether they belong to the same billiard.

In the spectra considered here, we could easily spot single pairs of edge states using the relation (10.16). Examples are given in Table 10.1. It is natural to ask how the correlation shows up in the corresponding wave functions.

Correlated wave functions

We proceed to present three pairs of correlated wave functions of the ellipse billiard. The interior states were chosen to have different locations in Figure 8.6 (displaying the distribution of quantum weights on page 113, top part). At energies corresponding to $\rho \approx 0.57$ we took states with weights lying in the top branch of the rightmost bifurcation structure, in the middle, and in the bottom branch, respectively. The corresponding exterior states were identified using the pair relation (10.16). Table 10.1 lists

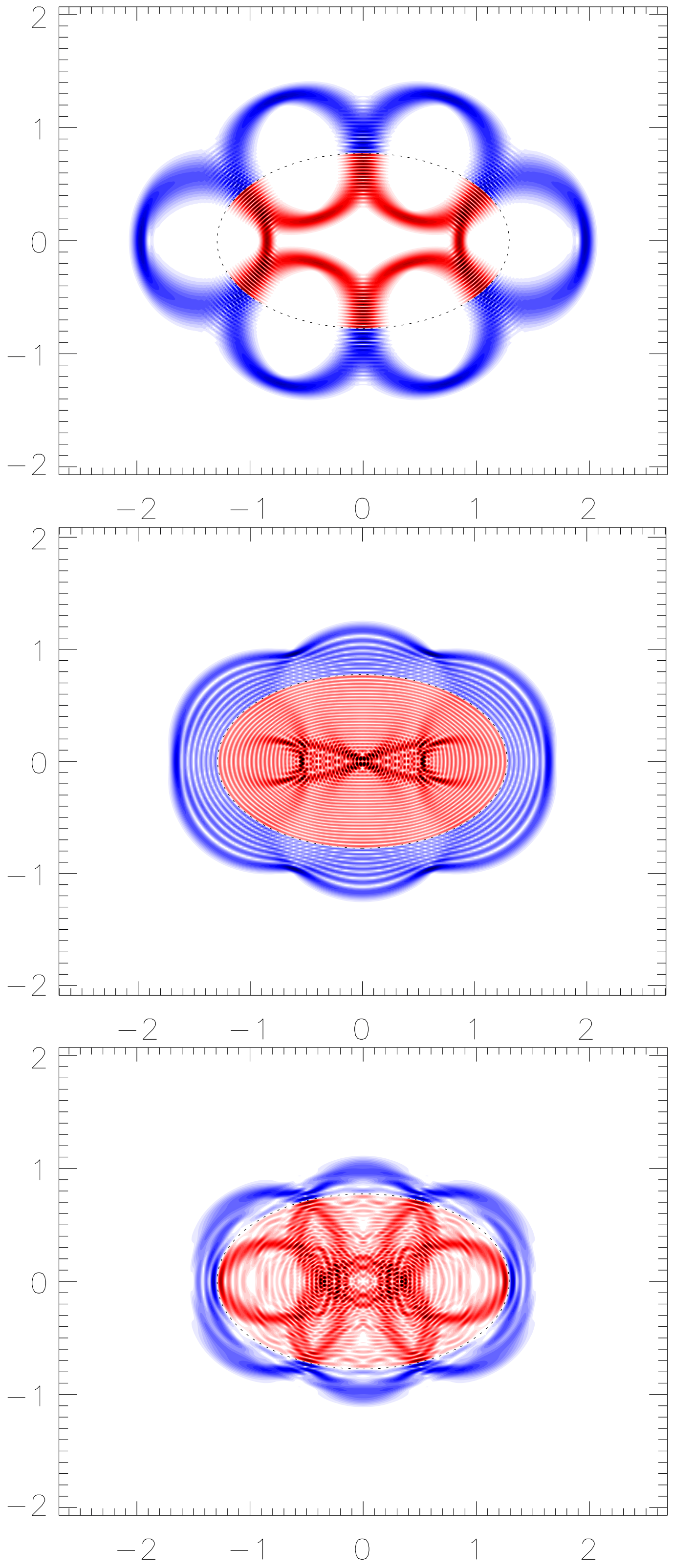

Figure 10.7: Pairs of correlated interior and exterior wave functions. The energies and weights are given Table 10.1. (Ellipse billiard at $b = 0.1$; the shading is proportional to the modulus of the wave function, and the boundary is indicated by a dotted line.)

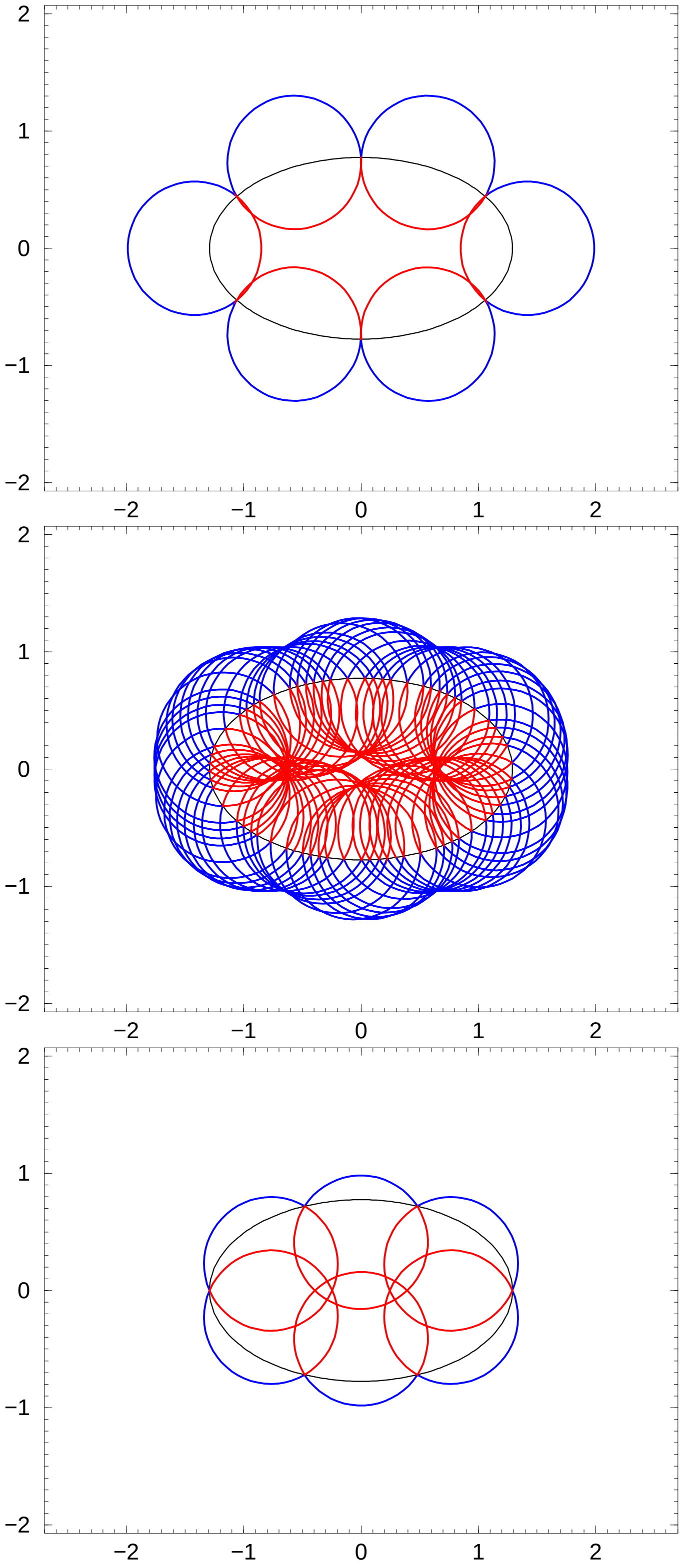

Figure 10.8: Dual pairs of classical periodic orbits in the ellipse billiard, at $\rho = 0.57$. The top and bottom orbits are stable, while the middle one in unstable. Their classical weights (8.10) correspond to the quantum weights (8.1) of the states in Fig. 10.7.

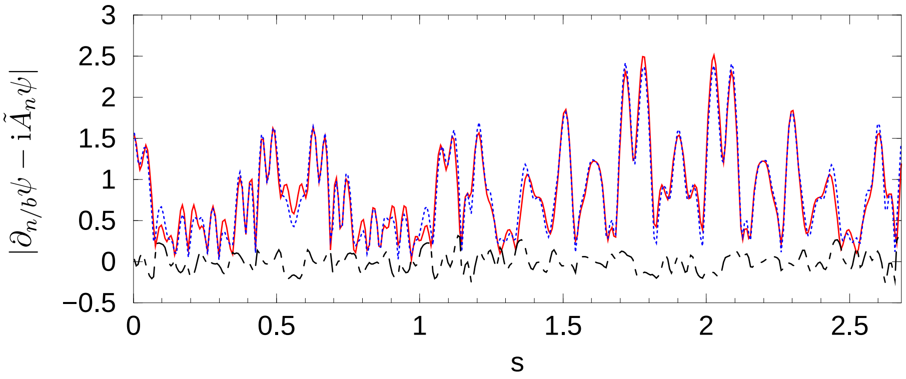

Figure 10.9: Boundary functions $|u| = |\partial_{n/b}\psi - \mathrm{i}\tilde{A}_n\psi|$ of the correlated wave functions depicted in Fig. 10.10 (along one half of the boundary). Solid line: interior ($\nu = 110.6567$), dotted line: exterior ($\nu' = 110.4841$). The difference is given as a dashed line.

the data for the three pairs.

In Fig. 10.7 we present superimpositions of the interior and the exterior wave functions. One clearly observes that the top and bottom wave functions are localized on dual periodic orbits. The structures of increased density of classical weights in Fig. 8.6 (page 113, bottom part) may indeed be attributed to periodic orbits which bifurcate as the cyclotron radius ρ is increased. The top and bottom wave functions were taken from a fork which belongs to orbits with period 6. They are shown in Fig. 10.8, along with their dual partners.

The middle wave functions in Figure 10.7, in contrast, are localized on a chaotic region in phase space confined by un-destroyed invariant tori. For comparison, an unstable pair of dual classical orbits from this region is given in the middle part of Fig. 10.8. Note that it exhibits the same spatial extension as the wave functions. Here, the correlation of interior and exterior wave functions is not evident from the visual inspection. However, comparing the normal derivatives of the wave functions on the boundary we observe that they are indeed very similar.

This is a feature shared by all pairs of correlated wave functions, including those which are based on a chaotic part of the phase space. Figure 10.9 compares the normal derivatives of a typical pair of correlated states taken from the stadium billiard. One observes that the moduli resemble each other, even though they are irregular. (The difference is indicated by the dashed line.) In general, as a consequence of (10.16), it is expected to be the smaller the closer two edge states are in energy. (If the energies happened to coincide, this would take place on a Landau level, and the continuation of one wave function would simply yield the other.)

Figure 10.10 superimposes the wave functions of the pair from the stadium billiard described in Fig. 10.9. Although they exhibit the typical irregular pattern of wave function based on a chaotic part of phase space, one can notice that the interior and exterior structures match. In the exterior wave function, scars of periodic orbits may be discerned if viewed in total (lower part of Fig. 10.10.)

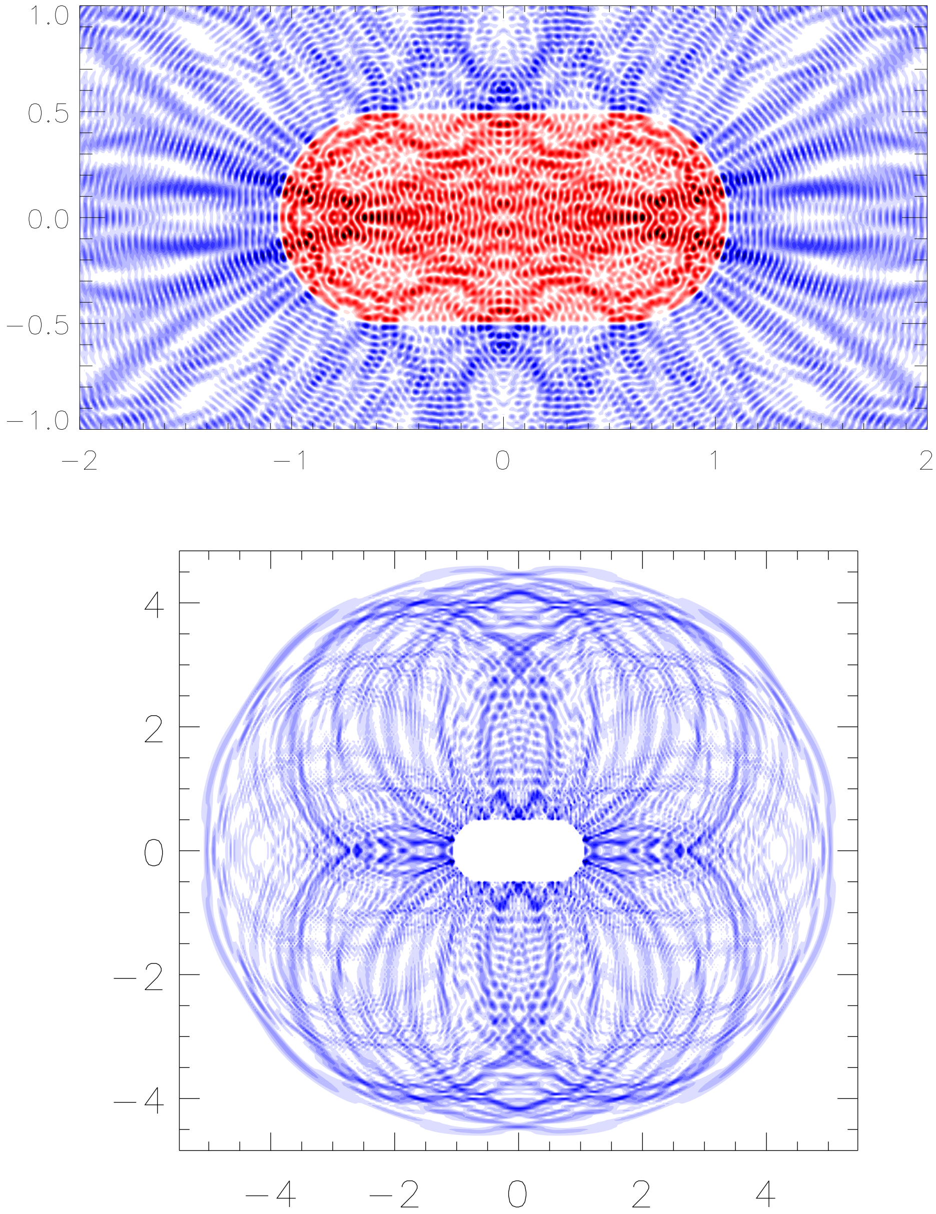

Figure 10.10: Top: A typical pair of correlated wave functions from the spectrum displayed in Fig. 9.6 (superimposed; $\nu = 110.6567$, $\nu' = 110.4841$, $b = 0.2$). The stadium-shaped boundary is not drawn but visible as a regular nodal line. The lower part shows the exterior wave function on a larger scale. (The circular scars match the cyclotron radius $\rho \simeq 2.10$.)

10.4 Conclusions

This thesis started out with a simple question — on the relation of the spectra of interior and exterior magnetic billiards. Cross-correlations were predicted and found, based on a duality between the respective classical motions. While one could anticipate to observe correlations between classical actions, ie, involving the Fourier transform of the spectral densities, it came as a surprise that the classical duality induces a connection even in the energy domain, between pairs of single edge states. This finding was confirmed statistically and demonstrated in exemplary cases.

We were able to perform the necessary numerical experiments only after developing a boundary integral scheme to quantize magnetic billiards. The method allowed for the first time to calculate exterior spectra and to access spectral intervals large and precise enough to permit the necessary statistical analysis. Moreover, it served as a starting point to derive the semiclassical trace formulas from first principles, solving an open problem in the field.

It turned out to be even more important to be able to apply a reasonable spectral measure for edge states. The edge state density introduced in this work was shown to suppress consistently the irrelevant bulk contributions, facilitating the statistical analysis of interior and exterior spectra. It was found to uncover the universal spectral autocorrelations expected for classically chaotic systems. The quantum weights involved turned out to be *the* vital ingredients to unravel the cross correlations.

We believe that our definition of edge states is a very natural choice, arguably the most natural one. Both, the mean and fluctuating part of the edge density have a clear physical interpretation. They are consistent with the notion of edge states as quasi one-dimensional states, which correspond to skipping motion. As a natural direction of further research one should ask whether the proposed spectral measure is applicable and useful in other areas, specifically for the physics of the (fractional) Quantum Hall effect, where the concept of edge states is frequently employed without a clear definition.

The experimental setups of mesoscopic physics are typically based on the Quantum Hall geometry, often with an antidot as a scattering obstacle. The latter may be considered a magnetic billiard placed close to leads which run to infinity. Unlike the isolated billiards considered in the present work, the exterior of the billiard now exhibits a continuous spectrum. It is worthwhile asking whether and how the cross-correlations survive in this case, ie, to what extend one can infer from the scattering information to the properties of the corresponding interior billiard problem.

Appendix A

Mathematical appendix

A.1 The stationary phase approximation

The method of the stationary phase provides asymptotic expansions of integrals with rapidly oscillating integrands, like $\int g(x)\mathrm{e}^{2\pi\mathrm{i}\nu f(x)}\mathrm{d}x$. One can show that for large ν the leading order contribution is due to the stationary points of the phase f. Expanding f to second order around these points and using the Gaussian integral,

$$\int_{-\infty}^{\infty} \mathrm{e}^{\mathrm{i}ax^2}\mathrm{d}x = \left(\frac{\pi}{|a|}\right)^{\frac{1}{2}} \mathrm{e}^{\mathrm{i}\,\mathrm{sgn}(a)\frac{\pi}{4}} \,, \tag{A.1}$$

one obtains the following statements: For functions $f, g \in C^{\infty}(\mathbb{R})$, with f displaying a finite number of non-degenerate stationary points $\mathbf{x}_j$, such that $f'(\mathbf{x}_j) = 0$ the asymptotic expansion reads [139]

$$\int g(x)\mathrm{e}^{2\pi\mathrm{i}\nu f(x)}\mathrm{d}x = \frac{1}{\sqrt{\nu}} \sum_{x_j} \frac{g(x_j)}{|f''(x_j)|^{\frac{1}{2}}} \mathrm{e}^{2\pi\mathrm{i}\nu f(x_j)+\mathrm{i}\frac{\pi}{4}\,\mathrm{sgn}(f''(x_j))} \left(1+\mathrm{O}(\nu^{-1})\right) \,, \tag{A.2}$$

as $\nu \to \infty$. For functions of an N-dimensional argument, $f, g \in C^{\infty}(\mathbb{R}^N)$, an analogous form can be found [140]:

$$\int g(\mathbf{x})\mathrm{e}^{2\pi\mathrm{i}\nu f(\mathbf{x})}\mathrm{d}^N\mathbf{x} \sim \left(\frac{\mathrm{i}}{\nu}\right)^{\frac{N}{2}} \sum_{\mathbf{x}_j} \frac{g(\mathbf{x}_j)}{|\det f''(\mathbf{x}_j)|^{\frac{1}{2}}} \mathrm{e}^{2\pi\mathrm{i}\nu f(\mathbf{x}_j)-\mathrm{i}\nu_j\frac{\pi}{2}} \,. \tag{A.3}$$

Here, ν_j gives the number of negative eigenvalues of the matrix $f''(\mathbf{x}_j)$.

A peculiar δ-function

As an immediate application, the stationary phase approximation allows to show that the complex function

$$\delta_\varepsilon(\xi) := \frac{1}{(2\pi\mathrm{i})^{\frac{1}{2}}} \frac{\exp\left(\mathrm{i}\,\frac{\xi^2}{2\varepsilon}\right)}{\sqrt{\varepsilon}} \tag{A.4}$$

has the property of a one-dimensional Dirac δ-function,

$$\int \delta_\varepsilon(\xi)\,\mathrm{d}\xi = 1 \tag{A.5}$$

$$\int g(\xi)\,\delta_\varepsilon(\xi)\,\mathrm{d}\xi = g(0)\,(1+\mathrm{O}(\varepsilon)) \qquad \text{as } \varepsilon \to 0. \tag{A.6}$$

This follows from Eqs. (A.1) and (A.2) with $\nu = 1/\varepsilon$ and $f = x^2/2$, and is not easily proven otherwise. The product of (A.4) for the two Cartesian components of the vector $\mathbf{r}$ yields the two dimensional δ-function

$$\lim_{\varepsilon\to 0} \frac{1}{2\pi \mathrm{i} b^2} \frac{1}{\varepsilon} \exp\left[\mathrm{i}\frac{(\mathbf{r}-\mathbf{r}_0)^2}{2\varepsilon b^2}\right] = \delta(\mathbf{r}-\mathbf{r}_0)\ , \tag{A.7}$$

which shows up in (2.51).

A.2 The singular integrals

The Fourier integrals defined in (4.49), (4.50) depend on a window function e. Our choice is (4.51) which switches off the asymptotically singular functions m and l sufficiently smoothly. For the logarithmic integrals one obtains

$$\begin{aligned}
\mathrm{L}_\ell(s_0) &= \int_{-\sigma_e}^{\sigma_e} \mathrm{d}s'\ \exp\Big[\mathrm{i}\Big(2\pi\ell/\mathscr{L} - \frac{\hat{\mathbf{t}}_0\times\mathbf{r}_0}{b^2}\Big)s'\Big]\mathrm{L}_\nu\Big(\frac{s'^2}{b^2}\Big)\ e(s') \\
&\qquad\qquad \times\Big(\mathrm{i}\Big[\alpha_\mathrm{c} + \frac{s'}{b^2}\Big] \mp \lambda\Big[\frac{2\nu}{b^2} - (\alpha_\mathrm{c} - \mathrm{i}\kappa_0)\frac{s'}{b^2}\Big]\Big) \\
&= \Big(\mathrm{i}\alpha_\mathrm{c} \mp \lambda\frac{2\nu}{b^2}\Big)\ \mathrm{I}_{\cos} + \big(-1 \pm \lambda(\kappa_0 + \mathrm{i}\alpha_\mathrm{c})\big)\ \mathrm{I}_{\sin}
\end{aligned} \tag{A.8}$$

with

$$\begin{aligned}
\mathrm{I}_{\cos} := {}& \frac{\cos(\pi\nu)}{4\pi}\ \frac{-1}{\Omega_l\,\varphi^+\,\varphi^-}\Big\{\pi^2\sin(\varphi)\Big[\log\Big(\frac{\sigma_e^2}{b^2}\Big) + \Psi(\tfrac{1}{2}-\nu) - 2\Psi(1)\Big] \\
&+ 2\varphi^+\varphi^-\ \mathrm{Si}(\varphi) + \varphi\,\varphi^+\ \mathrm{Si}(\varphi^-) + \varphi\,\varphi^-\ \mathrm{Si}(\varphi^+)\Big\}
\end{aligned} \tag{A.9}$$

and

$$\begin{aligned}
\mathrm{I}_{\sin} := {}& \frac{\cos(\pi\nu)}{4\pi}\ \frac{1}{\Omega_l^2 b^2\,(\varphi^+)^2\,(\varphi^-)^2} \\
&\times\Big\{\pi^2\varphi\,\varphi^+\varphi^-\ \cos(\varphi)\Big[\log\Big(\frac{\sigma_e^2}{b^2}\Big) + \Psi(\tfrac{1}{2}-\nu) - 2\Psi(1)\Big] \\
&\quad - \pi^2(3\varphi^2-\pi^2)\sin(\varphi)\Big[\log\Big(\frac{\sigma_e^2}{b^2}\Big) + 2 + \Psi(\tfrac{1}{2}-\nu) - 2\Psi(1)\Big] \\
&\quad - 2(\varphi^+)^2(\varphi^-)^2\ \mathrm{Si}(\varphi) - \varphi^2(\varphi^-)^2\ \mathrm{Si}(\varphi^+) - \varphi^2(\varphi^+)^2\ \mathrm{Si}(\varphi^-)\Big\}\ ,
\end{aligned} \tag{A.10}$$

where $\Omega_l(s_0) = 2\pi\ell/\mathscr{L} - \frac{\hat{\mathbf{t}}_0\times\mathbf{r}_0}{b^2}$, $\varphi = \Omega_l(s_0)\,\sigma_e$, $\varphi^\pm = \varphi\pm\pi$, and Si is the Sine Integral. The finite part integral reads

$$\begin{aligned}
\mathrm{M}_\ell(s_0) &= \mp\lambda\frac{\cos(\pi\nu)}{2\pi} \,⨎_{-\sigma_e}^{\sigma_e} \mathrm{d}s'\ \mathrm{e}^{\mathrm{i}(2\pi\ell/\mathscr{L} - \frac{\hat{\mathbf{t}}_0\times\mathbf{r}_0}{b^2})s'}\,\frac{-1}{s'^2}\cos^2\Big(\frac{\pi}{2}\frac{s'}{\sigma_e}\Big) \\
&= \mp\lambda\frac{\cos(\pi\nu)}{2\pi}\lim_{\varepsilon\to 0}\Big[2\int_\varepsilon^{\sigma_e}\cos(\Omega_l s)\frac{-1}{s^2}\cos^2\Big(\frac{\pi}{2}\frac{s}{\sigma_e}\Big)\mathrm{d}s + \frac{2}{\varepsilon}\Big]
\end{aligned}$$

$$
\begin{aligned}
&= \mp\,\lambda\frac{\cos(\pi\nu)}{2\pi}\Big(\frac{1}{2\sigma_e}\big\{2(\cos(\varphi)+\varphi\;\mathrm{Si}(\varphi))+\cos(\varphi^+)+\varphi^+\,\mathrm{Si}(\varphi^+)\\
&\quad+\cos(\varphi^-)+\varphi^-\;\mathrm{Si}(\varphi^-)\big\}+\lim_{\varepsilon\to 0}\Big[-\frac{1}{2\varepsilon}\big\{4+\mathrm{O}(\varepsilon)\big\}+\frac{2}{\varepsilon}\Big]\Big)\\
&= \mp\,\lambda\frac{\cos(\pi\nu)}{4\pi\sigma_e}\big\{2\varphi\;\mathrm{Si}(\varphi)+\varphi^+\;\mathrm{Si}(\varphi^+)+\varphi^-\;\mathrm{Si}(\varphi^-)\big\}\;. \qquad \text{(A.11)}
\end{aligned}
$$

Asymptotically, we have

$$
\mathrm{M}_\ell(s_0)\sim\mp\,\lambda\,\frac{\cos(\pi\nu)}{2}\,\Omega_l(s_0)\,\mathrm{sgn}(\ell) \qquad \text{as } |\ell|\to\infty. \qquad \text{(A.12)}
$$

Note that with the choice (4.51) the limit of the remaining kernel is

$$
\begin{aligned}
&\lim_{s\to s_0}\Big[\widehat{\mathrm{q}}(s,s_0)-e(s-s_0)\,\big(\mathrm{l}(s,s_0)+\mathrm{m}(s,s_0)\big)\Big]\\
&=\frac{\cos(\pi\nu)}{4\pi}\Big[\kappa_0(1\mp\lambda\mathrm{i}\alpha_\mathrm{c})\mp\lambda\big(-\frac{2\nu}{b^2}-\frac{\pi^2}{2\sigma_e^2}\big)\Big] \qquad \text{(A.13)}
\end{aligned}
$$

which is *not* just the constant part of (4.39), but contains a term which depends on the width σ_e of the window function.

Appendix B

Angular momentum representation

B.1 Free Green function

In Section 2.5, the magnetic Green function was obtained by a direct evaluation of the Fourier integral. In this appendix, we derive its angular momentum decomposition. It allows us to correct some erroneous results in the literature [9, 39], and to discuss the irregular Green function. Moreover, the solutions of the radial Schrödinger equation, which are obtained below, are needed in Chapter 7.

The symmetric gauge must be employed since only this choice renders the angular momentum a constant of the motion. In polar coordinates, the inhomogeneous Schrödinger equation (2.53) then assumes the form

$$\Big[-\frac{1}{4}(\partial_{\tilde r}^2+\frac{1}{\tilde r}\partial_{\tilde r})+\frac{1}{4}(\tilde r+\mathrm{i}\frac{\partial_\vartheta}{\tilde r})^2-\nu\Big]\mathrm{G}_\nu=-\frac{1}{4}\,\delta(\tilde{\mathbf{r}}-\tilde{\mathbf{r}}_0)\ . \tag{B.1}$$

An ansatz in terms of the difference of polar angles,

$$\mathrm{G}_\nu(\mathbf{r},\mathbf{r}_0)=\frac{1}{2\pi}\sum_{m=-\infty}^{\infty}\mathrm{e}^{\mathrm{i}m(\vartheta-\vartheta_0)}G_m(\tilde r,\tilde r_0)\ , \tag{B.2}$$

which cannot be justified a priori, allows to separate radial and angular coordinates. For $\tilde r\neq\tilde r_0$, the G_m solve the radial Schrödinger equation in the free plane

$$\Big[\partial_{\tilde r}^2+\frac{1}{\tilde r}\partial_{\tilde r}-\frac{(\tilde r^2-m)^2}{\tilde r^2}+4\nu\Big]G_m(\tilde r,\tilde r_0)=0 \tag{B.3}$$

The definition

$$G_m(\tilde r,\tilde r_0)=\tilde r^{|m|}\,\mathrm{e}^{-\tilde r^2/2}\,g_m(\tilde r^2) \tag{B.4}$$

leads to an equation for g_m,

$$zg_m''(z)+(1+|m|-z)g_m'(z)-\Big(\frac{1}{2}-\nu+\frac{|m|-m}{2}\Big)g_m(z)=0\ , \tag{B.5}$$

which is known as Kummer's differential equation and satisfied by regular and irregular hypergeometric functions [43], ${}_1\mathrm{F}_1$ and U, respectively. For energies different from the Landau levels, it follows that a pair of independent solutions u_1, u_2 of the radial Schrödinger equation (B.3) is given by

$$u_1(\tilde r)=\tilde r^{|m|}\,\mathrm{e}^{-\tilde r^2/2}\ {}_1\mathrm{F}_1\Big(\frac{1}{2}-\nu+\frac{|m|-m}{2},1+|m|,\tilde r^2\Big) \tag{B.6}$$

and

$$u_2(\tilde{r}) = \tilde{r}^{|m|}\, \mathrm{e}^{-\tilde{r}^2/2}\, \mathrm{U}\Big(\frac{1}{2} - \nu + \frac{|m| - m}{2}, 1 + |m|, \tilde{r}^2\Big)\ . \tag{B.7}$$

Both are real valued solutions. u_1 is bounded at $\tilde{r} = 0$, and diverges as $\tilde{r} \to \infty$. The function u_2, on the other hand, decays like a Gaussian in this limit, but displays a (logarithmic) singularity as $\tilde{r} \to 0$.

Another fundamental system of equation (B.3) is obtained if one replaces u_2 by

$$u_2^{\mathrm{irr}}(\tilde{r}) = \tilde{r}^{|m|}\, \mathrm{e}^{+\tilde{r}^2/2}\, \mathrm{U}\Big(\frac{1}{2} + \nu + \frac{|m| + m}{2}, 1 + |m|, -\tilde{r}^2\Big)\ . \tag{B.8}$$

This is a *complex* valued solution [44], which we call "irregular". Apart from its logarithmic singularity at $\tilde{r} \to 0$, it diverges exponentially as $\tilde{r} \to \infty$.

Both, u_1 and u_2, are needed to form a solution G_m of the inhomogeneous equation (B.1), since the δ-function implies a discontinuity of the derivative,

$$\partial_1 G_m(\tilde{r}_0 + 0, \tilde{r}_0) - \partial_1 G_m(\tilde{r}_0 - 0, \tilde{r}_0) = \frac{1}{\tilde{r}_0}\ . \tag{B.9}$$

The requirement that the Green function must vanish as $\tilde{r} \to \infty$, together with its continuity at $\tilde{r} = \tilde{r}_0$, leads necessarily to the form

$$G_m(\tilde{r}, \tilde{r}_0) = \frac{1}{\tilde{r}_0 W(\tilde{r}_0)} \begin{cases} u_1(\tilde{r}) u_2(\tilde{r}_0) & \text{if } r < r_0 \\ u_2(\tilde{r}) u_1(\tilde{r}_0) & \text{if } r > r_0\ , \end{cases} \tag{B.10}$$

with Wronskian $W = u_1 u_2' - u_1' u_2$. In total, the Green function in angular momentum decomposition and symmetric gauge is given by

$$\begin{aligned} \mathrm{G}_\nu(\mathbf{r}; \mathbf{r}_0) = \frac{-1}{4\pi} \sum_{m=-\infty}^{\infty} \mathrm{e}^{\mathrm{i}m(\vartheta - \vartheta_0)}\, & \frac{\Gamma\Big(\frac{1}{2} - \nu + \frac{|m|-m}{2}\Big)}{|m|!} \left(\frac{r r_0}{b^2}\right)^{|m|} \exp\Big(-\frac{r^2 + r_0^2}{2b^2}\Big) \\ & \times {}_1\mathrm{F}_1\left(\frac{1}{2} - \nu + \frac{|m| - m}{2}, 1 + |m|, z_<\right) \\ & \times \mathrm{U}\Big(\frac{1}{2} - \nu + \frac{|m| - m}{2}, 1 + |m|, z_>\Big) \end{aligned} \tag{B.11}$$

$$\begin{aligned} = \frac{-1}{4\pi} \sum_{m=-\infty}^{\infty} \mathrm{e}^{\mathrm{i}m(\vartheta - \vartheta_0)}\, & \frac{\Gamma\Big(\frac{1}{2} - \nu + \frac{|m|-m}{2}\Big)}{|m|!} \left(\frac{r r_0}{b^2}\right)^{-1} M_{\nu + \frac{m}{2}, \frac{|m|}{2}}(z_<) \\ & \times W_{\nu + \frac{m}{2}, \frac{|m|}{2}}(z_>) \end{aligned} \tag{B.12}$$

with

$$z_< := \min\left(\frac{\mathbf{r}^2}{b^2}, \frac{\mathbf{r}_0^2}{b^2}\right) \quad \text{and} \quad z_> := \max\left(\frac{\mathbf{r}^2}{b^2}, \frac{\mathbf{r}_0^2}{b^2}\right)\ . \tag{B.13}$$

Note that this expression differs slightly from the (incorrect) results in [39] and [9; eq (6.2.26)].

An independent solution to the inhomogeneous problem (B.1) may obtained if one drops the requirement that the Green function should vanish as $\tilde{r} \to \infty$. It involves the irregular solution (B.8) and leads to the Green function

$$\begin{aligned} \mathrm{G}_\nu^{(\mathrm{irr})}(\mathbf{r};\mathbf{r}_0) = \frac{-1}{4\pi} \sum_{m=-\infty}^{\infty} \mathrm{e}^{\mathrm{i}(\vartheta-\vartheta_0+\pi)m} \, \frac{\Gamma\Big(\frac{1}{2}+\nu+\frac{|m|+m}{2}\Big)}{|m|!} \left(\frac{rr_0}{b^2}\right)^{|m|} \exp\left(\frac{r^2+r_0^2}{2b^2}\right) \\ \times {}_1\mathrm{F}_1\left(\frac{1}{2}+\nu+\frac{|m|+m}{2}, 1+|m|, -z_<\right) \\ \times \mathrm{U}\Big(\frac{1}{2}+\nu+\frac{|m|+m}{2}, 1+|m|, -z_>\Big) \,, \end{aligned} \tag{B.14}$$

which we call “irregular”. This expression was derived by Tiago *et al* [40]. Unlike the regular Green function (B.11), this one diverges exponentially, once the distance between initial and final point exceeds one cyclotron diameter. This property renders the irregular Green function impractical for most purposes.

B.2 The null field method

The null field method is an alternative scheme to quantize magnetic billiards in the interior [40]. We include it for completeness, although its practical use is limited.

Let us start with equation (4.4) which reads in terms of the irregular Green function

$$\int_\Gamma \mathrm{G}_\nu^{(\mathrm{irr})}(\mathbf{r};\mathbf{r}_0)\partial_{n/b}\psi^* \frac{\mathrm{d}\Gamma}{b} = 0 \,, \tag{B.15}$$

where we chose $\mathbf{r}_0 \in \mathbb{R}^2 \backslash \mathcal{D}$, Dirichlet boundary conditions, and the symmetric gauge. Rather than transforming this into an integral equation, we put $\mathbf{r}_0$ onto a (large) circle which is centered on the origin and surrounds the billiard domain with a radius R_p.

Now assume that the billiard boundary is given as a function $r(\theta)$ of the polar angle, and expand the unknown boundary function in a Fourier series,

$$\sum_\ell \mathrm{e}^{\mathrm{i}\theta\ell} c_\ell = \partial_{n/b}\psi^*\big(r(\theta)\big) \,. \tag{B.16}$$

Using the angular momentum decomposition (B.14) of the Green function, equation (B.15) assumes the form

$$\sum_{\ell,m=-\infty}^{\infty} \mathrm{e}^{-\mathrm{i}\theta_0 m} a_m B_{m\ell} c_\ell = 0 \,, \tag{B.17}$$

with

$$\begin{aligned} a_m = (-)^m \frac{\Gamma\Big(\frac{1}{2}+\nu+\frac{|m|+m}{2}\Big)}{|m|!} \left(\frac{R_p}{b^2}\right)^{|m|} \exp\left(\frac{R_p^2}{2b^2}\right) \\ \times \mathrm{U}\Big(\frac{1}{2}+\nu+\frac{|m|+m}{2}, 1+|m|, -\frac{R_p^2}{b^2}\Big) \end{aligned} \tag{B.18}$$

and

$$\begin{aligned} B_{m\ell} &= \int_0^{2\pi} \mathrm{e}^{\mathrm{i}(m+\ell)\theta} \left(\frac{r(\theta)}{b^2}\right)^{|m|} \exp\left(\frac{r^2(\theta)}{2b^2}\right) \\ &\quad \times {}_1\mathrm{F}_1\left(\frac{1}{2}+\nu+\frac{|m|+m}{2}, 1+|m|, -\frac{r^2(\theta)}{b^2}\right) \mathrm{d}\theta \qquad \text{(B.19)} \\ &= \int_0^{2\pi} \mathrm{e}^{\mathrm{i}(m+\ell)\theta} \left(\frac{r(\theta)}{b^2}\right)^{|m|} \exp\left(-\frac{r^2(\theta)}{2b^2}\right) \\ &\quad \times {}_1\mathrm{F}_1\left(\frac{1}{2}-\nu+\frac{|m|-m}{2}, 1+|m|, \frac{r^2(\theta)}{b^2}\right) \mathrm{d}\theta \; . \qquad \text{(B.19a)} \end{aligned}$$

Here, we divided out the constants. Equation (B.17) must hold for all polar angles θ_0. For negative arguments the function U is known to be complex and non-zero [44]. Hence, we can divide by a_m for all R_p, which leaves the condition for the existence of a nontrivial solution c_ℓ to

$$\det(B_{m\ell}) = 0 \; . \qquad \text{(B.20)}$$

It is a spectral equation, given by Tiago *et al* [40] (except for a misprint in their paper).

Appendix C

The product relation of the map operators

We show that the relations (6.23) for the products of the interior and exterior map operators (6.22) hold semiclassically. They were needed to prove the factorization of the spectral function. Since the only relevant contribution to the product stems from regions where the initial and final points are close, we are allowed to replace the boundary locally by a piece of constant curvature. It follows that the expressions (6.68) – (6.71) derived for the disk billiards may be employed to show that the kernel of the product (6.23) acts like a δ-function. Assuming $\delta\varphi = (s - s_0)/R$ to be small we find

$$\begin{aligned}
&\left(\mathrm{p}_{\mathrm{S}}^{\mathrm{int}}\mathrm{p}_{\mathrm{L}}^{\mathrm{ext}}\right)(s, s_0) = \\
=&\frac{1}{2\pi\mathrm{i}}\,\frac{b}{R}\int \mathrm{d}\varphi' \left(\frac{\mathrm{d}^2(2\pi\nu\mathrm{a}_{\mathrm{S}})}{\mathrm{d}\varphi\,\mathrm{d}\varphi_0}(\varphi' - \varphi_0)\,\frac{\mathrm{d}^2(2\pi\nu\mathrm{a}_{\mathrm{L}})}{\mathrm{d}\varphi_0\,\mathrm{d}\varphi'}(\varphi_0 + \delta\varphi - \varphi')\right)^{\frac{1}{2}} \\
&\quad\times \mathrm{e}^{2\pi\mathrm{i}\nu(\mathrm{a}_{\mathrm{S}}(\varphi'-\varphi_0)+\mathrm{a}_{\mathrm{L}}(\varphi_0+\delta\varphi-\varphi'))} \begin{cases} -\Theta(\varphi' - \varphi_0)\Theta(\varphi' - \varphi_0 + \delta) & \text{if } \Gamma_{\mathrm{d}} > 1 \\ -1 & \text{if } \Gamma_{\mathrm{d}} < 1 \end{cases} \\
\simeq&\frac{1}{\pi}\,\frac{b\nu}{R}\int \mathrm{d}\varphi' \left|\frac{\mathrm{d}^2(\pi\mathrm{a}_{\mathrm{L}})}{\mathrm{d}\varphi'\,\mathrm{d}\varphi_0}(\varphi_0 - \varphi')\right| \mathrm{e}^{2\pi\mathrm{i}\nu+2\pi\mathrm{i}\nu\partial_{\varphi_0}\mathrm{a}_{\mathrm{L}}(\varphi_0-\varphi')\,\delta\varphi} \begin{cases} -\Theta(\varphi' - \varphi_0) \\ -1 \end{cases} \\
=&\frac{1}{\pi}\,\frac{b\nu}{R}\,\mathrm{e}^{2\pi\mathrm{i}\nu}\int \mathrm{d}\varphi'\,\frac{\mathrm{d}u_{\mathrm{L}}}{\mathrm{d}\varphi'}\,\mathrm{e}^{2\mathrm{i}\nu u_{\mathrm{L}}\,\delta\varphi} \begin{cases} \Theta(\varphi' - \varphi_0) & \text{if } \Gamma_{\mathrm{d}} > 1 \\ 1 & \text{if } \Gamma_{\mathrm{d}} < 1\,. \end{cases}
\end{aligned} \tag{C.1}$$

Here, the dependence on $\delta\varphi$ was expanded linearly in the phase, and neglected in the prefactor. The latter is cancelled by the change of the integration variable to $u_{\mathrm{L}} := \pi\partial_{\varphi_0}\mathrm{a}_{\mathrm{L}}(\varphi_0 - \varphi')$. Likewise, one finds for the second combination of interior and exterior operators:

$$\left(\mathrm{p}_{\mathrm{L}}^{\mathrm{int}}\mathrm{p}_{\mathrm{S}}^{\mathrm{ext}}\right)(s, s_0) = \frac{1}{\pi}\,\frac{b\nu}{R}\,\mathrm{e}^{2\pi\mathrm{i}\nu}\int \mathrm{d}\varphi'\,\frac{\mathrm{d}u_{\mathrm{S}}}{\mathrm{d}\varphi'}\,\mathrm{e}^{2\mathrm{i}\nu u_{\mathrm{S}}\,\delta\varphi} \begin{cases} -\Theta(\varphi' - \varphi_0) & \text{if } \Gamma_{\mathrm{d}} > 1 \\ 0 & \text{if } \Gamma_{\mathrm{d}} < 1\,, \end{cases} \tag{C.2}$$

with $u_{\mathrm{S}} := \pi\partial_{\varphi_0}\mathrm{a}_{\mathrm{S}}(\varphi_0 - \varphi')$. The sum of the kernels now assumes the form of a semiclassical δ-function, once the integration is carried out. The ranges of integration differ for weak and strong fields. They can be found in Table C.1. Setting $\overline{\varphi} \equiv$

If $\Gamma_{\rm d} > 1$						
φ' :	$\varphi_0 - \overline{\varphi}$	$\longrightarrow$	φ_0-	φ_0+	$\longrightarrow$	$\varphi_0 + \overline{\varphi}$
$u_{\rm S}$:	$\frac{1}{2}\Gamma_{\rm d}^2\cos(\overline{\varphi})$	$\longrightarrow$	$\Gamma_{\rm d} + \frac{1}{2}\Gamma_{\rm d}^2$	$-\Gamma_{\rm d} + \frac{1}{2}\Gamma_{\rm d}^2$	$\longrightarrow$	$\frac{1}{2}\Gamma_{\rm d}^2\cos(\overline{\varphi})$
$u_{\rm L}$:	$\frac{1}{2}\Gamma_{\rm d}^2\cos(\overline{\varphi})$	$\longrightarrow$	$-\Gamma_{\rm d} + \frac{1}{2}\Gamma_{\rm d}^2$	$\Gamma_{\rm d} + \frac{1}{2}\Gamma_{\rm d}^2$	$\longrightarrow$	$\frac{1}{2}\Gamma_{\rm d}^2\cos(\overline{\varphi})$
If $\Gamma_{\rm d} < 1$						
φ' :	$\varphi_0 - \pi$	$\longrightarrow$	φ_0-	φ_0+	$\longrightarrow$	$\varphi_0 + \pi$
$u_{\rm S}$:	$-\frac{1}{2}\Gamma_{\rm d}^2$	$\longrightarrow$	$\Gamma_{\rm d} + \frac{1}{2}\Gamma_{\rm d}^2$	$-\Gamma_{\rm d} + \frac{1}{2}\Gamma_{\rm d}^2$	$\longrightarrow$	$-\frac{1}{2}\Gamma_{\rm d}^2$
$u_{\rm L}$:	$-\frac{1}{2}\Gamma_{\rm d}^2$	$\longrightarrow$	$-\Gamma_{\rm d} + \frac{1}{2}\Gamma_{\rm d}^2$	$\Gamma_{\rm d} + \frac{1}{2}\Gamma_{\rm d}^2$	$\longrightarrow$	$-\frac{1}{2}\Gamma_{\rm d}^2$

Table C.1: Ranges of integration needed in eq (C.3).

$2\arcsin(1/\Gamma_{\rm d})$ one gets

$$\begin{aligned}
&\big({\rm p}_{\rm S}^{\rm int}{\rm p}_{\rm L}^{\rm ext} + {\rm p}_{\rm L}^{\rm int}{\rm p}_{\rm S}^{\rm ext}\big)(s,s_0) = \\
&= \frac{1}{\pi}\,\frac{b\nu}{R}\,{\rm e}^{2\pi{\rm i}\nu}\begin{cases} \displaystyle\int_{\Gamma_{\rm d}+\frac{1}{2}\Gamma_{\rm d}^2}^{\frac{1}{2}\Gamma_{\rm d}^2\cos(\overline{\varphi})} {\rm d}u_{\rm L}\,{\rm e}^{2{\rm i}\nu u_{\rm L}\delta\varphi} - \int_{-\Gamma_{\rm d}+\frac{1}{2}\Gamma_{\rm d}^2}^{\frac{1}{2}\Gamma_{\rm d}^2\cos(\overline{\varphi})} {\rm d}u_{\rm S}\,{\rm e}^{2{\rm i}\nu u_{\rm S}\delta\varphi} & \text{if } \Gamma_{\rm d} > 1 \\ \displaystyle\int_{\Gamma_{\rm d}+\frac{1}{2}\Gamma_{\rm d}^2}^{-\Gamma_{\rm d}+\frac{1}{2}\Gamma_{\rm d}^2} {\rm d}u_{\rm L}\,{\rm e}^{2{\rm i}\nu u_{\rm L}\delta\varphi} & \text{if } \Gamma_{\rm d} < 1 \end{cases} \\
&= -\,{\rm e}^{2\pi{\rm i}\nu}\,\frac{1}{\pi}\,\frac{\sin\left(2\sqrt{\nu}\,\frac{s-s_0}{b}\right)}{\frac{s-s_0}{b}}\,{\rm e}^{{\rm i}\pi\sqrt{\nu}\Gamma_{\rm d}(s-s_0)/b} \xrightarrow{2\sqrt{\nu}\to\infty} -\,{\rm e}^{2\pi{\rm i}\nu}\,\delta\!\left(\frac{s-s_0}{b}\right)\,.
\end{aligned} \tag{C.3}$$

This proves the identity (6.23). In a similar fashion, one finds that the product (6.24) does not contribute semiclassically.

Appendix D

Scaled spectra

In the following, we collect a number of formulas for spectra defined in the semiclassical direction. As discussed in Sections 2.3 and 3.3.2, those spectra are obtained by decreasing the magnetic length b at fixed cyclotron radius ρ (unlike conventional spectra, where ρ is increased at fixed b). Since the spectra are noted in terms of the scaled energy $\nu = \rho^2/b^2$ in both cases, the superscript-(ρ) is used to indicate spectra taken at fixed ρ.

Scaled spectroscopy has the advantage that the classical dynamics remains fixed as the spectral variable is increased. This allows to ensure a certain type of classical motion throughout the spectral interval, cf Sect. 5.1, and to extract classical actions easily by Fourier transformation, cf Sect. 9.2.

However, one should be aware of the fact that the obtained spectrum does not belong to one self-adjoint operator. Rather, a sweep through a family of operators is performed as the spectral variable is increased. Clearly, the energies are real and the eigenvectors are still proper solutions of the Schrödinger equation, but the latter are not orthogonal. Moreover, it may happen that two energies coalesce and vanish as an external parameter is varied.

Many formulas in the main part of this thesis hold for spectra at fixed ρ as well, after the substitution $b \to \rho/\sqrt{\nu}$. In particular, this is the case for the spectral functions and the trace formulas (which are to leading order in ν), but not the spectral densities. The smooth number counting function (3.10), for example, reads

$$\overline{\mathrm{N}}^{(\rho)}(\nu) = \frac{\mathscr{A}}{\rho^2\pi}\,\nu^2 - \frac{\mathscr{L}}{2\pi\rho}\,\nu + \frac{1}{6}\,. \tag{D.1}$$

However, care is needed for the spectral density of edge states, which is now given as

$$d^{(\rho)}_{\mathrm{edge}}(\nu) = \sum_{n=1}^{\infty} w_n^{(\rho)}\delta(\nu - \nu_n^{(\rho)})\,, \tag{D.2}$$

with the weights defined at constant ρ,

$$w_n^{(\rho)} := \frac{\mathrm{d}\nu_n^{(\rho)}(\Lambda)}{\mathrm{d}\Lambda}\Big|_{\Lambda=0}\,. \tag{D.3}$$

Here, we find

$$\overline{\mathrm{N}}^{(\rho)}_{\mathrm{edge}}(\nu) = \frac{1}{2}\,\frac{\mathscr{L}}{2\pi\rho}\,\nu^2 \mp \frac{1}{2}\nu\,. \tag{D.4}$$

Appendix E

Numerical evaluation of the Green function

We are not aware of any published numerical procedure to evaluate the irregular confluent hypergeometric function U if both, the (energy) parameter and the argument are large. It seems that presently only the Mathematica software (Wolfram Research Inc.) is able to compute the function, at least for moderately large ν. Even this sophisticated system *fails* for $\nu > 75$. Anyhow, it is not an option to use it for serious numerical calculations since the evaluation takes a prohibitively long time.

Therefore, we describe our method to compute the gauge independent part of the regular Green function in more detail. For low energies $\nu < 12$, the function $\mathrm{U}(1/2 - \nu, 1; z)$ may be easily calculated by its series representation [43; eq. (13.1.6)]. i.e. in terms of the regular confluent hypergeometric function ${}_1\mathrm{F}_1$. For very large z an asymptotic expansion in terms of ${}_2\mathrm{F}_0$ may be employed [141; eq. (6.7.1)].

For energies $\nu > 12$ the numerical convergence of the series expression deteriorates strongly in some intervals of the z range (starting at $z \approx 2\nu$). Here, one may employ the stable recurrence relation.

$$(\nu - \tfrac{1}{2})\, \widehat{\mathrm{G}}^0_\nu(z) = (z - 2\nu + 2)\, \widehat{\mathrm{G}}^0_{\nu-1}(z) - (\nu - \tfrac{3}{2})\, \widehat{\mathrm{G}}^0_{\nu-2}(z) \tag{E.1}$$

which is straightforward, but time consuming. Alternatively, asymptotic expansions for the irregular Whittaker function can be used [44; eqs. (8.1.5), (8.1.10), (8.1.18a)] which are given to third order in the large parameter ν. Together with [43; eq. (13.5.15)], they correspond to the changing logarithmic, oscillatory, transient, and exponentially decaying behaviour of the Green function as the distance z increases. For most values of z they allow to calculate the Green function to a reasonably high precision and with acceptable numerical effort. However, between the ranges of validity of the different asymptotic expressions there are small gaps where no formula is appropriate, cf. Figure E.1. In the gap between the logarithmic and the oscillatory domains, which is at small z, one may employ the series summation even for large $\nu \gg 12$. For the two gaps between the oscillatory, the transient, and the exponential regimes, which are around $z \approx 4\nu$, this is possible only up to, say $\nu = 16$. For larger ν we interpolate between adjacent regions of validity employing the *uniform approximation* of the irregular Whittaker function around the classical turning point. Neglecting higher orders in ν, the resulting expression for the Green function (2.66) reads

$$\widehat{\mathrm{G}}^0_\nu(z) \approx C \frac{(\frac{3}{2}q)^{\frac{1}{6}}}{|z^2 - 4\nu z - 1|^{\frac{1}{4}}} \mathrm{Ai}\Big(\mathrm{sgn}(z - z_0)\, \big(\tfrac{3}{2}q\big)^{\frac{2}{3}}\Big) \tag{E.2}$$

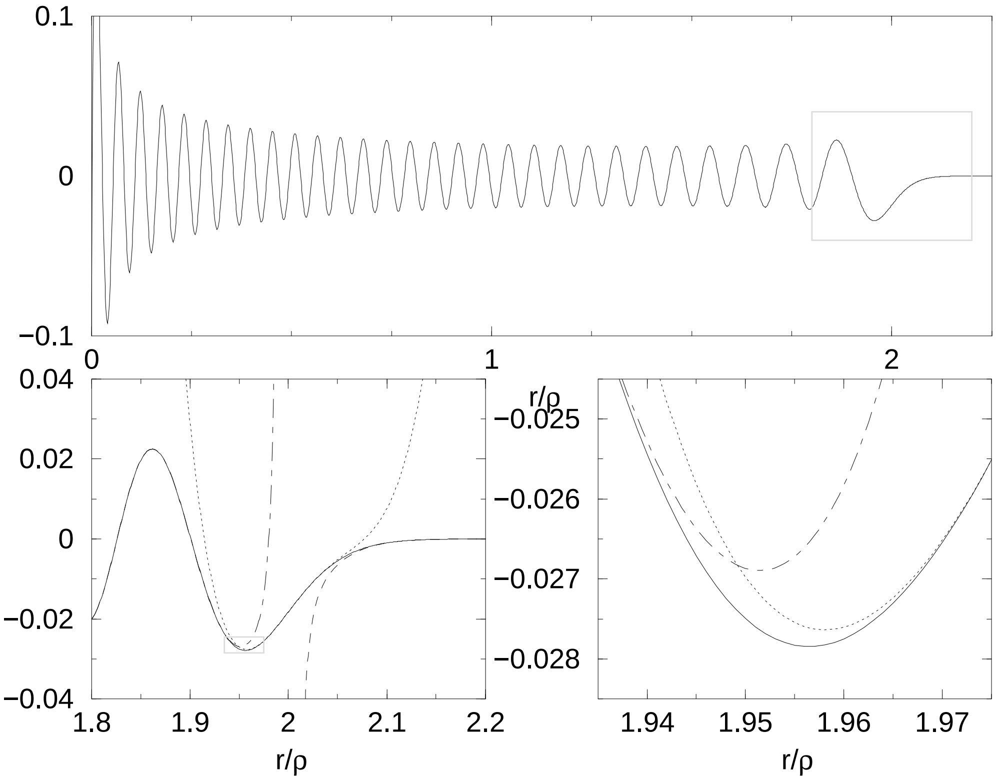

Figure E.1: (a) Gauge independent part $\widehat{\mathrm{G}}^0_\nu(z)$ of the regularized Green function at $\nu = 57.75$. It has a logarithmic singularity at $r = 0$, and decays exponentially for $r > 2\rho$. (b) In the transition regions between oscillatory, transient, and decaying regimes the asymptotic expressions to third order are not valid (chain, dotted, dashed line respectively.) (c) Here, on may interpolate using an uniform approximations to the irregular Whittaker function (solid line.)

where Ai is the regular Airy function and

$$q := \begin{cases} \nu\Big(\dfrac{\pi}{2} - \mathrm{atan}\Big(\dfrac{z-2\nu}{w}\Big)\Big) + \dfrac{1}{2}\log\Big(\dfrac{z_0}{z}\dfrac{1+2\nu z+w}{1+2\nu z_0}\Big) - \dfrac{1}{2}w & \text{if } z < z_0 \\ \dfrac{1}{2}w + \dfrac{1}{2}\mathrm{atan}\Big(\dfrac{2\nu z+1}{w}\Big) - \dfrac{\pi}{4} - \nu\log\Big(\dfrac{z-2\nu+w}{z_0-2\nu}\Big) & \text{if } z > z_0 \end{cases} \tag{E.3}$$

with

$$z_0 := 4\nu\left(\tfrac{1}{2} + \tfrac{1}{2}\sqrt{1+\tfrac{1}{4\nu^2}}\right) \qquad \text{and} \qquad w := \sqrt{\left|z^2 - 4\nu z - 1\right|}. \tag{E.4}$$

The constant C may be calculated for values of z where the saddle point expressions are valid, and is interpolated linearly within the gaps.

The thresholds mentioned above are a reasonable compromise between computational cost and precision. We observe a peak numerical error (minimum of relative and absolute) of 6.5×10^{-5} at $\nu = 22$, by comparison with the results of Mathematica, which are assumed to be exact for $\nu < 70$. For increasing ν, the numerical error decreases monotonically, what allows us to estimate it to smaller than 3.7×10^{-5} for $\nu > 70$. It was checked that numerical errors of that order do not affect the results presented in this work.

List of important Symbols

Most important:

cyclotron radius: ρ
magnetic length: b
scaled energy: $\nu = \dfrac{\rho^2}{b^2}$

Latin symbols:

$\mathscr{A}$	area of the billiard domain ($\mathscr{A} = \lvert\mathcal{D}\rvert$)
$\mathscr{A}_\gamma$	area enclosed by the trajectory of γ (6.55)
$\mathscr{A}_{\text{skip}}$	area determining the phase space of skipping orbits, Fig. 3.6
$\mathrm{Ai}(z)$	Airy function
$\mathrm{A}(\gamma)$	geometric part of the action of the periodic orbit γ (6.42)
$\mathbf{A}(\mathbf{r})$	vector potential at arbitrary gauge (2.11)
$\tilde{\mathbf{A}}(\mathbf{r})$	scaled vector potential at arbitrary gauge ($\tilde{\mathbf{A}}(\tilde{\mathbf{r}}) = 2\mathbf{A}(b\tilde{\mathbf{r}})/(Bb)$)
$\mathbf{A}_{\text{Lan}}(\mathbf{r}),\ \mathbf{A}_{\text{sym}}(\mathbf{r})$	vector potential in Landau gauge (2.12) (symmetric gauge (2.13))
$\mathrm{a}_{\mathrm{S}}(\mathbf{r};\mathbf{r}_0),\ \mathrm{a}_{\mathrm{L}}(\mathbf{r};\mathbf{r}_0)$	geometric part of the action for the short (long) arc (2.59), (6.1), (6.2)
$\hat{a}_{\mathrm{R}},\ \hat{a}_{\mathrm{L}}$	annihilation operator of right (left) circular quanta (2.21)
B	magnetic induction ($B = \boldsymbol{\nabla} \times \mathbf{A}$)
$\mathcal{B}$	billiard bounce map (3.4)
$\mathrm{Bi}(z)$	Airy function [43]
b	magnetic length (2.17), (2.36)
$C(\nu_0)$	cross correlation function (10.3), (10.4)
$\mathbf{c},\ \tilde{\mathbf{c}}$	(scaled) center of cyclotron motion ($\mathbf{c} \in \mathbb{R}^2$) (2.25)
$\mathcal{D}$	domain of the interior billiard ($\mathcal{D} \subset \mathbb{R}^2$)
$D(t)$	Fourier transform of $C(\nu_0)$ (10.13)
$D_k(z)$	parabolic cylinder function (Whittakers form) [43]
$d(\nu)$	standard spectral density (3.9)
$d_{\text{edge}}(\nu)$	spectral density of edge states (8.2), (8.7)
$\overline{d}_{\text{edge}}(\nu)$	smooth spectral density of edge states (8.3)

$d^{\mathrm{osc}}_{\mathrm{edge}}(\nu)$	fluctuating part of the spectral density of edge states (8.9)
$d^{(\rho)}_{\mathrm{edge}}(\nu)$	spectral density of edge states in the semiclassical direction (D.2)
$\overline{d}_{\mathrm{skip}}(\nu)$	smooth spectral density of skipping states (3.15)
$d^{\mathrm{osc}}_{\mathrm{skip}}(\nu)$	fluctuating part of the spectral density of skipping states (6.57)
E	(kinetic) energy
$\widetilde{E}$	proper scaled energy ($\widetilde{E} = E/(\hbar\omega) = 2\nu$), page 12
$f(n)$	weighted classical sum over n-orbits $\gamma^{(n)}$ (10.10)
${}_1\mathrm{F}_1(a,b;z)$	regular confluent hypergeomeric function [43]
$e(s)$	compact window function (4.51)
$\mathscr{G}$	generating function of the billiard bounce map (3.5)
$\mathrm{G}_\nu(\mathbf{r};\mathbf{r}_0)$	free Green function at energy ν, with $\mathbf{r}_0$ the initial point (2.54)
$\mathrm{G}^{(\mathrm{sc})}_\nu(\mathbf{r};\mathbf{r}_0)$	semiclassical free Green function at energy ν, (2.61), (2.62)
$\mathrm{G}^0_\nu(z),\ \widehat{\mathrm{G}}^0_\nu(z)$	gauge independent part of the (regularized) free Green function at energy ν (2.64), (2.66), (2.67)
$\mathrm{G}^{0(\mathrm{sc})}_\nu(z)$	gauge independent part of the semiclassical free Green function at energy ν (2.63)
$g(z)$	normalized Gaussian window function, $g(z) \equiv (2\pi\sigma_g^2)^{-\frac{1}{2}} \exp\big(-z^2/(2\sigma_g^2)\big)$, with “small” σ_g
$\hat{g}(t)$	Fourier transform of g(z)
H	magnetic Hamiltonian (2.14)
$\widetilde{\mathrm{H}}$	scaled Hamiltonian (2.39)
$h(z),\ \hat{h}(t)$	normalized Gaussian window function, cf $g(z)$, with “large” width σ_h, (and its Fourier transform)
$\mathbf{j}(\mathbf{r})$	probability current density (2.35)
$K(\tau)$	form factor (9.5), (9.6)
$K(a,b;z)$	confluent hypergeomeric function (7.32)
$\mathrm{K}_{k\ell}$	smooth matrix (4.46)
$\mathrm{k}(s;s_0)$	smooth integral kernel (4.42)
$\mathscr{L}$	circumference of the billiard domain ($\mathscr{L} = \lvert\Gamma\rvert$)
$\mathscr{L}_\gamma$	length of the trajectory of γ (6.54)
L	canonical angular momentum (2.13)
$\mathrm{L}_\nu(z)$	asymptotically logarithmic form of the regularized gauge independent Green function (2.71)
$\mathcal{L}$	magnetic Lagrangian (2.1)
$\widetilde{\mathcal{L}}$	scaled Lagrangian (2.37)
$\mathrm{L}_{k\ell}$	logarithmic matrix (4.47)
$\mathrm{l}(s;s_0)$	logarithmic part of the regularized kernel (4.41)
$\mathcal{M}(\nu)$	scaled magnetization (3.26)
$\mathcal{M}_{\mathrm{edge}}(\nu)$	scaled edge magnetization (3.27), (8.15)

$\overline{\mathcal{M}}_{\mathrm{edge}}(\nu)$	smooth edge magnetization (8.17)
$M_{k,\mu}(z)$	Whittaker function [43]
$M_{\max}$	maximum winding number in magnetic disk (6.75)
$\mathrm{M}(\gamma)$	stability matrix of γ (6.46)
$\mathrm{M}_{k\ell}$	hypersingular matrix (4.48)
m	angular (or longitudinal) momentum quantum number (7.1), (7.36) (or else integer)
$m_{\max}$, $m_{\min}$	maximum (minimum) angular momentum quantum number corresponding to kipping motion in the disk (7.2)
$m_{\circ}$	particle mass
$\mathrm{m}(s;s_0)$	hypersingular part of the regularized kernel (4.40)
$\widetilde{\mathrm{m}}(\nu)$	scaled magnetization density (3.24)
$\widetilde{\mathrm{m}}_{\mathrm{edge}}(\nu)$	edge magnetization density (3.29), (8.18)
$\overline{\mathrm{m}}_{\mathrm{edge}}(\nu)$	smooth edge magnetization density (3.31)
$\widetilde{\mathrm{m}}^{\mathrm{osc}}(\nu)$	fluctuating part of the scaled magnetization density (6.59)
$\widetilde{\mathrm{m}}^{\mathrm{osc}}_{\mathrm{edge}}(\nu)$	fluctuating part of the edge magnetization density (8.20)
$\mathcal{N}$	normalization constant of the wave function
$\mathrm{N}(\nu)$	spectral number counting function (spectral staircase) (3.8)
$\overline{\mathrm{N}}(\nu)$	smooth number counting function (3.10)
$\mathrm{N}_{\mathrm{edge}}(\nu)$	edge state counting function (8.4)
$\overline{\mathrm{N}}_{\mathrm{edge}}(\nu)$	smooth part of the edge state counting function (8.5)
$\mathrm{N}^{\mathrm{osc}}_{\mathrm{edge}}(\nu)$	fluctuating part of the edge state counting function (8.6)
$\overline{\mathrm{N}}_{\mathrm{skip}}(\nu)$	smooth counting function for skipping states (3.14)
$\mathrm{N}^{\mathrm{skip}}_{\mathrm{osc}}(\nu)$	fluctuating part of the counting function for skipping states (6.18), (6.25), (6.50), (6.79), (6.80), (8.8)
n_{γ}	number of reflections in γ, page 83
$\hat{\mathbf{n}}$	normal vecor of billiard boundary, pointing *outwards* (3.2)
$\mathcal{P}^{N}_{\mathrm{int}}$, $\mathcal{P}^{N}_{\mathrm{ext}}$	angular increment of N-orbit in interior (exterior) disk (6.74), (6.78)
P	semiclassical map operator (6.17)
$p(s,s_0)$	kernel of semiclassical map operator (6.20), (6.21), (6.22)
p_s	Birkhoff coordinate conjugate to s, page 25
$\mathbf{p}$, $\tilde{\mathbf{p}}$	(scaled) canonical momentum vector (2.2), (2.18)
Q	boundary integral operator (4.12) – (4.15), (4.22)
q	particle charge ($q\,B > 0$)
q_m	quantized relative distance of the center of motion from the boundary (7.47)

$\mathrm{q}(\mathbf{r};\mathbf{r}_0)$	boundary integral kernel (4.27) – (4.30)
$\mathrm{q}^{(\mathrm{sc})}(\mathbf{r};\mathbf{r}_0)$	semiclassical boundary integral kernel (6.10), (6.13), (6.15)
$\widehat{\mathrm{q}}(s;s_0)$	regularized boundary integral kernel (4.37)
R	disk radius
$\widetilde{R}$	scaled disk radius ($\widetilde{R} \equiv R/b$)
r_γ	number of repetitions in γ, page 83
$\mathbf{r}, \tilde{\mathbf{r}}$	(scaled) particle position vector ($\mathbf{r} \in \mathbb{R}^2$), (2.18)
$\mathrm{Si}(z)$	sine integral [43]
s	curvilinear coordinate on boundary ($s_j \equiv s(\mathbf{r}_j)$), (3.1)
T	Larmor period ($T = 2\pi/\omega$)
T_{cyc}	cyclotron period ($T_{\mathrm{cyc}} = \frac{1}{2}T$)
$\tilde{t}$	scaled time ($\tilde{t} = \omega t$)
$\hat{\mathbf{t}}$	tangent vecor of billiard boundary (3.2)
$\mathrm{U}(a,b;z)$	irregular confluent hypergeomeric function [43]
$\mathrm{U}(\mathbf{r};\mathbf{r}_0)$	free quantum propagator (2.50)
u_n	edge magnetization weight of state $\vert\psi_n\rangle$ (8.16)
u_γ	classical edge magnetization weight of orbit γ (8.20)
$\tilde{v}$	scaled velocity ($\tilde{v} = v/(\omega b) = 2\rho/b$)
$\mathbf{v}$	velocity vector (2.6)
$\hat{\mathbf{v}}_{\mathrm{S}}, \hat{\mathbf{v}}_{\mathrm{L}}$	normalized velocity vector at point of incidence for short (long) arc(6.7), Fig. 6.1
$\hat{\mathbf{v}}^0_{\mathrm{S}}, \hat{\mathbf{v}}^0_{\mathrm{L}}$	normalized velocity vector after reflection for short (long) arc (6.7), Fig. 6.1
W	classical action (time domain) (2.43), (2.45)
$W_{k,\mu}(z)$	Whittaker function [43]
w_n	quantum weight of state $\vert\psi_n\rangle$ (8.1)
w_γ	classical weight of orbit γ (8.10)

Greek symbols:

$\alpha(\mathbf{r};\mathbf{r}_0)$	relative distance of the initial and the final point ($0 \leq \alpha \leq \frac{\pi}{2}$) (6.5), Fig. 6.1
α_j	$\alpha(\mathbf{r}_j;\mathbf{r}_{j+1})$ (6.28), Fig. 6.2
α_{c}	(4.22), page 52
α_Λ	phase shift (depending on boundary condition Λ) (7.10), (7.39), (7.26)
$\beta(\mathbf{r};\mathbf{r}_0),\ \beta^0(\mathbf{r};\mathbf{r}_0)$	relative direction of the normal vector at incidence (reflection) (6.6), Fig. 6.1
$\beta_j,\ \beta^0_j$	(6.29), Fig. 6.2
Γ	billiard boundary ($\Gamma = \partial\mathcal{D}$) (3.1)
Γ_{d}	relative radius of the magnetic disk (6.60)
$\gamma,\ \gamma^{(n)}$	physical periodic orbit (with n reflections), page 80

ε	parametrization of the angular momentum ($1 < \varepsilon < 1$) (7.19)
ζ	relative distance (2.57)
η	index for type of arc, $\eta \in \{\mathrm{S}, \mathrm{L}\}$
$\Theta(x)$	Heaviside step function
θ	polar angle
$\kappa(s)$	curvature of the billiard boundary at the point s (3.3)
Λ	dimensionless boundary mixing parameter (3.7)
λ	boundary mixing parameter (3.6)
μ_γ	Maslov index (number of conjugate points in γ), page 83
ν	scaled energy (2.40)
$\xi(\nu)$	spectral function (4.23), (7.31), (7.40)
$\xi^{(\mathrm{sc})}(\nu)$	semiclassical spectral function (7.12), (7.38)
Φ	radial WKB phase in the disk (7.6), (7.7),
φ	polar angle in the disk ($\varphi \equiv s/R$)
ρ	cyclotron radius (2.36)
$\boldsymbol{\rho}$	radius vector ($\boldsymbol{\rho} = \mathbf{r} - \mathbf{c} \in \mathbb{R}^2$) (2.7)
σ_j	arc parametrization ($-1 < \sigma_j < 1$) (6.51)
σ_e	width of the compact window function $e(s)$ (4.51), page 52
$\sigma_g,\ \sigma_h$	width of the normalized Gaussians $g(\nu),\ h(\nu)$
τ_γ	scaled time of flight of γ (6.56)
$\chi(\mathbf{r})$	gauge field, page 7
$\widetilde{\chi}(\tilde{\mathbf{r}})$	scaled gauge field ($\widetilde{\chi} \equiv \widetilde{\chi}(\tilde{\mathbf{r}})$, $\widetilde{\chi}_0 \equiv \widetilde{\chi}(\tilde{\mathbf{r}}_0)$) (2.38)
$\Psi(z)$	digamma function [43]
ψ	stationary wave function
ω_c	cyclotron frequency ($\omega_\mathrm{c} = 2\omega > 0$)
ω	Larmor frequency (2.20)

Bibliography

[1] M. C. Gutzwiller, *Periodic orbits and classical quantization conditions*, J. Math. Phys. **12**, 343–358 (1971).

[2] M. V. Berry and M. Tabor, *Closed orbits and regular bound spectrum*, Proc. Roy. Soc. Lond. A **349**, 101 (1976).

[3] A. M. Ozorio de Almeida, *Hamiltonian Systems: Chaos and Quantization*, Cambridge University Press, 1988.

[4] M. C. Gutzwiller, *Chaos in Classical and Quantum Mechanics*, Springer-Verlag, Berlin, 1990.

[5] F. Haake, *Quantum Signatures of Chaos*, Springer-Verlag, Berlin, 1990.

[6] M.-J. Giannoni, A. Voros, and J. Zinn-Justin, editors, *Proceedings of the 1989 Les Houches Summer School on "Chaos and Quantum Physics"*, North-Holland, Amsterdam, 1991.

[7] L. E. Reichl, *The Transition to Chaos (in Conservative Classical Systems: Quantum Manifestations)*, Springer-Verlag, Berlin, 1992.

[8] M. Brack and R. K. Bhaduri, *Semiclassical Physics*, volume 96 of *Frontiers in Physics*, Addison-Wesley, Reading, 1997, Errata in http://www.physik.uni-regensburg.de/∼brm04014/Publications.html.

[9] C. Grosche and F. Steiner, *Handbook of Feynman integrals*, volume 145 of *Springer Tracts in Modern Physics*, Springer-Verlag, Berlin, 1998.

[10] M. C. Gutzwiller, *The interplay between classical and quantum chaos (Resource Letter ICQM-1)*, Am. J. Phys. **66**(4), 304–324 (1998).

[11] S. Tabachnikov, *Billiards*, volume 289 of *Panoramas et Synthèses*, Société Mathématique de France, 1995.

[12] O. Bohigas, M. J. Giannoni, and C. Schmit, *Characterization of chaotic quantum spectra and universality of level fluctuations*, Phys. Rev. Lett. **52**(1), 1–4 (1984).

[13] E. J. Heller, *Bound state eigenfunctions of classically chaotic Hamiltonian systems: Scars of periodic orbits*, Phys. Rev. Lett. **53**, 1515–1518 (1984).

[14] E. Heller, *Semiclassical wave packet propagation and chaos in quantum mechanics*, In Giannoni et al. [6].

[15] N. Argaman, F. M. Dittes, E. Doron, J. P. Keating, A. Y. Kitaev, M. Sieber, and U. Smilansky, *Correlations in the actions of periodic-orbits derived from quantum chaos*, Phys. Rev. Lett. **71**(26), 4326–4329 (1993).

[16] J.-P. Eckmann and C.-A. Pillet, *Spectral duality for planar billiards*, Commun. Math. Phys. **170**, 283–313 (1995).

[17] B. Dietz and U. Smilansky, *A scattering approach to the quantization of billiards - The inside-outside duality*, Chaos **3**, 581–590 (1993).

[18] C. M. Marcus, A. J. Rimberg, R. M. Westervelt, P. F. Hopkins, and A. C. Gossard, *Conductance fluctuations and chaotic scattering in ballistic microstructures*, Phys. Rev. Lett. **69**(3), 506–509 (1992).

[19] M. Kac, *Can one hear the shape of a drum?*, Am. Math. Monthly **73**, 1–23 (1966).

[20] N. Nakamura and H. Thomas, *Quantum billiard in a magnetic field: Chaos and diamagnetism*, Phys. Rev. Lett. **61**(3), 247–250 (1988).

[21] O. Bohigas, M.-J. Giannoni, A. M. Ozorio de Almeida, and C. Schmit, *Chaotic dynamics and the GOE-GUE transition*, Nonlinearity **8**, 203–221 (1995).

[22] Z. Yan and R. Harris, *Stadium in a magnetic field: Time-reversal invariance symmetry breaking and energy level statistics*, Europhys. Lett. **32**(5), 437–442 (1995).

[23] Z.-L. Ji and K.-F. Berggren, *Transition from chaotic to regular behavior of electrons in a stadium-shaped quantum dot in a perpendicular magnetic field*, Phys. Rev. B **52**, 1745–1750 (1995).

[24] M. A. M. de Aguiar, *Eigenvalues and eigenfunctions of billiards in a constant magnetic field*, Phys. Rev. E **55**(5), 4555–4561 (1996).

[25] K. Richter, D. Ullmo, and R. A. Jalabert, *Orbital magnetism in the ballistic regime: geometrical effects*, Phys. Rep. **276**, 1–83 (1996).

[26] L. D. Landau and E. M. Lifshitz, *The classical theory of fields*, volume 2 of *Course of theoretical physics*, Butterworth-Heinenann, Oxford, 1975.

[27] L. Landau, *Diamagnetismus der Metalle*, Z. Phys. **64**, 629–637 (1930).

[28] C. Cohen-Tannoudji, B. Diu, and F. Laloe, *Quantum mechanics*, volume 1, Wiley-Interscience, New York, 1977.

[29] J. Avron, I. Herbst, and B. Simon, *Schrödinger operators with magnetic fields. I. General interactions*, Duke Math. J. **45**, 847883 (1978).

[30] B. Helffer, *On spectral theory for Schrödinger operators with magnetic fields*, Advanced Studies in Pure Mathematics **23**, 113–141 (1994).

[31] E. Schrödinger, *Der stetige Übergang von der Makro- zur Mikromechanik*, Die Naturwissenschaften **14**, 664 (1926).

[32] R. P. Feynman and A. R. Hibbs, *Quantum Mechanics and Path Integrals*, McGraw-Hill, New York, 1965.

[33] L. S. Schulman, *Techniques and Applications of path integration*, John Wiley & Sons, New York, 1981.

[34] M. C. Gutzwiller, *Phase-integral approximation in momentum space and the bound states of an atom*, J. Math. Phys. **8**, 1979–2000 (1967).

[35] M. Morse, *Variational Analysis*, Wiley, New York, 1973.

[36] K. L. Glasser, *Summation over Feynman histories: Charged particle in a uniform magnetic field*, Phys. Rev. **133**(3), B831–834 (1964).

[37] S. Levit and U. Smilansky, *A new approach to Gaussian path integrals and the evaluation of the semiclassical propagator*, Ann. Phys. (N.Y.) **103**, 198–207 (1977).

[38] B. K. Cheng, *Exact evaluation of the propagator for a charged particle in a constant magnetic field*, Physica Scripta **29**, 351–352 (1984).

[39] S. Klama and U. Rössler, *The Green's function of confined electrons in an external magnetic field: analytical formulation*, Ann. Phys. (Leipzig) **1**(6), 460–466 (1992).

[40] M. L. Tiago, T. O. de Carvalho, and M. A. M. de Aguiar, *Boundary integral method for quantum billiards in a constant magnetic field*, Phys. Rev. A **55**(1), 65–70 (1997).

[41] M. V. Berry and K. E. Mount, *Semiclassical approximations in wave mechanics*, Rep. Prog. Phys. **35**, 315–397 (1972).

[42] T. Ueta, *Green's function of a charged particle in magnetic fields*, J. Phys. Soc. Jpn. **61**, 4314–4324 (1992).

[43] M. Abramowitz and I. Stegun, *Handbook of Mathematical Functions*, Dover Publications, New York, 1965.

[44] H. Buchholz, *The Confluent Hypergeometric Function*, Springer-Verlag, Berlin, 1969.

[45] P. M. Morse and H. Feshbach, *Methods of Theoretical Physics*, McGraw-Hill, New York, 1953.

[46] A. Comtet, *On the Landau levels on the hyperbolic plane*, Ann. Phys. (N.Y.) **173**, 185–209 (1987).

[47] A. Comtet, B. Georgeot, and S. Ouvry, *Trace formula for Riemann surfaces with magnetic field*, Phys. Rev. Lett. **71**, 3786–3789 (1993).

[48] T. Tasnádi, *Hard chaos in magnetic billiards (on the hyperbolic plane)*, J. Math. Phys. (1998).

[49] B. Gutkin, *Hyperbolic magnetic billiards on surfaces of constant curvature*, Commun. Math. Phys. **217**, 33–53 (2001).

[50] J. E. Avron, M. Klein, and A. Pnueli, *Hall conductance and adiabatic charge transport of leaky tori*, Phys. Rev. Lett. **69**, 128–131 (1992).

[51] G. V. Dunne, *Hilbert space for charged particles in perpendicular magnetic fields*, Ann. Phys. (N.Y.) **215**, 233–263 (1992).

[52] E. V. Ferapontov and A. P. Veselov, *Integrable Schrödinger operators with magnetic fields: Factorization method on curved surfaces*, J. Math. Phys. **42**, 590–607 (2001).

[53] A. Buchleitner and D. Delande, *Spectral aspects of the microwave ionization of atomic Rydberg states*, Chaos, Solitons & Fractals **5**(7), 1125–1141 (1995).

[54] A. Holle, J. Main, G. Wiebusch, H. Rottke, and K. H. Welge, *Quasi-Landau spectrum of the chaotic diamagnetic hydrogen atom*, Phys. Rev. Lett. **61**, 161–164 (1988).

[55] T. W. Nee and R. E. Prange, *Quantum spectroscopy of the low field oscillations of the surface impedance*, Phys. Lett. **25A**(8), 582–583 (1967).

[56] E. A. Kaner, N. M. Makarov, and I. M. Fuks, *The spectrum and damping of surface electron states in a magnetic field*, Sov. Phys. - JETP **28**(3), 483–488 (1969).

[57] K. von Klitzing, G. Dorda, and M. Petter, *New method for high-accuracy determination of the fine-structure constant based on quantized Hall resistance*, Phys. Rev. Lett. **45**(6), 494–497 (1980).

[58] R. B. Laughlin, *Quantized Hall conductivity in 2 dimensions*, Phys. Rev. B **23**(10), 5632–5633 (1981).

[59] B. I. Halperin, *Quantized Hall conductance, current-carrying edge states, and the existence of extended states in a two-dimensioinal disordered potential*, Phys. Rev. B **25**(4), 2185–2190 (1982).

[60] M. Büttiker, *Absence of backscattering in the quantum Hall effect in multiprobe conductors*, Phys. Rev. B **38**, 9375–9389 (1988).

[61] K. Shizuya, *Edge current in the Quantum Hall Effect*, Phys. Rev. Lett. **73**(21), 2907–2910 (1994).

[62] N. Macris, P. A. Martin, and J. V. Pulé, *On edge states in semi-infinite quantum Hall systems*, J. Phys. A **33**, 1985–1996 (1999).

[63] J. Fröhlich, G. M. Graf, and J. Walcher, *On the extended nature of edge states of Quantum Hall Hamiltonians*, Ann. Henri Poincaré **1**(3), 405–442 (2000).

[64] H. Schulz-Bades, J. Kellendonk, and T. Richter, *Simultaneous quantization of edge and bulk Hall conductivity*, J. Phys. A **33**, L27–L32 (2000).

[65] M. Robnik and M. V. Berry, *Classical billiards in magnetic fields*, J. Phys. A **18**, 1361–1378 (1985).

[66] O. Meplan, F. Brut, and C. Gignoux, *Tangent map for classical billiards in magnetic fields*, J. Phys. A **26**, 237–246 (1993).

[67] N. Berglund and H. Kunz, *Integrability and ergodicity of classical billiards in a magnetic field*, J. Stat. Phys. **83**, 81–126 (1996).

[68] T. Tasnádi, *The behavior of nearby trajectories in magnetic billiards*, J. Math. Phys. **37**(11), 5577–5598 (1996).

[69] T. Tasnádi, *Hard chaos in magnetic billiards (On the Euclidean plane)*, Commun. Math. Phys. **187**, 597–621 (1997).

[70] Z. Kovács, *Orbit stability in billiards in magnetic field*, Phys. Rep. **290**, 49–66 (1997).

[71] A. V. Aivazyan and M. L. Lyubimova, *The Spectrum of stochastic motion in near-circular magnetic billiards.*, Physics–Doklady **42**(12), 641–645 (1997).

[72] L. G. G. V. Dias da Silva and M. A. M. de Aguiar, *Periodic orbits in magnetic billiards*, Europ. Phys. J. B **16**(4), 719–728 (2000).

[73] Y. G. Sinai, *Introduction to Ergodic Theory*, Princeton Univ. Press, 1976.

[74] L. Bunimovich, *On the ergodic properties of certain billiards*, Anal. Appl. **8**, 254–255 (1974).

[75] U. Smilansky, *Semiclassical quantization of chaotic billiards – a scattering approach*, in *Proceedings of the 1994 Les Houches Summer School on "Mesoscopic Quantum Physics"*, edited by E. Akkermans, G. Montambaux, J.-L. Pichard, and J. Zinn-Justin, volume LXI, Elsevier, 1995.

[76] M. V. Berry, *Regular and Irregular Motion*, in *Topics in Nonlinear Mechanics*, edited by S. Jorna, number 46 in Am. Inst. Ph. Conf. Proc., pages 16–120, 1978.

[77] A. J. Lichtenberg and M. A. Lieberman, *Regular and Stochastic Motion*, volume 38 of *Applied Mathematical Sciences*, Springer-Verlag, Berlin, 1983.

[78] B. Gutkin, U. Smilansky, and E. Gutkin, *Hyperbolic billiards on surfaces of constant curvature*, Commun. Math. Phys. **208**(1), 65–90 (1999).

[79] M. V. Berry, *Quantizing a classically ergodic system: Sinai's billiard and the KKR method*, Ann. Phys. (N.Y.) **131**, 163–216 (1981).

[80] H. Primack and U. Smilansky, *Quantization of the three-dimensional Sinai billiard*, Phys. Rev. Lett. **74**, 4831–4834 (1995).

[81] S. D. Prado, M. A. M. de Aguiar, J. P. Keating, and R. Egydio de Carvalho, *Semiclassical theory of magnetization for a two-dimensional non-interacting electron gas*, J. Phys. A **27**, 6091–6106 (1994).

[82] M. E. Rensink, *Electron eigenstates in uniform magnetic fields*, Am. J. Phys. **37**(9), 900–904 (1969).

[83] J. Blaschke and M. Brack, *Periodic orbit theory of a circular billiard in homogeneous magnetic fields*, Phys. Rev. A **56**(1), 182–194 (1997), Erratum in Phys. Rev. A **57**, 3136 (1997).

[84] R. Narevich, R. E. Prange, and O. Zaitsev, *Square billiard with a magnetic flux*, Phys. Rev. E **62**(2), 2046–2059 (2000).

[85] V. Krusche, *Das Quadrat- und Rechteck-Billard im Magnetfeld*, PhD thesis, Universität Ulm, 2000.

[86] N. S. Koshlyakov, M. M. Smirnov, and E. B. Gliner, *Differential Equations of Mathematical Physics*, North-Holland, Amsterdam, 1964.

[87] R. Balian and C. Bloch, *Distribution of eigenfrequencies for the wave equation in a finite domain: I. Three-dimensional problem with smooth boundary surface*, Ann. Phys. (N.Y.) **60**, 401–447 (1970), Erratum in Ann. Phys. **84**, 559-563 (1974).

[88] M. Sieber, H. Primack, U. Smilansky, I. Ussishkin, and H. Schanz, *Semiclassical quantization of billiards with mixed boundary conditions*, J. Phys. A **28**, 5041–5078 (1995).

[89] E. Akkermans, J. E. Avron, R. Narevich, and R. Seiler, *Boundary conditions for bulk and edge states in Quantum Hall systems*, Europ. Phys. J. B **1**(1), 117–121 (1998).

[90] H. P. Baltes and E. R. Hilf, *Spectra of Finite Systems*, B.I.-Wissenschaftsverlag, Mannheim, 1978.

[91] N. Macris, P. A. Martin, and J. V. Pulé, *Large volume asymptotics of Brownian integrals and orbital magnetism*, Ann. Inst. Henri Poincaré Physique théorique **66**(2), 147–183 (1997).

[92] R. Narevich and D. Spehner, *Weyl expansion of a circle billiard in a magnetic field*, J. Phys. A **32**(19), L227–L230 (1999).

[93] M. V. Berry and C. J. Howls, *High orders of the Weyl expansion for quantum billiards: resurgence of periodic orbits, and the Stokes phenomenon*, Proc. Roy. Soc. Lond. A **447**, 527–555 (1994).

[94] R. Peierls, *Surprises in Theoretical Physics*, Princeton University, New Jersey, 1970.

[95] H.-J. van Leeuwen, *Problemès de la théorie électronique du magnétisme*, Le Journal de Physique el le Radium **Série VI**(12), 261–377 (1921).

[96] N. W. Ashcroft and N. D. Mermin, *Solid state physics*, Saunders College, Fort Worth, 1976.

[97] J. van Ruitenbeek and D. A. van Leeuwen, *Size effects in orbital magnetism*, Mod. Phys. Lett. B **7**(16), 1053–1069 (1993).

[98] H. Kunz, *Surface Orbital Magnetism*, J. Stat. Phys. **76**, 183–207 (1994).

[99] P. John and L. G. Suttorp, *Boundary effects in a magnetized free-electron gas: Green function approach*, J. Phys. A **28**(21), 6087–6097 (1995).

[100] R. Narevich, D. Spehner, and A. Akkermans, *Heat kernel of integrable billiards in a magnetic field*, J. Phys. A **31**, 4277–4287 (1998).

[101] F. von Oppen, *Magnetic susceptibility of ballistic microstructures*, Phys. Rev. B **50**(23), 17151–17161 (1994).

[102] O. Agam, *The magnetic response of chaotic mesoscopic systems*, J. Phys. I France **4**, 697–730 (1994).

[103] D. Ullmo, K. Richter, and R. A. Jalabert, *Orbital magnetism in ensembles of ballistic billiards*, Phys. Rev. Lett. **74**(3), 383–386 (1995).

[104] K. Richter and B. Mehlig, *Orbital magnetism of classically chaotic quantum systems*, Europhys. Lett. **41**(6), 587–592 (1998).

[105] K. Tanaka, *Semiclassical study of the magnetization of a quantum dot*, Ann. Phys. (N.Y.) **268**, 31–60 (1998).

[106] K. Richter, *Semiclassical theory of mesoscopic quantum systems*, volume 161 of *Springer Tracts in Modern Physics*, Springer-Verlag, Berlin, 2000.

[107] R. E. Kleinman and G. F. Roach, *Boundary integral equations for the three-dimensional Helmholtz equation*, SIAM Review **16**(2), 214–236 (1974).

[108] R. J. Riddell, *Boundary-distribution solution of the Helmholtz equation for a region with corners*, J. Comp. Phys. **31**, 21 (1979).

[109] M. V. Berry and M. Wilkinson, *Diabolical points in the spectra of triangles*, Proc. Roy. Soc. Lond. A **392**, 15–43 (1984).

[110] P. A. Boasman, *Semiclassical accuracy for billiards*, Nonlinearity **7**, 485–537 (1994).

[111] I. Kosztin and K. Schulten, *Boundary integral method for stationary states of two-dimensional quantum systems*, Int. J. Mod Phys. C **8**(2), 293–325 (1997).

[112] B. W. Li, M. Robnik, and B. Hu, *Relevance of chaos in numerical solutions of quantum billiards*, Phys. Rev. E **57**(4), 4095–4105 (1998).

[113] S. W. McDonald and A. N. Kaufman, *Wave chaos in the stadium: Statistical properties of short-wave solutions of the Helmholtz equation*, Phys. Rev. A **37**(8), 3067–3086 (1988).

[114] P. A. Martin, *Acoustic scattering and radiation problems, and the null-field method*, Wave Motion **4**, 391–408 (1982).

[115] K. Hornberger and U. Smilansky, *The boundary integral method for magnetic billiards*, J. Phys. A **33**, 2829–2855 (2000).

[116] M. Guiggiani, *Formulation and numerical treatment of boundary integral equations with hypersingular kernels*, in *Singular Integrals in Boundary Element Methods*, edited by V. Sladek and J. Sladek, Computational Mechanics Publications, Billerica, 1998.

[117] G. H. Golub and C. F. van Loan, *Matrix Computations*, Johns Hopkins University Press, Baltimore, 1983.

[118] O. Bohigas, *Random matrices and chaotic dynamics*, In Giannoni et al. [6].

[119] M. Berry, *Semiclassical theory of spectral rigidity*, Proc. Roy. Soc. Lond. A **400**, 229–251 (1985).

[120] N. Argaman, Y. Imry, and U. Smilansky, *Semiclassical analysis of spectral correlations in mesoscopic systems*, Phys. Rev. B **47**(8), 4440–4457 (1993).

[121] B. Helffer and A. Morame, *Magnetic bottles in connection with superconductivity*, Preprint, 2000.

[122] M. V. Berry and M. Tabor, *Calculating bound spectrum by path summation in action-angle variables*, J. Phys. A **10**, 371–379 (1977).

[123] R. Balian and C. Bloch, *Distribution of eigenfrequencies for the wave equation in a finite domain: III. Eigenfrequency density oscillations*, Ann. Phys. (N.Y.) **69**, 76–160 (1972).

[124] E. B. Bogomolny, *Semiclassical quantization of multidimensional systems*, Nonlinearity **5**, 805–866 (1992).

[125] E. Doron and U. Smilansky, *Semiclassical quantization of chaotic billiards: a scattering theory approach*, Nonlinearity **5**, 1055–1084 (1992).

[126] B. Georgeot and R. E. Prange, *Exact and semiclassical Fredholm solutions of quantum billiards*, Phys. Rev. Lett. **74**, 2851–1854 (1995).

[127] T. Harayama, A. Shudo, and S. Tasaki, *Semiclassical Fredholm determinant for strongly chaotic billiards*, Nonlinearity **12**, 1113–1149 (1999).

[128] M. Sieber, *Billiard systems in three dimensions: the boundary integral equation and the trace formula*, Nonlinearity **11**, 1607–1623 (1998).

[129] M. Marcus and H. Minc, *A Survey of Matrix Theory and Matrix Inequalities*, Dover Publishing, New York, 1992.

[130] T. Harayama and A. Shudo, *Zeta function derived from the boundary element method*, Phys. Lett. A **165**, 417–426 (1992).

[131] S. Tasaki, T. Harayama, and A. Shudo, *Interior Dirichlet eigenvalue problem, exterior Neumann scattering problem, and boundary element method for quantum billiards*, Phys. Rev. E **56**(1), R13–R16 (1997).

[132] M. Sieber, N. Pavloff, and C. Schmit, *Uniform approximation for diffractive contributions to the trace formula in billiard systems*, Phys. Rev. E **55**(3), 2279–2299 (1997).

[133] S. C. Creagh and R. G. Littlejohn, *Semiclassical trace formulas in the presence of continuous symmetries*, Phys. Rev. A **44**, 836–850 (1991).

[134] L. D. Landau and E. M. Lifshitz, *Quantum mechanics*, volume 3 of *Course of theoretical physics*, Butterworth-Heinenann, Oxford, 1975.

[135] E. C. Titchmarsch, *Introduction to the theory of Fourier integrals*, Clarendon Press, Oxford, 1948.

[136] T. A. Brody, J. Flores, J. B. French, P. Mello, A. Pandey, and S. Wong, *Random-matrix physics - Spectrum and strength fluctuations*, Rev. Mod. Phys. **53**(3), 385–479 (1981).

[137] J. M. Robbins, *Discrete symmetries in periodic-orbit theory*, Phys. Rev. A **40**(4), 2128–2136 (1989).

[138] K. Hornberger and U. Smilansky, in preparation.

[139] A. Erdélyi, *Asymptotic Expansions*, Dover, New York, 1956.

[140] N. Bleistein and R. A. Handelsman, *Asymptotic expansions of integrals*, Holt, Rinehart and Watson, New York, 1975.

[141] W. Magnus, F. Oberhettinger, and R. P. Soni, *Formulas and Theorems for the Special Functions of Mathematical Physics*, Springer-Verlag, Berlin, 3rd edition, 1966.

Name	Klaus Hornberger
Geburtsdatum	12. August 1971
Geburtsort	München
Familienstand	ledig

Schulbildung

1978 – 1982	Eduard-Spranger-Grundschule München
1982 – 1991	Lion-Feuchtwanger-Gymnasium München
10. Juli 1991	**Abitur** Leistungskurse Mathematik und Physik Grundkurse Englisch und Geschichte
1991 – 1992	Wehrdienst

Studium der Physik

1992 – 1997	Ludwig-Maximilians-Universität München
28. April 1994	**Physik Vordiplom**
12. August 1997	**Physik Diplom** Betreuer Dr. A. Buchleitner und Prof. A. Schenzle “Strahlungszerfall nichtdispergierender Wellenpakete” angefertigt am Max-Planck-Institut für Quantenoptik
Sep. – Dez. 1997	freier Mitarbeiter am MPI für Quantenoptik

Promotion in Physik

Feb. 1998 – März 2000	Weizmann Institute of Science, Rehovot, Israel Betreuer Prof. U. Smilansky
April 2000 – Mai 2001	MPI für Physik komplexer Systeme, Dresden Betreuer Priv. Doz. A. Buchleitner
17. Mai 2001	**Promotion** an der Fakultät für Physik der LMU München

Stipendien

Feb. 1995 – Aug. 1997	Studienstiftung des deutschen Volkes
Feb. 1998 – März 2000	Minerva Stipendium